GUIDING DEVELOPMENT OF FUEL CELL CATALYSTS WITH

STATISTICALLY ROBUST TRANSMISSION ELECTRON MICROSCOPY

A Dissertation

Presented to the Faculty of the Graduate School

Of Cornell University

In Partial Fulfillment of the Requirements for the Degree of

Doctor of Philosophy

by

Elliot Scott Padgett

August 2019

GUIDING DEVELOPMENT OF FUEL CELL CATALYSTS WITH

STATISTICALLY ROBUST TRANSMISSION ELECTRON MICROSCOPY

Elliot Scott Padgett, Ph. D.

Cornell University 2019

Hydrogen fuel cells in fuel cell electric vehicles (FCEVs) are a promising technology to reduce, and eventually eliminate, carbon dioxide emissions from transportation. The Pt nanoparticles used to catalyze the fuel cell's electrochemical reactions are an important limiting factor because at present levels, the cost of the Pt catalyst will prevent widespread adoption of FCEVs. Catalysts must be developed to reduce the amount of Pt while meeting vehicle power demands even after many years of use.

Strategically improving catalysts requires detailed and statistically robust characterization of their microscopic structure to understand the connections between catalyst synthesis, structure, performance, and durability. This dissertation presents the development and application of (scanning) transmission electron microscopy ((S)TEM) techniques to guide advancement of catalysts through nanostructural characterization.

We develop a robust strain mapping technique for complex catalyst specimens. We deploy a new exit wave power cepstrum (EWPC) transform to nanobeam electron diffraction (NBED) patterns to enable precise, high-throughput, dose-efficient strain measurement. This approach is suitable for statistically representative measurements of many particles without special requirements such as zone-axis orientation. We apply this strain mapping technique to core-shell Pt-Co nanoparticles in combination with a continuum elastic theory model and demonstrate two mechanisms contributing to the relaxation of strain at the catalyst surface:

lattice dislocations and Poisson expansion due to the spherical geometry. Comparison with electrochemical measurements suggests that the geometrical Poisson relaxation accounts for the activity of catalysts with thin shells, but catalysts with thick shells experience additional activity loss from dislocation-driven relaxation.

We then turn to the larger-scale catalyst structure, investigating the impact of porous carbon support morphology, local reactant transport, and catalyst durability. Using statistical analysis of STEM images, we compare Pt and Pt-Co catalysts on porous and solid carbon supports. Comparison of 3D tomographic images and electrochemical accessibility measurements indicated that carbon pores prevent ionomer adsorption for particles embedded within them, improving the catalyst activity, while allowing proton access through condensed water. By comparing images and composition maps before and after electrochemical stability tests, we find that porous carbon supports suppress Pt particle coalescence, accounting for improved overall durability.

BIOGRAPHICAL SKETCH

Elliot Padgett was born in Denver, Colorado to Bruce Padgett and Dr. Carolyn Burkhardt-Padgett. He was raised in Castle Rock, Colorado by Bruce and Carolyn along with his older brother Julian. Elliot attended Swarthmore College and earned a B.A. in physics with a minor in computer science in 2013. During the summer and fall of 2012, he engaged in computational research into the jamming transition in granular systems under the supervision of Prof. Andrea Liu at University of Pennsylvania and Prof. Amy Graves at Swarthmore College. During his undergraduate studies, Elliot became motivated to help address climate change through his career and sought out graduate programs that would provide opportunities to contribute to research for clean energy technologies. In 2013 Elliot began graduate studies in applied physics at Cornell University and received a M.S. in 2017 and Ph.D. in 2019. His graduate research was supervised by Prof. David Muller and focused on the development and application of advanced transmission electron microscopy techniques for nanomaterials used in fuel cells and other electrochemical energy systems. After completing research at Cornell, Elliot will move to Washington, DC with his wife Megan Holtz to begin a fellowship at the U.S. Department of Energy Fuel Cell Technologies Office.

To my parents, who taught me to discover and care for the Earth, leading me to begin this dissertation.

To Megan, whose love and support allowed me to complete it.

ACKNOWLEDGEMENTS

The work presented in this dissertation could not have happened without the generous support and guidance of my advisor and committee chair, Prof. David Muller. I set out for graduate school with the dream of pursuing clean energy-related research, and Prof. Muller quickly welcomed me into his group and allowed me to live that dream. His management put state the art techniques and equipment at my disposal and granted me considerable independence to engage in truly unique research. I want to thank my minor committee members, Prof. Lena Kourkoutis and Prof. Héctor Abruña. Beyond serving on my committee, they contributed greatly to my professional development and to the work presented in this dissertation. Prof. Kourkoutis and her group members helped make a big and vibrant electron microscopy community at Cornell, expanding space for exchange of ideas, expertise, and food at the annual summer picnic. Prof. Héctor Abruña welcomed me into his lab and group meetings to help me broaden my horizons into the worlds of electrochemistry and nanoparticle synthesis.

Many Muller group members have contributed to the work in this dissertation in a variety of ways and made the Muller group a productive place to work. I am especially grateful to the more senior group members who dedicated significant time to train and mentor me, including Robert Hovden, Megan Holtz, Pinshane Huang, and Julia Mundy. I also want to particularly thank the group members who made significant direct contributions to the research presented in this dissertation. In particular, Megan Holtz contributed to the electron energy loss spectroscopy methods development and data acquisition for Chapters 2 and 5, as well as experiments and development of strain mapping methods and software for Chapters 2 and 3. Megan also contributed extensive editing of this dissertation and related journal publications as well as discussion and planning of research projects. Paul Cueva introduced the concept of cepstral analysis for scanning transmission electron diffraction and helped realize its application to

techniques including strain mapping for Chapters 2 and 3. Robert Hovden trained me to do electron tomography and passed on a very useful body of MATLAB code that was essential for the work presented in Chapters 4 and 5 and Appendices B and C. Robert also posed the original challenge that led to the novel tomography techniques presented in Appendix C and spearheaded the development of the open source *tomviz* software, which was used to create the 3D renderings of tomography results throughout this dissertation. Yi Jiang helped investigate reconstruction algorithms and develop software to address the electron tomography challenges confronted in Chapters 4 and 5 and Appendices B and C.

I was fortunate to work with two excellent undergraduate students in the Muller group, Nina Andrejevic and Matthew Ko, who both helped share the burden of acquiring and processing electron tomography data and put in the initiative to steer their projects in interesting new directions. I also had the opportunity to work with multiple visiting summer researchers, including Vera Beermann, from Peter Strasser's research group at Technischen Universität Berlin, Rubén Rizo from Elena Pastor's group a La Universidad de La Laguna, and Connor Cash, who was taking a sabbatical from the world of renewable energy finance and business. These visiting researchers brought both productive collaborations and valuable outside perspective. Many other group members contributed through interesting discussions, related research work, keeping the lab running, and assisting me in times of need including Celesta Chang, Michael Cao, Zhen Chen, Gabriela Calinao Correa, Yu-Tsun Shao, Xiyue Zhang, Krishnan Chandler, Barnaby Levin, Qingyun Mao, Yimo Han, and Kayla Nguyen.

The Kourkoutis group, especially Katherine Spoth, played an important role in enabling the cryo-tomography experiments presented in Chapter 4. Many other Kourkoutis group members contributed help in the lab and interesting, useful discussions, including Michael Zachman, Berit

Goodge, Ismail El Baggari, Jade Noble, Ben Savitzky, David Baek, Michelle Smeaton, Yue Yu, Taylor Moon, and William Xu.

In Abruña group, Ryo Wakabayashi, Hongsen Wang, Yao Yang all generously took time to help me learn to navigate the chemistry lab, alongside many others who provided interesting opportunities for discussion and collaboration, including Seung-Ho Yu, James McKone, Yin Xiong, Na Zhang, Johary Rivera-Meléndez, Luxi Shen, Dong Ren, Rebecca Potash, James Pastore, and Abby Van Wassen.

My time at Cornell was enriched by the broader materials research community at Cornell as well, with several individuals and research groups deserving thanks. Prof. Frank DiSalvo made his lab available to me as I was exploring nanomaterials synthesis and very patiently shared his extensive knowledge of materials synthesis and solid-state chemistry through several long discussions with me. Jessica DaSilva in Prof. Tobias Hanrath's research group provided gold-decorated strontium titanate nanocube samples and thoughtful troubleshooting related to surface adhesion issues for the work in Appendix C. Eric Langenberg in Prof. Darrell Schlom's research group provided the strained lead titanate films, a relatively well-defined but interesting system, for the development of strain mapping methods presented in Chapter 2. I would like to thank Earl Kirkland for his efforts teaching me and other students about both the theory and practical aspects of electron microscopy.

The work in this dissertation could not have been done without the staff members of the Cornell Center for Materials Research (CCMR) who keep the labs running, and spend countless hours training students, troubleshooting equipment, and resolving crises in the lab. I would particularly like to thank John Grazul, who taught me to prepare samples using the ultramicrotome, managed the microscopes I used for the bulk of the work presented in Chapters 4 and 5, and graciously helped whenever problems arose, even on holidays when more sensible

graduate students would not have been in the lab. Mariena Silvestry Ramos managed the primary instrument used for Chapters 2 and 3. Mick Thomas, Don Werder, and Phil Carubia have all also provided indispensable help at various times during my time at Cornell.

I am grateful for the opportunities I had for extensive collaboration with researchers at General Motors (GM), whose contributions were essential to much of the work presented in this dissertation. The collaboration with GM was ideal in many ways for research presented in this dissertation, as the scale of the fuel cell research resources at GM allowed them to provide consistent, reproducible measurements of materials' properties and performance, which was essential to make those measurements comparable to quantitative microanalysis. I would like to thank Anusorn "Anu" Kongkanand and Zhongyi "Vic" Liu, who led the GM research collaborations with Cornell. The opportunity to collaborate with Anu was extremely valuable to me. Anu was generous with his time and knowledge, and patiently discussed the broad science and engineering aspects of our project to both deepen my understanding and lead the project to new insights. When I expressed interest in studying strain effects in practical catalyst materials, Anu helped plan experiments including making and testing a new series of catalysts, resulting in Chapter 3 of this dissertation, for which I am deeply grateful. Many members of the fuel cell research team at GM had contributed as well, including Venkata Yarlagadda, Ratandeep Kukreja, Wenbin Gu, Swami Kumaraguru, Joseph Ziegelbauer, and Thomas Moylan. I would also like to thank the contributions of Koji Moriyama at Honda, which is partnered with GM on fuel cell research and development. The GM and Honda fuel cell research teams provided catalyst and device samples used for the work in Chapters 1-5, and Appendix C, as well as measurements and insights on materials and devices for Chapters 3-5.

I am grateful for the efforts of Marcus Hanwell, Shawn Waldon, Cory Quammen, and others at Kitware in developing the open source *tomviz* software for electron tomography, which was

TABLE OF CONTENTS

LIST OF FIGURES

LIST OF TABLES

1 INTRODUCTION

1.1 Hydrogen Fuel Cell Electric Vehicles

Addressing climate change will require essentially complete elimination of greenhouse gas emissions from human activities in the coming decades.[1] Transportation is one of the largest sources of greenhouse gas emissions, especially in the United States where it accounted for 29% of emissions in 2017, more than any other sector.[2][a] The large majority of these transportation emissions are from internal combustion engines (ICEs) in cars, trucks, and other vehicles burning petroleum-based fuels.

The ICE has become ubiquitous in large part because of the extraordinarily high energy density of petroleum fuels. However, if we are to eliminate carbon dioxide emissions from transportation, the ICE cannot continue to dominate the market. Capturing and sequestering emissions from small-scale, disperse vehicles burning fossil fuels is not practical. Biofuels with zero net lifecycle emissions may play a role, but they are limited by the availability of agricultural land and will likely need to be reserved for the most demanding applications, such as aviation. The ICE will thus need to be replaced with a zero-emission alternative for the majority of vehicles.

Electrochemical power systems, including lithium-ion batteries and hydrogen fuel cells, are the most promising approach to cleanly power the majority of transportation. Both batteries and fuel cells convert stored chemical energy directly to electricity, as illustrated in Figure 1.1, to power

---

[a] Worldwide, transportation emissions account for a somewhat smaller fraction, around 14% in 2010,[1] but this share likely to increase as many developing economies will likely become more similar to US.

electric vehicles with no direct emissions.[b] For batteries, the chemical energy is stored internally in the electrode materials, while for fuel cells the chemical energy is stored externally as hydrogen fuel. Both battery and fuel cell electric vehicles (BEVs and FCEVs) provide much higher overall energy efficiency than ICE vehicles. The energy densities of their electrochemical power systems are also high enough that with their higher energy conversion efficiencies they can have a comparable range to ICE vehicles.
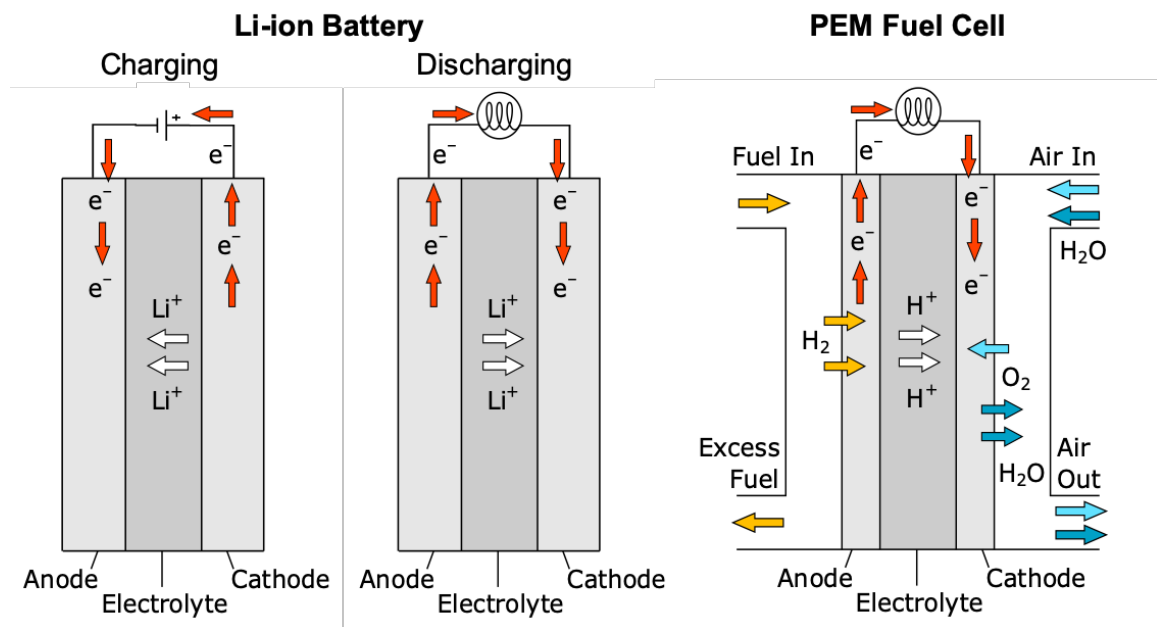
Figure 1.1: Schematic illustration of operation of lithium-ion batteries (left) and proton exchange membrane (PEM) fuel cells (right).

---

[b] There are fuel cell systems that use carbon-containing fuels such as direct ethanol/methanol fuel cells, hydrogen fuel cells with onboard reformers, and methane-fueled solid oxide fuel cells, and these do generate carbon dioxide emissions. Beyond their emissions drawbacks, these systems are also generally less practical for most transportation applications and will not be considered here.

The overall emissions of BEVs and FCEVs depend on their original energy source. BEV emissions come from the source used to generate the electricity that they are charged with. FCEVs require hydrogen fuel, which can be generated by several methods, such as water electrolysis using electricity or by reforming methane or other fossil fuels to produce hydrogen and carbon dioxide. Either BEVs or FCEVs will thus be emissions free if clean energy sources or emissions-capture are employed, providing a path to future emissions-free transportation. Presently neither is emissions-free because of the continued widespread use of fossil fuels for electricity generation without carbon capture. However, because of the high efficiency of their electrochemical power systems, both BEVs and FCEVs currently provide large reductions in emissions in comparison to ICE vehicles essentially everywhere in the US.[3–5]

While batteries and fuel cells are in some sense competing in the space of clean transportation technologies, they are optimal for different types of applications, making them complementary technologies. The differing advantages of BEVs and FCEVs are a result of the differences in how each system stores energy, giving them different scaling relationships between the vehicle range and cost, illustrated in Figure 1.2. A rechargeable battery is both an energy conversion and energy storage device, which makes the BEV system simple with low baseline cost. However, adding energy storage capacity to extend a vehicle's range requires adding more batteries, making system cost scale quickly and leading batteries to ultimately dominate the cost of long-range BEVs. A fuel cell decouples energy conversion from energy storage. This results in a large upfront system cost to provide both hydrogen storage and a fuel cell large enough to provide sufficient power for the vehicle, but adding additional fuel storage capacity is relatively inexpensive, making the overall cost scale slowly with the vehicle range. As shown in Figure 1.2, this provides BEVs with a cost advantage for applications requiring a relatively short range, like personal cars, and FCEVs with a cost advantage for applications requiring a longer range, like freight trucks and buses.
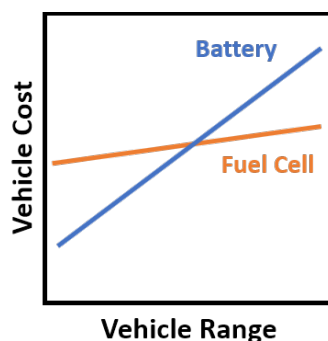
Figure 1.2: Illustration of scaling relationships between cost and range for battery and fuel cell electric vehicles.

Both BEVs and FCEVs are early in their commercialization, although BEVs are starting to see significant commercial success. Worldwide, there are around 10,000 FCEVs,[6] 3 million BEVs,[7] and 1.3 billion ICE vehicles[8]. Both BEVs and FCEVs have been clearly demonstrated as viable replacements for ICE vehicles, although they will need further cost reductions to compete at a large scale. FCEVs are especially in need of continued research and development efforts to reduce cost. This includes improving the fuel cell and its related system components, as well as the infrastructure for the production and distribution of hydrogen fuel. Many factors contributing to the cost of fuel cells and related technologies will be improved by economies of scale as production ramps up to high volumes. However, fuel cells also rely on some expensive, scarce materials – notably platinum, which is used for electrochemical catalysis – that may become more limiting as fuel cells become widespread. The improvement of these catalyst materials is a critical area for fuel cell research and development, and one of the primary objectives of this dissertation. In particular, efforts must focus on improving the cost, durability, and performance[c] of fuel cell catalyst

---

[c] I will use the general term "performance" to refer to both the energy conversion efficiency and power.

materials. These three factors are closely related and are to some degree interchangeable: improving the performance or durability of the catalyst allows less material to be used, reducing cost.

This introduction will briefly discuss typical fuel cell architecture and materials, the factors impacting fuel cell performance, the needs for fuel cell catalyst engineering, and transmission electron microscopy methods used to guide the development of fuel cell catalyst materials. Several textbooks are available providing a broad introduction to fuel cell technologies, such as O'Hayre et al.,[9] including different types of fuel cells that utilize different fuels, reactions, and materials. Our focus will be on hydrogen-fueled proton-exchange membrane fuel cells, which are well suited to transportation applications due to their near room-temperature operation and high power density. We will cover topics needed to understand how the catalyst microstructure impacts the cell performance and durability, which are the main topics of this dissertation, and other important topics will be covered only briefly. The chapter will conclude by outlining the dissertation.

1.2 Fuel Cell Architecture and Materials

The overall reaction performed by a hydrogen fuel cell is the same as the combustion of hydrogen: $2H_2 + O_2 \rightarrow 2H_2O$. However, the fuel cell extracts electricity by splitting this into two electrochemical half-reactions that push electrons through an external circuit. One side of the fuel cell – the anode or fuel electrode – splits hydrogen into protons and electrons, while the other – the cathode or air electrode – combines protons, electrons, and oxygen into water.
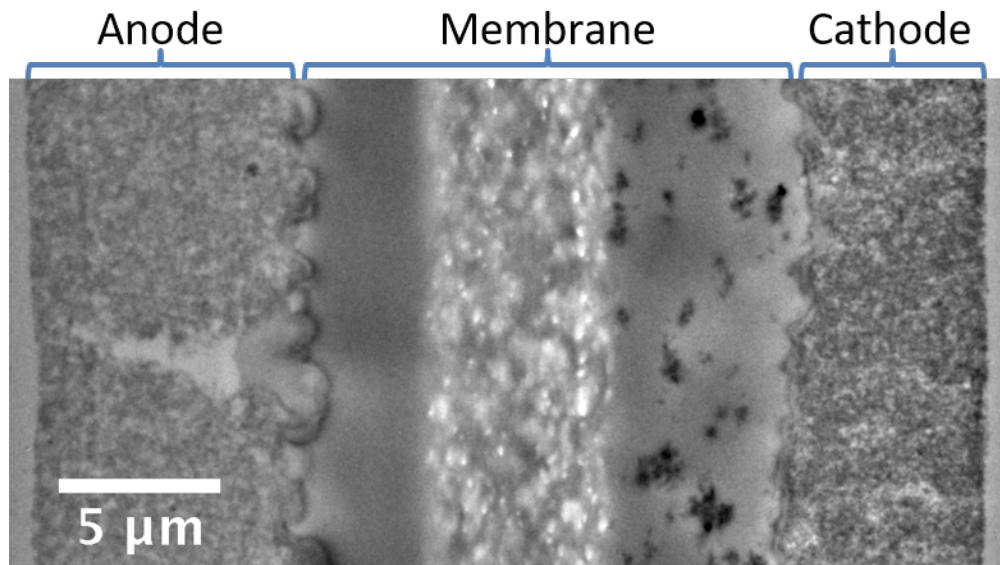
Figure 1.3: Cross-section of a fuel cell membrane electrode assembly (MEA) imaged in a transmission electron microscope. The MEA consists of an anode (left), membrane (center), and cathode (right). The membrane in this case includes engineered structures to improve mechanical stability and reduce gas crossover.

Separating these half reactions requires a medium that conducts protons but not electrons. Some fuel cells use an aqueous electrolyte for this purpose, but this results in a relatively bulky and low-power fuel cell. The material best suited to compact, high-power fuel cells is a polymer electrolyte membrane or proton exchange membrane (PEM), which is made from a proton-conducting polymer that is processed into a thin, flexible sheet. The most common membrane material is Nafion, which has a fluorocarbon backbone to provide mechanical strength and sulfonic acid sidechains to provide proton conductivity. To minimize resistance, fuel cell membranes are generally made as thin as possible while retaining mechanical integrity and limiting the diffusive crossover of reactant gases, with modern membranes being less than 20 μm thick. The anode-membrane-cathode sandwich is called a membrane electrode assembly (MEA). Figure 1.3 shows a cross-section of an automotive fuel cell MEA imaged in a transmission electron microscope.

For practical systems, many MEAs are connected in series in a fuel cell stack. Fuel cell stacks also include additional components, including porous diffusion media that help distribute gasses evenly across the electrodes and bipolar plates that connect adjacent cells, but these will not be covered in this thesis.
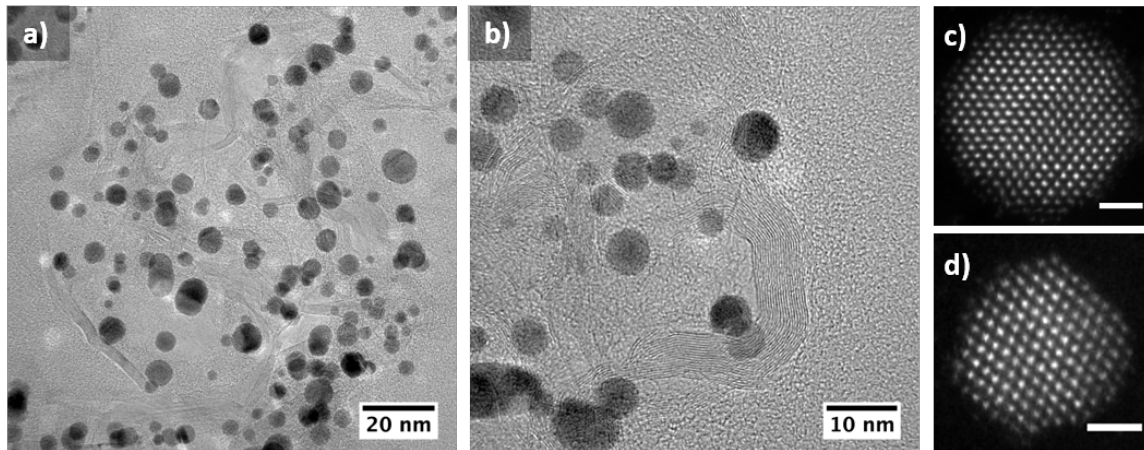
Figure 1.4: Images of fuel cell catalyst nanoparticles in a cross-section of the cathode from a Toyota Mirai, a commercially available fuel cell vehicle. (a,b) Bright-field transmission electron microscopy images showing Pt-Co nanoparticles on a highly graphitic carbon support with a complex, open structure. Fringes visible in the carbon support correspond to planes in the graphitic structure. The carbon support and Pt-Co particles are embedded within an amorphous epoxy. (c,d) Aberration corrected high-angle annular dark field scanning transmission electron microscopy images of individual Pt-Co nanoparticles showing their atomic lattice. Scale bars are 1 nm.

The electrochemical half-reactions that occur in the fuel cell electrode take place on the surface of an electrocatalyst (often simply called a catalyst). Platinum is an effective catalyst for both fuel cell half-reactions, and composite materials containing platinum are the most common catalysts for high-power fuel cells. To reduce the cost and improve the power density of the catalyst, the platinum is made into nanoparticles, which provide a very high active surface area, commonly in the range of $50 - 100$ m^2/g$_{Pt}$. It is also necessary to ensure that protons, electrons, and gas all have pathways to reach the catalyst surface. To achieve this, the catalyst nanoparticles are typically

supported on a nanostructured carbon black, called the catalyst support or carbon support. Carbon supports are moderately good electron conductors and provide a path connecting the catalyst particles to the external circuit. Figure 1.4 shows images of Pt-Co catalyst nanoparticles and carbon supports in the cathode of a Toyota Mirai, a commercially available fuel cell vehicle.[10,11]

Assembled into a fuel cell electrode, carbon blacks also make an open, porous structure that allows gas to travel through the electrode to or from the catalyst surface. Proton conduction in the electrodes is provided by a proton-conducting polymer, called ionomer, that is chemically similar to the membrane (typically also Nafion) but is coated on the catalyst and carbon support. Figure 1.5 shows a schematic illustration of the transport pathways in the anode and cathode for protons, electrons, and gas through the ionomer, carbon support, and voids, respectively.
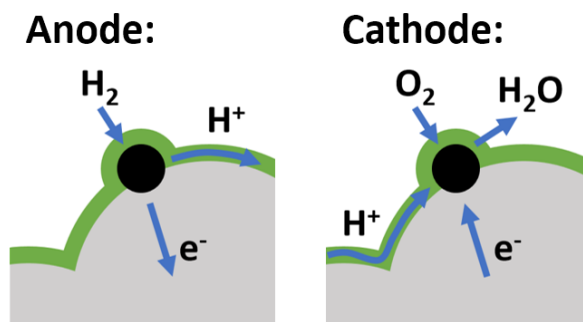
Figure 1.5: Illustration of transport pathways in a fuel cell anode (left) and cathode (right) to and from Pt (black) nanoparticles on a carbon support (grey) coated with ionomer (green). Electrons are conducted through the carbon support and protons through the ionomer. Hydrogen, oxygen, and water vapor diffuse through voids in the electrode and through ionomer coating the catalyst.

1.3   Factors in Fuel Cell Performance

This section describes the four general factors which together determine the current-voltage function that describes a fuel cell's performance, illustrated in Figure 1.6. In short, the theoretical

maximum voltage of the fuel cell is determined by the thermodynamics of the cell reactions, but losses from Ohmic resistance, reaction kinetics, and mass transport all contribute to voltage drops that grow with the cell current.
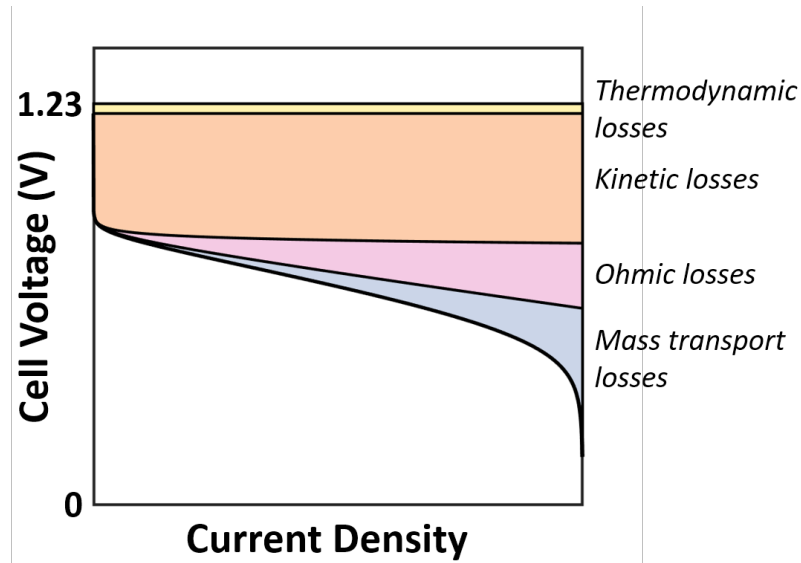
Figure 1.6: Current-voltage plot illustrating the different factors contributing to fuel cell performance. The standard open cell voltage is 1.23 V and non-standard thermodynamic conditions, reaction kinetics, Ohmic resistance, and mass transport all contribute losses that decrease the cell potential.

1.3.1 Fuel Cell Thermodynamics

The starting point for determining the performance of a fuel cell is its reversible or open cell voltage, which is the thermodynamic maximum voltage across the cell if it is if operated to provide an infinitesimal current so that there are no "unnecessary" losses. This cell voltage is determined by the two half reactions taking place at the cell's electrodes, the hydrogen oxidation reaction (HOR):

$$H_2 \rightarrow 2H^+ + 2e^-, \qquad E^0_{HOR} = 0 \text{ V}, \tag{1.1}$$

9

and the oxygen reduction reaction (ORR):

$$\frac{1}{2}O_2 + 2H^+ + 2e^- \rightarrow H_2O, \qquad E^0_{ORR} = 1.23 \text{ V}, \qquad (1.2)$$
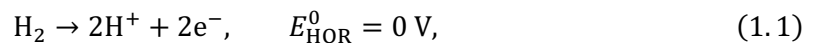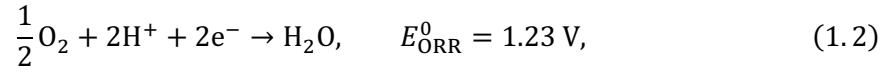
where E^0_{HOR} and E^0_{ORR} are the standard electrode potentials of the two reactions, respectively, corresponding to room temperature, atmospheric pressure, and unit activity for all reactants and products. Together, these make the overall cell reaction

$$H_2 + \frac{1}{2}O_2 \rightarrow H_2O, \qquad E^0 = 1.23 \text{ V}, \qquad (1.3)$$
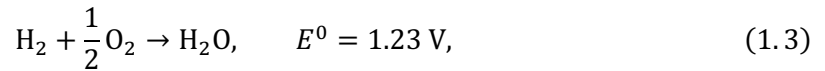
where E^0 is the reversible cell potential under the same standard conditions. In general, fuel cells are operated at non-standard conditions, with typical PEM fuel cells using operating temperatures around 80°C, pressures around 2-3 bar, and air, which contains around 20% oxygen. The electrode and cell potentials for non-standard conditions can be calculated using the Nernst equation and a thermodynamic correction for the temperature and entropy change for the overall reaction. However, the typical PEM fuel cell conditions only change the reversible cell potential by around 10-20 mV, making them minor considerations in the overall performance. For practical purposes it is sufficient to remember 1.23 V as the thermodynamic maximum cell voltage.

1.3.2 *Ohmic resistance*

The simplest significant contribution to fuel cell voltage losses is Ohmic resistance, which scales linearly with the current. The largest contribution to the overall cell resistance is typically the proton exchange membrane. The membrane conductivity is impacted by operating conditions such as humidity and temperature, and metal ions such as Co^{2+} and Ni^{2+} that have leached from the catalyst can displace protons in the membrane to degrade the conductivity. Ion conduction in the

electrode ionomer may also contribute somewhat to the overall cell resistance. Electronic resistance in the electrodes is usually negligible with carbon catalyst supports but may be significant if non-carbon supports are used.

1.3.3 Reaction kinetics

A very important consideration for fuel cells is their reaction kinetics, which depend on the detailed mechanisms of the electrochemical reactions. For a thorough discussion of electrochemical kinetics see an electrochemistry textbook such as Bard and Faulkner's *Electrochemical Methods: Fundamentals and Applications*. Like all chemical reactions, electrochemical reactions proceed through intermediate steps. For example, in the HOR, hydrogen atoms that start in diatomic molecules must adsorb onto a surface, to which they transfer their electrons, before departing as protons. Transitioning between the starting state (molecular hydrogen), stable intermediates (adsorbed hydrogen), and the final state (solvated protons), requires passing higher-energy unstable intermediate states (moving onto and off of the surface). These energy barriers slow down the reaction and determine its rate. For a simple one-step (one barrier) reaction $a\text{A} + b\text{B} \rightarrow c\text{C}$ with reactant concentrations [A] and [B], the reaction rate r is given by the Arrhenius law:

$$r = k[\text{A}]^m[\text{B}]^n, \tag{1.4}$$

$$k = k_0 \exp\left[-\frac{E_a}{k_B T}\right], \tag{1.5}$$

where k is the rate constant, E_a is the energy barrier or activation energy, k_B is Boltzmann's constant, T is the absolute temperature, and k_0, m, and n are constants specific to the reaction mechanism. The rate of a particular chemical reaction is thus sensitive to the temperature and the concentrations of the reactants.

Electrochemical reactions provide an additional lever to alter the reaction rate: applying a voltage to change the electrode potential away from its thermodynamic equilibrium value. The difference between the actual and equilibrium electrode potential is called the "overpotential," which changes the relative energy of intermediate states and therefore alters the reaction rate. In a galvanic cell, which extracts electrical energy from thermodynamically favored reactions, this means we can give up some of the thermodynamically granted energy for the reaction to proceed faster. The resulting tradeoff between the current density j and overpotential η, for a reaction with a single rate-limiting step, is described by the Butler-Volmer equation:

$$j = j_0 \left[\exp\left[\frac{(1-\alpha)ze}{k_B T} \eta \right] - \exp\left[\frac{-\alpha ze}{k_B T} \eta \right] \right], \tag{1.6}$$

where α is the dimensionless charge transfer coefficient specific to the reaction (but typically around 0.5), z is the number of electrons involved in the reaction, and e is the elementary charge. j_0 is the exchange current density, which follows an Arrhenius law dependence on temperature, activation energy, and concentrations of reactants and products, considering both the forward and reverse reactions, as described above.

Making the exchange current density j_0 as high as possible will minimize kinetic losses in a fuel cell. Fuel cells often use operating conditions with higher temperature and pressure, which are more favorable for reaction kinetics. The catalyst is also selected and engineered to minimize the energy barriers and provide a large active surface area. With a Pt catalyst, the HOR has phenomenally fast kinetics, making its overpotential typically negligible even with very small amounts of Pt. The ORR, however, has very slow kinetics and contributes a significant overpotential even with the best available catalysts, making it a key limitation for fuel cells. Pt is

the best ORR catalyst among pure metals and can be improved as a catalyst through several engineering strategies discussed in Section 1.4.

For practical purposes, the activity of a catalyst is described in terms of the amount of current a quantity of catalyst can provide at a given potential. Quantitatively, this can be expressed through three interrelated quantities: the mass activity (MA), which is the current per mass of catalyst, the specific activity (SA), which is the current per active surface area of catalyst, and the electrochemically active surface area (ECSA) of the catalyst, given per mass of catalyst. The MA is the product of the SA and ECSA. The SA is a more fundamental quantity, describing the catalytic properties of the surface.

1.3.4 Mass transport

If the consumption of reactants outpaces the diffusion of new reactants to the catalyst, losses will occur because the depletion of reactants harms both the thermodynamics and kinetics of the reaction. These mass transport losses η_{conc} are often described in a simple mathematical form:

$$\eta_{conc} = k_B T \left(1 + \frac{1}{\alpha}\right) \ln\left(\frac{j_L}{j_L - j}\right), \qquad (1.7)$$

where j_L is the limiting current, which depends on the initial concentration, the electrode geometry, and the effective diffusivity in the electrode. This relation captures the main important features of mass transport losses, which are generally minimal at low current but grow abruptly approaching the limiting current. As a result, mass transport is an important factor determining the maximum power of a fuel cell. In practice, the details of transport losses are complex because of the heterogeneity of the catalyst and electrode. The equation above describes bulk mass transport effects, where reactants are depleted in broadly across the electrode. Local mass transport effects,

where reactants are depleted in the immediate vicinity of catalyst nanoparticles, are important as well and will be discussed more in the following section.

1.4   The Importance of ORR Catalyst Engineering

ORR kinetics are generally the largest source of voltage loss for well-optimized MEAs under normal operating conditions, making the ORR catalyst a key limitation for the fuel cell overall.[12] Because of the high cost and scarcity of Pt, it must be used sparingly or Pt costs will obstruct the wide adoption of fuel cells.[13] Non-precious metal fuel cell catalysts have also been widely studied, but a limited number of materials are sufficiently stable in the corrosive conditions of the fuel cell. The available non-precious metals provide lower efficiency and power density compared to Pt, making them less suitable for transportation applications. The use of Pt does not need to be eliminated completely - modern ICE vehicles use ~5 g of precious metals, including Pt, in catalytic converters to manage harmful emissions such as NO_x. Once ORR catalysts are improved to the point where FCEVs use a similar amount of precious metal catalyst as ICE vehicles, we can reasonably declare the Pt cost problem solved.[12,13] Commercially available FCEVs use around 30-40 g_{Pt} and next-generation FCEVs under development use around 10 g_{Pt}, so this goal is probably achievable in the coming years. Further advancements will likely go toward improving the overall efficiency of the fuel cell.

Fuel cell catalyst R&D has long focused on improving ORR MA as an effective strategy for deceasing platinum use.[12] A simple strategy to improve the mass activity of a Pt catalyst is to increase its ECSA by making the Pt into smaller-sized nanoparticles. This approach is effective to a point, but eventually the SA of small nanoparticles begins to decline because an increasing fraction of the Pt surface is from low-activity edge sites instead of the more active crystal facets, resulting in a maximum MA for particles around 2 nm in diameter.[14] Furthermore, Pt particles

below about 4-5 nm in diameter have a relatively low stability, making it difficult to meet the durability needs of transportation applications.[15] Catalyst particles can be made with a large effective size but low Pt content by depositing a monolayer of Pt coating on another material,[16–18] and catalyst specific activity can also be improved by synthesis of shape-controlled nanoparticles to select for the most active surface sites.[19–24] While these approaches have intriguing potential, they have yet to be demonstrated in practical, cost-effective fuel cell devices.[13]

The most promising demonstrated approach to improve the specific activity beyond that of optimally-sized Pt particles is the addition of a secondary metal (such as Co or Ni) to form a Pt alloy and removal of the secondary metal from the surface sites.[25–28] The removal of the secondary metal from the near-surface is known as dealloying, and helps prepare a stable Pt surface that is significantly more active than pure Pt. The apparent mechanism for this enhancement is compressive strain exerted on the Pt surface by the underlying alloy, which typically has a smaller lattice constant.[29,30] This compressive strain decreases the oxygen binding strength of the surface to lower the activation energy barrier for the ORR.[31–34] However, the details of strain effects in real fuel cell catalysts have not been well explored, in part due to a lack of effective characterization techniques suitable for the complexities of the system. Direct characterization of the strain state of real fuel cell catalysts is one focus of this dissertation.

Recent progress in catalyst MA has allowed significant reductions in the quantities of Pt needed for automotive fuel cells. However, when little catalyst surface area is available, local transport becomes an important problem because high local reactant flux is required for reactants to reach a small number of active sites. Mass transport limits the maximum power that a fuel cell can deliver and is a key factor in determining the overall system size and cost. Challenges with local transport are currently a major limitation in further reducing fuel cell cost.[13] It is known that local oxygen transport is a dominant contributor to mass transport losses[13,35–38] and that the distribution of Pt

particles, ionomer, and pore structures are all contributing factors.[13,38] Oxygen transport losses can be mitigated by ensuring that catalysts have high ECSA[13] and by the development of accessible carbon support structures.[39] The best approach to design the catalyst and carbon support structure to optimize local transport remains an open question, which is addressed in this dissertation.

The durability of ORR catalysts is also a major concern. Owners expect many years of use from their vehicles, with the average household vehicle in the US being over 10 years old.[40] Fuel cell materials must be able to retain acceptable performance after extended periods of corrosive conditions. Pt-based fuel cell catalysts degrade by several mechanisms[41] which generally lead to a loss of active surface area and specific activity. Pt tends to dissolve slowly and redeposit either in the membrane where it forms an inactive "Pt band"[42–49] or on catalyst particles, driving a net growth in particle size known as Ostwald ripening.[15,30,42,50] Particles may also migrate on the carbon support, collide with other particles and coalesce, increasing their size.[30,51–53] The carbon support is also not thermodynamically stable, and may corrode at very high potentials where the kinetics are significant. However, it is possible to manage the fuel cell system to prevent the cathode from exposure to high potentials. Pt alloy catalysts tend to lose their secondary metal over time, which irreversibly dissolves into the membrane. This leads to a loss of the specific activity advantage of the catalysts over pure Pt[44,49,54] and also harms the membrane conductivity by displacing protons.

These various degradation mechanisms harm the fuel cell performance both by decreasing the catalyst activity and by exacerbating local transport problems by decreasing the active surface area. Fuel cells with low initial Pt content have little margin for error, and it is essential to minimize catalyst degradation.[13,55] Good progress has been made in understanding the structural origins of some aspects of catalyst stability, such as particle size effects.[15] Detailed understanding of the role of the catalyst structure in all the various degradation mechanisms is still being developed. An optimized catalyst must simultaneously mitigate all possible degradation mechanisms while also

meeting the challenging requirements of cost, activity, and transport accessibility. Developing a more detailed understanding of the role of catalyst structure in durability is a third goal of this dissertation.

1.5   Nanocharacterization of Fuel Cell Catalyst Materials

Nanocharacterization has an essential role in describing catalyst structure to understand the outcomes of materials synthesis and processing and the origins of performance. The (scanning) transmission electron microscope ((S)TEM) provides a powerful toolbox of techniques to describe the structure and properties of materials down to atomic length scales.

The most basic measurement that a (S)TEM can perform is microscopic imaging. However, there are a wide variety of different imaging modes available, each of which is best suited to different uses. There are two broad categories of imaging modes, illustrated in Figure 1.7. In TEM, a broad area of the specimen is illuminated with the electron beam and a magnified image is formed using the objective lens. In STEM, the beam is focused to a sharp probe and rastered across the sample while a variety of signals can be collected to form an image. Both TEM and STEM can provide images with atomic resolution, and the availability of aberration correctors have made atomic resolution imaging widespread.

Both TEM and STEM allow flexibility in the signal used to form the images. In TEM, an objective aperture can select directly transmitted or diffracted electrons to vary the sensitivity to crystal structure and atomic number, or the image can be energy filtered using a spectrometer to produce an image sensitive to chemical composition and bonding. In STEM, electrons scattered out to different angles can be collected by the placement of the detector used for image formation. A bright field detector collects directly transmitted electrons, yielding contrast similar to bright

field TEM, including phase contrast effects and a relatively weak sensitivity to atomic number. An annular dark field (ADF) detector collects electrons scattered out to a specific range of angles. In practice, the collection angles of detectors are varied by adjusting the projector lenses to set the camera length, which is the effective distance between the specimen and detector. If electrons scattered at high angles are collected with the ADF detector (HAADF), the image signal predominantly reflects the density, thickness, and atomic number of the specimen. HAADF provides high sensitivity to the atomic number because the primary scattering process is Rutherford scattering. If electrons scattered to low angles are collected by the ADF detector (LAADF) the atomic number sensitivity is weaker and diffraction contrast effects, reflecting crystal orientation and defects, become significant.

Because the STEM electron beam is focused to a small probe, STEM allows the convenient collection of localized analytical signals to describe the chemical composition and bonding. Two common techniques are used for this: electron energy loss spectroscopy (EELS), which disperses the transmitted electron beam in a spectrometer to measure the energy lost to the specimen, and energy dispersive X-ray spectroscopy (EDXS, EDX or XEDS) which collects X-rays emitted from the specimen when electrons relax into core energy levels after excitation by the incident beam. EELS can provide a wide range of information on the specimen, including elemental composition, chemical bonding, and optical or electronic properties. EDXS provides elemental composition measurements that are more easily processed and quantified than corresponding EELS measurements, but typically with lower spatial resolution because of the limited collection efficiency of most EDXS detectors.
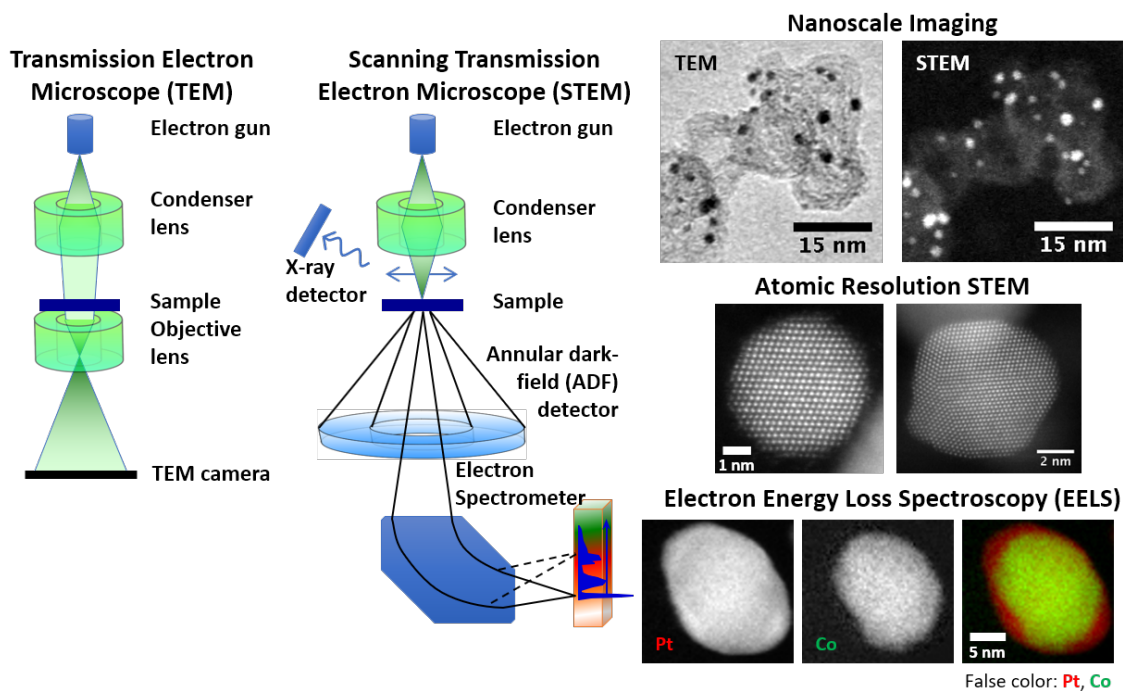
Figure 1.7: Schematic illustrations and example images for commonly used (scanning) transmission electron microscope ((S)TEM) techniques for fuel cell catalysts. In TEM mode, the microscope illuminates a broad area of the sample with the condenser lens and forms an image with the objective lens. In STEM mode, the microscope forms a small probe with the condenser lens, which it rasters across the image while collecting a signal to form an image. Available STEM signals include scattered electrons collected on the annular dark field (ADF) detector, X-rays emitted from the beam-sample interaction (EDXS), and measuring the energy-loss of electrons with an electron spectrometer (EELS).

Newly developed pixelated detectors with high dynamic range and fast readout are opening a new frontier of characterization techniques for the STEM. These detectors allow the full distribution of scattered electrons to be collected at each pixel in the STEM image in place of the traditional scalar signal from monolithic detectors, as illustrated in Figure 1.8. The techniques that this enables go by several names, including scanning electron diffraction and 4D STEM. Of particular interest for fuel cell catalysts is the scanning nanobeam electron diffraction (NBED) technique, where the beam is converged to ~1 nm spatial resolution to provide localized diffraction

19

patterns with distinct diffraction spots to measure the crystal structure. This technique offers the exciting possibility of efficient measurement of spatially-varying strain in real fuel cell catalysts. Effective direct characterization of strain in complex nanoparticle systems has been largely unavailable because of a lack of suitable, high-throughput characterization techniques. While NBED provides an exciting opportunity for these measurements, the data is complex due to dynamical diffraction effects and the 3D structure of catalyst nanoparticles, including varying thickness and random particle orientations. Development of a strain mapping technique that is robust to these complexities is one challenge addressed in this dissertation.

Any of the (S)TEM techniques described above, in principle, can be combined with serial-imaging techniques, such as in-situ experiments, where dynamic changes to a specimen are monitored as it is subjected to a stimulus, or electron tomography, where a 3D image of the specimen is reconstructed from a series of images taken at different angles. This collection of techniques makes the (S)TEM a well-equipped nanoscience laboratory, which can provide rich descriptions of the structure of fuel cell catalysts.

Fuel cell catalysts impose some unique requirements for effective nanocharacterization. Practical catalyst nanoparticles are commonly heterogeneous, with a wide variety of structures contributing to the bulk properties. A researcher performing microscopic characterization of heterogeneous samples must identify the important variations in the sample and ensure that conclusions are drawn from statistically representative measurements. Whenever possible, measurement techniques used should be able to provide high throughput to provide sufficient sampling. This is a classic limitation of microscopic measurements, which in contrast to bulk techniques provide rich detail but poor sampling. Microscopists can push the boundaries of their techniques to mitigate these limitations with rapid experimental measurements and automated data analysis. Whenever data throughput is limiting, the microscopist must carefully asses variation in

the sample and take selective measurements that represent the sample as a whole to the greatest extent possible. Above all, it is essential to present data in a manner that honestly reflects its limitations. In a complex community of technical specialists, it is entirely possible for cherry-picked data to lead to the belief that cherry trees are all fruit and no leaves. These considerations direct the development and application of TEM techniques throughout this dissertation. The investigations presented here demonstrate that carefully executed, statistically robust microscopic measurements can quantitatively account for and explain bulk electrochemical properties of heterogeneous catalyst materials.
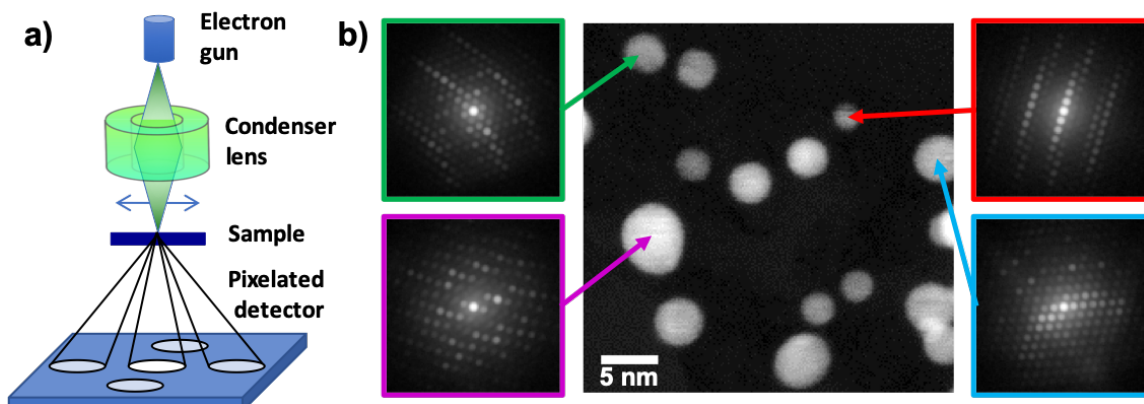
Figure 1.8: Schematic illustration (a) of the scanning nanobeam electron diffraction (NBED) technique with a pixelated detector and example NBED data (b) for Pt-Co nanoparticle catalysts showing diffraction patterns from nanoparticles with random orientations. The image in the center is a virtual ADF image calculated from the NBED dataset.

1.6   Thesis Outline

The first half of this dissertation will focus on characterization of strain in nanoparticle catalysts, with the goal of accounting for catalyst activity in terms of microstructure. Chapter 2 presents a newly-developed technique for strain mapping using NBED that improves its robustness for complex and non-ideal specimens. This approach uses a transformation to convert the NBED

into the exit wave power cepstrum (EWPC) space, which allows separation of useful lattice information from tilt and thickness effects to enable precise strain measurement. This approach is demonstrated experimentally to characterize domain structure in strained ferroelectric oxide films and to map strain profiles across Pt-Co fuel cell catalyst nanoparticles, even at random orientations. Chapter 3 presents the application of this NBED-EWPC strain mapping technique to core-shell Pt-Co nanoparticle catalysts to understand the mechanisms of strain relaxation and their consequences for catalyst activity. We also develop a simple analytical model to describe the strain profile and surface strain for spherical core-shell particles. We report on two mechanisms for strain relaxation: lattice dislocations and Poisson-expansion-driven relaxation resulting from the spherical geometry. We compare to a series of dealloyed Pt-Co catalysts prepared with varying Pt shell thicknesses to rationalize the trends in the specific activity in terms of the nanoparticle's strain state.

The second half of the dissertation focuses on the importance of the larger-scale catalyst structure determined by the catalyst support. We investigate the role of carbon support porosity in catalyst performance and durability by comparing two widely used, representative carbons: porous high surface-area carbon (HSC) black – the most common commercial variant being Ketjen Black – and solid carbon black – with Vulcan being the common commercial variant. In Chapter 4 we examine the distribution of Pt particles across each of these carbon support types and the structure of pores in HSC using 3D imaging with electron tomography. We correlate quantitative structural measurements made from the tomograms to electrochemical measurements of the chemically active Pt surface area and accessibility to protons and gas to reveal different transport mechanisms to particles on the carbon interior and exterior. In Chapter 5 we investigate the durability of Pt and Pt-Co catalysts with HSC and Vulcan supports by using STEM imaging and elemental mapping in MEAs before and after stability testing. Using statistical analysis of the STEM results and

electrochemical measurements we find that the HSC support provides improved durability by suppressing the coalescence of particles that leads to active surface area loss.

Chapter 6 concludes the dissertation by summarizing the major results from Chapters 2-5 and suggesting directions for future research. Additional supporting information and useful methods are presented in the appendices. Appendix A presents the detailed derivation of the continuum elastic strain model for core-shell particles that is discussed in Chapter 3. Appendix B covers useful practical information and methods for high-resolution electron tomography, especially for fuel cell catalyst materials. Appendix C demonstrates a newly-developed sample preparation strategy for full-range electron tomography of nanoparticle specimens.

1.7   References

[1] R.K. Pachauri and L.A. Meyer, Climate Change 2014: Synthesis Report. Contribution of Working Groups I, II and III to the Fifth Assessment Report of the Intergovernmental Panel on Climate Change (IPCC, Geneva, Switzerland, 2014).

[2] Inventory of U.S. Greenhouse Gas Emissions and Sinks: 1990–2017 (United States Environmental Protection Agency, 2019).

[3] How Clean Are Hydrogen Fuel Cell Electric Vehicles? (Union of Concerned Scientists, 2014).

[4] R. Nealer, D. Reichmuth, and D. Anair, Cleaner Cars Cradle to Grave (Union of Concerned Scientists, 2015).

[5] D. Reichmuth, New Data Show Electric Vehicles Continue to Get Cleaner (Union of Concerned Scientists, 2018).

[6] Hydrogen: Tracking Clean Energy Progress (International Energy Agency, 2019).

[7] Global EV Outlook 2018 (International Energy Agency, 2018).

[8] Vehicles in Use (International Organization of Motor Vehicle Manufacturers, 2019).

[9] R. O'Hayre, S.-W. Cha, W. Colella, and F.B. Prinz, Fuel Cell Fundamentals (John Wiley & Sons, Inc, Hoboken, NJ, USA, 2016).

[10] T. Yoshida and K. Kojima, Interface Mag. **24**, 45 (2015).

[11] N. Konno, S. Mizuno, H. Nakaji, and Y. Ishikawa, SAE Int. J. Altern. Powertrains **4**, 123 (2015).

[12] H.A. Gasteiger, S.S. Kocha, B. Sompalli, and F.T. Wagner, Appl. Catal. B Environ. **56**, 9 (2005).

[13] A. Kongkanand and M.F. Mathias, J. Phys. Chem. Lett. **7**, 1127 (2016).

[14] M. Shao, A. Peles, and K. Shoemaker, Nano Lett. **11**, 3714 (2011).

[15] E.F. Holby, W. Sheng, Y. Shao-Horn, and D. Morgan, Energy Environ. Sci. **2**, 865 (2009).

[16] J. Zhang, Y. Mo, M.B. Vukmirovic, R. Klie, K. Sasaki, and R.R. Adzic, J. Phys. Chem. B **108**, 10955 (2004).

[17] K. Sasaki, H. Naohara, Y. Cai, Y.M. Choi, P. Liu, M.B. Vukmirovic, J.X. Wang, and R.R. Adzic, Angew. Chemie Int. Ed. **49**, 8602 (2010).

[18] A. Kongkanand, N.P. Subramanian, Y. Yu, Z. Liu, H. Igarashi, and D.A. Muller, ACS Catal. **6**, 1578 (2016).

[19] J. Zhang, H. Yang, J. Fang, and S. Zou, Nano Lett. **10**, 638 (2010).

[20] J. Wu, J. Zhang, Z. Peng, S. Yang, F.T. Wagner, and H. Yang, J. Am. Chem. Soc. **132**, 4984 (2010).

[21] M.K. Carpenter, T.E. Moylan, R.S. Kukreja, M.H. Atwan, and M.M. Tessema, J. Am. Chem. Soc. **134**, 8535 (2012).

[22] S. Il Choi, S. Xie, M. Shao, J.H. Odell, N. Lu, H.C. Peng, L. Protsailo, S. Guerrero, J. Park, X. Xia, J. Wang, M.J. Kim, and Y. Xia, Nano Lett. **13**, 3420 (2013).

[23] L. Gan, C. Cui, M. Heggen, F. Dionigi, S. Rudi, and P. Strasser, Science. **346**, 1502 (2014).

[24] C. Chen, Y. Kang, Z. Huo, Z. Zhu, W. Huang, H.L. Xin, J.D. Snyder, D. Li, J. a Herron, M. Mavrikakis, M. Chi, K.L. More, Y. Li, N.M. Markovic, G. a Somorjai, P. Yang, and V.R. Stamenkovic, Science. **343**, 1339 (2014).

[25] F. Hasché, M. Oezaslan, and P. Strasser, ChemCatChem **3**, 1805 (2011).

[26] Q. Jia, K. Caldwell, J.M. Ziegelbauer, A. Kongkanand, F.T. Wagner, S. Mukerjee, and D.E. Ramaker, J. Electrochem. Soc. **161**, F1323 (2014).

[27] K.M. Caldwell, D.E. Ramaker, Q. Jia, S. Mukerjee, J.M. Ziegelbauer, R.S. Kukreja, and A. Kongkanand, J. Phys. Chem. C **119**, 757 (2015).

[28] B. Han, C.E. Carlton, A. Kongkanand, R.S. Kukreja, B.R. Theobald, L. Gan, R. O'Malley, P. Strasser, F.T. Wagner, and Y. Shao-Horn, Energy Environ. Sci. **8**, 258 (2015).

[29] P. Strasser, S. Koh, T. Anniyev, J. Greeley, K. More, C. Yu, Z. Liu, S. Kaya, D. Nordlund, H. Ogasawara, M.F. Toney, and A. Nilsson, Nat. Chem. **2**, 454 (2010).

[30] H.L. Xin, J.A. Mundy, Z. Liu, R. Cabezas, R. Hovden, L.F. Kourkoutis, J. Zhang, N.P. Subramanian, R. Makharia, F.T. Wagner, and D. a Muller, Nano Lett. **12**, 490 (2012).

[31] B. Hammer, Y. Morikawa, and J.K. Nørskov, Phys. Rev. Lett. **76**, 2141 (1996).

[32] B. Hammer and J.K. Nørskov, in Chemisorpt. React. Support. Clust. Thin Film. Towar. an Underst. Microsc. Process. Catal., edited by R.M. Lambert and G. Pacchioni (Springer Netherlands, Dordrecht, 1997), pp. 285–351.

[33] A. Ruban, B. Hammer, P. Stoltze, H.. Skriver, and J.. Nørskov, J. Mol. Catal. A Chem. **115**, 421 (1997).

[34] M. Mavrikakis, B. Hammer, and J.K. Nørskov, Phys. Rev. Lett. **81**, 2819 (1998).

[35] A.Z. Weber, R.L. Borup, R.M. Darling, P.K. Das, T.J. Dursch, W. Gu, D. Harvey, A. Kusoglu, S. Litster, M.M. Mench, R. Mukundan, J.P. Owejan, J.G. Pharoah, M. Secanell, and I. V. Zenyuk, J. Electrochem. Soc. **161**, F1254 (2014).

[36] T.A. Greszler, D. Caulk, and P. Sinha, J. Electrochem. Soc. **159**, F831 (2012).

[37] H. Liu, W.K. Epting, and S. Litster, Langmuir **31**, 9853 (2015).

[38] A.Z. Weber and A. Kusoglu, J. Mater. Chem. A **2**, 17207 (2014).

[39] V. Yarlagadda, M.K. Carpenter, T.E. Moylan, R.S. Kukreja, R. Koestner, W. Gu, L. Thompson, and A. Kongkanand, ACS Energy Lett. **3**, 618 (2018).

[40] National Household Travel Survey (U.S. Department of Transportation, 2017).

[41] J.C. Meier, C. Galeano, I. Katsounaros, J. Witte, H.J. Bongard, A.A. Topalov, C. Baldizzone, S. Mezzavilla, F. Schüth, and K.J.J. Mayrhofer, Beilstein J. Nanotechnol. **5**, 44 (2014).

[42] P.J. Ferreira, G.J. la O', Y. Shao-Horn, D. Morgan, R. Makharia, S. Kocha, and H.A. Gasteiger, J. Electrochem. Soc. **152**, A2256 (2005).

[43] S. Chen, H.A. Gasteiger, K. Hayakawa, T. Tada, and Y. Shao-Horn, J. Electrochem. Soc. **157**, A82 (2010).

[44] F.T. Wagner, S.G. Yan, and P.T. Yu, in Handb. Fuel Cells (John Wiley & Sons, Ltd, Chichester, UK, 2010).

[45] A. Ohma, S. Yamamoto, and K. Shinohara, ECS Trans. **11**, 1181 (2007).

[46] J. Zhang, B.A. Litteer, W. Gu, H. Liu, and H.A. Gasteiger, J. Electrochem. Soc. **154**, B1006 (2007).

[47] P. Yu, M. Pemberton, and P. Plasse, J. Power Sources **144**, 11 (2005).

[48] W. Bi, G.E. Gray, and T.F. Fuller, Electrochem. Solid-State Lett. **10**, B101 (2007).

[49] D.D. Papadias, R.K. Ahluwalia, N. Kariuki, D. Myers, K.L. More, D.A. Cullen, B.T. Sneed, K.C. Neyerlin, R. Mukundan, and R.L. Borup, J. Electrochem. Soc. **165**, F3166 (2018).

[50] C.E. Carlton, S. Chen, P.J. Ferreira, L.F. Allard, and Y. Shao-Horn, J. Phys. Chem. Lett. **3**, 161 (2012).

[51] C.G. Granqvist and R.A. Buhrman, J. Catal. **42**, 477 (1976).

[52] M.S. Wilson, F.H. Garzon, K.E. Sickafus, and S. Gottesfeld, J. Electrochem. Soc. **140**, 2872 (1993).

[53] K. More, R. Borup, and K. Reeves, ECS Trans. **3**, 717 (2006).

[54] Q. Jia, J. Li, K. Caldwell, D.E. Ramaker, J.M. Ziegelbauer, R.S. Kukreja, A. Kongkanand, and S. Mukerjee, ACS Catal. **6**, 928 (2016).

[55] G.S. Harzer, J.N. Schwämmlein, A.M. Damjanović, S. Ghosh, and H.A. Gasteiger, J. Electrochem. Soc. **165**, F3118 (2018).

2   ROBUST STRAIN MAPPING AT SUBNANOMETER RESOLUTION AND SUBPICOMETER PRECISION USING THE EXIT-WAVE POWER-CEPSTRUM TRANSFORM AND SCANNING NANOBEAM ELECTRON DIFFRACTION

2.1   Abstract

Scanning nanobeam electron diffraction (NBED) with fast pixelated detectors is a valuable technique for rapid, spatially resolved mapping of lattice structure over a wide range of length scales. However, intensity variations caused by dynamical diffraction and sample mistilts can hinder the measurement of diffracted disk centers necessary for quantification. Robust data processing techniques are needed to provide accurate and precise measurements for complex samples and non-ideal conditions. Here we present an approach to address these challenges using a transform, called the exit wave power cepstrum (EWPC), inspired by cepstral analysis in audio signal processing. The EWPC transforms NBED patterns to real-space patterns with sharp peaks corresponding to inter-atomic spacings. We describe a simple analytical model for interpretation of these patterns, that cleanly decouples lattice information and the intensity variations in NBED patters caused by tilt and thickness. Strain mapping by tracking the inter-atomic spacing peaks in EWPC patterns is demonstrated for two practical applications: mapping of ferroelectric domains in epitaxially strained $PbTiO_3$ films and mapping of strain profiles in arbitrarily-oriented core-shell Pt-Co nanoparticle fuel-cell catalysts. The EWPC transform enables lattice structure measurements to be made with sub-nm precision, is robust to sample mistilts, and works for randomly-oriented nanoparticles.

2.2　Introduction

Characterization of nanoscale variations in lattice structure is essential for understanding the properties of many materials systems. (Scanning) transmission electron microscopy ((S)TEM) provides a powerful toolset for this, with several techniques for mapping local crystal structure, strain, and lattice distortions.[1–3] Aberration correctors have made atomic resolution STEM and TEM imaging widely available and effective for direct measurement of real-space lattice structure at the single-atom level. However, direct atomic resolution imaging is limited to relatively small fields of view (FOVs) around ~100 nm, requires a high beam dose and a specimen oriented on a high-symmetry zone axis, and is sensitive to instabilities such as sample drift, vibration, electromagnetic interference, and scan distortion.

Recent advances in fast, high-dynamic-range pixel-array detectors[4–6] are making scanning diffraction techniques, including nanobeam electron diffraction (NBED) and convergent beam electron diffraction (CBED), a promising approach for characterization of local lattice structure.[7] In NBED, a relatively low convergence angle is used such that the diffracted disks do not overlap and can be measured similarly to conventional TEM diffraction.[8] In CBED strain mapping, a highly convergent probe is used and the strain is extracted through measurement of the higher order Laue zone (HOLZ) lines formed by dynamical scattering.[9] Both CBED and NBED techniques allow high precision, high spatial resolution lattice structure measurements over FOVs reaching up to micrometer length scales while imposing fewer constraints on stability.[10,11] In comparison to CBED, NBED is compatible with a wide range of sample thicknesses and orientations, making it a more versatile scanning diffraction technique.[7,12]

However, several challenges arise in applying NBED for structural characterization of complex specimens. Intensity variations caused by dynamical diffraction and sample mistilts can hinder

accurate and precise measurement of the centers of the relatively broad diffracted disks used in high resolution NBED.[13–15] Effective methods for extracting lattice information must ensure high computational efficiency, precision with limited beam dose, and robustness under nonideal conditions including background signals, varying peak intensities, and internal structure within the diffracted disks. One experimental technique that has be successfully deployed to improve NBED patterns is precession electron diffraction (PED), where the incident beam is tilted off of the optic axis of the microscope and precessed around the optic axis during NBED pattern acquisition.[16,17] PED can increase the number of higher order diffraction spots present by bringing the Ewald sphere to intersect more reciprocal lattice points, while also averaging out dynamical effects to create a more kinematic-like diffraction pattern with more internally uniform diffraction spots.[18–20] However, employing precession methods for NBED adds experimental complexity, acquisition time, and limits the achievable spatial resolution. Furthermore, precise localization of broad diffracted disks is a difficult computation task even with the relatively ideal conditions provided by PED. While a wide variety of techniques for data processing and disk localization have been employed – including correlation methods,[10,15] iterative fitting methods,[13,21] center of mass calculation,[11] and the circular Hough transform[22] – these challenges remain a limitation to the application of NBED to complex materials systems.

In this paper we propose a transformation to aid in the extraction of lattice structure and strain information from nanobeam diffraction maps, both with and without PED. Our approach is inspired by the use of cepstral analysis in signal processing. Cepstral analysis was developed for echo detection and pitch determination, and was subsequently used for a wide variety of audio and image processing applications, especially the analysis of speech.[23–25] In audio processing, to track the time evolution of an audio signal, a short segment is selected using a window function and processed using short-time Fourier analysis. The power cepstrum (PC) of a time-domain function is calculated

by first taking the logarithm of the power spectrum to produce a frequency-domain function. By then taking the power spectrum of this frequency-domain function, a new real-space function, similar to the autocorrelation function, is obtained; this is the PC.

The PC provides a very useful separation property for signals that are convolved in the time domain. In the frequency domain these signals become multiplicative, and then additive after the application of a logarithm. The originally convolved functions remain additive after the second Fourier transform to the time-domain PC, allowing convenient, independent measurement of signals with differing time-scales.

The measurement of crystal structure with NBED is analogous to short-time Fourier analysis of audio signals, with the goal instead being the determination of spatial variations in crystal structure. In NBED, a small real-space area is selected by the probe, and the diffraction pattern reveals its periodic structure in reciprocal space. The Fourier transform of the real-space structure is "calculated" physically by the diffraction process. Several of the problems complicating lattice structure measurements from NBED patterns, including intensity variations from sample mistilt and dynamical scattering, can be approximated as multiplicative in diffraction space and (therefore) convolutions in real space. Analogy to audio signal processing suggests that a real-space cepstrum may be useful for separating these effects from the lattice structure of interest. The first steps of producing real-space cepstrum are performed physically by diffraction process, so a real-space cepstrum can calculated by taking the power spectrum of the log-scaled NBED pattern. This can be shown to be equivalent to the power cepstrum of the exit wave, and so we denote this transform the exit wave power cepstrum (EWPC).

The process of calculating the EWPC is illustrated in Figure 2.1. Figure 2.1(a) shows a NBED pattern for a face-centered cubic Pt-Co alloy oriented on the 110 zone axis with the direct beam

saturated in post-processing for display purposes. Figure 2.1(b) shows the logarithm of the NBED pattern, which flattens the intensity variation between the diffraction spots and brings more spots into the intermediate intensity range. Figure 2.1(c) shows the EWPC transform of the NBED, or the magnitude of the Fourier transform of Figure 2.1(b). The EWPC pattern is similar to an autocorrelation of the real lattice or a Patterson function,[26] and concentrates the signal from the diffracted disks into sharp real-space points corresponding to inter-atomic spacings. This transform makes precise fitting of the peaks for measurement of the lattice structure numerically convenient and separates the effects of tilt and thickness on the NBED pattern from the lattice structure information.
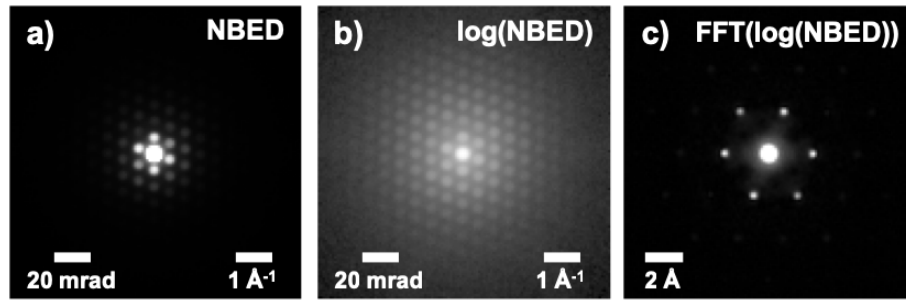
Figure 2.1: Illustration of the EWPC transform for an FCC Pt-Co alloy oriented on the 110 zone axis. Nanobeam electron diffraction (NBED) pattern shown with (a) linear and (b) logarithmic intensity scales. (c) The EWPC transform for this diffraction pattern, calculated as the fast Fourier transform (FFT) of the log of the NBED pattern.

In this manuscript we present a simple model of the EWPC transform in the context of NBED and experimentally demonstrate its key features for strain mapping. We then demonstrate its practical value for two applications: ferroelectric domains in epitaxially strained $PbTiO_3$ films and core-shell Pt-Co nanoparticle catalysts. For the $PbTiO_3$ films we show EWPC mapping is robust to large mistilts caused by ferroelastic strain. For the Pt-Co nanoparticles we show that the EWPC transform enables sub-nm resolution strain mapping that is robust to random particle orientations

and suitable to provide strain measurements in ~nm thick shells. These examples show that the EWPC transform is a powerful tool for NBED strain mapping that provides high spatial resolution and precision and is dose efficient and robust for complex samples.

2.3 Theory of the EWPC

2.3.1 Cepstral Analysis and the Exit Wave Power Cepstrum

Cepstral analysis was originally developed for the analysis of human speech, with the goal of determining the time evolution of the pitch in audio signals.[23] Cepstral analysis provides a means for separating the fundamental pitch frequency from convolved formants that shape the wave. In particular, the power cepstrum of a function $f(t)$ is defined as the power spectrum of the log of the power spectrum of $f(t)$:

$$\mathrm{PC}(f(t)) = \left| \mathcal{F}\left(\ln\left(\left| \mathcal{F}(f(t)) \right|^2 \right) \right) \right|^2,$$

(0.1)

where $\mathcal{F}$ denotes a Fourier transform. For convolved functions $\alpha(t) * \beta(t)$ with Fourier transforms $A(\omega) = \mathcal{F}(\alpha(t))$ and $B(\omega) = \mathcal{F}(\beta(t))$, the power cepstrum provides a useful separation property:

$$
\begin{aligned}
\mathrm{PC}(\alpha(t) * \beta(t)) &= \left| \mathcal{F}\left(\ln(|A(\omega) \cdot B(\omega)|^2) \right) \right|^2 \\
&= \left| \mathcal{F}\left(\ln(|A(\omega)|^2) + \ln(|B(\omega)|^2) \right) \right|^2 \\
&= \left| \mathcal{F}\left(\ln\left(\left| \mathcal{F}(\alpha(t)) \right|^2 \right) + \ln\left(\left| \mathcal{F}(\beta(t)) \right|^2 \right) \right) \right|^2 \\
&= \left| \mathcal{F}\left(\ln\left(\left| \mathcal{F}(\alpha(t)) \right|^2 \right) \right) + \mathcal{F}\left(\ln\left(\left| \mathcal{F}(\beta(t)) \right|^2 \right) \right) \right|^2.
\end{aligned}
$$

(0.2)

For $\alpha(t), \beta(t)$ with well-separated frequency bands, this allows additive separation of the signals,

$$PC\big(\alpha(t) * \beta(t)\big) \approx PC\big(\alpha(t)\big) + PC\big(\beta(t)\big), \tag{0.3}$$

as desired for independent analysis of pitch and formants in audio.

This situation is closely analogous to the problem of lattice mapping using nanobeam diffraction, where our goal is to measure the spatial variation of the periodic lattice structure in a sample. Sample tilt and thickness create modulations in the intensity of diffracted beams, similar to the effect of formants on an audio power spectrum, which we would ideally separate from the lattice information. These similarities suggest that some form of cepstral analysis may be useful in nanobeam diffraction mapping as well.

A useful criterion for structuring our approach can be provided by considering the trade-off presented by the choice of probe size in nanobeam diffraction. A probe that provides high localization in real space will result in delocalization of the reciprocal lattice information in diffraction space by broadening diffracted peaks into disks. As a result, measurement of the lattice structure in diffraction space may become imprecise or computationally inconvenient. This challenge can be avoided by a transform that provides a means for lattice measurement in real space.

These considerations lead us to define the exit wave power cepstrum (EWPC) as follows:

$$EWPC_\phi(\boldsymbol{x}) = PC\big(\phi(\boldsymbol{x})\big) = \left|\mathcal{F}\left(\ln\left(\left|\mathcal{F}\big(\phi(\boldsymbol{x})\big)\right|^2\right)\right)\right|^2 = \left|\mathcal{F}\left(\ln\big(I(\boldsymbol{q})\big)\right)\right|^2. \tag{0.4}$$

For exit wave $\phi(\boldsymbol{x})$ with real-space position $\boldsymbol{x}$ and reciprocal-space scattering vector $\boldsymbol{q}$. The EWPC can easily be calculated from the diffraction pattern $I(\boldsymbol{q}) = \left|\mathcal{F}\big(\phi(\boldsymbol{x})\big)\right|^2$, which

"calculates" the first part of the power cepstrum transform physically. The EWPC concentrates the signal from the set of periodic diffracted disks into sharp real-space points that are convenient for high-precision lattice measurements while also separating out "undesirable" effects from specimen tilt and thickness, as we will discuss in detail below.

2.3.2 Interpretation of EWPC Patterns

We will use a simple model of nanobeam electron diffraction (NBED) to illustrate the separation properties of the EWPC and provide a basis for the interpretation of EWPC patterns for diffraction mapping.

To provide an illustrative and simplified analytical model of the real-space exit wave $\phi(x)$ and the EWPC we can begin by approximating the specimen as a strong phase object, such that:

$$\phi(x) = \phi_P(x)\exp\left(i\sigma\bar{V}(x)\right), \tag{0.5}$$

where $\phi_P(x)$ is the probe function, σ is a scaling factor, and $\bar{V}(x)$ is the projected specimen potential. The diffraction pattern is

$$I(q) = \left|\mathcal{F}\big(\phi(x)\big)\right|^2$$

$$= \left|\mathcal{F}\big(\phi_P(x)\big) * \mathcal{F}\left(\exp\left(i\sigma\bar{V}(x)\right)\right)\right|^2$$

$$= |\Phi_P(q) * \mathcal{V}(q)|^2, \tag{0.6}$$

where $\Phi_P(q)$ is the diffraction-space probe and $\mathcal{V}(q) = \mathcal{F}\left(\exp\left(i\sigma\bar{V}(x)\right)\right)$. In the kinematical or weak phase approximation, we take $\exp\left(i\sigma\bar{V}(x)\right) \approx 1 + i\sigma\bar{V}(x)$, so that $\mathcal{V}(q)$ is essentially the Fourier transform of the projected specimen potential. In the strong phase approximation, the additional higher order terms can be thought of as multiple scattering corrections.

33
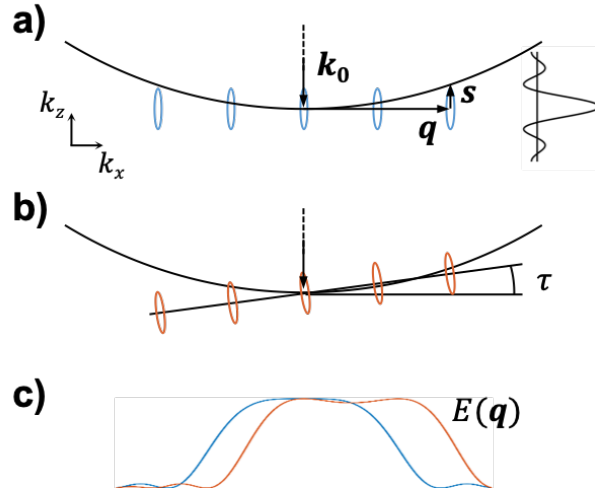
Figure 2.2: Diagram of Ewald sphere intersecting with reciprocal lattice points broadened by finite specimen thickness for (a) an on-axis specimen and (b) a specimen tilted at angle τ, with incident wavevector $\boldsymbol{k_0}$, scattering vector $\boldsymbol{q}$, and excitation error $\boldsymbol{s}$. Coordinates oriented with $\boldsymbol{k_x}$ to the right, $\boldsymbol{k_y}$ into the page, and $\boldsymbol{k_z}$ up. (c) The resulting amplitude-attenuating envelope function $\boldsymbol{E(q)}$ for each case.

The strong phase model can be extended to account for kinematical specimen tilt and thickness effects by inclusion of the Ewald sphere.[27,28] The reciprocal space distance between the Ewald sphere and the reciprocal lattice points is expressed by the excitation error $s(\boldsymbol{q})$. For electrons with incident wavevector $\boldsymbol{k_0}$, the excitation error for an on-axis specimen is $s(\boldsymbol{q}) \approx q^2/2k_0$, where $q^2 = q_x^2 + q_y^2$. A tilt in the reciprocal lattice by an angle τ about the k_y-axis will add an additional term $\Delta s = -q_x \sin\tau \approx -q_x\tau$, for a total excitation error $s(\boldsymbol{q}) \approx q^2/2k_0 - q_x\tau$.

A sample of thickness T can be represented in real space by a top-hat function in the z-direction multiplied on the infinite lattice. In reciprocal space, this finite thickness broadens the reciprocal

lattice points by convolving with the Fourier transform of the top-hat function, $\text{sinc}(k_z T/2)$. The excitation error thus leads to an attenuation of the diffracted amplitude[d]:

$$I(\boldsymbol{q}) = \left|\Phi_P(\boldsymbol{q}) * \left(E(\boldsymbol{q}) \cdot \mathcal{V}_0(\boldsymbol{q})\right)\right|^2, \tag{0.7}$$

Where $\mathcal{V}_0$ is the "tilt-free" object function, defined such that $\mathcal{V}(\boldsymbol{q}) = E(\boldsymbol{q}) \cdot \mathcal{V}_0(\boldsymbol{q})$, and

$$E(\boldsymbol{q}) = \text{sinc}\left(\frac{s(\boldsymbol{q})T}{2}\right) = \text{sinc}\left(\left(\frac{q^2}{2k_0} - q_x\tau\right)\frac{T}{2}\right). \tag{0.8}$$

The function $E(\boldsymbol{q})$ can be viewed as an envelope function attenuating the diffraction pattern. For finite thickness samples, multiple scattering will also tend to broaden the envelope of the diffraction pattern, although this effect is difficult to model analytically. This effect can also be included within $E(\boldsymbol{q})$ for purposes of this simple model. Typically, this envelope function varies slowly in comparison to the convergence angle of the probe[e], and so we can make the approximation:

$$I(\boldsymbol{q}) \approx \left|E(\boldsymbol{q}) \cdot \left(\Phi_P(\boldsymbol{q}) * \mathcal{V}_0(\boldsymbol{q})\right)\right|^2 = |E(\boldsymbol{q})|^2 \cdot |\Phi_P(\boldsymbol{q}) * \mathcal{V}_0(\boldsymbol{q})|^2. \tag{0.9}$$

This approximation allows for separation of the tilt envelope in the EWPC:

$$\text{EWPC}_\phi(\mathbf{x}) \approx \left|\mathcal{F}\left(\ln(|E(\boldsymbol{q})|^2 \cdot |\Phi_P(\boldsymbol{q}) * \mathcal{V}_0(\boldsymbol{q})|^2)\right)\right|^2$$

---

[d] Here we have neglected phase shifts on the diffracted beams, which do not impact the diffracted intensities.

[e] For a sample tilted very far from a major zone axis, the assumption of a slowly varying envelope function degrades, and the effect of tilt will remain convolved into the EWPC to some degree rather than separating linearly, causing some blurring of the pattern.

$$= \left| \mathcal{F}\left(\ln(|E(\boldsymbol{q})|^2) + \ln(|\Phi_P(\boldsymbol{q}) * \mathcal{V}_0(\boldsymbol{q})|^2) \right) \right|^2. \tag{0.10}$$

The second term above can be further simplified with the assumption of nanobeam diffraction conditions. In particular, we will assume that the probe $\Phi_P(\boldsymbol{q})$ is a flat, top-hat function in diffraction space, and the separation between Bragg points in $\mathcal{V}_0(\boldsymbol{q})$ is larger than twice the convergence semi-angle, so that the diffracted disks do not overlap. We can approximate $\mathcal{V}_0(\boldsymbol{q})$ as a sum of delta functions at the Bragg points $\boldsymbol{G}_i$ with amplitudes $b_{\boldsymbol{G}i}$:

$$\mathcal{V}_0(\boldsymbol{q}) = \sum_{\boldsymbol{G}_i} b_{\boldsymbol{G}i}\, \delta(\boldsymbol{q} - \boldsymbol{G}_i). \tag{0.11}$$

This convolves with the probe function:

$$\Phi_P(\boldsymbol{q}) * \mathcal{V}_0(\boldsymbol{q}) = \Phi_P(\boldsymbol{q}) * \sum_{\boldsymbol{G}_i} b_{\boldsymbol{G}i}\, \delta(\boldsymbol{q} - \boldsymbol{G}_i)$$

$$= \sum_{\boldsymbol{G}_i} b_{\boldsymbol{G}i}\Phi_P(\boldsymbol{q}) * \delta(\boldsymbol{q} - \boldsymbol{G}_i)$$

$$= \sum_{\boldsymbol{G}_i} b_{\boldsymbol{G}i}\Phi_P(\boldsymbol{q} - \boldsymbol{G}_i). \tag{0.12}$$

For non-overlapping diffracted spots, the operations outside the sum may be passed inside

$$\ln(|\Phi_P(\boldsymbol{q}) * \mathcal{V}_0(\boldsymbol{q})|^2) = \ln\left(\left| \sum_{\boldsymbol{G}_i} b_{\boldsymbol{G}i}\Phi_P(\boldsymbol{q} - \boldsymbol{G}_i) \right|^2 \right)$$

$$= \sum_{\boldsymbol{G}_i} \ln(|b_{\boldsymbol{G}i}\Phi_P(\boldsymbol{q} - \boldsymbol{G}_i)|^2). \tag{0.13}$$

For a simple, top-hat probe function with convergence semi-angle α,

$$\Phi_P(\boldsymbol{q}) = \begin{cases} 1, & |\boldsymbol{q}| < \alpha \\ 0, & |\boldsymbol{q}| > \alpha \end{cases}, \tag{0.14}$$

these operations may further be passed onto the coefficients alone:

$$\ln(|\Phi_P(\boldsymbol{q}) * \mathcal{V}_0(\boldsymbol{q})|^2) = \sum_{\boldsymbol{G}_i} \ln(|b_{\boldsymbol{G}i}|^2) \Phi_P(\boldsymbol{q} - \boldsymbol{G}_i)$$

$$= \Phi_P(\boldsymbol{q}) * \ln(|\mathcal{V}_0(\boldsymbol{q})|^2). \tag{0.15}$$

With these simplifications, the EWPC becomes:

$$\text{EWPC}_\phi(\mathbf{x}) \approx \left| \mathcal{F}\left(\ln(|E(\boldsymbol{q})|^2) + \Phi_P(\boldsymbol{q}) * \ln(|\mathcal{V}_0(\boldsymbol{q})|^2) \right) \right|^2$$

$$= \left| \mathcal{F}\left(\ln(|E(\boldsymbol{q})|^2) \right) + \mathcal{F}\left(\Phi_P(\boldsymbol{q}) \right) \cdot \mathcal{F}\left(\ln(|\mathcal{V}_0(\boldsymbol{q})|^2) \right) \right|^2$$

$$= \left| \mathcal{F}\left(\ln\left(|\mathcal{F}(\epsilon(\boldsymbol{x}))|^2 \right) \right) + \phi_P(\boldsymbol{x}) \cdot \mathcal{F}\left(\ln\left(|\mathcal{F}(v_0(\boldsymbol{x}))|^2 \right) \right) \right|^2, \tag{0.16}$$

where we have defined the real-space tilt-blur function $\epsilon(\boldsymbol{x}) = \mathcal{F}^{-1}(E(\boldsymbol{q}))$, and the real-space tilt-free object function $v_0(\boldsymbol{x}) = \mathcal{F}^{-1}(\mathcal{V}_0(\boldsymbol{q}))$.

We will generally have $\epsilon(\boldsymbol{x})$ and $l_0(\boldsymbol{x})$ with well-separated frequency bands, allowing us to assume no overlap between these terms:

$$\text{EWPC}_\phi(\mathbf{x}) \approx \text{PC}(\epsilon(\boldsymbol{x})) + |\phi_P(\boldsymbol{x})|^2 \cdot \text{PC}(v_0(\boldsymbol{x})). \tag{0.17}$$

This provides a simple interpretation of EWPC patterns. The lattice information in contained in the power cepstrum of the tilt-free real-space lattice $\text{PC}(v_0(\boldsymbol{x}))$. The lattice power cepstrum is similar to a Patterson function[26] or an autocorrelation of the real lattice, and will contain peaks corresponding to inter-atomic spacings, although the logarithm in the cepstral transform will result in different peak intensities from a Patterson function or autocorrelation. Like a Patterson function,

the lattice power cepstrum is higher symmetry than the real lattice, losing any inversion asymmetry. These peaks will be attenuated by a probe function envelope $|\phi_P(x)|^2$. This is intuitively appealing – we observe the interatomic spacings and orientations in the region illuminated by the probe – and sets a lower bound for the size of probe that can be used. The effect of the Ewald sphere intersecting the reciprocal lattice, which is sensitive to both sample tilt and thickness, is additively separated into the term $\mathrm{PC}\big(\epsilon(x)\big)$ and concentrated into the short-length region of the EWPC pattern.

For simplicity, the calculations of the EWPC in this paper will generally omit the outermost power of two from the definition, which has no practical importance for purposes of strain mapping. All of our patterns are thus calculated from nanobeam diffraction patterns using the transform:

$$\mathrm{EWPC} = \Big| \mathcal{F}\big(\ln(I(\boldsymbol{q})) \big) \Big|. \tag{0.18}$$

In practice, it is also useful to multiply the log-scale diffraction pattern by a window function to prevent the introduction of artifacts caused by non-periodic boundaries. A Hann window is used for this purpose in calculations throughout the paper.

2.3.3 *Lattice and Strain Mapping Using EWPC Patterns*

Lattice mapping can be achieved by calculating the positions of the inter-atomic spacing peaks in EWPC patterns. These peaks will include full-unit-cell translations, which will generally have the brightest peaks, as well as intra-unit-cell spacings. If peaks are identified to correspond to known lattice spacings, this provides a direct measurement of the local lattice parameters.

Systems with spatially varying lattice distortions or strain are of particular interest for high resolution lattice mapping. Calculation of lattice distortions or strain requires the selection of a

reference structure. It is often ideal to use the local lattice parameters of the material in its undeformed state as a reference, and strain calculated using this convention is known as the "material strain". However, the local, undeformed lattice parameters are often not known, making this approach impractical. An alternative is to use a single fixed reference, giving a quantity known as the "Lagrange strain".[2] The Lagrange strain can be calculated from a lattice map alone, without the need for any prior knowledge of the crystal structure.

To determine the projected strain tensor, a 2X2 matrix D is calculated that transforms the reference lattice points onto the measured points. This distortion matrix D includes both rigid rotation of the lattice and strain deformation. These may be separated by polar decomposition:

$$D = R * U = V * R, \tag{0.19}$$

where R is a unitary rotation matrix, and U and V are the non-rotational deformation transformations. The choice of U or V determines the coordinate system of the strain tensor: U is in "lattice coordinates", corresponding to the provided reference vectors, and V in "image coordinates", corresponding to the q_x and q_x directions in the diffraction pattern (independent of the rotation of the reference vectors). The strain tensor ε is then calculated as:

$$\varepsilon = U - 1, \text{or } \varepsilon = V - 1. \tag{0.20}$$

The components of the strain tensor, ε_{xx}, ε_{yy}, and $\varepsilon_{xy} = \varepsilon_{yx}$ are the x-direction stretch, y-direction stretch, and diagonal xy-direction stretch or shear, respectively. These quantities, along with the in-plane lattice rotation θ determined from R, are often of interest and can be examined directly. For some systems, such as core-shell nanoparticles, the geometry leads to varying strain directions that are not easily interpreted in rectangular coordinates. An alternative formulation is the "strain ellipse", which describes the strain through the semi-major axis, semi-minor axis, and

angle of the ellipse formed by applying the strain transformation to a circle. This is mathematically equivalent to describing the strain in its local eigenbasis, with the eigenvalues defining the semi-major and semi-minor axes of the strain ellipse and the direction of the eigenvectors defining the angle of principal strain.

2.4 Materials and Methods

2.4.1 TEM Sample Preparation

Cross-sectional specimens of $PbTiO_3$ thin films on $DyScO_3$ and $GdScO_3$ substrates were prepared using focused ion beam lift-out and thinning with a FEI Strata 400 Focused Ion Beam with a final 2 keV milling step to reduce surface damage. Specimens of carbon-supported Pt-Co nanoparticle fuel cell catalysts were prepared by cross-sectioning of a fuel cell membrane electrode assembly that had undergone an accelerated stability test. Details of catalyst, cell assembly, and stability testing are reported in another manuscript.[29] Cross-sections were cut using a Leica Ultracut UCT Ultramicrotome at a nominal thickness of 40 nm and collected on lacey carbon-coated TEM grids. The monolayer MoS_2 specimen was suspended on a holey amorphous silica support film.

2.4.2 Scanning Transmission Electron Microscopy (STEM)

STEM imaging, electron energy loss spectroscopy (EELS), and diffraction mapping were performed in a FEI Titan Themis (S)TEM operated at 300 kV (120 kV for 2D materials). Atomic resolution imaging was performed using a convergence semi-angle of 21.4 mrad with the image signal collected on a high angle annular dark field (HAADF) detector. EELS mapping of Pt-Co nanoparticles was performed using a Gatan GIF Quantum 965 spectrometer in single-range EELS mode. Maps were acquired with a convergence semi-angle of 21.4 mrad, a ~200 pA beam current, a 10 ms dwell time, and ~1 Å pixel size, leading to a total dose of ~10^9 e$^-$/nm^2. Composition maps

were extracted by integrating the signal from the Co $L_{2,3}$ and Pt $M_{4,5}$ edges after background subtraction using exponential and linear-combination-of-power-laws background fits, respectively. EELS calculations were performed in MATLAB using functions in the image processing toolbox.

Lattice maps from atomic resolution STEM imaging were calculated using high-quality images made from 12-24 cross correlated acquisitions taken with a short dwell time (0.5-2 us) to minimize drift and improve signal. Using a 40 pA beam, this corresponded to a typical beam dose around 10^7 e^-/nm^2. Rough atomic positions were found by segmenting the image using a threshold after morphological background subtraction. Then, precise atomic positions were found by fitting with a two-dimensional Gaussian function near each rough atomic position. The atomic columns for Pb and Ti were then separated based on their HAADF intensity. To find the polarization, we calculate the offset of Ti from the center of the Pb cage, which is found by comparing the measured Ti position to the averaged positions of the 4 nearest Pb neighbors. Strain calculations were made from the atomic positions following the same conventions detailed in the following section.

2.4.3   STEM Nanobeam Diffraction Mapping

Nanobeam diffraction maps were acquired in STEM microprobe mode using the EMPAD[4] pixelated detector, which has high dynamic range and single electron sensitivity to allow collection of all scattered electrons as well as the unsaturated direct beam. Typical acquisitions used a 1 ms exposure time and 256X256 real-space pixels. With the ~1 ms detector readout time this results in a total acquisition time of ~2 minutes. Typical doses ranged from $10^3 - 10^6$ e^-/nm^2 depending on the required resolution and field of view. The detector reads out 128X128 pixels per frame, (with 124X124 used for diffraction pattern acquisition,) in 32-bit floating point numbers, resulting in ~4 GB files for typical acquisitions.

2.4.4   Calculation of Nanobeam Diffraction Lattice Maps

All computation was performed in MATLAB. Essential functions and example code are provided in the supplemental information. Prior to calculating the EWPC transform, a constant value is added to the raw diffraction patterns to make all values greater than zero for numerical convenience when computing logarithms. For calculation of 2D EWPC transforms a discrete fast Fourier transform is used, with a 2D Hann window to minimize edge artifacts.

Peaks are identified for lattice mapping using small rectangular masks that include the peak maximum for all pixels in the region of interest. At least two peaks must be tracked. At each real space pixel and for each peak mask, the mapping routine first determines a coarse (1-pixel precision) peak position from the pixel with maximum EWPC intensity within the mask. A high precision (sub-pixel) measurement of the peak maximum is then calculated using an optimization routine initialized at the coarse peak position. The objective function for the optimization calculates the value of the EWPC transform at a single point using a continuous Fourier transform, as well as the same constant offset and 2D Hann window used for 2D EWPC calculations. Optimization was performed using the Nelder-Mead simplex method (MATLAB's fminsearch). The optimization algorithm is constrained within the peak region using a modified objective function. The convergence tolerance of the optimization algorithm can also be adjusted to improve computation time. Strain mapping calculations were performed on a high-end desktop computer (2015 iMac 27"; 4.0GHz Quad-core Intel Core i7; 32GB 1600MHz DDR3 SDRAM). Typically, ~10 ms of computation time was required per EWPC peak fit, allowing strain map calculations within a few minutes.

After peak maxima are located for the entire map, lattice parameters may be calculated directly, or lattice distortions may be tracked by calculation of a 2X2 strain tensor. For calculation of the

strain tensor, a transformation matrix D is first determined for each real-space pixel by fitting the peak positions to reference points, (using MATLAB's fitgeotrans,) either absolute lattice vectors for known structures or relative, internal references for the Lagrange strain.

2.5   Results and Discussion

2.5.1   Properties of EWPC Patterns

A series of experiments was conducted to validate and illustrate the model presented in the theory section and to guide use of EWPC patterns for strain mapping. The EWPC transform leverages the additive separation properties provided by the log-scaled NBED to separate the effects of tilt and thickness from useful lattice information. Figure 2.3 illustrates these properties for NBED patterns (a) taken from domains in a $PbTiO_3$ that are oriented on the 100 zone axis (left) and tilted ~60 mrad off axis (right). As the EWPC transform (Figure 2.3b) is the Fourier transform of the log-scaled NBED, it can be used for filtering as done in conventional Fourier filtering. The slowly-varying envelope function $E(\boldsymbol{q})$ formed by tilt and thickness effects has its information concentrated into the short-distance region near the origin in the EWPC space. Selecting this region (highlighted in red in Figure 2.3b) with a low-pass filter of the log-scaled NBED isolates the envelope, as shown in Figure 2.3c. The lattice information is concentrated in the peaks at longer distances in the EWPC space. Selecting these with a high-pass filter of the log-scaled NBED isolates the periodic diffraction spots, as shown in Figure 2.3d. These two components can be additively recombined to reconstruct the original log-scaled NBED. The relative tilt between the left and right halves of Figure 2.3 primarily changes the envelope function, impacting short-distance region of EWPC separately from lattice information. However, the separation is imperfect for such a high tilt angle because the assumption of a slowly-varying envelope function required for complete separation is violated. This is visible in the slight blurring of the EWPC peaks at the

right in Figure 2.3b, although these peaks remain sharp and suitable for fitting to measure the lattice structure.
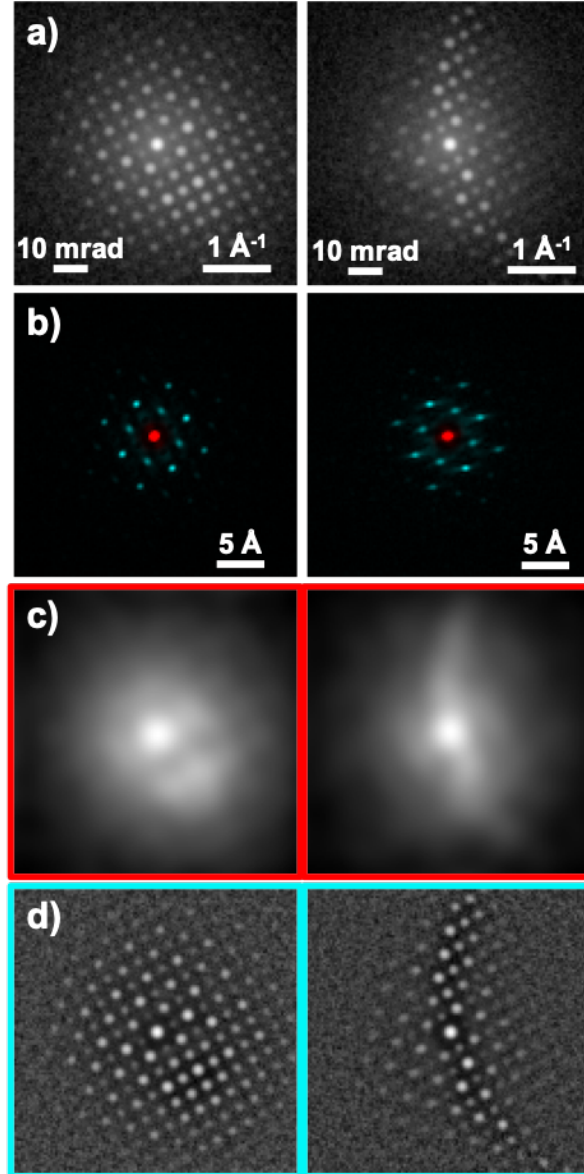
Figure 2.3: Illustration of additive separation of the tilt-envelope and the lattice information using the EWPC transform. (a) Log-scaled NBED patterns for PbTiO$_3$ oriented on 100 axis (left) and tilted ~60 mrad off axis. (b) EWPC patterns corresponding to the NBED patterns in (a). The short-distance region is selected with a low-pass filter shown by red coloring in (b), and the resulting low-pass filtered log(NBED) pattern (c) corresponds to the envelope function. The long-distance region is selected with a high-pass

44

filter shown by red coloring in (b), and the resulting high-pass filtered log(NBED) pattern (d) corresponds to the periodic diffraction information. The patterns in (c) and (d) additively recombine to the log(NBED) pattern in (a).
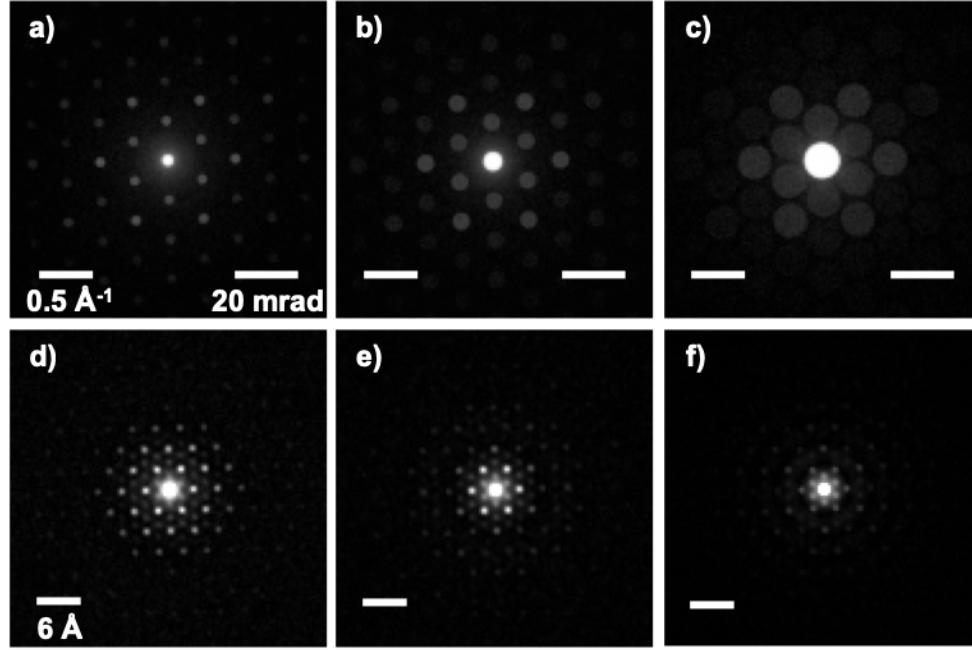
Figure 2.4: Diffraction patterns (a-c) and corresponding EWPC patterns (d-f) for different convergence semi-angles of the STEM probe acquired with 120 keV beam energy on monolayer MoS_2. Convergence semi-angles are (a,d) 1.3 mrad, (b,e) 2.5 mrad, (c,f) 5 mrad, corresponding to diffraction-limited resolutions (FWHM probe diameter) of 1.6 nm, 0.8 nm, and 0.4 nm, respectively.

The choice of STEM convergence angle in NBED determines both the real-space resolution and the size of the diffracted discs, which may impact the precision and ease of calculation of lattice structure. Figure 2.4 illustrates the impact of the convergence angle on EWPC patterns (d-f) calculated from NBED patterns (a-c) from monolayer MoS_2. As shown in Equation 17, the probe creates an envelope function multiplied over the lattice structure peaks in the EWPC pattern. Smaller convergence angles give a wider probe that makes more inter-atomic spacing peaks apparent in the EWPC pattern. Larger convergence angles give a smaller probe, attenuating the

intensity of higher-order spacings. In contrast to direct diffraction, the intensity of the peaks, and not their localization, is affected by the convergence angle. Including more higher-order peaks in a lattice structure may improve precision. It is notable that weak higher order peaks are also present in the tails of the probe envelope, although these peaks represent lattice structure information that is more delocalized than the lower order peaks within the central part of the probe envelope.

The lower bound on the spatial resolution achievable for EWPC structure determination comes as the convergence angle approaches a value where the disks in the NBED pattern would overlap. At this point the probe envelope in the EWPC pattern shrinks so that the first order lattice spacing peaks are lost. EWPC lattice measurement may be done using a FWHM probe diameter just larger than the unit cell. For example, Figure 2.4(c,d) show NBED and EWPC patterns taken with a 5 mrad convergence angle, giving a probe with a 0.4 nm diffraction-limited full-width half maximum (FWHM), just larger than the 0.315 nm unit cell of MoS_2. The first-order spots are present and viable to fit, although they are significantly attenuated because their corresponding 0.315 nm spacing is larger than the half-width half maximum (HWHM) probe radius of 0.2 nm. Near-unit cell spatial resolution is thus possible, although this attenuation will reduce the precision of lattice structure measurements and require a larger electron dose for high-precision measurements. With a HWHM probe radius equal to the unit cell size, giving 2-unit-cell resolution, or larger, the attenuation and precision loss will be relatively minor.
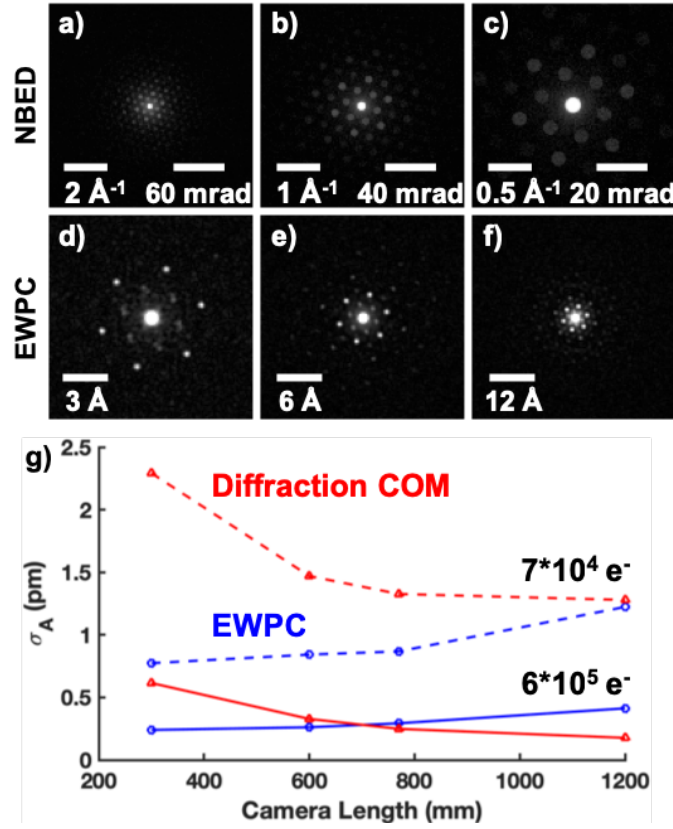
Figure 2.5: Comparison of diffraction patterns (a-c) and corresponding EWPC patterns (d-f) of monolayer MoS_2 at different camera lengths. Camera lengths are 300 mm for (a,d), 600 mm for (b,e) and 1200 mm for (c,f). Comparison of standard deviation of lattice parameter σ_A calculated from the center of mass (COM) of diffraction spots (red) and from EWPC peak fits (blue) for different camera lengths. Dotted lines show calculation for lower-dose patterns with $\sim 7*10^4$ electrons per pattern and solid lines are for higher-dose patterns with $6*10^5$ electrons per pattern.

Another important experimental consideration is the camera length used for NBED pattern acquisition. Changing the camera length will scale the size of the NBED pattern on the detector and the calculated EWPC pattern, as illustrated in Figure 2.5. The EWPC pattern scales inversely to the NBED pattern, with the EWPC pattern expanding as the NBED pattern shrinks. EWPC patterns using relatively small camera lengths therefore may be useful for resolving very similar lattice spacings.

The precision of lattice measurements from either direct diffraction or EWPC patterns will also be affected by the choice of camera length. Figure 2.5(g) illustrates the trend in precision by plotting the standard deviation of the average lattice parameter σ_A calculated from the center of mass (COM) of the {110} diffraction spots and from fits to the first-order EWPC peak. The comparison is made for both relatively low dose patterns with ~$7*10^4$ electrons per pattern and relatively high dose patterns with ~$6*10^5$ electrons per pattern, corresponding to beam currents of ~10 pA and ~100 pA for 1 ms acquisitions. Our choice of a monolayer material, which does not display strong diffraction artifacts, is a best-case scenario for the COM measurements. With the higher dose, both approaches provide overall similar precision well below 1 pm. EWPC fitting shows better precision at lower camera lengths, which allow the inclusion of more diffraction spots in the EWPC to improve the peak signal-to-noise ratio (SNR), while the diffraction COM shows better precision at higher camera lengths where the diffracted discs are spread over more pixels. Intermediate camera lengths provide good precision for both techniques and moving toward conditions more optimum for either provides mild improvements. At the lower dose, both techniques show the same trend with camera length, although EWPC fitting outperforms diffraction COM somewhat, achieving sub-pm precision at lower camera lengths. This difference is likely due to the inclusion of electrons from all diffraction spots in the calculation of the first-order EWPC peaks. The precision of the diffraction COM technique degrades markedly at the lowest 300 mm camera length, where the diffracted discs are only ~2 pixels across.

2.5.2   Lattice Mapping of Ferroelectric Domains in PbTiO₃

Ferroelectric materials present one interesting class of systems for high resolution lattice mapping because atomic displacements in the crystal often drive the ferroelectric polarization. Many ferroelectric systems experience ferroelastic distortions of their unit cell on the order of a

few percent of the lattice parameters and rotations of a few degrees. Ferroelectric domains span wide length scales from nanometers to microns and can have atomically abrupt domain walls with emergent properties that may not be present in the bulk. While studying the domain and domain wall structure by STEM is an important step in understanding these materials, ferroelastic strain and other complexity in the specimen may introduce challenges such as varying crystallographic tilt which requires more robust characterization methods than direct lattice imaging with atomic resolution STEM. Lattice mapping with nanobeam electron diffraction and the EWPC transform combines the potential for high spatial resolution, large fields of view, and robust measurement to address these challenges.

Here we demonstrate this approach for ferroelectric $PbTiO_3$ films epitaxially strained on lattice-mismatched substrates. $PbTiO_3$ has a tetragonal unit cell with its long axis in the direction of the ferroelectric polarization. The mismatched substrate causes the $PbTiO_3$ to form domains of alternating lattice elongation to accommodate the strain.
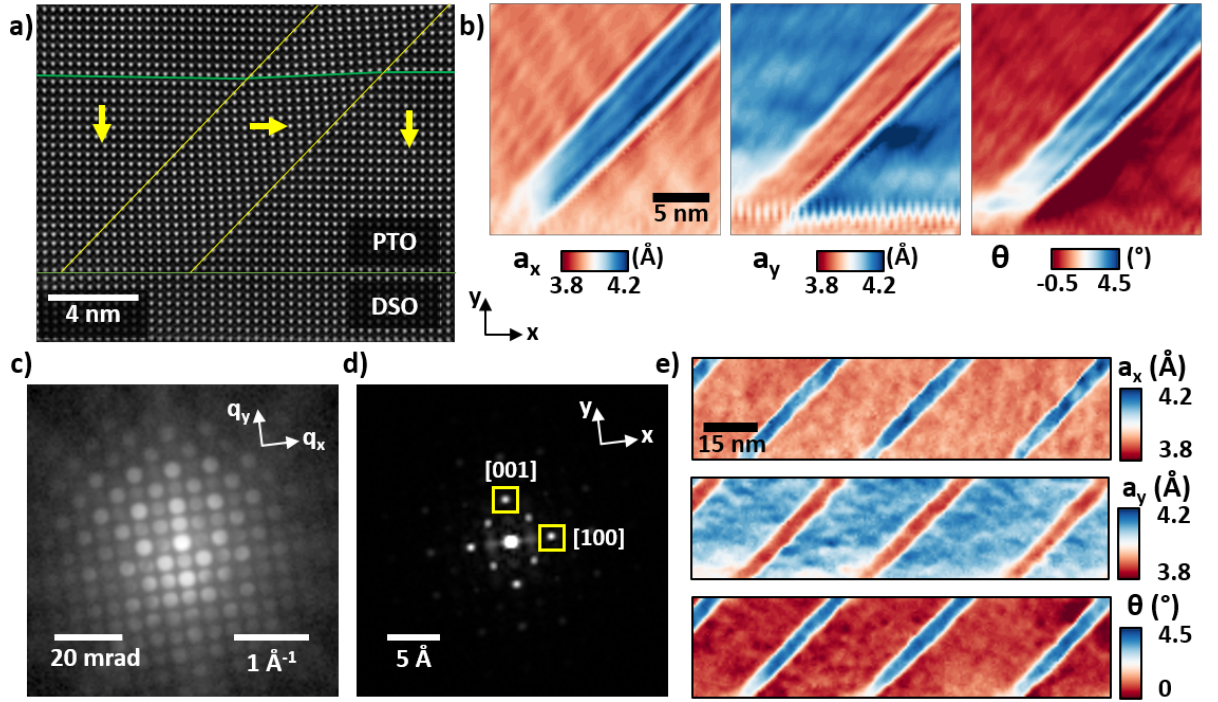
Figure 2.6: Lattice parameter mapping of ferroelastically strained PbTiO$_3$ by AC-STEM and EWPC. a) HAADF-STEM atomic resolution image of the PbTiO$_3$ (PTO) on a DyScO$_3$ (DSO) substrate. By inspecting the Ti displacement, the polarization direction can be found. At ferroelectric domains, a rotation of the lattice is observed. b) lattice parameters measured from fitting the atomic positions in the in-plane (a_x) direction, out-of-plane direction (a_y), and the rotation of the unit cell, θ. c) the NBED pattern of a single domain and d) the corresponding EWPC pattern. By mapping the spots indicated in d) the lattice parameters and rotation can be measured as shown in e).

Figure 2.6 presents lattice mapping of this domain structure for PbTiO$_3$ on a DyScO$_3$ substrate

using the EWPC approach and aberration-corrected STEM (AC-STEM) imaging and atom-fitting

for validation. Figure 2.6(a) shows an AC-STEM image of the PbTiO$_3$/ DyScO$_3$ domain structure

with wide "c" domains at the left and right where the long axis of the unit cell is oriented out of the

plane of the film (in the "y" direction). These are separated by a narrower "a" domain with the

polarization oriented in the plane of the film (in the "x" direction in the image plane) that cuts

diagonally across the field of view. Figure 2.6(b) shows quantitative lattice maps calculated from

50

atom-fitting, including the lattice parameters a_x and a_y and the lattice rotation θ. These maps confirm that the structure consists of domains where the tetragonal unit cell's long 4.156 Å axis and short 3.902 Å axis alternate directions together with a 3° rotation between the domains.

Figure 2.6(c) and (d) show NBED and EWPC patterns for a PbTiO$_3$ c-domain with the EWPC peaks used for fitting marked with yellow boxes. Figure 2.6(e) shows maps of the lattice parameters and lattice rotation calculated by tracking the EWPC peaks, which are both qualitatively and quantitatively consistent with the lattice maps from atomic resolution imaging. Mapping using the EWPC technique provides the additional advantages of allowing large fields of view and requiring a 3-4 orders of magnitude lower beam dose.
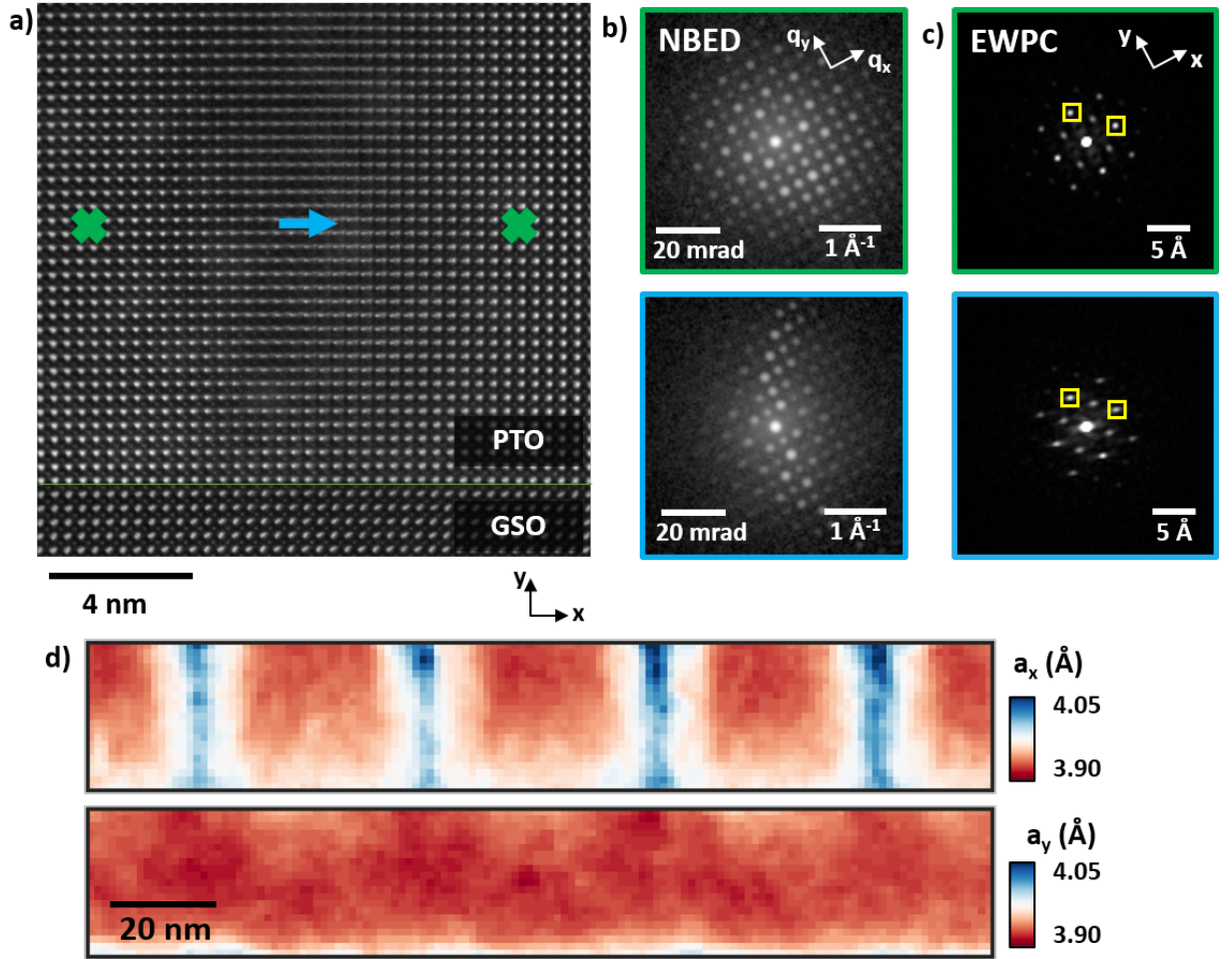
Figure 2.7: Mapping the lattice parameter of on and off-axis regions of $PbTiO_3$ that occur in ferroelectric domain configurations of $PbTiO_3$ / $GdScO_3$ (PTO/GSO). a) Atomic resolution STEM shows that at the domain marked in blue, the crystal tilts off axis and atomic resolution is lost. b) NBED and c) EWPC patterns from the regions of the crystal corresponding to ones like marked in green and blue in a). NBED shows a clear tilting off axis in the blue region, but the EWPC spots remain clear. d) EWPC is still able to map the in-plane (a_x) and out-of-plane (a_y) lattice parameters.

Depending on the film-substrate lattice mismatch, a domain structure may form in which some domains tilt in the plane of the film, such that the domain structure cannot be visualized with both domains simultaneously on axis. Figure 2.7 illustrates this situation with a $PbTiO_3$ film on a $GdScO_3$ substrate. The lattice structure of one domain cannot be resolved in atomic resolution

imaging (Figure 2.7(a)), and NBED patterns (Figure 2.7(b)) show that this domain has a relative tilt of ~60 mrad or ~3.4°. This presents a major challenge for characterization of this domain structure by AC-STEM. However, in EWPC patterns for the two domains (Figure 2.7(c)) the atomic-spacing peaks remain quite sharp even for the off-axis domain. While some blurring of one set of peaks is present, it does not prevent lattice mapping from the EWPC patterns, shown in Figure 2.7(d). These maps reveal the domain structure to be an a_1-a_2 type, with wide domains oriented with their long axis in the film plane along the optic axis and narrow domains oriented in the film and image planes ("x" direction).

2.5.3 Strain Mapping of Core-Shell Pt-Co Catalyst Nanoparticles

Another application space where high-resolution strain characterization can be highly valuable is catalytic nanoparticles. Application of strain to a catalytic surface to alter chemical binding strengths is an important strategy to enhance the catalytic activity.[30–32] Nanoparticles are commonly used as catalytic materials because of their high surface area to volume ratios and strain engineering can be achieved through core-shell nanoparticle structures. Direct lattice imaging can be used effectively to characterize lattice structure and strain for some nanoparticles, such as strongly faceted, unsupported particles that can easily be aligned and imaged on zone axis. [33–35] Supported catalysts, which are used in applications such as chemical processing and fuel cells, tend to have catalyst particles at random orientations, especially for non-crystalline supports such as carbon blacks. Furthermore, these materials are frequently heterogeneous, and high throughput characterization is needed to ensure statistically representative measurements. These concerns make direct imaging methods poorly suited for supported catalyst nanoparticles but allow NBED-EWPC strain mapping to excel.
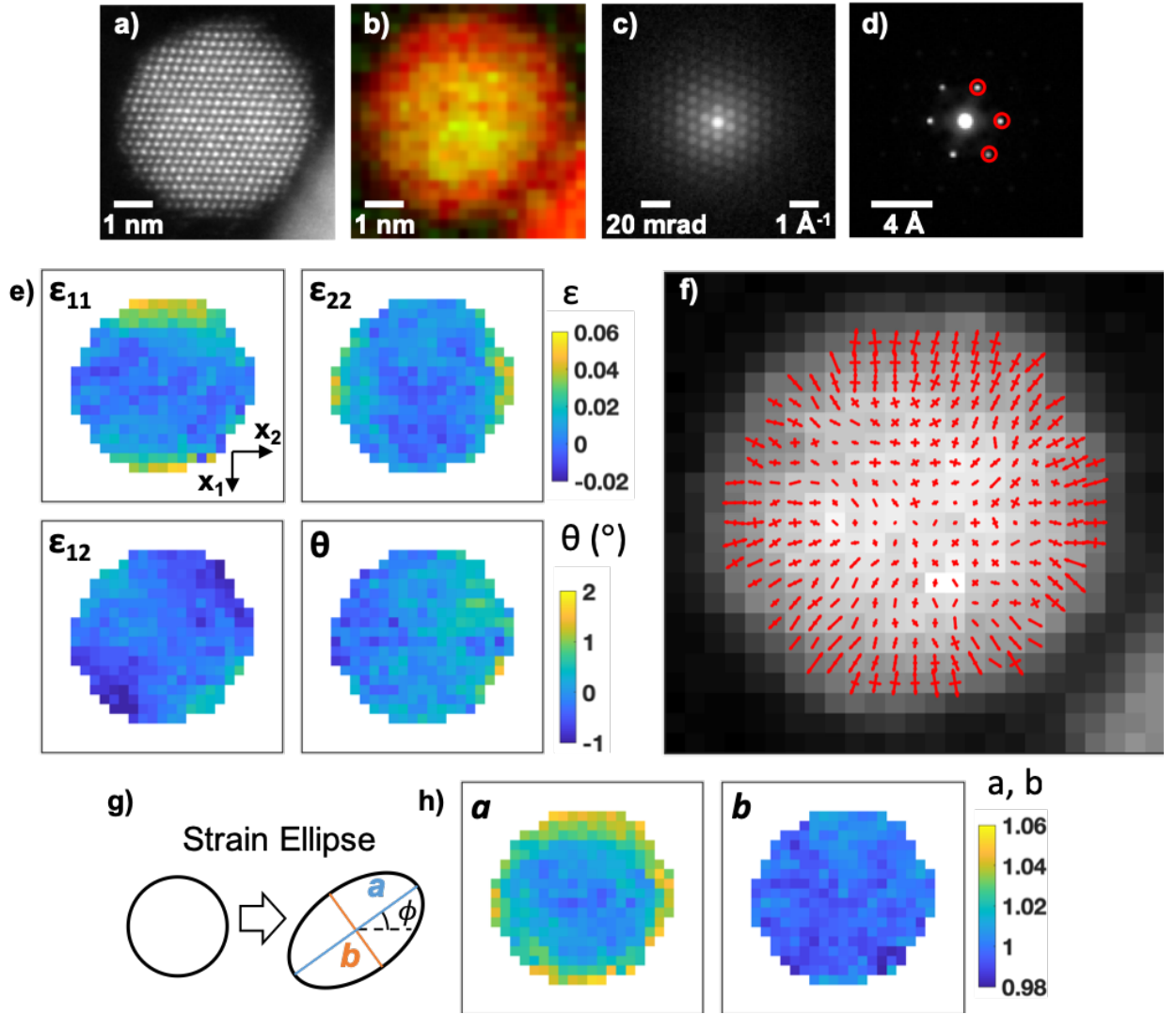
Figure 2.8: Strain mapping of a core-shell Pt-Co fuel cell catalyst nanoparticle. (a) Atomic resolution STEM image of the particle oriented on the 110 zone axis. (b) EELS composition map showing Pt in red and Co in green. Conditions were then switched to microprobe mode for the same particle for NBED mapping. (c) Averaged NBED pattern and (d) corresponding EWPC pattern from the center of the particle. EWPC spots circled in red in (d) were used for strain mapping. (e) Maps of strain tensor elements for Lagrange strain referenced to the particle center. (f) Visualization of principal strain vectors as red arrows for both the principal and orthogonal secondary strain directions. (g) Schematic of the strain ellipse construction, with semi-major axis *a*, semi-minor axis *b*, and angle of principal strain ϕ. (h) Visualizations of the strain ellipse axes *a* and *b*.

To demonstrate the effectiveness of EWPC strain mapping for catalytic nanoparticles, we will examine the strain distribution in Pt-Co/C fuel cell catalyst nanoparticles. Pt-alloy fuel cell catalyst nanoparticles are generally prepared with a thin Pt shell which experiences a compressive strain from the smaller lattice constant of the alloy core.[36–39] This compressive strain is intended to decrease the oxygen binding strength on the surface to enhance the oxygen reduction activity. One challenge to this approach is that the catalyst particles degrade and lose catalytic activity during use because of electrochemical cycling and the harsh acidic environment in the fuel cell, which lead to growth of the Pt shells to thicknesses ranging from one to several nanometers.[29,40] Growth in the shell thickness is expected to lead to relaxation of the surface strain, resulting in loss of catalytic activity, but the details of this process are poorly understood because of the lack of suitable strain characterization.

To simulate a lifetime of fuel cell use, the Pt-Co/C catalyst examined here has been subjected to an electrochemical stability test, as described in a separate publication.[29] Figure 2.8(a) shows a ~5 nm diameter nanoparticle oriented on the 110 axis. An electron energy loss spectroscopy (EELS) map (Figure 2.8b) of the Co $L_{2,3}$ and Pt $M_{4,5}$ edges shows that a ~1 nm thick Pt shell is present around the Pt-Co core. Compressive strain in the Pt shell is visible in the AC-STEM image (Figure 2.8(a)) as a slight inward bowing of the near-surface lattice planes. A NBED map of this particle was acquired using a 1.75 mrad convergence angle giving a 0.7 nm diffraction-limited resolution. An averaged NBED pattern and corresponding EWPC pattern are shown in Figure 2.8(c) and (d), respectively. The three strong peaks circled in the EWPC pattern corresponding to the 200, 020, 220 spacings were tracked for strain mapping. The Lagrange strain was calculated using the center of the particle as a reference, and the resulting strain tensor components and lattice rotation are shown in Figure 2.8(e). The primary effect visible is the radially outward Poisson expansion resulting from the tangential compression of the Pt shell. In rectangular coordinates, this manifests

as high ε_{11} at the top and bottom, high ε_{22} at left and right, and ε_{12} that is high at top-left and bottom right and low at top-right and bottom left. The changing strain direction around the shell can make these tensor components difficult to interpret. An alternative is to visualize principal strain vectors, as shown in Figure 2.8(f) which can more directly show that the strain is primarily a radially outward expansion in the shell. The principal strain can also be presented using the strain ellipse construction, which is formed by applying the strain transformation to a unit circle, as illustrated in Figure 2.8(g). The semi-major and semi-minor axes of the strain ellipse, *a* and *b*, (Figure 2.8(h)) indicate the magnitudes of the two principal strain vectors. For this approximately spherical core-shell geometry, the semi-major axis is approximately the radial strain, and the semi-minor axis is approximately the tangential strain. By adjusting to the varying strain direction, the strain ellipse axes produce a visualization of the particle's core-shell structure that is simpler to interpret.

The on-axis particle shown in Figure 2.8 could in principal have its strain mapped from direct imaging, as previously reported for an unsupported Pt nanoparticle.[33] Reaching the required precision on the order of a few picometers using AC-STEM imaging requires both high SNR and correction of STEM imaging distortions, typically by image stack acquisition and registration in post-processing. These requirements impose high dose requirements – on the order of $10^8 – 10^9$ e⁻/nm².[33] High beam dose can be problematic as particles may rotate from damage to support or momentum transferred from incident electrons. NBED-EWPC strain mapping is dramatically more dose efficient, with a dose of around 10^6 e⁻/nm² used here. NBED-EWPC strain mapping also compares favorably on dose to EELS as a method to visualize core-shell structure, as the EELS map in Figure 2.8(b) required 10^9 e⁻/nm².
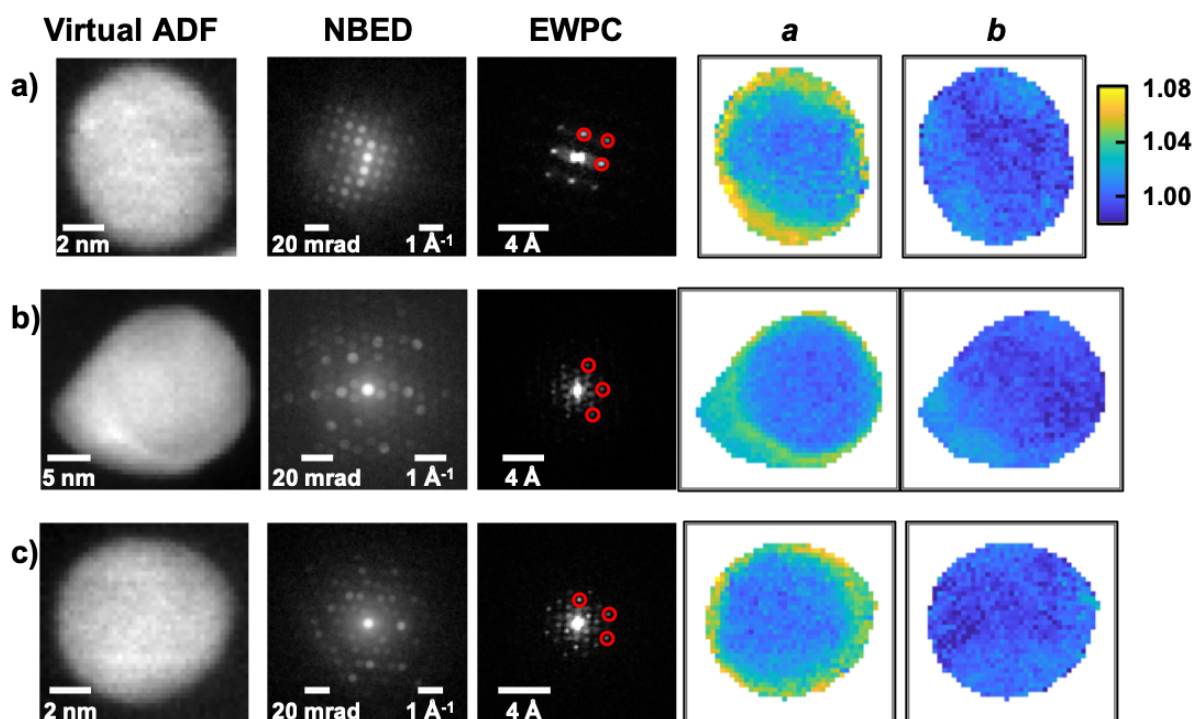
Figure 2.9: Strain mapping of three off-axis Pt-Co nanoparticles, including, from left to right, a virtual ADF image of the particle, an averaged NBED pattern from the particle center, the corresponding EWPC pattern with spots used for mapping circled in red, and the Lagrange strain referenced to the particle center visualized through the semi-major axis *a* and semi-minor axis *b* of the strain ellipse. The particle shown in (a) is oriented near the 200 zone axis, while the particles in (b) and (c) are far from any major zone axis.

EWPC strain mapping can also overcome the major challenges of random particle orientations and varying mistilt in strained particles. Given the mechanical imprecision of TEM stages, it is generally impractical to orient any given nanoparticle onto zone axis. On-axis particles such as the one in Figure 2.8 typically must be sought out and relying on these for strain mapping will compromise throughput and statistical representativeness. Figure 2.9 shows three examples of particles with varying orientations. Some particles are oriented near a major zone axis, like in Figure 2.9 (a), which is a couple degrees from the 200 orientation. Similar to the example in Figure 2.7, these particles will have the same peaks visible as they would if oriented precisely on axis. The

peaks show some mild blurring but are easily sharp enough for mapping. More commonly, particles selected at random are not close to any major zone axis, as in Figure 2.9(b) and (c). However, these patterns nearly all have sharp peaks suitable for tracking and calculation of the Lagrange strain. Varying mistilt caused by lattice distortions also generally do not cause EWPC peaks to disappear, in contrast to diffraction spots, making both random particle orientations and varying internal mistilts not significant obstacles to producing strain maps.

These methods are also suitable for high throughput characterization of nanoparticle strain. A typical 256X256 NBED map takes ~2 minutes to acquire and can contain several particles suitable for strain mapping. The example maps shown here typically have ~40X40 real space pixels for a single particle map. With the high-end desktop computer used for this study, less than 30s of computation was needed to produce a strain map of a nanoparticle with the off-particle pixels excluded. With only a few minutes needed per map between acquisition and computation the throughput of this technique is at least as high as EELS mapping of the core-shell structure for the same system, which has previously been used for a statistical study including hundreds of nanoparticle composition maps.[40] Strain mapping with the EWPC transform and EMPAD detector is practical method to collect and analyze tens or hundreds of particle maps as needed for statistics.

2.6   Summary and Outlook

In this manuscript we have demonstrated the EWPC transform for NBED to enable robust mapping of strain and lattice structure in complex specimens. We presented a simplified analytical model to aid in interpretation of transformed patterns. This model indicates that the EWPC transform allows additive separation of the effects of tilt and thickness from the lattice information contained in periodic diffraction spots. The resulting peaks correspond to real-space inter-atomic spacings, similar to a Patterson pair-correlation function. The EWPC-peaks are attenuated by a

function corresponding to the real-space probe, and first-order inter-atomic spacings can be measured for probe sizes just above the unit cell-size. This allows the method to attain near-unit-cell resolution, which is sub-nm for many materials. Fitting of the EWPC peaks can provide sub-pm precise lattice parameter measurements, and precision is optimum for NBED patterns acquired with low camera lengths to allow inclusion of many diffraction spots. Measurement of lattice structure from EWPC peaks is also highly dose efficient, using ~1000X less dose than comparable atomic-resolution STEM measurements.

We have demonstrated the practical use of the EWPC transform for mapping domains of ferroelectric distortions in strained $PbTiO_3$ films and compressively strained Pt shells in core-shell Pt-Co nanoparticle fuel cell catalysts. The distortions in the $PbTiO_3$ films measured with the EWPC technique were consistent with measurements by atomic-resolution STEM atom-fitting, while providing a larger field of view and lower beam dose. Use of the EWPC technique provided the additional benefit of allowing quantitative lattice mapping in domains tilted ~3-4° off zone-axis, which could not be resolved in atomic-resolution STEM. For the core-shell Pt-Co nanoparticles, the EWPC technique allowed sub-nm resolution mapping of strain in Pt shells thinner than a few nanometers. The technique was further demonstrated to be capable of mapping strain in off-axis particles and providing high-throughput analysis for statistically representative study of heterogeneous nanoparticle samples.

The EWPC transform for NBED mapping has the potential to be a useful tool in a wide range of applications. The sharp interatomic spacing peaks make precise fitting for lattice structure extraction numerically convenient, which may be beneficial even when precession is used. The EWPC properties allowing separation of useful lattice information from tilt and thickness effects make the technique robust for application to complex and challenging specimens. The EWPC peaks

maintain stable intensity to allow precise mapping even with varying mistilt, and the presence of

sharp peaks when far from major zone axis enable strain mapping in randomly oriented crystallites.

2.7   References

[1] A. Béché, J.L. Rouvière, J.P. Barnes, and D. Cooper, Ultramicroscopy **131**, 10 (2013).

[2] J.M. Zuo and J.C.H. Spence, *Advanced Transmission Electron Microscopy* (Springer New York, New York, NY, 2017).

[3] M.J. Hÿtch and A.M. Minor, MRS Bull. **39**, 138 (2014).

[4] M.W. Tate, P. Purohit, D. Chamberlain, K.X. Nguyen, R. Hovden, C.S. Chang, P. Deb, E. Turgut, J.T. Heron, D.G. Schlom, D.C. Ralph, G.D. Fuchs, K.S. Shanks, H.T. Philipp, D.A. Muller, and S.M. Gruner, Microsc. Microanal. **22**, 237 (2016).

[5] A. Mac Raighne, G. V. Fernandez, D. Maneuski, D. McGrouther, and V. O'Shea, J. Instrum. **6**, C01047 (2011).

[6] K. Müller, H. Ryll, I. Ordavo, S. Ihle, L. Strüder, K. Volz, J. Zweck, H. Soltau, and A. Rosenauer, Appl. Phys. Lett. **101**, 212110 (2012).

[7] C. Ophus, Microsc. Microanal. 1 (2019).

[8] K. Usuda, T. Mizuno, T. Tezuka, N. Sugiyama, Y. Moriyama, S. Nakaharai, and S. Takagi, Appl. Surf. Sci. **224**, 113 (2004).

[9] P.M. Jones, G.M. Rackham, and J.W. Steeds, Proc. R. Soc. A Math. Phys. Eng. Sci. **354**, 197 (1977).

[10] V.B. Ozdol, C. Gammer, X.G. Jin, P. Ercius, C. Ophus, J. Ciston, and A.M. Minor, Appl. Phys. Lett. **106**, (2015).

[11] Y. Han, K.X. Nguyen, M. Cao, P.D. Cueva, S. Xie, M.W. Tate, P. Purohit, S.M. Gruner, J. Park, and D.A. Muller, Nano Lett. **18**, 3746 (2018).

[12] A. Béché, J.L. Rouvière, L. Clément, and J.M. Hartmann, Appl. Phys. Lett. **95**, 123114 (2009).

[13] K. Müller, A. Rosenauer, M. Schowalter, J. Zweck, R. Fritz, and K. Volz, Microsc. Microanal. **18**, 995 (2012).

[14] D. Cooper, T. Denneulin, N. Bernier, A. Béché, and J.L. Rouvière, Micron **80**, 145 (2016).

[15] T.C. Pekin, C. Gammer, J. Ciston, A.M. Minor, and C. Ophus, Ultramicroscopy **176**, 170 (2017).

[16] R. Vincent and P.A. Midgley, Ultramicroscopy **53**, 271 (1994).

[17] P.A. Midgley and A.S. Eggeman, IUCrJ **2**, 126 (2015).

[18] J.L. Rouviere, A. Béché, Y. Martin, T. Denneulin, and D. Cooper, Appl. Phys. Lett. **103**, (2013).

[19] M.P. Vigouroux, V. Delaye, N. Bernier, R. Cipro, D. Lafond, G. Audoit, T. Baron, J.L. Rouvière, M. Martin, B. Chenevier, and F. Bertin, Appl. Phys. Lett. **105**, (2014).

[20] J.S. Barnard, D.N. Johnstone, and P.A. Midgley, Ultramicroscopy **174**, 79 (2017).

[21] C. Mahr, K. Müller-Caspary, T. Grieb, M. Schowalter, T. Mehrtens, F.F. Krause, D. Zillmann, and A. Rosenauer, Ultramicroscopy **158**, 38 (2015).

[22] R. Yuan, Y. Meng, J. Zhang, and J.-M. Zuo, Microsc. Microanal. **23**, 180 (2017).

[23] A.M. Noll, J. Acoust. Soc. Am. **41**, 293 (1967).

[24] B.P. Bogert, M.J.R. Healy, and J.W. Tukey, Proc. Symp. Time Ser. Anal. **15**, 209 (1963).

[25] A. V. Oppenheim and R.W. Schafer, IEEE Signal Process. Mag. **21**, (2004).

[26] A.L. Patterson, Phys. Rev. **46**, 372 (1934).

[27] J.C.H. Spence, *High-Resolution Electron Microscopy*, 4th ed. (Oxford University Press, New York, NY, 2013).

[28] A. Howie, in *Electron Microsc. Mater. Sci.*, edited by U. Valdre and A. Zichinchi (Academic Press, New York, NY, 1971), pp. 275–300.

[29] E. Padgett, V. Yarlagadda, M.E. Holtz, M. Ko, B.D.A. Levin, R.S. Kukreja, J.M. Ziegelbauer, R.N. Andrews, J. Ilavsky, A. Kongkanand, and D.A. Muller, J. Electrochem. Soc. **166**, F198 (2019).

[30] B. Hammer, Y. Morikawa, and J.K. Nørskov, Phys. Rev. Lett. **76**, 2141 (1996).

[31] A. Ruban, B. Hammer, P. Stoltze, H.. Skriver, and J.. Nørskov, J. Mol. Catal. A Chem. **115**, 421 (1997).

[32] M. Mavrikakis, B. Hammer, and J.K. Nørskov, Phys. Rev. Lett. **81**, 2819 (1998).

[33] A.B. Yankovich, B. Berkels, W. Dahmen, P. Binev, S.I. Sanchez, S.A. Bradley, A. Li, I. Szlufarska, and P.M. Voyles, Nat. Commun. **5**, 4155 (2014).

[34] J.-S. Kim, H.-K. Kim, S.-H. Kim, I. Kim, T. Yu, G.-H. Han, K.-Y. Lee, J.-C. Lee, and J.-P. Ahn, ACS Nano acsnano.9b01394 (2019).

[35] N. Bhattarai, G. Casillas, A. Ponce, and M. Jose-Yacaman, Surf. Sci. **609**, 161 (2013).

[36] F. Hasché, M. Oezaslan, and P. Strasser, ChemCatChem **3**, 1805 (2011).

[37] Q. Jia, K. Caldwell, J.M. Ziegelbauer, A. Kongkanand, F.T. Wagner, S. Mukerjee, and D.E. Ramaker, J. Electrochem. Soc. **161**, F1323 (2014).

[38] K.M. Caldwell, D.E. Ramaker, Q. Jia, S. Mukerjee, J.M. Ziegelbauer, R.S. Kukreja, and A. Kongkanand, J. Phys. Chem. C **119**, 757 (2015).

[39] B. Han, C.E. Carlton, A. Kongkanand, R.S. Kukreja, B.R. Theobald, L. Gan, R. O'Malley, P. Strasser, F.T. Wagner, and Y. Shao-Horn, Energy Environ. Sci. **8**, 258 (2015).

[40] H.L. Xin, J.A. Mundy, Z. Liu, R. Cabezas, R. Hovden, L.F. Kourkoutis, J. Zhang, N.P. Subramanian, R. Makharia, F.T. Wagner, and D. a Muller, Nano Lett. **12**, 490 (2012).

3   STRAIN RELAXATION IN CORE-SHELL Pt-Co CATALYST

NANOPARTICLES

3.1   Abstract

Surface strain is known to play a key role in enhancing the activity of Pt-alloy nanoparticle oxygen reduction catalysts. However, the details of strain effects in real fuel cell catalysts have not been well explored, in part due to a lack of effective characterization techniques suitable for the complexities of the system. This chapter investigates these effects using strain mapping with nanobeam electron diffraction and a continuum elastic model of strain in simple core-shell particles. We find that surface strain is relaxed both by lattice defects at the core-shell interface and by relaxation across particle shells caused by Poisson expansion in the spherical geometry. The continuum elastic model finds that in the absence of lattice dislocations, geometric relaxation results in a surface strain that scales with the average composition of the particle, regardless of the shell thickness. We investigate the impact of these strain effects on catalytic activity for a series of Pt-Co catalysts treated to vary their shell thickness and core-shell lattice mismatch. For catalysts with the thinnest shells the activity is consistent with an Arrhenius dependence on the surface strain expected for coherent strain in dislocation-free particles, while catalysts with thicker shells showed greater activity losses indicating strain relaxation caused by dislocations as well.

3.2   Introduction

The challenging kinetics of the oxygen reduction reaction (ORR) continue to present major hurdles for the commercialization of proton exchange membrane fuel cell technologies for transportation applications. ORR kinetics are the greatest source of voltage losses for well-

optimized membrane electrode assemblies (MEAs),[1] limiting the overall cell efficiency and requiring the use of scarce Pt-based catalysts to provide high power density.

Pt-based nanoparticles alloyed with a secondary transition metal such as Co or Ni are the most promising catalysts demonstrated to be viable in MEAs.[2] In practice, these nanoparticles generally have a core-shell structure, as the acidic fuel cell environment dissolves the secondary non-precious metal near the catalyst structure, leaving a Pt shell surrounding an alloy core. Typically the catalyst is prepared by dealloying[3–6] by acid leaching to form the core-shell structure prior to the assembly of the MEA, where unnecessary dissolution of the secondary metal harms the conductivity of the membrane. During the lifetime of the fuel cell redeposition of dissolved Pt and leaching of the secondary metal causes the thickness of the Pt shell to grow up to several nanometers.[7,8]

Pt-alloy catalysts such as Pt-Co or Pt-Ni provide significant enhancements in specific activity over comparable pure Pt particles or surfaces. Two mechanisms are generally posited for this activity enhancement – strain or electronic charge transfer ("ligand effects"). Each of these mechanisms would alter the binding strength of adsorbed intermediate species in the ORR by altering the electronic structure of the Pt surface, as described by the Hammer-Norskov d-band model.[9–12] However, the Pt shell for operating catalysts is generally thicker than a single monolayer, making electronic charge transfer unlikely to impact the surface electronic structure because of the short electronic screening length in metals.[f] Thus while charge transfer effects may be important for some ORR catalysts, strain is the more probable mechanism under normal circumstances for Pt alloy catalysts. The importance of strain in surface reactivity has been understood theoretically for some time and validated for ideal surfaces.[11,12] In the case of Pt-Co and Pt-Ni ORR catalysts, the

---

[f] Thomas-Fermi screening length of ~0.6Å for Pt is expected, compared to 2.8Å inter-atomic spacing.

alloy core has a smaller lattice constant than pure Pt, resulting in a compressive strain exerted on the Pt shell. In the d-band model, the compressive strain is expected to broaden the Pt d-band, pushing its center down away from the Fermi level and weakening the bonding strength of oxygen intermediates.

The expected enhancement of ORR activity is observed for Pt-Co and Pt-Ni catalysts, and the advantage in activity over pure Pt is lost as the Pt shell grows in thickness due to electrochemical aging. However, few details are understood about the connections between structure, strain, and activity for Pt-alloy fuel cell catalysts and how the intended strain-induced activity is lost from catalyst degradation over the lifetime of the fuel cell. Macroscopic averages of the strain estimated by X-ray diffraction show a correlation between strain and activity but are in poor qualitative agreement with theory.[13] In particular, the strain effects expected for the spherical core-shell geometry typical of catalyst nanoparticles are not widely understood, and the differences from more widely understood planar films not always appreciated. Furthermore, fuel cell catalysts operating in a MEA environment are complex, with heterogeneous structures and many effects contributing to the observed bulk activity that are challenging to disentangle. It is important to understand real-world strain effects and their role in ORR activity to enable the strategic development of durable, high performance catalyst materials.

Progress on this front has been limited by lack of characterization tools suitable for measuring strain in realistic fuel cell catalyst nanoparticles. Nanoscale strain characterization has been demonstrated using techniques including atomic resolution imaging and nanobeam electron diffraction (NBED), but prior demonstrated methods are poorly suited to the complexity of core-shell nanoparticle catalysts. To be effective for this system, a strain characterization technique must be able to provide sub-nm spatial resolution and be robust to varying specimen thickness, background, and crystal orientation to provide high throughput for statistically representative

measurements. As shown in the previous chapter, NBED with the exit wave power cepstrum (EWPC) transform is a powerful technique to overcome these challenges.

In this chapter we apply the NBED-EWPC technique alongside a simple continuum elastic model for core-shell particles to explore the basic strain effects relevant for Pt-M nanoparticle catalysts. We examine the strain distributions present in dealloyed and electrochemically aged catalysts. Two mechanisms for strain relaxation are identified: geometrical relaxation from Poisson expansion in spherical shells and dislocation-driven relaxation. We demonstrate that consideration of these two mechanisms can account for the loss of catalytic activity observed in a controlled series of catalysts dealloyed to different shell thicknesses.

3.3   Materials and Methods

3.3.1   Catalyst materials and MEA assembly

The Pt-Co catalysts used in this study were synthesized using an impregnation method followed by chemical dealloying. The catalyst was loaded on the carbon black support at 30wt% Pt. Both Vulcan and HSC carbon supports were used, and these catalysts and supports are described in more detail in a prior publication.[8] The electrochemically aged particles are sampled from both Pt-Co/HSC and Pt-Co/Vulcan catalysts, while the series of dealloyed catalyst particles are supported on HSC.

Membrane electrode assemblies (MEAs) were fabricated with the electrocatalysts of interest on the cathode. MEAs had an active area of 50 cm^2 and Pt loadings of 0.1 and 0.025 mg$_{Pt}$/cm^2 for the cathode and anode, respectively. Perfluorosulfonic acid (PFSA) Nafion$^{\circledR}$ D2020 was used in the electrode at an ionomer to carbon weight ratio of 0.8 and 18 μm thick PFSA-based membranes were used. A 240 μm thick carbon paper with a 30 μm thick microporous layer (MPL) coated on

top was used as the gas diffusion layer (GDL). The MEAs were fabricated using a catalyst-coated-membrane approach following a lamination procedure discussed in detail elsewhere.[1]

The series of dealloyed catalysts, with properties summarized in Table 3.1, was prepared starting with a dealloyed $Pt_{3.2}Co_1$/HSC catalyst with a shell thickness of ~0.5 nm. Prior to the initial dealloying the alloy composition was approximately Pt_1Co_1. The $Pt_{3.2}Co_1$/HSC catalyst was subjected to additional dealloying via an acid leach for 1 day and 3 days, resulting in compositions of $Pt_{3.8}Co_1$ and $Pt_{4.8}Co_1$, respectively. A portion of the $Pt_{4.8}Co_1$/HSC catalyst was annealed and dealloyed again via acid leaching, resulting in a composition of $Pt_{5.5}Co_1$. A Pt/HSC catalyst was also prepared and annealed to have a particle size approximately equal to that of the Pt-Co catalysts.

Table 3.1: Summary of properties of the series of dealloyed catalysts.

Catalyst	$Pt_{3.2}Co_1$/HSC	$Pt_{3.8}Co_1$/HSC	$Pt_{4.8}Co_1$/HSC	$Pt_{5.5}Co_1$/HSC	Pt/HSC
ECSA (m^2/g_{Pt})	60	59	58	61	55
Mass Activity (A/mg_{Pt})	0.49	0.44	0.34	0.42	0.26
Specific Activity ($\mu A/cm^2_{Pt}$)	822	748	585	692	469

3.3.2   *MEA testing*

The catalysts in assembled MEAs were electrochemically aged following an accelerated stability test (AST) recommended by the U.S. Department of Energy (DOE)[14] consisting of 30,000 trapezoidal voltage cycles between 0.6 and 0.95 V with a 2.5 s dwell time at each voltage and a 0.5 s ramp time. The AST was performed at 80°C, 100% relative humidity, and ambient pressure. ORR activity measurements were performed in MEA and are reported at 0.9 V_{RHE} at 80°C, 100% relative humidity, and 1 bar of O_2.[1] The electrochemically active surface area (ECSA) of Pt was measured by CO stripping in an MEA.[15]

3.3.3   TEM sample preparation

Samples of the electrochemically aged catalysts for (scanning) transmission electron microscopy ((S)TEM) were prepared by cross-sectioning the MEAs with an ultramicrotome. Strips cut from the MEAs were embedded in EMbed 812 Resin (Electron Microscopy Sciences) and cured at 60°C overnight. Sections were cut using a Leica Ultracut UCT Ultramicrotome at 40 – 50 nm thickness. Sections were collected on square-mesh Cu TEM grids with lacy carbon. Samples were cleaned with oxygen-argon plasma prior to TEM measurements.

3.3.4   NBED measurements

Nanobeam electron diffraction (NBED) mapping was performed in a FEI Titan Themis (S)TEM operated at 300 kV in STEM microprobe mode. Diffraction patterns were acquired on the EMPAD[16] pixelated detector, which has high dynamic range and single electron sensitivity to allow collection of all scattered electrons as well as the unsaturated direct beam. Typical acquisitions used a 1 ms exposure time with a beam current around 10-15 pA and 256 x 256 real-space pixels.

3.3.5   Calculation of strain maps

All computation was performed in MATLAB. Lattice strain was calculated by tracking peaks in the exit wave power cepstrum (EWPC) calculated from the diffraction pattern using methods described in detail in the previous chapter. Strain maps were calculated for individual particles selected out of larger NBED maps, which typically include several particles. After peak maxima are located for the map, the 2 x 2 Lagrange strain tensor is calculated using the particle center as a reference. The strain ellipse axes are calculated from the eigenvalues of the strain tensor.

3.4   Results and Discussion

3.4.1   Elastic Continuum Theory for Core-Shell Particles

Elastic continuum theory provides an analytically tractable approach to describe the surface strain expected for core-shell particles under simple assumptions. Here we investigate an analytical model for an ideal spherical core-shell particle with isotropic elastic properties and a coherently strained shell. This model provides basic intuition for understanding strain effects and is a reasonable set of assumptions for some simple catalysts. However, it ignores atomistic effects, which are likely to be salient for Pt-Co catalysts with structures on the order of a few atomic spacings, and does not account for crystal defects such as grain boundaries and dislocations. Variations in the particle geometry, including non-spherical particles or uneven shell thickness, will also cause the strain to deviate from this simple model, although these effects could be investigated numerically within the assumptions of elastic continuum theory by finite element modelling.

A detailed derivation of the core-shell model, starting from published calculations for similar systems,[17–19] is presented in Appendix A, and here we will present the general setup and key results. We will consider a core-shell particle with total radius R and core radius r_c. Our task is to determine the distribution of strain throughout the particle, and especially at the particle surface given the particle geometry, lattice mismatch between the core and shell, and the elastic moduli of the materials. For simplicity, this discussion refers to the Pt-M system with negative lattice mismatch and compressive strain. We also assume that the elastic moduli of the core and shell materials are the same.

The particle consists of two regions: the spherical core and the spherical outer shell. If the core and shell are considered in their relaxed state, a gap is present between the outer surface of the core and the inner surface of the shell because of the difference in lattice parameter. The condition of coherent strain is introduced by a boundary condition requiring that these surfaces are brought into contact. This creates an isotropic pressure in the core and a compressive strain on the shell. As a result of the spherical geometry, Poisson expansion in the shell causes the compressive strain to decay going outward across the shell, decreasing as the inverse cube of the distance from the particle center r.
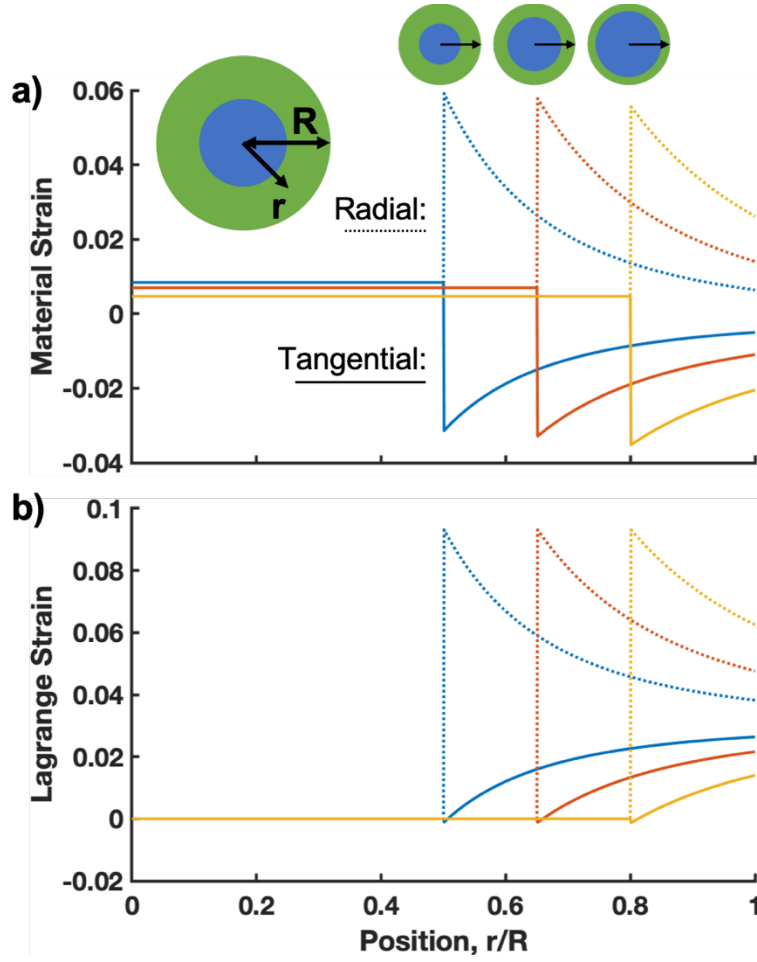
Figure 3.1: Theoretical tangential (solid) and radial (dotted) strain profiles for core shell particles with Poisson ratio $\nu=0.39$, lattice mismatch $\delta=-4\%$, and core-radius fractions $\chi=0.5$ (blue), 0.65 (red), 0.8 (yellow). The material strain (a) is referenced to the local relaxed lattice parameter, while the Lagrange strain (b) is referenced to the lattice parameter at the particle core. The core, at left, experiences a small expansive strain that decreases at higher χ. The particle shell experiences a contraction in the tangential direction and expansion in the radial direction that decays with distance into the shell.

The strain profile depends only on the Poisson ratio ν, the core-shell lattice mismatch $\delta = (a_c - a_s)/a_s$ for core lattice parameter a_c and shell lattice parameter a_s, and the ratio of the core radius to the total radius $\chi = r_c/R$. χ^3 is also the core volume as a fraction of the total particle volume, and $(1 - \chi^3)$ is the shell volume as fraction of the total particle volume.

We will refer to two useful conventions for the strain. The material strain, defined as $\varepsilon(\boldsymbol{r}) = a(\boldsymbol{r})/a_0(\boldsymbol{r})$, has the lattice parameter $a(\boldsymbol{r})$ referenced to the local relaxed lattice parameter $a_0(\boldsymbol{r})$. An alternative convention is the Lagrange strain, defined as $\varepsilon_L(\boldsymbol{r}) = a(\boldsymbol{r})/a(\boldsymbol{r_0})$, which is referenced to the strained lattice parameter at some reference point $\boldsymbol{r_0}$. While the material strain is conceptually straightforward and the relevant quantity for considering impacts on chemical bonding and catalytic activity, the Lagrange strain is a more experimentally accessible quantity because it does not require prior knowledge of the local relaxed lattice.

Figure 3.1 illustrates strain profiles for different values of χ, and with ν=0.39 and δ=-4%, corresponding approximately to a particle with a Pt_1Co_1 core and a Pt shell. The material strain profiles in (a) show that the core experiences an isotropic expansive strain exerted by the shell, which increases for thicker shells. The particle shell experiences a tangential compression and a corresponding radial Poisson expansion with an overall larger magnitude. Both tangential and radial strains relax gradually across the shell. Figure 3.1(b) shows the corresponding Lagrange strain profiles which are useful for interpretation of experimentally measured strain. The radial Lagrange strain shows a prominent peak at the core/shell interface with a large magnitude, while the tangential Lagrange strain increases slowly in the shell and maintains a relatively small magnitude.

It is interesting to note that nowhere in the shell does the compressive tangential material strain equal the lattice mismatch. The strain magnitude is greatest at the core/shell interface, but there it is less than the lattice mismatch because of the expansion of the core exerted by the shell. Additional relaxation across the shell results in a tangential strain at the surface that is significantly lower than the lattice mismatch, especially for thicker shells.

For catalytically active nanoparticles, this model can quantify the material strain at the particle surface:

$$\varepsilon_s^{\theta\theta}(r = R) = \delta\chi^3, \tag{3.1}$$

$$\varepsilon_s^{rr}(r = R) = \frac{-2\nu}{1 - \nu}\delta\chi^3. \tag{3.2}$$

The tangential strain $\varepsilon_s^{\theta\theta}$ is the product of the lattice mismatch and the core volume fraction χ^3, while the radial strain ε_s^{rr} also includes a Poisson-ratio correction with a numerical value of around 1.3 for Pt. This simple result is intuitively appealing. For the ideal case of coherent strain and uniform shell thickness the tangential strain is the same as the lattice mismatch averaged over the particle volume and can be determined from the average composition alone. The surface strain will only reach the core lattice mismatch in the limit of an infinitely thin shell, and as noted above, with the χ^3 scaling decreases rapidly with increasing shell thickness.

3.4.2   Observation of Strain Profiles in real Pt-Co Nanoparticle Catalysts

In this study we have measured strain in practical Pt-Co fuel cell catalyst nanoparticles using nanobeam electron diffraction (NBED) mapping and the exit wave power cepstrum (EWPC) transform to allow robust calculation of local lattice distortions from the NBED patterns. This approach is discussed in detail in the previous chapter. Here we will begin by discussing the visualization and interpretation of strain distributions in Pt-Co nanoparticles and qualitative observations of the predictions of the elastic continuum model.

All experimentally measured strain presented here is the Lagrange strain, as there is no way to determine an ideal relaxed local lattice parameter. The reference point for the Lagrange strain is typically taken at the center of the particle, or at the center of the apparent core, if it differs from

the particle center. Observed strain will be complicated by the fact that our measurements are a projection through particle and the finite size of the electron beam. Observed strain profiles should not be compared directly to the theoretical profiles shown in Figure 3.1, which are sampled at a 1D line in 3D space. Correcting for the projection will be considered in more detail in the following section, where we will interpret observed strain profiles by comparison with simulated profiles combining the elastic continuum model and a simple imaging model.
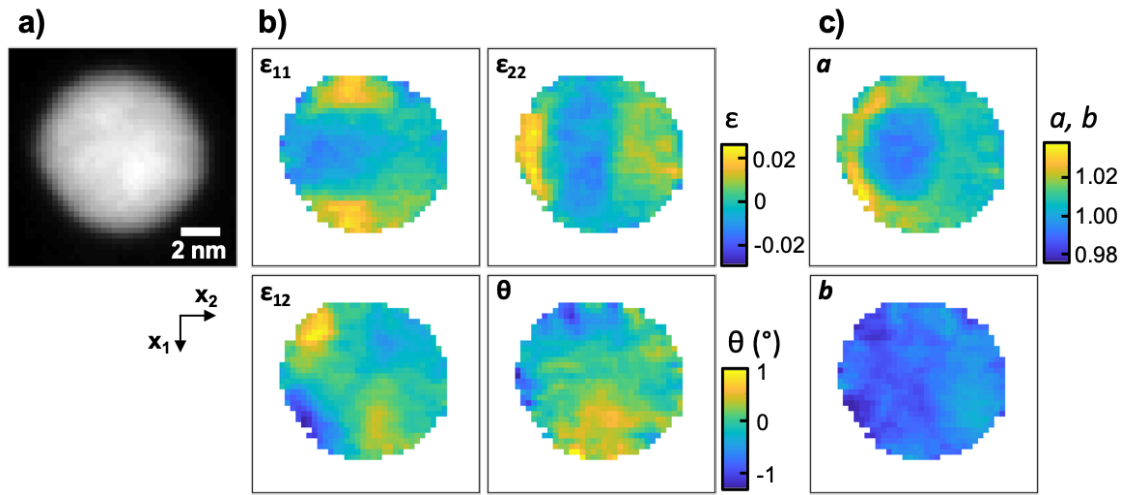
Figure 3.2: Projected strain maps for an electrochemically aged Pt-Co fuel cell catalyst nanoparticle. (a) Virtual annular dark field image of the particle calculated from the NBED dataset. (b) Maps of the lattice rotation θ and the strain tensor elements $\varepsilon_{11}, \varepsilon_{22}, \varepsilon_{12}$ in rectangular coordinates for the Lagrange strain referenced to the particle center. (c) Maps of the strain ellipse semi-major axis a and semi-minor axis b, clearly showing the particle's core-shell structure.

Figure 3.2 shows projected strain maps for a single Pt-Co nanoparticle in the cathode of an electrochemically aged fuel cell MEA. As shown in the virtual annular dark field (ADF) image (a) the particle is roughly spherical with a ~8 nm diameter. Figure 3.2(b) shows maps of the Lagrange strain tensor elements $\varepsilon_{11}, \varepsilon_{22}, \varepsilon_{12}$ for vertical, horizontal, and diagonal strain, respectively, and the lattice rotation θ. The $\varepsilon_{11}, \varepsilon_{22}, \varepsilon_{12}$ show that the particle is

expanded radially outward near its edges, with high values of ε_{11} at the top and bottom, high values of ε_{22} at the left and right, and high or low values for ε_{12} on the primary and secondary diagonals, respectively.

Because the direction of the strain changes around the shell, it is difficult to discern the underlying core shell structure of the particle from strain tensor components in rectangular coordinates. Expressing the strain in polar coordinates is also problematic because it requires identification of a center point, and depending on the geometry of each individual particle the choice of an appropriate center point may not be clear. An alternative formulation that avoids these challenges is the strain ellipse, which described in more detail in the previous chapter. The strain ellipse is formed conceptually by transforming a unit circle with the locally measured strain tensor. The semi-major axis a and semi-minor axis b of the strain ellipse are the distortion magnitude in the direction of most strain and the orthogonal direction of lowest strain, respectively. For compressively strained core-shell particles a is approximately the radial strain and b is approximately the tangential strain, as illustrated in the previous chapter.

Figure 3.2(c) shows maps of the strain ellipse axes for the example particle. The core-shell structure of the particle is clearly apparent in the semi-major axis map a. As in Figure 3.1(b), the core appears as a relatively flat, low strain region with a sharp high-strain ring around it at the core-shell interface. The core in this particular particle is offset to the left, leaving a relatively thick shell with more relaxed strain at the right and thin shell with high strain at the left.
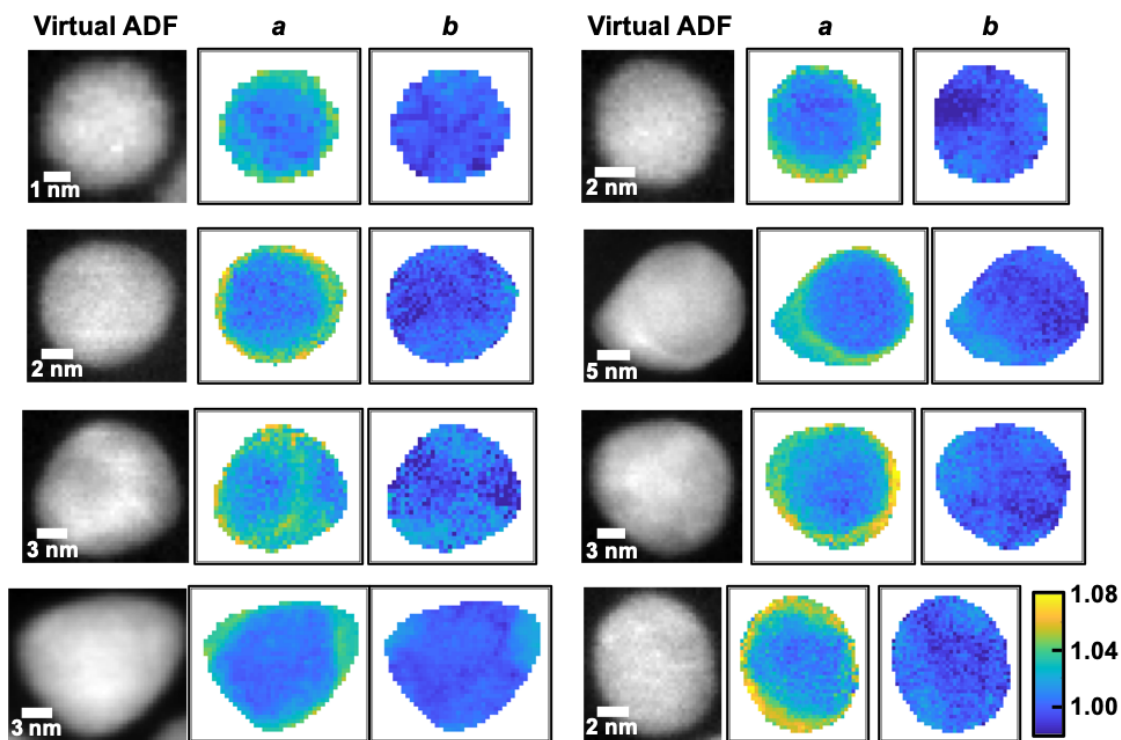
Figure 3.3: Strain maps for a selection of electrochemically aged Pt-Co fuel cell catalyst nanoparticles, including virtual annular dark field images, and maps of the strain ellipse semi-major axis *a* and semi-minor axis *b*.

One advantage of the NBED-EWPC strain mapping technique is the potential for relatively high throughput characterization, which is essential for allowing statistically representative study in intrinsically heterogeneous fuel cell catalyst materials. To illustrate this, Figure 3.3 shows a selection of 8 strain maps for Pt-Co particles in an electrochemically aged fuel cell cathode, including a virtual ADF image and the strain ellipse axis maps for each The typical acquisition time per particle was in the range of 2-10 seconds. A large variety of strain distributions is observed in this selection, reflecting the variety of particle sizes, shapes, and internal structures. We observe relatively thin shells with high strain, and regions of thicker shells with significant strain relaxation. Thin shells on larger particles show higher strain than equally thin shells on smaller particles, reflecting the dependence of strain on the core radius fraction.

3.4.3 Coherent Strain Relaxation

To test the continuum elastic model's prediction of geometrically driven strain relaxation across shell we will make a quantitative examination of experimental strain profiles in shells of different thicknesses. As mentioned previously, the strain measured experimentally by NBED is not directly comparable to the predicted profiles shown in Figure 3.1 because of the effects of projection through the particle and blur due to the finite beam size. We account for these effects by the addition of a simple image model that integrates the strain parallel to the image plane across the thickness of the particle and smooths the profile with a Gaussian function matching the diffraction-limited beam size.

Figure 3.4 shows a comparison of experimental strain profiles for two particles to profiles simulated using the continuum elastic model and simple imaging model. Figure 3.4(a) shows a particle with a relatively thin Pt shell, with a strain profile sample along the magenta arrow plotted in (b). The tangential strain remains relatively low across the particle with a slight increase toward either end, while the radial strain increases significantly and peaks a short distance in from either surface. Figure 3.4(c) shows a simulated profile for a particle of the same size assuming a Pt_1Co_1 core and with a 1 nm shell thickness selected for consistency with the experimental profile in (b). The simulated profile including the imaging model is qualitatively consistent with and quantitatively very similar to the experimental profile. It is important to note that as a result of the imaging effects, the maximum observed radial strain is much lower than the maximum theoretical strain at the core/shell interface and is also displaced somewhat in position out into the shell. The observed profile at the core/shell interface is also considerably less sharp because a significant amount of strained shell is included in the projected measurement within the core.

The relaxation of strain across the Pt shell can be investigated by examining the strain in a region with a relatively thick shell, as shown in Figure 3.4(d), with the strain profile sampled at the magenta arrow plotted in (e). A simulated profile assuming a Pt_1Co_1 core and a 4 nm shell thickness is plotted in Figure 3.4(f). One caveat is that the shell thickness is not uniform across this particle, so the assumption of spherical symmetry made in the model is not obeyed and the profile is expected to differ somewhat from the model prediction. Thick but uniform shells were generally not observed in the particles examined in this study, with thick shells in limited areas being the norm, as shown in Figure 3.3. Nonetheless, the experimental and simulated profiles in Figure 3.4(e,f) are qualitatively quite similar, and the gradual relaxation of strain across the thick shell predicted by the model is observed in the experimental profile.
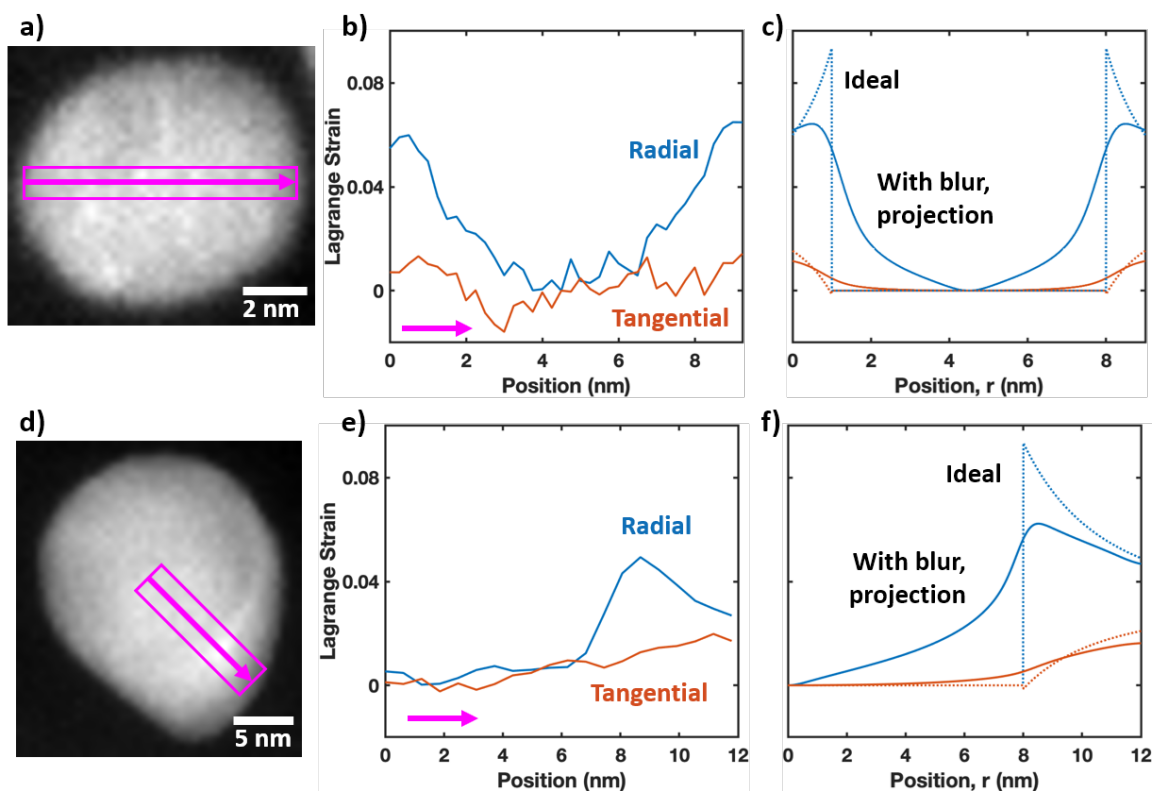
Figure 3.4: Line profiles of radial and tangential strain for electrochemically aged Pt-Co nanoparticles with a relatively thin Pt shell (a-c) and a relatively thick

Pt shell (d-f). Virtual annular dark field images (a,d) of the nanoparticles with magenta arrow and box indicating the line profile regions used for calculation of the experimental strain profiles (b,e). Simulated profiles (c,f) were calculated for geometry similar to each experimental profile using the continuum mechanics model. The dotted lines show the strain along a single 1D line from the center to the edge of the 3D particle, while the solid lines include the effects of projection through the 3D particle and blurring from the finite beam size. Simulations assume a $Pt_{0.5}Co_{0.5}$ core and a pure Pt shell, with a thickness of 1 nm for (c) and 4 nm for (f).

These results demonstrate that despite the experimental complications in strain mapping Pt-Co nanoparticles using NBED, the maps can be interpreted to understand the underlying strain profiles by use of simple modeling. Furthermore, the consistency between the continuum elastic model and observed strain profiles, as well as the observed gradual relaxation of strain across thick Pt shells is evidence that the predicted geometric mechanism of strain relaxation is present in core-shell Pt-Co nanoparticles. This effect, which is not present in the more widely understood system of strained planar films, is important to consider for catalytic nanoparticles and other core-shell systems.

3.4.4   *Dislocation-driven Strain Relaxation*

In planar films, the primary mechanism of strain relaxation is the introduction of dislocations. This becomes energetically favored when the film thickness surpasses a critical thickness where the energy cost of the strain exerted on the film exceeds the energy cost of the added dislocations. Dislocations may play an important role in relaxing strain in core-shell nanoparticles as well, especially considering the large core-shell lattice mismatch sometimes present, for example ~4% in the case of our Pt-Co system. In particular, edge dislocations may be expected to appear at the core-shell interface with a missing plane of Pt atoms in the shell to relieve the compressive strain from the core.

Dislocations create distinctive strain fields[20] which can be used to recognize their presence in strain maps. Figure 3.5(a) illustrates the strain fields expected around an edge dislocation, which take a dumbbell-like shape. The strain in both the vertical ε_{11} and horizontal directions ε_{22} shows an expansion on the side of the missing atomic plane and a compression on the side of the extra plane. The shear strain ε_{12} and lattice rotation θ each have dumbbells oriented perpendicular to those for ε_{11} and ε_{22} as the lattice bends around the dislocation core, although with opposite sign. However, as noted above, the strain tensor components in rectangular coordinates can be difficult to interpret in core-shell nanoparticles because of the changing direction of strain. Instead, the strain ellipse axes can show the regions of compression and expansion on either side of the dislocation, and the lattice rotation will show the expected dumbbell shape that should be easily recognized because the lattice rotation map would otherwise ideally be flat for a spherical core-shell particle.
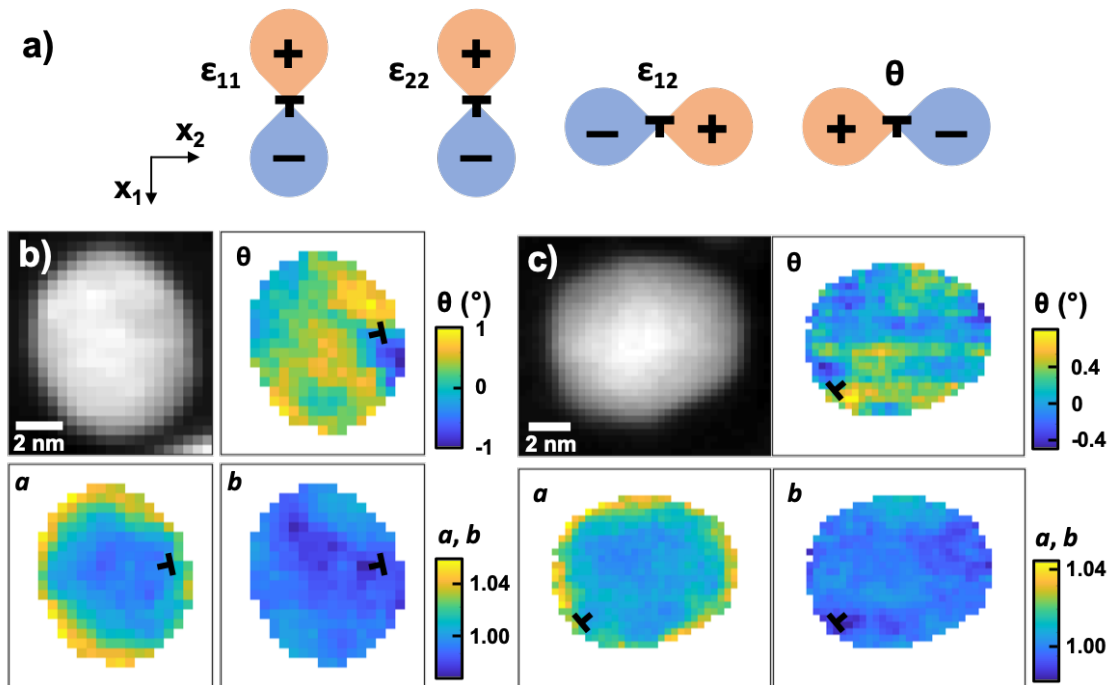
Figure 3.5: Observation of dislocations in core-shell Pt-Co nanoparticles. (a) Cartoon of the expected dipole-like form of the strain field tensor components $\varepsilon_{11}, \varepsilon_{22}, \varepsilon_{12}$ and lattice rotation θ around an edge dislocation, marked with

the ⊥ symbol. Strain maps of visible dislocations on an electrochemically aged particle (b) and a chemically dealloyed particle (c) including the virtual ADF image, lattice rotation θ, and strain ellipse semi-major axis a and semi-minor axis b.

Figure 3.5(b) and (c) show strain maps of Pt-Co particles with dislocations identified and marked with the ⊥ symbol. The particle in (b) was electrochemically aged while the particle in (c) was subjected to an aggressive chemical dealloying to create a thicker Pt shell. In both cases, the dislocation appears to occur at the core-shell interface with a clear dumbbell visible in the lattice rotation θ, a relaxation of strain in the nearby shell visible in the semi-major axis a, and a compressed point visible in the semi-minor axis b. Other locations on the particle show some of these signatures as well, although less clearly, suggesting that more dislocations may be present. Dislocations may have mixed screw and edge character, causing them to wind around the particle and potentially be less visible in strain maps from any particular angle. Quantifying the density or overall impact of dislocations is not a straightforward task because of their possibly complex 3D structure in core-shell nanoparticles. Nonetheless, these observations confirm that dislocations are present in Pt-Co nanoparticles whose shells have grown in thickness from either electrochemical aging or chemical dealloying and contribute to the relaxation of surface strain. Similar dislocations were not observed in the initial $Pt_{3.2}Co_1$/HSC sample.

3.4.5 *Rationalizing trends in ORR activity from strain microstructure*

The ultimate objective of this study is to relate the nanostructure and strain state of Pt-Co nanoparticles to their catalytic activity for oxygen reduction to expand the understanding that drives development of improved catalyst materials. Surface strain is a primary driver of catalytic activity, and the insights discussed in the previous sections can bring clarity to explain trends in activity that have previously been only vaguely understood.

The connection between strain and catalytic activity has been understood theoretically for some time from the d-band model.[9–12] By shifting the electronic d-band of the active metal, a change in surface strain is expected to give a linear change in the binding energy.[11,12] Under the assumption that the reaction has a single rate determining step (we are on the side of the volcano plot, and not the top) the catalytic activity, which is expected to follow an Arrhenius law depending exponentially on the energy barrier, will show an exponential Arrhenius dependence on the strain.

To examine the dependence of the activity on the microscopic strain state investigated in the previous sections, a series of Pt-Co/HSC catalysts was prepared with varying degrees of chemical dealloying intended to vary the Pt shell thickness. The Pt-Co/HSC catalyst in particular was selected because of its highly uniform 4-5nm diameter size distribution, spherical morphology, and disinclination toward particle coalescence,[8] making it closely match the ideal model presented in this chapter. The initial catalyst has a composition of $Pt_{3.2}Co_1$ and was initially dealloyed to have a shell thickness of ~0.5 nm. Prior to the initial dealloying the alloy composition was approximately Pt_1Co_1. The $Pt_{3.2}Co_1$ catalyst was subjected to additional dealloying via acid leaching, resulting in compositions of $Pt_{3.8}Co_1$ and $Pt_{4.8}Co_1$. A portion of the $Pt_{4.8}Co_1$ catalyst was annealed to redistribute the cobalt and dealloyed again via acid leaching, resulting in a composition of $Pt_{5.5}Co_1$ with a presumed structure having a thinner shell than the $Pt_{4.8}Co_1$ catalyst and lower Co content in the core. A Pt/HSC catalyst was also prepared and annealed to have a particle size approximately equal to that of the Pt-Co catalysts. No significant difference in electrochemically active surface area (ECSA) was found for this collection of catalysts, implying that differences in activity due to particle size effects should be negligible. The specific oxygen reduction reaction (ORR) activity was measured for each of these catalysts and is compared to the expected strain in Figure 3.6.

The elastic continuum model presented in this chapter indicated that in the absence of dislocations (coherently strained interfaces only) the surface strain can be determined from the

average composition alone (Equation 3.1) following a linear relationship. The theoretically expected surface strain, determined from the composition, of each of these catalysts is plotted in Figure 3.6(a). Note that the change in composition from $Pt_{3.2}Co_1$ to $Pt_{4.8}Co_1$, assuming an ideal geometry, is expected to produce only a small change in Pt shell thickness from ~0.5 nm to ~0.7 nm. This small change in shell thickness is expected to result in a significant ~40% strain relaxation from coherent geometric relaxation alone. However, the measured ORR specific activity decreases much more quickly after this dealloying than would be expected for an Arrhenius law dependence on the strain determined from the initial $Pt_{3.2}Co_1$ catalyst and the Pt reference. This outcome suggests that additional strain relaxation is taking place, which can likely be attributed to the introduction of dislocations into the thicker shells formed in the heavily dealloyed catalysts, as observed in Figure 3.5(c).
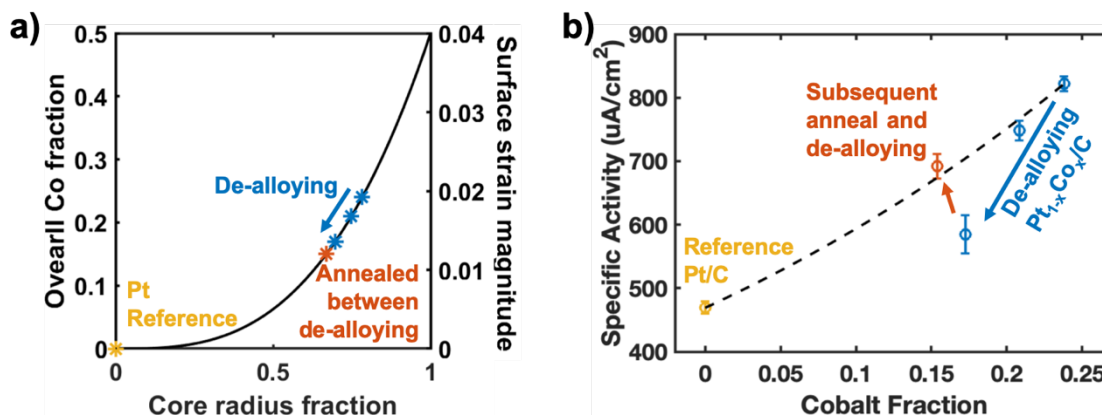
Figure 3.6: Correlation of theoretically expected strain to specific oxygen reduction reaction activity for a series of dealloyed Pt-Co catalysts. (a) Plot of theoretically expected relationship between core radius fraction χ, average composition and tangential surface strain magnitude assuming coherent strain and a core composition of approximately Pt1Co1 and a -4% lattice mismatch. Stars mark points corresponding to the dealloyed Pt-Co series and a similarly sized Pt reference, with positions based on the average composition. (b) Plot of the experimentally measured specific oxygen reduction activity and average composition for the catalysts. The dotted line shows the expected trend assuming coherent surface strain that is linear with the average composition and activity following an Arrhenius law

dependence on the strain between the Pt reference and the initial Pt-Co catalyst.

The activity recovers significantly, however, when the $Pt_{4.8}Co_1$ catalyst is annealed and dealloyed further by acid leaching reaching an overall composition of $Pt_{5.5}Co_1$. The ORR activity returns to the value expected for Arrhenius dependence with the expected coherent strain. The annealing process would be expected to uniformly redistribute the metal atoms in the catalyst particles and remove dislocations, and the subsequent dealloying would produce a comparatively thinner shell, more similar to that in $Pt_{3.2}Co_1$ than $Pt_{4.8}Co_1$. This change toward a thinner Pt shell and smaller lattice mismatch from the lower Co content in the core makes the formation of dislocations less energetically favorable.

3.5   Conclusion

This chapter has explored basic strain effects in core-shell Pt-Co nanoparticle catalysts and their impact on ORR activity. An analytical model for the strain in core-shell particles derived from continuum elastic theory was presented and showed that for particles with coherently-strained, defect free core-shell interfaces, strain relaxes gradually across the particle shell as a result of Poisson expansion. The strain at the surface of coherently-strained particles is a simple function of the core-shell lattice mismatch and the relative size of the particle core, allowing the expected strain to be inferred from the average composition. Strain was characterized experimentally using NBED, which allows robust, high throughput strain measurements at sub-nm resolution. Experimentally measured strain profiles were generally consistent with profiles predicted from the elastic continuum model with projection and beam size effects taken into account, showing strain relaxation across thick Pt shells. Edge dislocations were also observed at the core-shell interface of particles that had been electrochemically aged or heavily acid leached. Strain relaxation in Pt-Co

nanoparticle catalysts was thus shown to result from two mechanisms: geometric relaxation and dislocations. The continuum elastic model indicates that geometric relaxation produces the same loss of surface strain for particles of the same average composition regardless of their shell thickness, while dislocations are expected to be favored for thicker shells and a larger core-shell lattice mismatch. The impact of these two effects on ORR activity was investigated for a series of progressively dealloyed Pt-Co/HSC catalysts prepared to vary the shell thickness and core composition. For lightly dealloyed particles with thinner Pt shells, the activity followed a trend expected for Arrhenius dependence on the surface strain predicted for coherent strain with the continuum elastic model. However, for heavily dealloyed catalysts with relatively thick shells and a large lattice mismatch the activity fell faster than expected for coherent strain alone, indicating that dislocation-driven strain relaxation contributes to the activity loss as well for these catalysts.

3.6   References

[1] H.A. Gasteiger, S.S. Kocha, B. Sompalli, and F.T. Wagner, Appl. Catal. B Environ. **56**, 9 (2005).
[2] A. Kongkanand and M.F. Mathias, J. Phys. Chem. Lett. **7**, 1127 (2016).
[3] F. Hasché, M. Oezaslan, and P. Strasser, ChemCatChem **3**, 1805 (2011).
[4] Q. Jia, K. Caldwell, J.M. Ziegelbauer, A. Kongkanand, F.T. Wagner, S. Mukerjee, and D.E. Ramaker, J. Electrochem. Soc. **161**, F1323 (2014).
[5] K.M. Caldwell, D.E. Ramaker, Q. Jia, S. Mukerjee, J.M. Ziegelbauer, R.S. Kukreja, and A. Kongkanand, J. Phys. Chem. C **119**, 757 (2015).
[6] B. Han, C.E. Carlton, A. Kongkanand, R.S. Kukreja, B.R. Theobald, L. Gan, R. O'Malley, P. Strasser, F.T. Wagner, and Y. Shao-Horn, Energy Environ. Sci. **8**, 258 (2015).
[7] H.L. Xin, J.A. Mundy, Z. Liu, R. Cabezas, R. Hovden, L.F. Kourkoutis, J. Zhang, N.P. Subramanian, R. Makharia, F.T. Wagner, and D. a Muller, Nano Lett. **12**, 490 (2012).
[8] E. Padgett, V. Yarlagadda, M.E. Holtz, M. Ko, B.D.A. Levin, R.S. Kukreja, J.M. Ziegelbauer, R.N. Andrews, J. Ilavsky, A. Kongkanand, and D.A. Muller, J. Electrochem. Soc. **166**, F198 (2019).
[9] B. Hammer, Y. Morikawa, and J.K. Nørskov, Phys. Rev. Lett. **76**, 2141 (1996).
[10] B. Hammer and J.K. Nørskov, in *Chemisorpt. React. Support. Clust. Thin Film. Towar. an Underst. Microsc. Process. Catal.*, edited by R.M. Lambert and G. Pacchioni (Springer Netherlands, Dordrecht, 1997), pp. 285–351.
[11] A. Ruban, B. Hammer, P. Stoltze, H.. Skriver, and J.. Nørskov, J. Mol. Catal. A Chem. **115**, 421

(1997).

[12] M. Mavrikakis, B. Hammer, and J.K. Nørskov, Phys. Rev. Lett. **81**, 2819 (1998).

[13] P. Strasser, S. Koh, T. Anniyev, J. Greeley, K. More, C. Yu, Z. Liu, S. Kaya, D. Nordlund, H. Ogasawara, M.F. Toney, and A. Nilsson, Nat. Chem. **2**, 454 (2010).

[14] US Department of Energy Fuel Cell Technologies Office, *Multi-Year Research, Development, and Demonstration Plan: 3.4 Fuel Cells* (2017).

[15] T.R. Garrick, T.E. Moylan, M.K. Carpenter, and A. Kongkanand, J. Electrochem. Soc. **164**, F55 (2017).

[16] M.W. Tate, P. Purohit, D. Chamberlain, K.X. Nguyen, R. Hovden, C.S. Chang, P. Deb, E. Turgut, J.T. Heron, D.G. Schlom, D.C. Ralph, G.D. Fuchs, K.S. Shanks, H.T. Philipp, D.A. Muller, and S.M. Gruner, Microsc. Microanal. **22**, 237 (2016).

[17] A.S. Saada, *Elasticity: Theory and Applications*, 2nd ed. (J. Ross Publishing, Ft. Lauderdale, FL, 2009).

[18] X. Cai, H. Mirafzal, K. Nguyen, V. Leppert, and D.F. Kelley, J. Phys. Chem. C **116**, 8118 (2012).

[19] K. Gong and D.F. Kelley, J. Chem. Phys. **141**, 194704 (2014).

[20] W.G. Moffatt, G.W. Pearsall, and J. Wulff, *The Structure and Properties of Materials* (Wiley, New York, NY, 1964).

4   CONNECTING FUEL CELL CATALYST NANOSTRUCTURE AND ACCESSIBILITY USING QUANTITATIVE STEM TOMOGRAPHY

4.1   Abstract

Further reduction of Pt in hydrogen fuel cells is hampered by reactant transport losses near the catalyst surface, especially for degraded catalysts. Strategically mitigating these performance losses requires an improved understanding of the catalyst nanostructure, which controls local transport and catalyst durability. We apply cryo-tomography in a scanning transmission electron microscope (STEM) to quantify the three-dimensional structure of carbon-supported Pt catalysts and correlate to their electrochemical accessibility. We present results for two carbon supports: Vulcan, a compact support with a large majority of Pt observed on the exterior, and HSC, a porous support with a majority of Pt observed within interior carbon pores, which have relatively constrictive openings. Increasing Pt content shifts the Pt distribution to the exterior on both carbon supports. By correlating to the electrochemical surface area, we find that all Pt surface area is accessible to protons in liquid. However, the interior Pt fraction quantitatively tracks Pt utilization losses at low humidity, indicating that the interior Pt is inaccessible to the proton-conducting ionomer, likely because narrow carbon pore openings block ionomer infiltration. These results imply different proton transport mechanisms for interior and exterior Pt, and quantitatively describe the catalyst structure, supporting development of transport and durability models.[g][1]

4.2   Introduction

For hydrogen-powered fuel cell vehicles to be competitive in the automotive market, the cost of fuel cell systems must be further reduced. Among other measures, cathodes with low Pt loading must be used to decrease the precious metal cost to a level comparable to the internal combustion engine[2,3]. Dramatic progress has been made in recent years in improving the oxygen reduction reaction (ORR) mass activity of Pt-based catalysts through dealloying[4–7], shape/size-control[8–13], and Pt monolayer[14–16] approaches. However, unresolved transport problems, which cause severe losses in high power performance, have prevented reduction of platinum loading below 0.1 mg/cm^2.[2] Recent studies have identified oxygen transport resistance that is localized at the Pt-ionomer interface as a dominant contributor to these losses[2,17–20]. Because the local resistance scales inversely with the Pt surface area, its associated losses become dominant at high power in low-Pt cathodes and limit the practical value of high activity catalysts for reducing fuel cell Pt loadings. Furthermore, the adverse effects of local oxygen resistance are exacerbated by Pt surface area losses that occur as a result of catalyst degradation, potentially causing severe performance losses after fuel cell use.[2,18,20] Addressing localized transport resistance is therefore a high priority in fuel cell research and development.

The catalyst support plays an important role in determining the local environment around the Pt surface, impacting the catalyst performance and stability. Carbon blacks are the most commonly used class of supports for Pt-based nanoparticles due to their high electronic conductivity, high surface area, relatively high stability, and low cost. Carbon supports vary in their morphology and chemical properties, which play critical roles in determining the performance and stability of the catalyst.[21–25] In particular, the porosity of the carbon support is a key morphological parameter. Some carbon supports have a large number of micropores in the interior of the carbon primary

particles, with one popular example being KetjenBlack®, also known as high-surface-area carbon (HSC). HSC-supported catalysts contain a large fraction of Pt particles located in the interior micropores,[26,27]. By contrast, compact carbon supports, such as Vulcan®, have very little internal porosity and thus have most Pt particles on the carbon exterior[26].

Pt supported on porous carbons shows ORR mass activities 2-3 times higher than on compact carbons,[23–25,28] giving higher fuel cell voltage at low and moderate current densities, where ORR kinetics dominate. This is partly due to improved Pt dispersion on porous carbons, leading to higher Pt electrochemical surface area (ECSA), and also partly due to Pt-ionomer interactions, which will be discussed below. At high currents, catalysts on compact supports perform better due to the higher accessibility of Pt on the support exterior.[24,25] However, the improvement in ORR kinetics with porous carbon supports can be large enough to allow the cell to operate at higher voltages than with solid carbon supports even at high current densities (above 1.5 A cm^{-2} in [[25]]). While the higher surface area of porous supports results in faster mass loss to carbon corrosion under unusual voltage excursions, the improved dispersion of Pt on porous carbons can offer advantages for catalyst stability under normal operation.[23–25]

Pt particles embedded in interior pores may be accessed through distinct transport mechanisms and experience a distinct electrochemical environment from Pt on the support exterior. Understanding these local transport phenomena, and potential benefits and drawbacks, is an important and complex challenge. The internal particles have been shown to be mostly electrochemically active and are believed to have access to proton and O_2 through small openings (1-5 nm) in the carbon micropores, but it is believed that the pores are too small for ionomer to intrude and form a direct proton conduction path to the Pt surface.[17,25,29–31] It is hypothesized that condensed water can conduct protons in these pores, although the mechanism and the magnitude of proton conductivity remain unclear.[32–34] The apparent requirement of condensed water in pores

for proton conduction can lead to Pt utilization losses at low relative humidity (RH) for porous catalyst supports.[31] Depending on the size and geometry of carbon micropores, oxygen transport to interior Pt may be restricted as well[29,30]. However, limiting the coverage of ionomer on the Pt surface may be beneficial in some ways, as ionomer adsorption has been found to cause increased local O_2 transport loss[19] and impair ORR kinetics[25,35,36]. Improved ORR kinetics on Pt surfaces free of ionomer adsorption are likely responsible for much of the enhanced mass activity observed for HSC-supported catalysts, which contain a high fraction of internal Pt that does not directly contact the ionomer.[36]

Understanding the structure of Pt/C catalysts is essential for unraveling the fundamental mechanisms and implications of this complex, interacting set of phenomena. Many studies have used (scanning) transmission electron microscopy (S)TEM to investigate the nanostructure of fuel cell catalysts but understanding transport pathways is a problem that inevitably requires 3D information. Researchers at the University of Yamanashi combined surface-sensitive secondary electron imaging with STEM imaging to distinguish interior and exterior particles and investigate their differing impacts on cell performance.[24,37] This approach, however, does not provide a full 3D description of the catalyst. Ito et al. employed 3D TEM tomography to image HSC and Vulcan-supported Pt.[26] Their experiments found Pt almost exclusively on the exterior of Vulcan and mostly in the porous interior of HSC, and suggested that interior Pt on HSC must be utilized to account for the observed ECSA. While these studies have provided valuable characterization of catalyst structure, more comprehensive and detailed nanoscale 3D study is needed, especially quantitative measurements that can be correlated to transport, accessibility, and durability metrics, in order to build mechanistic understanding and inform structure-based models.

This work seeks to quantitatively investigate 3D structure of Pt/C catalysts using electron tomography to relate the catalyst structure and accessibility. Electron tomography is a unique tool

for investigating the 3D structure of inhomogeneous materials, including fuel cell electrocatalysts, at nanometer resolution [38,39]. The electron tomography procedure used in this study is illustrated in Figure 4.1. A series of STEM images is acquired as the specimen is rotated about an axis perpendicular to the optical axis of the microscope, forming a "tilt series". The tilt series is reconstructed to generate a 3D image of the specimen called a tomogram or reconstruction. The tomogram is visualized, providing qualitative insight into the structure, and segmented by assigning a material identification to each voxel, allowing quantitative analysis. This allows us to observe and quantify aspects of the 3D structure of the specimen that are inaccessible to conventional 2D imaging, including the internal pore structure of carbon supports, and the surface areas and positions (e.g. inside/outside the support) of Pt nanoparticles.
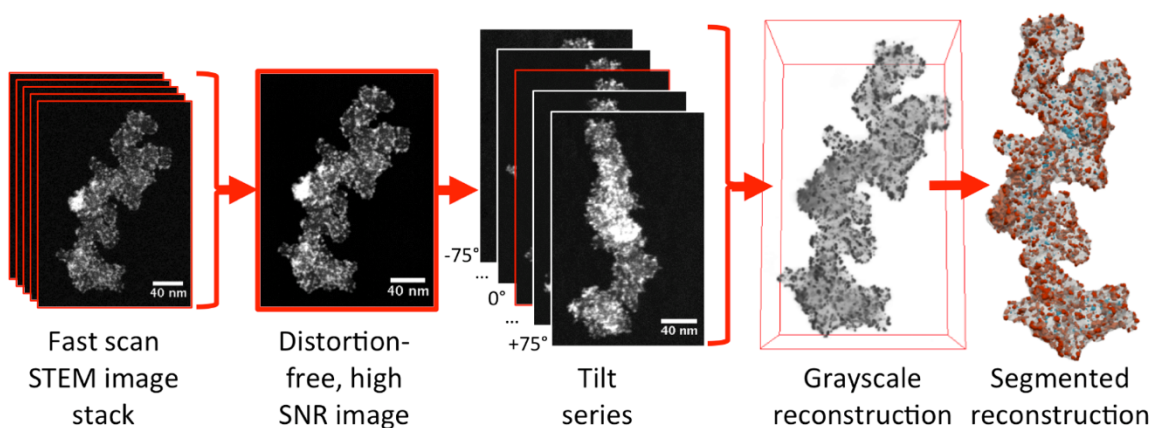
Figure 4.1. Illustration of electron tomography procedure, shown for 50wt%Pt/Vulcan catalyst nanoparticles. High signal to noise ratio (SNR), distortion-free images are produced by summing aligned stacks of fast-acquisition STEM images. A tilt series of images, acquired as the specimen tilts from approximately -75° to 75° at 2° intervals, is aligned to a common coordinate system and reconstructed to a 3D image of the specimen. The reconstruction is segmented to identify the material type represented in each voxel to allow quantitative analysis and more informative visualization, for instance here showing the carbon surface in grey, interior Pt particles in blue, and exterior Pt particles in red.

Although the distribution of ionomer across the catalyst is an important parameter in reactant transport, ionomer is highly susceptible to damage caused by electron radiation[40]. High-resolution electron tomography requires a very large radiation dose, and ionomer is thus likely to suffer severe damage during tomogram acquisition, leading to unreliable characterization. For this reason, this work uses tomograms of ionomer-free specimens only and makes inferences regarding the ionomer distribution through correlation to measurements of electrochemical accessibility.

In this investigation, we examine Pt catalysts supported on Vulcan®, a low porosity support, and HSC, a high porosity support, each loaded at 50wt%Pt, and 10wt%Pt. This sample space allows us to determine trends in the Pt distribution as a function of carbon morphology and Pt content. For each of these samples, electron tomography was performed to make quantitative measurements of the sizes, surface areas, and positions of Pt particles. Tomography measurements were made using large fields of view to provide robust statistical measurements from over 6000 Pt nanoparticles in total from seven different data sets, using automatic segmentation and analysis to measure quantitative trends in the catalyst structure. We also performed tomography to investigate the structure of internal micropores in unloaded HSC, including the connectivity and sizes of pores and pore openings. These results were correlated to measurements of the catalysts electrochemical surface area (ECSA) in liquid using hydrogen adsorption and desorption (HAD) and utilization using carbon monoxide (CO) stripping at variable relative humidity (RH) in fuel cell membrane electrode assemblies (MEAs) to determine the role of catalyst morphology in the accessibility of Pt to gas and proton transport.

4.3 Methods

4.3.1 Materials

Pt nanoparticles deposited on two types of carbon black supports were used in this study. Vulcan XC-72® is a relatively compact carbon black with a Brunauer-Emmett-Teller (BET) surface area of ~250 m^2/g. Ketjenblack® is a high-surface-area carbon (HSC) with BET surface area of ~800 m^2/g. Pt was deposited on each carbon support using a wet impregnation method at two concentrations: 10 and 50 weight %. The mean Pt crystallite diameters were about 2.5-3 nm determined by XRD using the Scherrer equation at the Pt (220) peak.

4.3.2 Hydrogen Adsorption Surface Area Measurements

The electrochemical surface area (ECSA) of the catalyst powders was measured by hydrogen adsorption (HAD) at room temperature. Thin film catalyst layers were deposited on glassy carbon disk electrode (0.196 cm^2 area), mounted on an interchangeable rotating disk electrode (RDE) holders (Pine Instruments, USA). A Pt-foil counter electrode and saturated calomel (SCE) reference electrode were used. Detailed procedures on thin film applications and measurements can be found in reference [3]. The Pt ECSA was measured by integrating hydrogen adsorption peaks (assuming 210 $\mu C/cm^2$-Pt) in cyclic voltammograms in 0.1 M $HClO_4$ at a 20 mV/s sweep rate.

4.3.3 CO-Stripping MEA Utilization Measurements

CO-stripping measurements were performed on membrane electrode assemblies (MEAs) that were prepared using the decal-transfer method to make catalyst-coated membranes, as described elsewhere.[3] MEAs had an active area of 50 cm^2. The Pt loadings in the cathode were 0.05 and 0.40 mg$_{Pt}$/cm^2 for 10 and 50 wt% catalysts, respectively. Anode Pt loading was 0.05 mg$_{Pt}$/cm^2. Nafion® D2020 ionomer, with an equivalent weight of 950 g/equiv was utilized with an ionomer to carbon weight ratio of 0.95 and 0.6 in the cathode and anode. Reinforced 18 μm thick perfluorosulfonic acid (PFSA) membranes were used. The gas diffusion layers were made from 200 μm thick Teflon®-coated carbon fiber diffusion media with 30-μm microporous layers.

ECA measurement by CO stripping in MEAs is similar to that in a conventional liquid electrochemical cell, as previously described.[31] After letting the MEA equilibrate at the measurement relative humidity (RH) at 80°C for 30 min, several voltage cycles between 0.05-0.9 V were conducted to clean the catalyst surface. This was followed by 2 minutes of CO purge while holding the electrode at 0.05 V. The cathode channel was then flushed with N$_2$ for 1 minute, and a cyclic voltammogram starting from 0.05 V to 0.9 V was swept to quantify the CO oxidation charge. ECSA from the CO stripping was calculated assuming 420 μC/cm^2-Pt. The procedure was repeated at different RH from 10% to 100% RH. The utilization is defined as the fraction of the CO-stripping ECSA over the ECSA at 100%RH. The low-RH utilization shown in Figure 4.9(c) is calculated as the average of the utilization at 10% RH and 20% RH. The error bars in Figure 4.9(c) span from the utilization at 10% RH to that at 20% RH.

4.3.4 Electron Microscopy Sample Preparation

Catalyst powders were dispersed in methanol and dropped onto 100-mesh, hexagonal, copper TEM grids coated with carbon films of 3-4 nm nominal thickness and allowed to dry in air at room temperature. For the Pt-free HSC specimen, 5nm diameter spherical gold nanoparticles were deposited on the grid prior to the specimen to act as fiducial markers for tomography. To eliminate the possibility of etching the carbon supports, the samples were not plasma cleaned.

4.3.5 Transmission Electron Microscope Imaging

Transmission electron microscope (TEM) and Scanning transmission electron microscope (STEM) images were acquired in a FEI Tecnai F20 with a Schottky field emission gun and a 200 kV accelerating voltage. No objective aperture was used for TEM imaging. For STEM imaging, a convergence angle of ~7-10 mrad was used and the low angle annular dark field (LAADF) signal was collected to enhance the signal for carbon.

4.3.6 Electron Tomography Data Acquisition

Electron tomography experiments were performed using STEM imaging as described above with convergence angle of ~6.9 mrad to provide sub-nanometer resolution over a large depth of field. For automatic segmentation to be feasible, the imaging mode used for tomography must provide strong contrast for weakly-scattering carbon, so that carbon can be reliably distinguished from Pt and void. To meet this requirement, the low angle annular dark field signal was acquired with a camera length of 490mm, providing a strong overall signal and a smaller intensity difference between carbon and Pt relative to high angle annular dark field (HAADF). An alternative imaging mode that provides a strong signal for carbon is bright-field (BF) transmission electron microscopy. However, phase contrast from amorphous carbon introduces speckle noise in BF TEM imaging, as

illustrated in the published supplemental information,[1] which interferes with interpretation and analysis of the tomogram.

To simultaneously suppress carbon contamination and ice accumulation during data acquisition, samples were maintained at -100C in a Gatan model 914 cryo-tomography holder using liquid nitrogen and a Gatan model 900 cold stage controller. Samples were imaged over a typical tilt range of around ±75° at 2° increments with a 0.36 nm pixel size and 1024X1024 pixels per image. To reduce distortions in STEM images introduced by thermal drift of the sample, at each tilt we acquired a series of fast-scan images typically with ~1 second per frame and 24-32 seconds total acquisition. After data acquisition each image series was aligned by cross-correlation and summed to produce a high signal-to-noise ratio image at each tilt, averaging out scan noise and limiting drift-induced distortions to around 1-2 pixels. This permits a good reconstruction quality over the full ~350nm field of view.

4.3.7   Tomography Data Processing and Reconstruction

Tomography data preprocessing, reconstruction, segmentation, and analysis were performed in MATLAB, using custom code and functions from the Image Processing Toolbox and the Statistics and Machine Learning Toolbox, unless otherwise stated.

To prepare the summed-image tilt series for tomographic reconstruction, hot pixels due to x-ray noise were removed, the average background intensity due to the uniform carbon support film is subtracted from each image, and the images are normalized to maintain a constant average intensity. Images in the tilt series are aligned to a common coordinate system manually using Pt nanoparticles (or the added gold particles in the Pt-free dataset) as fiducial markers, then shifted and rotated to center the axis of rotation. Some datasets

also have ~1% scan non-orthogonality corrected using an image shear operation. Shear and rotation operations used linear interpolation. Images were then binned by two, resulting in a 0.71 nm pixels/voxel edge length.

For the Pt-free HSC, the tomogram was reconstructed using the weighted back-projection (WBP)[41] algorithm, implemented using the MATLAB *iradon* function. A 1.5 pixel radius Gaussian blur was subsequently applied to reduce noise and finite sampling artifacts. For carbon-supported Pt samples, the presence of Pt makes accurate reconstruction of the carbon more difficult. Because Pt is approximately 30 times brighter than an equal volume of carbon in LAADF STEM, minor artifacts in the Pt reconstruction fall in the intensity range of carbon. These artifacts appear as bright streaks or shadows and interfere significantly in the segmentation of carbon and voids. Tomograms were reconstructed using the simultaneous iterative reconstruction technique (SIRT)[42] with 20 iterations, which provided sufficient artifact suppression to allow recognition of the exterior carbon surface. A discussion of the choice of reconstruction algorithm is presented in the published supplemental information.[1]

4.3.8   3D Image Segmentation

The carbon-supported Pt tomograms were segmented automatically using a combination of threshold and morphological filtering operations, which provide additional suppression of artifacts. The segmentation procedure is described in detail in the published supplemental information.[1] Uncertainty in the segmentation procedure was estimated by repeating the Pt segmentation procedure and analysis for reasonable high, low, and medium platinum thresholds.

For the Pt-free HSC specimen, carbon was identified using simple thresholding of the smoothed reconstruction without any morphological filtering. Because the choice of threshold impacts the measured size of pores and pore openings, the analysis was repeated for reasonable low, medium, and high carbon thresholds to estimate uncertainty.

4.3.9 Analysis of Segmented Reconstructions

Once the reconstruction was segmented, individual Pt nanoparticles were identified, and Pt particle effective diameters were calculated from particle volumes assuming a spherical morphology. Surface areas were calculated for individual Pt particles were calculated using discrete Crofton formula code implemented by Legland, et al.[43] for larger particles ($\gtrsim$3 nm diameter) and by a spherical-particle approximation for smaller particles ($\lesssim$2 nm diameter). Pt particles touching the external void were identified as exterior to the carbon support, and those that only touched the filled carbon were identified as interior to the carbon support. This automatic delineation of interior and exterior Pt agreed with visual inspection more than 95% of the time.

Pt particle size distributions for interior and exterior particles and surface-area weighted size distributions are available in the published supplemental information.[1] The experimentally measured size distributions were fit to lognormal distributions truncated below 1 nm to account for our limited capability for detecting very small nanoparticles in tomography. Specific surface area from tomography was calculated using the total Pt surface area and volume, assuming the density of bulk Pt. All Pt surface area was included, including surfaces that contact the carbon support – no correction for the "degree of embeddedness"[44] was used. The exterior specific surface area was calculated using the surface area of exterior particles only and the volume of all particles, consistent with an assumption of interior particles being present but inaccessible. Further details of the analysis are presented in the supplemental information.

4.3.10 3D Visualizations

3D electron tomography visualizations were created using the open source tomography platform *tomviz* (http://www.tomviz.org/). Visualizations of segmented reconstructions were created using binary volumes for each material component exported from MATLAB created with medium thresholds. Surfaces are contour renderings at the value 0.5 for each binary component.

4.4   Results and Discussion

4.4.1   Primary Particle Structure

Each of the carbon support materials studied here contains some variation in morphology and atomic structure. Carbon aggregates tend to contain clusters of similar primary particles with similar structure extending over hundreds of nanometers.

In Vulcan, primary particles have a broad distribution of sizes which is roughly bimodal,[45] including smaller 10-20 nm diameter primary particles and large 25-40 nm diameter primary particles. Representative high resolution TEM (HRTEM) images of Vulcan primary particles in each size range (Figure 4.2) reveal that they have distinct atomic structures as well. The larger primary particles have thick graphitic shells around a relatively amorphous core, while the smaller primary particles are less dense, more amorphous, and do not show dense graphitic shells. Vulcan also includes a few very large 50-90 nm diameter primary particles, although these appear to accumulate very little Pt,[1] and are thus neglected in this investigation.
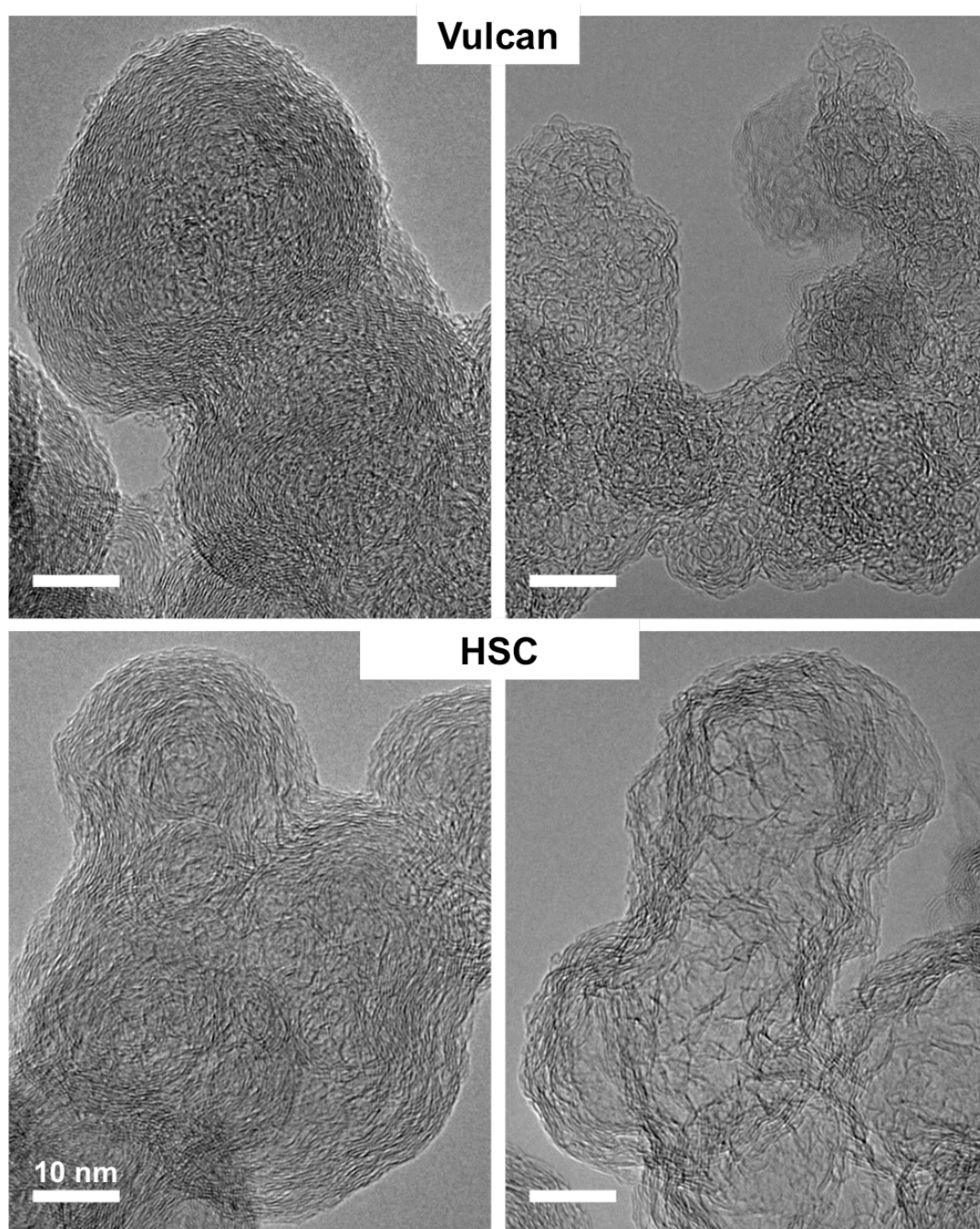
Figure 4.2. HRTEM images showing morphology and atomic structure of different primary particles in Vulcan carbon (top) and HSC carbon (bottom). Vulcan includes large 25-40 nm primary particles (left) that are dense, with thick graphitic shells around a relatively amorphous core, as well as small 10-20 nm primary particles that are less dense, more amorphous, somewhat porous, and do not show dense graphitic shells. HSC includes relatively

solid primary particles with 20-40 nm diameters and hollow primary particles with 15-35 nm diameters typically.

Primary particles in HSC do not segregate by size as dramatically as in Vulcan, although they show clear differences in morphology. HSC includes two distinct primary particle types, one which appears to be relatively dense and solid, and another that appears to have a relatively low density, particularly at the primary particle centers, making them appear hollow (Figure 4.3). The relatively solid primary particles appear to be slightly larger, with 20-40 nm diameters, than the hollow primary particles, which have 15-35 nm diameters typically. Representative HRTEM images of the primary particle types (Figure 4.2) show that the solid particles have a shell of relatively graphitic carbon, although it appears more disordered and less dense than in the large Vulcan particles. The interior of these particles appears to be filled with amorphous carbon. The hollow particles also show a relatively graphitic shell but have an interior with much lower density. The HRTEM image suggests that the interior may be empty or may contain a few loose, crumpled graphene sheets.
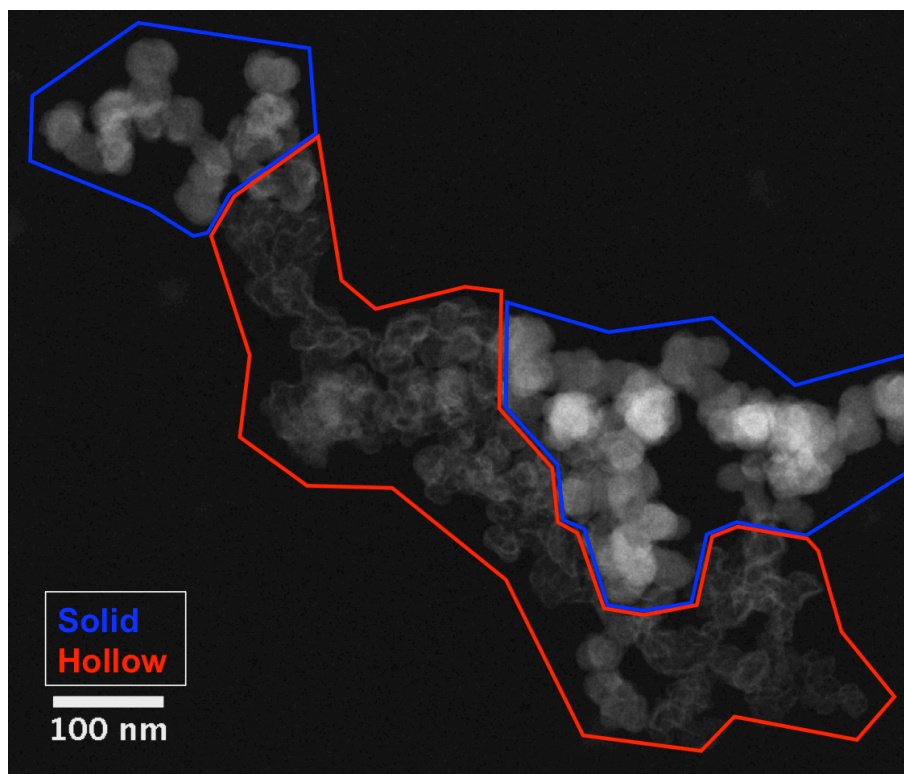
Figure 4.3. ADF STEM image of HSC carbon support without platinum, showing hollow primary particles (red) and solid primary particles (blue).

4.4.2   3D Structure of Porous Carbon Supports

Understanding the structure of the primary particle interior and its porosity is key to explaining the transport behavior and durability of HSC-supported catalysts. Because this structure cannot be inferred from two-dimensional imaging alone, we employed STEM tomography to investigate the 3D structure of HSC carbon supports (Figure 4.4).
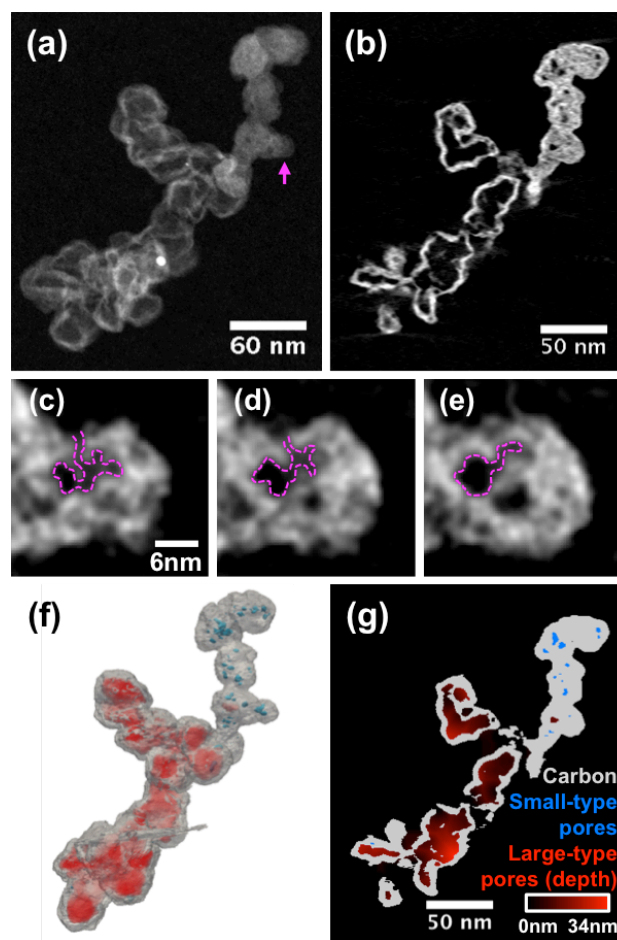
Figure 4.4. 3D reconstruction and analysis of non-platinized HSC carbon. (a) LAADF STEM image of the carbon aggregate. The two small bright particles are gold fiducial markers added to aid image alignment. (b) Cross section of 3D reconstruction perpendicular to the imaging axis, with brighter regions indicating higher carbon density and void regions shown in black. (c-e) Cross sections perpendicular to the imaging axis spaced ~1 nm apart from the more solid primary particle indicated by the magenta arrow in (a). The particle shows narrow ~1 nm channels that connect the exterior to a void with a ~5 nm diameter (highlighted with dashed magenta line). 3D visualization (f) and 2D slice (g), corresponding to the same cross section as in (b), of a segmented reconstruction with carbon shown in grey, smaller pores accessible only through narrow channels shown in blue, and larger pores accessible through wider openings highlighted in red, with red intensity increasing at greater distance from pore openings as shown by the color bar.

The HSC aggregate selected for STEM tomography (Figure 4.4a) includes both hollow (bottom left) and filled (top right) primary particle clusters. A cross-section from the tomographic reconstruction (Figure 4.4b) reveals the density (indicated by the intensity) and porosity of the carbon interior. The hollow primary particles show a clear, dense shell, and an interior with effectively zero intensity (same as background) in most regions. Some sparse strips of lower intensity material are visible in parts of the interior, interpretable as either loose graphene sheets or very thin walls between primary particles. Openings in the dense shell of the hollow particles are also visible, with typical diameters around 2-5 nm.

The filled primary particles show a significant amount of material with similar intensity to the shells on their interiors, as well as clear pore regions with zero intensity and some regions with intermediate intensity, interpretable as either low density carbon or small pores similar to or smaller than the ~1 nm resolution of the tomogram. The larger, round pores observed in filled HSC primary particles have typical diameters around 2-8 nm and are much smaller than the interior spaces in the hollow primary particles. Close inspection of the pores in filled primary particles show that narrow channels are observed connecting the larger pores to the carbon exterior. One such structure is shown in Figure 4.4(c-e), highlighted in magenta, with a ~1nm channel connecting a larger ~5nm diameter void to the primary particle exterior.

Segmentation of the tomogram to distinguish carbon and identify distinct pore regions yields additional insights into the structure of HSC. Figure 4.4(f) shows the segmented tomogram rendered in 3D, and Figure 4.4(g) shows a cross-section through the segmented tomogram (corresponding to the cross-section in (b)). The very narrow channels shown in (c-e) are not separated from carbon in the segmentation, so pores regions accessible through only these channels appear "closed", and are shown in blue in (f,g). Pore regions with larger openings are shown in red in (f,g), with the shade of red indicating the distance from the nearest exterior opening. The two

103

different types of pores are highly segregated on the carbon aggregate, with the large-opening pores found almost exclusively in the cluster of hollow primary particles, and the smaller, channel-connected pores found almost exclusively in the filled primary particles. Walls between the hollow primary particles are typically incomplete or absent entirely, and as a result these large pores form a single interconnected network throughout the cluster of hollow particles. Openings in the exterior walls are frequent enough that the distance to the nearest opening inside the pore network (g) is typically similar to the primary particle radius.

The prevalence of each type of primary particle was estimated from an ensemble of ADF STEM images by manual classification of primary particle clusters (as in Figure 4.3). Analysis of the integrated intensity of each type in the image ensemble and porosity of each type in the tomogram (detailed in the supplemental information) suggests that hollow carbon particles compose 43±7% of the total volume and 29±7% of the total mass in HSC.
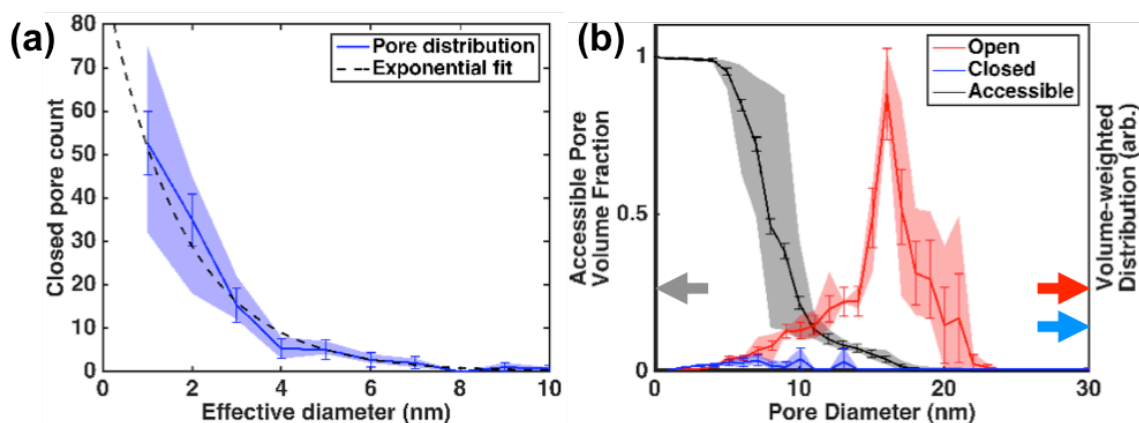
Figure 4.5. Pore size distributions for unplatinized HSC carbon. (a) Histogram of small-type (closed in segmentation) pore sizes shown with exponential fit. (b) Plot of volume-weighted size distribution for large-type (open in segmentation) and small-type pores (right axis) alongside the fraction of pore volume accessible through pore openings of a particular size (left axis). Error bars represent one standard error of statistical uncertainty and shaded regions represent uncertainty due to choice of carbon segmentation threshold.

The pore size distribution for the smaller type, channel-accessed pores can be determined from the segmented tomogram by approximated these pores as spherical to calculate the effective diameter of each pore. The corresponding distribution (Figure 4.5a) of diameters d is well fit by an exponential distribution $\sim e^{-d/\mu}$ with $\mu=1.7\pm0.3$ nm, provided that the distribution is truncated to the minimum detectable pore size. Determining a size distribution for the network of larger pores in hollow primary particles is less straightforward but can be achieved by assigning a local diameter to each semi-confined pore region (see supplemental for details). Figure 4.5b shows the volume-weighted pore size distribution for closed and open pores, accounting for the prevalence of each primary particle type. Open pores in hollow primary particles contribute vastly more to the total pore volume than closed pores. Open pores are larger, with most volume in pores with 10-20nm diameters, while closed pores have most volume at diameters less than 10nm. The impact of constrictive bottlenecks between pores and at pore openings can be assessed by tracking the limiting bottleneck diameter to access each pore region. The fraction of total pore volume that can be accessed through openings of a given size is shown in Figure 4.5b. This measurement overestimates the typical opening size somewhat because the size of some openings is exaggerated by blurring due to missing wedge artifacts in electron tomography. Despite this, it is evident that the vast majority of interior pore volume can only be accessed through bottlenecks significantly smaller than the pores.

Measurements of the primary pore diameter distribution from gas desorption isotherms have previously been reported, showing large pore volumes below ~6nm.[46] Because desorption isotherms measure the diameter of the pore opening rather than the interior volume[47], we suspect that these measurements are attributable to the small 2-5 nm openings into the hollow primary particles observed in tomography.

Overall, it is clear that the morphology of HSC carbon supports can be highly heterogeneous, with either hollow primary particles with large interior pores or mostly filled primary particles with smaller pores accessible through very small channels. Both pore structures can contain Pt nanoparticles in HSC-supported catalysts. Discussion of reactant transport must consider that Pt in either pore type can only be accessed through relatively small bottleneck constrictions. This restrictive pore geometry is also likely to limit the migration and coalescence of Pt nanoparticles on HSC supports, and will thus have implications for the catalyst durability as well.

Figure 4.6. 3D Visualizations (top) of segmented tomograms showing the carbon surface (transparent grey) and Pt nanoparticles on the carbon exterior (red) and in the carbon interior (blue). Cross sections (bottom) of 3D reconstructions perpendicular to the imaging axis for 10wt%Pt/HSC,

50wt%Pt/HSC, 10wt%Pt/Vulcan, and 50wt%Pt/Vulcan. Cross sections are shown with a gamma correction of 0.5 to improve visibility of carbon.

4.4.3 Impact of Support Morphology on Pt Distribution

The differences in primary particle structure and porosity between HSC and Vulcan result in dramatic differences in the distribution of platinum on each support. STEM tomography was performed for each of the Pt/HSC and Pt/Vulcan specimens to allow visualization and quantitative measurement of the platinum distribution. Figure 4.6 shows 3D visualizations of segmented tomograms for each of the samples, with carbon-interior Pt particles shown in blue and carbon-exterior Pt particles shown in red, alongside 2D cross-sections from the tomograms. It is qualitatively apparent that in HSC interior particles are dominant, as the 3D visualizations appear mostly blue, while in Vulcan exterior particles are dominant, as the 3D visualizations appear mostly red. Note that Vulcan does have interior Pt particles, which are clearly visible in the tomogram cross-sections, although they are relatively small, having diameters of only 1-2nm. As we will discuss in more detail below, the majority of Pt surface area resides in the carbon interior in all HSC specimens and on the carbon exterior in all Vulcan specimens.

For Vulcan, the variation in primary particle size and morphology was investigated by acquiring separate tomograms of small and large carbon primary particles for each platinum loading (Figure 4.7). To calculate quantitative values that are comparable to bulk properties, we consider the relative weighting of the large and small Vulcan primary particles. Weighting factors for the larger (22.5-45 nm) and smaller (0-22.5 nm) Vulcan primary particles was calculated using the size distribution reported by Ferraro et al.[45] and the concentration of platinum measured in the tomograms for each loading and Vulcan type.

While the larger primary particles have approximately 7 times more volume than small primary particles, we find that, due to their higher surface area and porosity, the smaller primary particles support approximately 2.7 times more Pt per carbon volume in 10%Pt/Vulcan and approximately 20% more in 50%Pt/Vulcan. This implies that small primary particles support approximately 28% of the Pt in 10%Pt/Vulcan, and 15% of the Pt in 50%Pt/Vulcan. Uncertainty in the weighting due to the choice of particle type cutoff diameter and platinum content was included in calculations. The two dominant primary particle types in HSC, hollow and filled, were discussed previously. All reconstructions shown here for HSC represent the filled primary particle type. Hollow HSC particles in the platinized samples were found to be more radiation sensitive, and reconstructions of sufficient quality for automated statistical analysis could not be obtained by the same methods. This may be caused by the Pt particles catalyzing beam-induced carbon oxidation with small amounts of water adsorbed on the sample surface. All platinized samples showed some degree of damage during tomography, although the hollow HSC structure showed more motion, possibly because the lower density of carbon provides less structural stability.
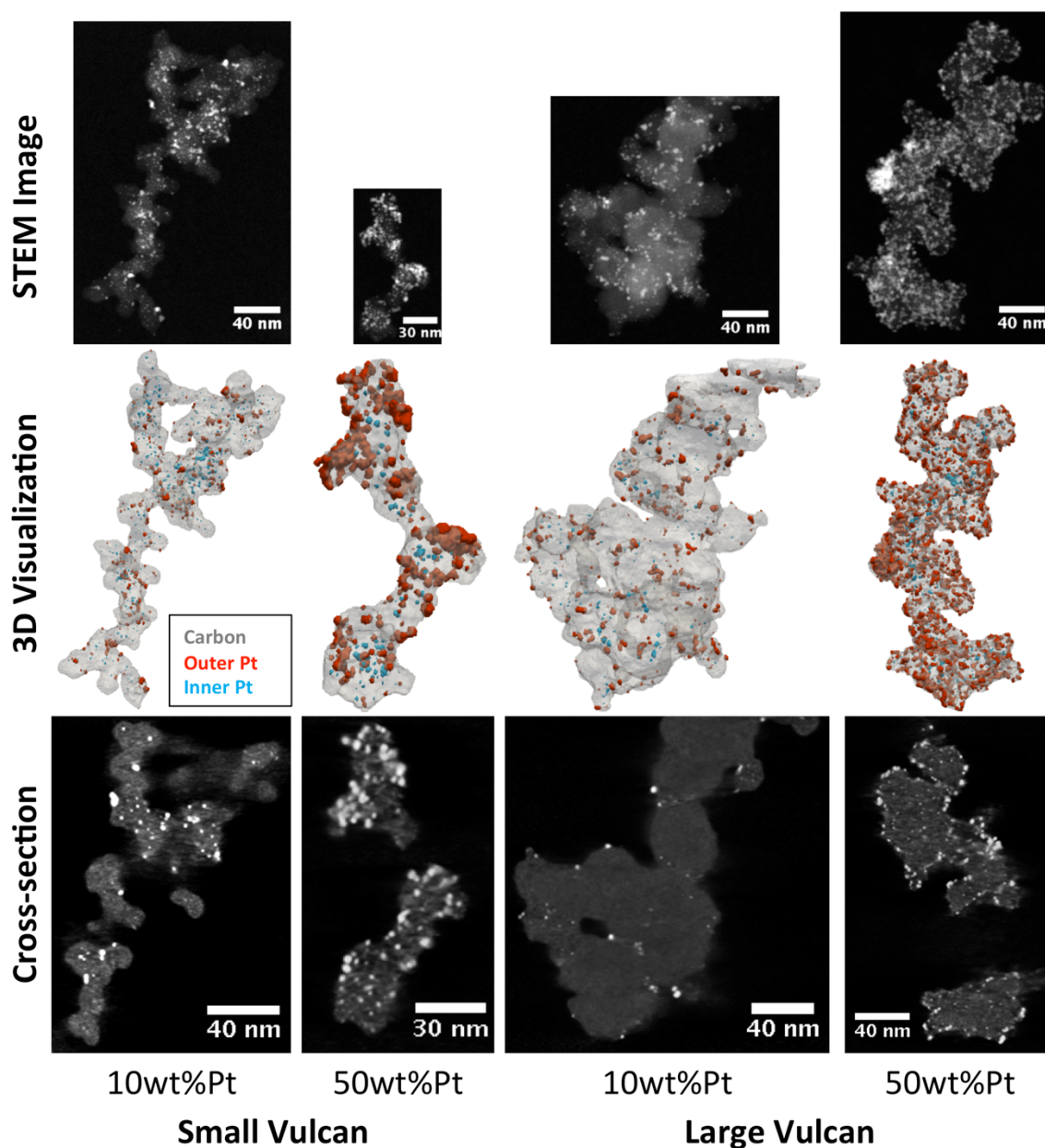
Figure 4.7. Visualizations comparing small and large Vulcan primary particles at 10wt% and 50wt% Pt loading. (Top) STEM images of aggregates chosen for tomography, shown to scale in indicate differing primary particle sizes. (Middl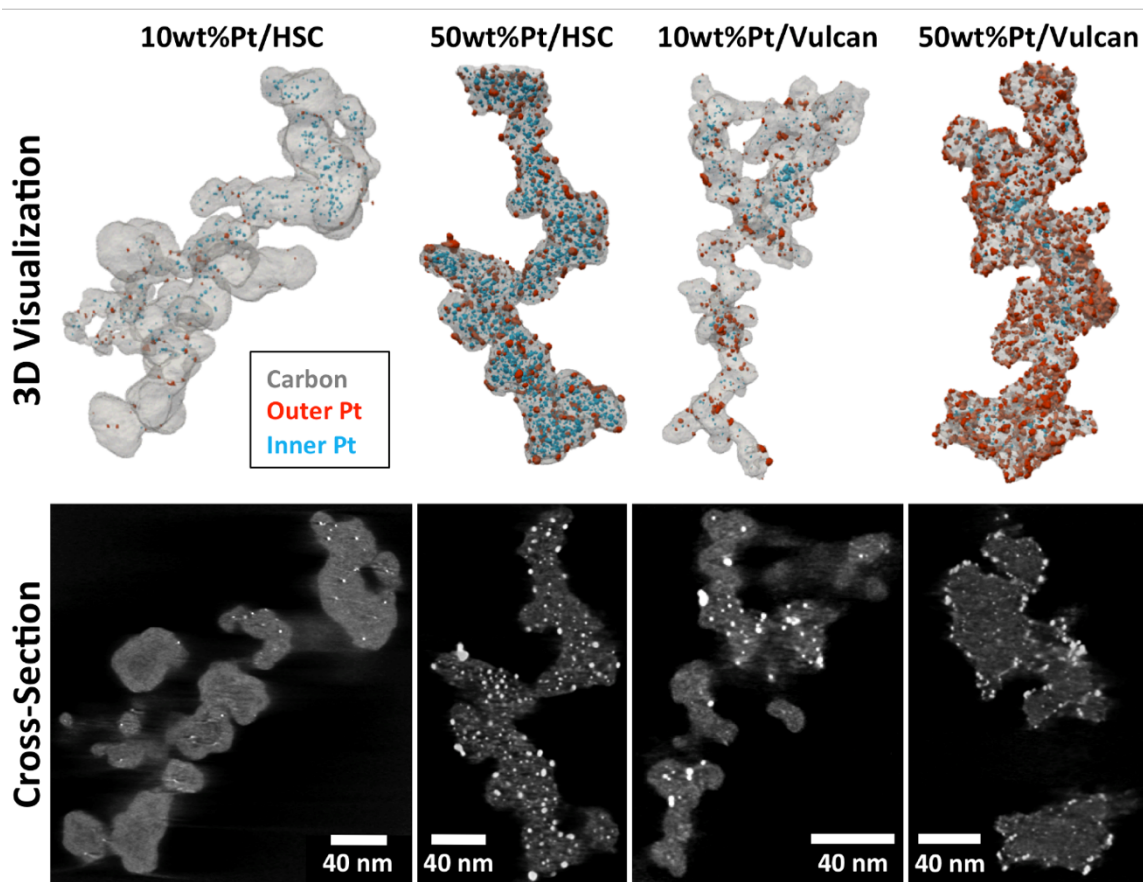e) 3D Visualizations of segmented tomograms showing the carbon surface (transparent grey) and Pt nanoparticles in on the carbon exterior (red) and in the carbon interior (blue). (Bottom) Cross sections of 3D reconstructions perpendicular to imaging axis. Cross sections are shown with a gamma correction of 0.5 to improve visibility of carbon.

Quantitative analysis of the segmented 3D reconstructions allows us to determine the trends in catalyst distribution as the support morphology and Pt content are varied (Figure 4.8). For HSC specimens we find that the majority of Pt surface area (60-70%) is embedded in the carbon interior (consistent with independent TEM tomography measurements[26,48]). For Vulcan specimens, the majority of Pt surface area resides on the carbon exterior, with the higher-porosity small primary particles having a relatively larger fraction on the support interior. For all specimens, increasing the Pt content decreases the fraction of catalyst area on the support interior. This effect, which is large for Vulcan and small for HSC, can have two main contributing factors: the number of additional nanoparticles that nucleate on the carbon interior or exterior, and how the particle size changes with loading. For HSC, as Pt content increases additional Pt particles have roughly equal probability of forming on the interior and exterior, causing no significant change in the fraction of Pt particles on the interior. In Vulcan, additional particles preferentially nucleate on the carbon exterior because of the limited interior space available, causing the interior particle fraction to drop. The observed Pt distributions are consistent with reasonable expectations for Pt nanoparticles synthesized directly on the carbon support, as was done in this study.
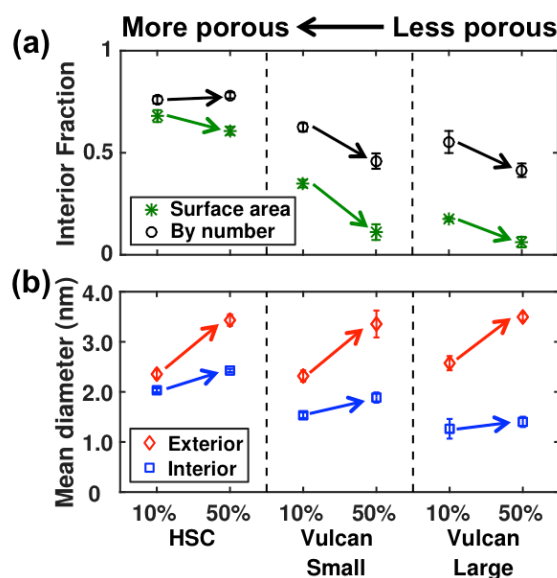
Figure 4.8. Trends in catalyst location and size for different support morphology and Pt content measured by electron tomography. (a) Number fraction of catalyst particles in the carbon interior (black) and surface area fraction of particles in the carbon interior (green), with error bars showing combined segmentation uncertainty and one standard error statistical uncertainty. (b) Mean particle diameters for interior (blue) and exterior (red) particles, with error bars showing 95% confidence intervals. Arrows indicate trends with increasing Pt content.

Figure 4.8(b) shows a comparison of mean diameters derived from distribution fits. The size distributions of Pt particles on the interior and exterior in all specimens are well fit by lognormal distributions truncated to account for the minimum detectable nanoparticle size.[1] For all carbon support morphologies, exterior particles have a larger mean size than interior ones. The mean diameter of interior particles becomes significantly larger with increasing support porosity, whereas the mean diameter of exterior particles changes little with support morphology. Increasing the Pt content tends to increase the mean particle size on all supports, but the mean size for exterior particles increases significantly more. Furthermore, the mean size for interior particles increases more for more porous supports. This indicates that interior pores confine the growth of large nanoparticles, especially in low porosity supports, where interior spaces can quickly become

111

saturated. As Pt content increases from 10wt% to 50wt%, the combination of preferential nucleation of additional nanoparticles on the exterior of Vulcan and the faster growth in exterior particle sizes relative to HSC results in a large decrease in the interior surface area fraction for Vulcan and a small one for HSC, as shown in Figure 4.8(a).

4.4.4   Electrochemical Accessibility of Catalysts

To understand the impacts of catalyst morphology on the accessibility of the Pt, we measured the electrochemically active surface area (ECSA) of the catalyst specimens using two techniques: hydrogen adsorption/desorption (HAD) in an acidic aqueous electrolyte and CO-stripping in fuel cell MEAs. Figure 4.9(a) shows a comparison of the specific surface area (SSA) measurements made by STEM tomography (closed symbols) and the electrochemical (open symbols) techniques. We find that the ECSA measured by HAD in acidic aqueous electrolyte (black circles) is broadly consistent with the total physical surface area observed in tomography (blue squares), showing decreasing SSA with increasing Pt loading on either support, and slightly higher SSA for HSC than for Vulcan at each loading. Note that the SSA calculated including only the surface area of exterior particles is insufficient to account for the ECSA. This indicates that all of the catalyst is accessible to protons in liquid within our uncertainty, including Pt surface that is in contact with the carbon or embedded inside the support. The HSC-supported Pt analyzed here is embedded in the relatively solid HSC structure. Because the vast majority of embedded catalyst particles appear to be proton-accessible, we infer that proton conduction can occur in the narrow ~1nm channels shown in Figure 4.4(c-e) when they are saturated with aqueous electrolyte.

The ECSA measured in MEAs by CO-stripping at 100% relative humidity (RH) follows the same trend with Pt content observed in HAD and tomography. However, the overall ECSA is lower in CO-stripping, compared to either HAD or tomography, especially for HSC. This may be due to

dissolution of very small Pt nanoparticles in the MEA as CO-stripping was performed after one day of fuel cell operation while HAD and tomography were done on fresh samples. In addition, ECSA measurement at elevated temperature (80 vs 25°C) have been shown to give slightly lower values.[49]
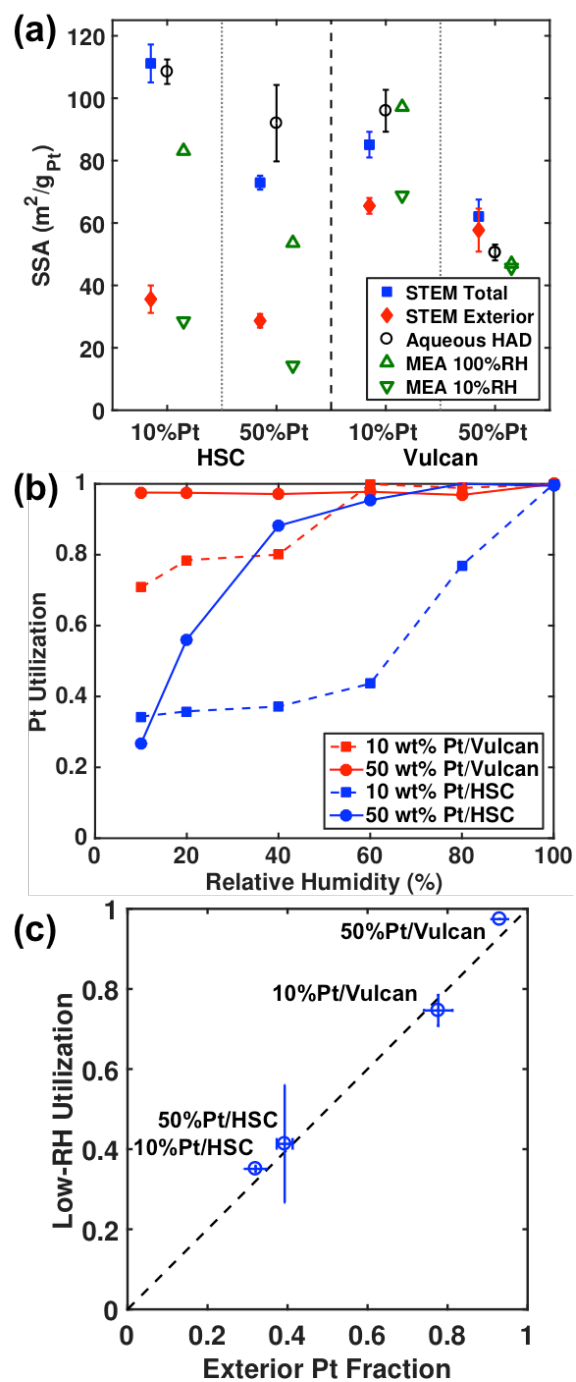
Figure 4.9. (a) Comparison of Pt specific surface area (SSA) measured by tomography and by electrochemical techniques. Error bars for the SSA measured by STEM tomography include segmentation uncertainty, one standard error of statistical uncertainty, and uncertainty in primary particle type weighting (for Vulcan supports only). Aqueous HAD ECSA data points represent the

mean of 3-4 trials, with error bars showing one standard error. ECSA in MEA shows the SSA measured by CO-stripping from 10% RH (bottom point) to 100% RH (top point). (b) Pt utilization measured by CO-stripping in MEA at 80°C with the RH varying from 10% to 100%. (c) Comparison of Pt surface area on exterior particles as a fraction of total Pt surface area measured by tomography and Pt utilization at low RH in CO-stripping ECSA measurements. Data points for low-RH utilization are the average of measurements at 10% RH and 20% RH, with error bars showing the range of values. Error bars for interior fraction by STEM tomography follow the same convention as in (a).

Shinozaki et al. showed that CO stripping could be useful in expressing the accessibility of Pt/C catalysts.[31] The electrochemical oxidation of CO requires H_2O and proton accessibility, through either ionomer or water condensed on the catalyst. As the RH decreases, only CO adsorbed on Pt that is in close proximity to ionomer will be oxidized.[50] Shinozaki et al. demonstrated that catalysts with a large fraction of interior Pt such as Pt/HSC showed a large decrease in CO stripping charge at low RH, while catalyst with a small fraction of interior Pt such as Pt/Vulcan showed negligible decrease in the CO stripping charge. This is consistent with the assumption that ionomer cannot infiltrate small pore openings to interact with Pt inside the carbon primary particles.

Using this method, we determined the Pt ECSA and utilization at different RH for the four catalysts (Figure 4.9b). The decrease in the CO stripping area with RH depends on the existence of pathways through ionomer or capillary-condensed water to Pt, which are influenced by the distribution of Pt particles with respect to the carbon, the carbon pore size, and the pore hydrophilicity. To quantify the Pt particles inside the carbon pores that are inaccessible to ionomer, CO stripping measurement should include measurements at low RH where capillary condensation is minimal. However, measurement at 0% RH is not possible because the CO oxidation reaction requires water. Quantification of the interior particle fraction is straightforward for most catalysts, where the CO stripping area reaches a plateau at low RH. However, for some catalysts, such as 50%Pt/HSC, the CO stripping area continues to change at low RH, contributing significant

uncertainty to the measurement. As shown in Figure 4.9(c), we find that the platinum utilization at low RH (10-20%), normalized to the ECSA at 100% RH, is consistent with the fraction of total surface area on the carbon support exterior measured by tomography. The overall agreement suggests that it is reasonable to interpret the utilization lost at low RH, measured by RH-dependent CO-stripping, as an indication of the fraction of catalyst surface that is embedded in primary pores of the support, and that these pores are not infiltrated by ionomer.

4.5   Conclusions

This investigation has used cryo-STEM tomography in a comparative, statistical study of the morphology of carbon supported fuel cell catalysts. The HSC and Vulcan carbon black supports studied each have substantial heterogeneity in their primary particle structures. The primary differences observed were in the size of primary particles in Vulcan and the extent of internal porosity in HSC. We found that HSC shows two distinct primary particle morphologies, one with large (15-20nm) primary pores accessible through pore openings a few nanometers in diameter, and the other with smaller primary pores a few nanometers in diameter and accessible through channels ~1nm or less in diameter. The majority of Pt surface area in HSC is embedded within these primary pores, while the majority of Pt surface on low-porosity Vulcan resides on the support exterior. For either support, increasing Pt content decreases the overall SSA and shifts the distribution of Pt surface to the support exterior. This is particularly significant on Vulcan, where the interior space becomes saturated with Pt. These quantitative measurements provide useful inputs for structure-based models of transport phenomena and catalyst degradation, which depend on the distribution of Pt particle sizes and positions on the carbon support and on the geometry of pores containing internal Pt particles.

We found that all of the Pt surface area observed in tomography is required to account for the electrochemical surface area observed in aqueous HAD measurements, indicating that essentially all the Pt surface is accessible to protons in liquid, including interior nanoparticles and interfaces with the carbon. We found that the fraction of Pt measured on the carbon interior by tomography is consistent with the Pt utilization lost at low relative humidity, as determined by RH-dependent CO-stripping. This supports the use of RH-dependent CO-stripping as an electrochemical technique to infer the fraction of embedded Pt in fuel cell catalysts, which is more accessible and higher-throughput than STEM tomography. Furthermore, these results help rationalize the participation of the Pt catalyst under different conditions in terms of the catalyst structure: at high humidity, condensed water in catalyst primary pores provides proton accessibility for interior Pt particles, while at low humidity neither water nor ionomer is available to transport protons to the interior Pt, precluding its participation. Further investigation is needed to understand how the morphology and location of the catalysts change after fuel cell operation, and how the complex structure of these catalysts affects oxygen and water transport in low-Pt fuel cell electrodes.

4.6   References

[1] E. Padgett, N. Andrejevic, Z. Liu, A. Kongkanand, W. Gu, K. Moriyama, Y. Jiang, S. Kumaraguru, T.E. Moylan, R. Kukreja, and D.A. Muller, J. Electrochem. Soc. **165**, F173 (2018).

[2] A. Kongkanand and M.F. Mathias, J. Phys. Chem. Lett. **7**, 1127 (2016).

[3] H.A. Gasteiger, S.S. Kocha, B. Sompalli, and F.T. Wagner, Appl. Catal. B Environ. **56**, 9 (2005).

[4] F. Hasché, M. Oezaslan, and P. Strasser, ChemCatChem **3**, 1805 (2011).

[5] Q. Jia, K. Caldwell, J.M. Ziegelbauer, A. Kongkanand, F.T. Wagner, S. Mukerjee, and D.E. Ramaker, J. Electrochem. Soc. **161**, F1323 (2014).

[6] K.M. Caldwell, D.E. Ramaker, Q. Jia, S. Mukerjee, J.M. Ziegelbauer, R.S. Kukreja, and A. Kongkanand, J. Phys. Chem. C **119**, 757 (2015).

[7] B. Han, C.E. Carlton, A. Kongkanand, R.S. Kukreja, B.R. Theobald, L. Gan, R. O'Malley, P. Strasser, F.T. Wagner, and Y. Shao-Horn, Energy Environ. Sci. **8**, 258 (2015).

[8] J. Zhang, H. Yang, J. Fang, and S. Zou, Nano Lett. **10**, 638 (2010).

[9] J. Wu, J. Zhang, Z. Peng, S. Yang, F.T. Wagner, and H. Yang, J. Am. Chem. Soc. **132**, 4984 (2010).

[10] M.K. Carpenter, T.E. Moylan, R.S. Kukreja, M.H. Atwan, and M.M. Tessema, J. Am. Chem. Soc. **134**, 8535 (2012).

[11] S.-I. Choi, S. Xie, M. Shao, J.H. Odell, N. Lu, H.-C. Peng, L. Protsailo, S. Guerrero, J. Park, X. Xia, J. Wang, M.J. Kim, and Y. Xia, Nano Lett. **13**, 3420 (2013).

[12] L. Gan, C. Cui, M. Heggen, F. Dionigi, S. Rudi, and P. Strasser, Science. **346**, 1502 (2014).

[13] C. Chen, Y. Kang, Z. Huo, Z. Zhu, W. Huang, H.L. Xin, J.D. Snyder, D. Li, J. a Herron, M. Mavrikakis, M. Chi, K.L. More, Y. Li, N.M. Markovic, G. a Somorjai, P. Yang, and V.R. Stamenkovic, Science. **343**, 1339 (2014).

[14] J. Zhang, Y. Mo, M.B. Vukmirovic, R. Klie, K. Sasaki, and R.R. Adzic, J. Phys. Chem. B **108**, 10955 (2004).

[15] K. Sasaki, H. Naohara, Y. Cai, Y.M. Choi, P. Liu, M.B. Vukmirovic, J.X. Wang, and R.R. Adzic, Angew. Chemie Int. Ed. **49**, 8602 (2010).

[16] A. Kongkanand, N.P. Subramanian, Y. Yu, Z. Liu, H. Igarashi, and D.A. Muller, ACS Catal. **6**, 1578 (2016).

[17] A.Z. Weber, R.L. Borup, R.M. Darling, P.K. Das, T.J. Dursch, W. Gu, D. Harvey, A. Kusoglu, S. Litster, M.M. Mench, R. Mukundan, J.P. Owejan, J.G. Pharoah, M. Secanell, and I. V. Zenyuk, J. Electrochem. Soc. **161**, F1254 (2014).

[18] T.A. Greszler, D. Caulk, and P. Sinha, J. Electrochem. Soc. **159**, F831 (2012).

[19] H. Liu, W.K. Epting, and S. Litster, Langmuir **31**, 9853 (2015).

[20] A.Z. Weber and A. Kusoglu, J. Mater. Chem. A **2**, 17207 (2014).

[21] E. Antolini, Appl. Catal. B Environ. **88**, 1 (2009).

[22] P.T. Yu, W. Gu, R. Makharia, F.T. Wagner, and H.A. Gasteiger, in *ECS Trans.* (ECS, 2006), pp. 797–809.

[23] X. Tuaev, S. Rudi, and P. Strasser, Catal. Sci. Technol. **6**, 8276 (2016).

[24] Y.-C. Park, H. Tokiwa, K. Kakinuma, M. Watanabe, and M. Uchida, J. Power Sources **315**, 179 (2016).

[25] A. Kongkanand, V. Yarlagadda, T.R. Garrick, T.E. Moylan, and W. Gu, ECS Trans. **75**, 25 (2016).

[26] T. Ito, U. Matsuwaki, Y. Otsuks, M. Hatta, K. Hayakawa, K. Maysutani, T. Tada, and H. Jinnai, Electrochemistry **79**, 374 (2011).

[27] H. Jinnai, R.J. Spontak, and T. Nishi, Macromolecules **43**, 1675 (2010).

[28] F.T. Wagner, S.G. Yan, and P.T. Yu, in *Handb. Fuel Cells* (John Wiley & Sons, Ltd, Chichester, UK, 2010).

[29] H. Iden, T. Mashio, and A. Ohma, J. Electroanal. Chem. **708**, 87 (2013).

[30] A. Ohma, T. Mashio, K. Sato, H. Iden, Y. Ono, K. Sakai, K. Akizuki, S. Takaichi, and K. Shinohara, Electrochim. Acta **56**, 10832 (2011).

[31] K. Shinozaki, H. Yamada, and Y. Morimoto, J. Electrochem. Soc. **158**, B467 (2011).

[32] I. V. Zenyuk and S. Litster, J. Phys. Chem. C **116**, 9862 (2012).

[33] I. V. Zenyuk and S. Litster, Electrochim. Acta **146**, 194 (2014).

[34] A. Nouri-Khorasani, K. Malek, A. Malek, T. Mashio, D.P. Wilkinson, and M.H. Eikerling, Catal. Today **262**, 133 (2016).

[35] R. Subbaraman, D. Strmcnik, A.P. Paulikas, V.R. Stamenkovic, and N.M. Markovic, ChemPhysChem **11**, 2825 (2010).

[36] S.S. Kocha, J.W. Zack, S.M. Alia, K.C. Neyerlin, and B.S. Pivovar, ECS Trans. **50**, 1475 (2013).

[37] M. Uchida, Y.-C. Park, K. Kakinuma, H. Yano, D.A. Tryk, T. Kamino, H. Uchida, and M. Watanabe, Phys. Chem. Chem. Phys. **15**, 11236 (2013).

[38] M. Weyland and P. Midgley, in *Transm. Electron Microsc.*, edited by C.B. Carter and D.B. Williams (Springer International Publishing, Cham, Switzerland, 2016).

[39] R. Leary, P.A. Midgley, and J.M. Thomas, Acc. Chem. Res. **45**, 1782 (2012).

[40] D.A. Cullen, R. Koestner, R.S. Kukreja, Z.Y. Liu, S. Minko, O. Trotsenko, A. Tokarev, L. Guetaz, H.M. Meyer, C.M. Parish, and K.L. More, J. Electrochem. Soc. **161**, F1111 (2014).

[41] R.A. Crowther, D.J. DeRosier, and A. Klug, Proc. R. Soc. A Math. Phys. Eng. Sci. **317**, 319 (1970).

[42] P. Gilbert, J. Theor. Biol. **36**, 105 (1972).

[43] D. Legland, K. Kiêu, and M.-F. Devaux, Image Anal. Stereol. **26**, 83 (2007).

[44] T. Ito, U. Matsuwaki, Y. Otsuka, G. Katagiri, M. Kato, K. Matsubara, Y. Aoyama, and H. Jinnai, in *Handb. Fuel Cells* (John Wiley & Sons, Ltd, Chichester, UK, 2010).

[45] G. Ferraro, E. Fratini, R. Rausa, P. Fiaschi, and P. Baglioni, Energy & Fuels **30**, 9859 (2016).

[46] M. Uchida, Y. Fukuoka, Y. Sugawara, N. Eda, and A. Ohta, J. Electrochem. Soc. **143**, 2245 (1996).

[47] S. Lowell and J.E. Shields, *Powder Surface Area and Porosity*, 3rd ed. (Springer Netherlands, Dordrecht, 1991).

[48] H. Jinnai, R.J. Spontak, and T. Nishi, Macromolecules **43**, 1675 (2010).

[49] T.R. Garrick, T.E. Moylan, M.K. Carpenter, and A. Kongkanand, J. Electrochem. Soc. **164**, F55 (2017).

[50] T.R. Garrick, T.E. Moylan, V. Yarlagadda, and A. Kongkanand, J. Electrochem. Soc. **164**, F60 (2017).

5   MITIGATION OF PEM FUEL CELL CATALYST DEGRADATION WITH POROUS CARBON SUPPORTS

5.1   Abstract

Maintaining high performance after extensive use remains a key challenge for low-Pt proton exchange membrane fuel cells for transportation applications. Strategically improving catalyst durability requires better understanding of the relationship between degradation mechanisms and catalyst structure. To investigate the effects of the carbon support morphology, we compare the electrochemical performance and durability of membrane electrode assemblies (MEAs) using Pt and Pt-Co catalysts with a range of porous, solid, and intermediate carbon supports (HSC, Vulcan, and acetylene black). We find that electrochemical surface area (ECSA) retention after a catalyst-targeted durability test tends to improve with increasing support porosity. Using electron microscopy, we investigate microstructural changes in the catalysts and reveal the underlying degradation mechanisms in MEA specimens. Pt migration to the membrane and catalyst coarsening, measured microscopically, together were quantitatively consistent with the ECSA loss, indicating that these were the only two significant degradation pathways. Changes in catalyst particle size, morphology, and Pt-Co core-shell structure indicate that Ostwald ripening is a significant coarsening mechanism for catalysts on all carbons, while particle coalescence is only

significant on the more solid carbon supports. Porous carbon supports thus appear to protect against particle coalescence, providing an effective strategy for mitigating catalyst coarsening.[h1]

5.2 Introduction

Hydrogen fuel cells are emerging as a useful technology for powering electric vehicles, although cost and durability remain key limitations to the widespread adoption of automotive fuel cells. While carbon-supported, platinum-based nanoparticles are the most promising demonstrated catalysts for automotive applications, which demand high power density, the high cost and limited availability of Pt necessitate development of low-Pt fuel cells (<10 g_{Pt} per vehicle).[2,3] Such low platinum loadings, which leave little margin for failure, present new challenges for meeting the strict performance demands of automotive applications.[3,4] In addition to a high mass activity, catalysts must minimize reactant transport resistances, which limit high power performance and ultimately determine the overall system size and cost. The performance criteria for automotive fuel cells must be met throughout the intended life of the cell, including after cell materials experience extensive periods of corrosive conditions. Detailed understanding of degradation pathways in membrane electrode assemblies (MEAs) and careful design of catalyst materials is needed to maximize durability and minimize loss of performance.

Because oxygen reduction reaction (ORR) kinetics are the greatest source of voltage loss in well-optimized MEAs, improving catalyst ORR mass activities (MA) has been the primary focus of catalyst research as an effective strategy for decreasing platinum use.[2] The mass activity is the

---

[h] This chapter is based on an article published in *Journal of the Electrochemical Society*.[1]

product of two more fundamental parameters: the electrochemically active surface area (ECSA) per platinum mass and the surface-area-normalized specific activity (SA). In addition to impacting MA, catalyst ECSA is an important parameter in its own right. In recent years, there has been growing awareness of the important role played by catalyst accessibility and reactant transport resistance in low-loaded fuel cells. In particular, researchers have identified oxygen transport resistance localized near the Pt surface to be a major limiting factor at high currents. The local oxygen transport resistance generally scales inversely with the Pt surface area and may be caused by poor dispersion of Pt particles, thin ionomer layers, ionomer interfaces, or constrictive pore structures.[3,5] Oxygen transport losses can be mitigated by designing accessible carbon support structures[6] and by ensuring that catalysts have high ECSA.[3] When considering catalyst durability, the oxygen transport problem highlights the importance of retaining high ECSA as well as mass activity to maintain adequate power performance over time.[4,7,8]

The mechanisms of SA and ECSA degradation have been the subject of investigation and debate in the literature for many years. Many processes take place simultaneously, which we will summarize separately for SA and ECSA in the following paragraphs.

The specific activity is determined by the chemical properties of the catalytic surface, including the type and density of active sites, the strength of chemical bonding to reaction intermediates, and adsorbed species such as ionomer. Pure Pt catalysts typically experience an increase in specific activity over time[9], due at least in part to increasing particle size, which increases the relative number of the most active surface sites[10]. This trend partly mitigates the loss in mass activity from ECSA losses, discussed below. Platinum alloy catalysts show more variable trends, either losing or gaining specific activity with electrochemical aging.[9,11,12] Loss of specific activity would be expected due to leaching of the secondary metal or increasing Pt shell thicknesses, which would decrease catalytic enhancements from either strain or electronic "ligand" effects.

For fuel cell electrodes, the ECSA is calculated from the electrochemically measured surface area (most commonly using either hydrogen underpotential deposition or carbon-monoxide electro-oxidation) divided by the *initial* platinum mass. Thus, the measured ECSA can decrease from two broad categories of mechanisms: (1) Pt mass loss, where Pt becomes electrically disconnected and thereby electrochemically inactive, and (2) catalyst coarsening, where Pt nanoparticles grow in size, decreasing their specific surface area. For each of these there are multiple distinct mechanistic pathways.

Platinum mass loss primarily occurs as a consequence of Pt dissolution. Dissolved platinum may be chemically reduced by crossover hydrogen gas, depositing in either the membrane or the electrode ionomer. Many researchers have reported Pt reduction in the membrane forming a "Pt band".[9,12–18] Significant Pt reduction in the electrode ionomer has been reported in fewer cases.[13] This may occur as the result of relatively severe hydrogen crossover and decreased hydrogen oxidation in the cathode due to passivation of the cathode Pt surface as Pt-O at some operating potentials.[9] Pt particles may also lose electrical connectivity by detachment from the carbon support or by disruption of the percolating conductive carbon network in the electrode, especially in cases of severe carbon corrosion.[19,20]

Two coarsening mechanisms have been described for fuel cell catalysts: Ostwald ripening and particle coalescence. Ostwald ripening is driven by the electrochemically-induced dissolution and redeposition of dissolved Pt on the surface of Pt particles. This process tends to increase particle sizes because smaller particles have lower stability and experience more rapid dissolution than larger, more stable particles.[21] Coalescence is a result of particle migration on the carbon support, leading to the collision and subsequent reshaping of particles.

Studies have disagreed on the attribution of observed coarsening between these two mechanisms. Many papers have provided evidence for Ostwald ripening as a coarsening mechanism due to the presence of significant amounts of dissolved Pt[13,21] and observations of the growth Pt shells on Pt-Co catalysts caused by Pt redeposition[22,23]. While some papers argue for Ostwald ripening as the only mechanism, others provide evidence that coalescence is also a significant mechanism, based on lognormal-like particle size distribution statistics with a long tail of larger particles that is not theoretically expected from Ostwald ripening[20,24,25], or based on the observation of particles in aged Pt-Co catalysts with multiple Pt-Co cores contained in the same Pt shell, formed as a result of particle collisions[23]. There is now significant evidence that both mechanisms can occur, but less comprehensive understanding of the factors determining their relative significance.

Because coalescence involves the migration of particles over the carbon support surface, it is reasonable to expect that the morphology and surface properties of the carbon should impact the frequency of coalescence. An examination of the literature reveals that most studies reporting Ostwald ripening as the dominant or only mechanism used a porous, high surface area carbon (HSC) such as Ketjen black,[13,14,21,22,26,27] while most reporting the occurrence of coalescence as well used a solid carbon, such as Vulcan[20,23,25,28,29]. It is perhaps surprising that only recently has research been reported that attempts to systematically determine the impact of the carbon support on catalyst coarsening mechanisms. One recent study reported suppression of coalescence on porous carbon supports in a comparison of carbons in an aqueous environment using in situ small angle X-ray scattering (SAXS) measurements of particle size distributions.[29] Another examined catalysts extracted from MEA cathodes after stability testing using electron tomography and lattice imaging reported higher rates of coalescence on Vulcan and graphitized carbon based on observations of the particle morphology and comparisons of particle/crystallite size.[28]

Given these indications that the carbon support morphology does impact the extent and mechanisms of catalyst degradation, selection and engineering of the carbon support is a promising pathway for improving catalyst durability. It is known that carbon support morphology also impacts the catalyst activity, with porous carbons providing higher activities by limiting detrimental ionomer adsorption on the Pt surface,[30–33] and reactant accessibility, by determining the pathways available for oxygen diffusion and proton conduction[6,30,34]. It is therefore important to understand the role of carbon support morphology on catalyst durability in realistic MEA environments under extended stability tests. Structurally sensitive but statistically robust methods are needed to investigate the changes taking place and the underlying degradation mechanisms in the catalyst and electrode.

In this chapter we investigate the role of carbon support morphology in the durability of Pt and Pt-Co catalysts in fuel cell MEAs using electrochemical measurements and scanning transmission electron microscopy (STEM) analysis of post-mortem MEA specimens. Vulcan (Vu) and Ketjen Black (HSC) carbons were chosen for this study as prototypical solid and porous carbon supports, respectively. Vulcan carbon has a moderate surface area among carbon blacks and has been shown to support Pt almost exclusively on its exterior, while HSC has a higher surface area and a majority of supported Pt is embedded within its internal pores. An intermediate porosity Acetylene Black carbon (AB) was also included for the electrochemical experiments. Electrochemical measurements of the catalyst activity and ECSA were made before and after catalyst-targeting accelerated stability tests and showed a general trend of improved activity and durability with increasing support porosity, as illustrated for Vu and HSC supports in Figure 5.1.

Analysis of the MEAs with Vulcan and HSC catalysts by STEM imaging and elemental mapping was used to investigate structural changes and reveal the underlying degradation mechanisms. We used automated image processing to ensure that we obtained statistically robust

125

and representative results from STEM imaging, including thousands of particles per sample for size distribution measurements. Our image analysis procedure was designed to more accurately reflect the surface area to volume ratios of irregular Pt particles in comparison to the common spherical particle approximation. This approach allows us to address traditional limitations to the statistical representativeness of (S)TEM microanalysis and make quantitative comparison to electrochemical measurements to infer and quantify degradation mechanisms. Together, these microscopic observations and electrochemical measurements provide a means to quantitatively explain the degradation pathways for different catalysts.
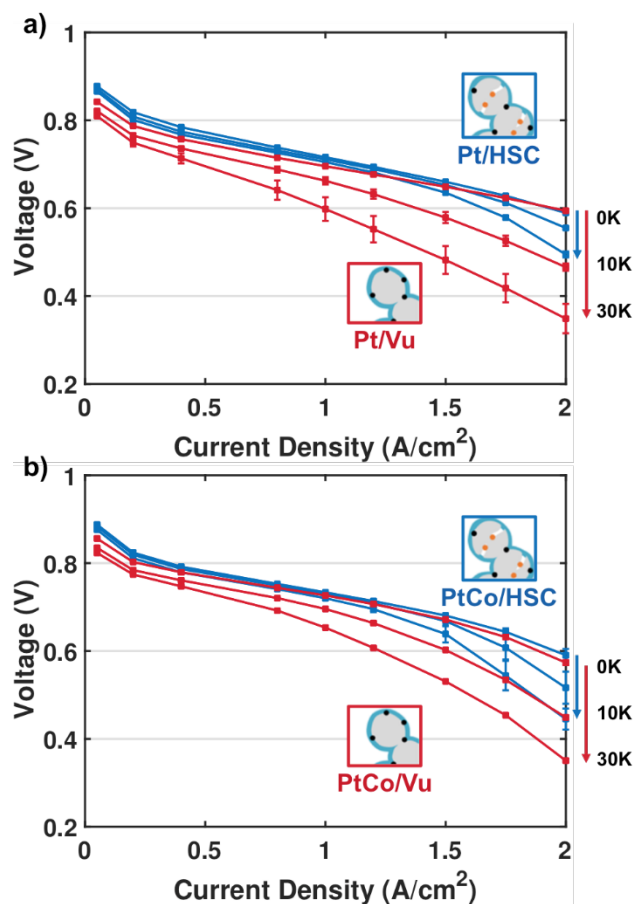
Figure 5.1: Fuel cell polarization curves comparing performance and durability of Pt (a) and Pt-Co (b) catalysts supported on porous HSC carbon (blue) and solid Vulcan carbon (red). Anode and cathode Pt loadings were 0.025 and

0.10 mg$_{Pt}$/cm^2. Anode/cathode operating conditions: H2/air, 94°C, 65/65% RH, 250/250 kPa$_{abs,outlet}$, stoichiometries of 1.5/2. Error bars represent one standard error of the mean.

5.3   Methods

5.3.1   Materials and MEA Assembly

Fuel cell and electrochemical evaluations of each catalyst were performed in a membrane electrode assembly with the electrocatalysts of interest on the cathode. The active area of the fuel cell single cell was 50 cm^2. The metal weight percent on carbon black supports of Pt in Pt and Pt-Co electrocatalysts was 20 and 30 respectively. The electrode Pt loadings were 0.1 and 0.025 mg$_{Pt}$/cm^2 for the cathode and anode, respectively. Perfluorosulfonic acid (PFSA) Nafion® D2020 was used in the electrode at an ionomer to carbon weight ratio of 0.8. 18 μm thick PFSA-based membranes were used to fabricate the MEAs. A 240 μm thick carbon paper with a 30 μm thick microporous layer (MPL) coated on top was used as the gas diffusion layer (GDL). The MEAs were fabricated using a catalyst-coated-membrane approach. The lamination procedure was discussed in detail elsewhere.[2]

The same ionomer to carbon weight ratio was used for MEA assembly for all catalysts. While the BET surface area varies between the different carbon supports, the higher surface area of the porous carbon supports is largely due to their internal pores, which are not infiltrated by ionomer.[34] Consequently, the distribution of ionomer on the carbon support exterior is not expected to vary dramatically.

5.3.2 Electrochemical Measurements

Two accelerated stability tests (ASTs) recommended by the U.S. Department of Energy (DOE)[35] were used in this study: one accelerates the metal particle decay and one accelerates the catalyst support decay. The *catalyst AST* consists of 30,000 trapezoidal voltage cycles between 0.6 and 0.95 V. The dwell time at each voltage was 2.5 s and the ramp time was 0.5 s. Each cycle takes 6 s. The catalyst *support AST* consists of 5000 voltage cycles between 1 and 1.5V at a scan rate of 0.5 V/s. Both ASTs were performed at 80°C, 100% relative humidity, and ambient pressure. The fuel cell performance, electrochemically active surface area, and oxygen reduction reaction mass activity were measured at 0, 10,000 and 30,000 cycles during catalyst AST and at 0, 100, 500, and 5000 cycles during catalyst support AST. ORR activity is reported at 0.9 V_{RHE} at 80°C, 100% relative humidity, and 1 bar of O_2. [2] Pt ECSA was measured by CO stripping in an MEA.[36]

5.3.3 X-ray Scattering Measurements

The X-ray scattering data were collected on a combined Bonse-Hart (USAXS) and pinhole (SAXS/WAXS) instrument at beamline 9-ID-C at the Advanced Photon Source located at Argonne National Laboratory. Details regarding the optics and instrumentation have been previously reported.[37] The X-ray beam was monochromated via a pair of Si(220) crystals to an energy of 24 keV. The beam spot size for USAXS was 0.8 x 0.6 mm (horizontal x vertical) and 0.8 x 0.2 mm for SAXS/WAXS. The X-ray beam exposure times for each sample were 120 seconds for USAXS, 30 seconds for SAXS, and 30 seconds for WAXS. The samples were prepared by lifting off a section of the applied cathode catalyst layer from the membrane side with single-sided, transparent tape. Spectra collected on a blank piece of tape were utilized as a blank for data reduction. The data were corrected and reduced with the NIKA software package[38], and analysis was conducted with the IRENA package[39]. Both packages were run on IGOR Pro 7.0 (Wavemetrics). Because only the

USAXS/SAXS regions are appropriate for determining the particle size distributions of these types of nanoparticles at an X-ray energy of 24 keV, the WAXS data are not presented.

5.3.4   (S)TEM Sample Preparation

MEA samples for (scanning) transmission electron microscopy ((S)TEM) were prepared by cross-sectioning with an ultramicrotome. Strips cut from MEAs were embedded in EMbed 812 Resin (Electron Microscopy Sciences) and cured at 60°C overnight. Sections were cut using a Leica Ultracut UCT Ultramicrotome at thicknesses from 40 nm to 150 nm. Sections were collected on slotted Cu TEM grids and square-mesh Cu TEM grids with lacy carbon, which provide greater stability for high resolution imaging and EELS measurements. Samples were cleaned with oxygen-argon plasma prior to TEM measurements.

5.3.5   STEM EDXS Measurements

Energy-dispersive X-ray spectroscopy (EDXS) quantification of Pt band losses was performed on a FEI Tecnai T12 Spirit S/TEM with a LaB_6 filament thermionic electron source operated at 120 kV in STEM mode. Spectroscopic maps were collected using an EDAX Genesis X-ray detector along with simultaneous bright-field and dark-field STEM images in a single scan per map covering the entire cathode and the region of the membrane including the Pt band. Measurements were made on 70 nm thick sections of EOL MEAs, and maps were collected from 3-5 different regions in each sample. Masks selecting the Pt band and cathode regions were drawn manually in ImageJ2[40] by inspection of the simultaneous STEM images along with higher resolution STEM images acquired prior to EDXS map acquisition. Pt that was included in the membrane by design was excluded from the Pt band masks. The relative Pt content of each region was determined from the summed spectra

in the region by integrating the Pt $L_{\alpha1,2}$ peak after subtracting a constant fitted background value. Calculations were performed in MATLAB.

Pt-Co composition, maps, and profiles were measured on a FEI Tecnai F20 S/TEM with a Schottky field emission gun operated at 200 kV in STEM mode using an Oxford X-Max 80 mm^2 X-ray detector and the INCA software. Measurements were made on ~150 nm thick MEA cross-sections and catalyst powders supported on lacy carbon, which provides better signal averaging and sample stability. The average composition in MEA cathodes was measured by scanning over the entire cathode in at least 5 distinct regions per sample. Further details are provided in the supplemental information.

5.3.6 STEM Imaging

STEM images of catalyst morphology were acquired using a FEI Tecnai F20 S/TEM with a Schottky field emission gun operated at 200 kV. Images were acquired with a convergence semi-angle of ~9.6 mrad and the image signal was collected on an annular detector at a 100 mm camera length to provide high angle annular dark field (HAADF) conditions. HAADF conditions provide approximately mass-thickness contrast which is sensitive to the atomic number Z with a scaling of approximately $Z^{1.7}$, making Pt and Pt-Co particles easily distinguishable from the background of lower-contrast carbon, ionomer, and embedding medium.

5.3.7 Quantitative Analysis of STEM Images

STEM images for quantitative analysis of Pt and Pt-Co particle sizes were acquired with fields of view ranging from 360 to 730 nm with a pixel size of approximately 3.5 Å. The images were prepared for segmentation of metal particles with a light Gaussian smoothing to reduce noise. The slowly-varying background from the carbon support and embedding medium was fit using a

greyscale morphological open operation with a 30 nm radius and removed. Particles were identified with a threshold selected to be low enough so that the smallest particles are included. The particle segmentation is then refined using an active contour with the Chan-Vese method[41] for 300 iterations. Particles touching the edge of the image are not included for analysis.

The segmented set of particles included some particles that are overlapping in projection. It is difficult for an automated routine to reliably distinguish single irregular particles from particles that are overlapping in projection. However, a reasonable approximation for the size of both, as well as single spherical particles, can be calculated using a local radius approximation rather than the more common spherical particle approximation. We implement this by using a watershed transform to determine local regions on each particle (or set of overlapping particles) and then assign each region a local radius equal to the maximum distance from the particle edge in that region. Each region is assigned a statistical weighting factor equal to the area of the region divided by the area of a circle of the same local radius. Size distributions are calculated using the local diameters and weighting factors for all particles. This procedure is described in further detail in the published supplemental information.[1] Calculations were performed in MATLAB using functions in the image processing toolbox.

5.3.8   STEM EELS Composition Maps

STEM electron energy loss spectroscopy (EELS) measurements were performed on an FEI Titan Themis S/TEM operated at 300kV, equipped with a Gatan GIF Quantum spectrometer in single-range EELS mode. A convergence semi-angle of 21.4 mrad and a beam current of around 250 pA were used to acquire spectroscopic images with a pixel size of approximately 1 Å. Composition maps were extracted by integrating the signal from the Co $L_{2,3}$ and Pt $M_{4,5}$ edges after background subtraction using exponential and linear combination of power laws background fits,

respectively. After integration, EELS maps were drift-corrected using an affine correction determined by comparing the simultaneous ADF signal to the fast-scanned overview image. The affine correction was constrained to only shear and stretch components consistent with uniform drift during STEM imaging. Calculations were performed in MATLAB using functions in the image processing toolbox.

5.3.9 *STEM Tomography and Subsequent EELS Mapping*

The sample was extracted from an EOL Pt-Co/HSC MEA by scraping the cathode side of the MEA and dispersing the resulting powder in ethanol using a bath ultrasonicator for approximately 30 minutes. The dispersion was then drop-cast on a wide-mesh Cu TEM grid with an ultrathin carbon film using a micropipette. The STEM tomography experiment and data analysis was performed following previously reported methods[34]. After tomography data acquisition, the sample was transferred to the aberration-corrected STEM for EELS mapping as described above. The same catalyst aggregate from the tomography experiment was located using low magnification STEM imaging. EELS maps were acquired for 37 Pt-Co particles, which were categorized as inside or outside the carbon support using the tomography reconstruction. To measure the distribution of shell Pt shell thicknesses, the boundaries of the Pt-Co core and overall particle were segmented in the Co and Pt EELS maps, respectively, using an active contour method. The Pt shell thickness was calculated at each pixel on the particle surface as the distance from the nearest pixel in the Pt-Co core. This approach yields essentially identical values to a conventional line profile measurement, but allows for a more statistically complete measurement.[1]

5.4   Results and Discussion

5.4.1   Catalyst and Catalyst Support Properties

Three carbon blacks with varying internal porosity were chosen as catalyst supports for this study: Vulcan (Vu), a typical solid carbon, Ketjen Black (HSC), a typical porous carbon, and an acetylene black (AB) carbon with intermediate porosity. The BET surface area and the Raman G/D band ratio, indicating the degree of graphitization, are summarized in Table 5.1. HSC and AB carbons both have high BET surface areas and low graphitization. AB has a slightly lower surface area and is slightly more graphitic than HSC. Vulcan has a significantly lower surface area and is somewhat more graphitic than HSC and AB.

Table 5.1: Physical properties of catalyst carbon supports.

Catalyst Support Type	Carbon BET area (m^2/g_C)	Raman G/D band ratio
HSC (Ketjen, EC300J)	780	0.6
AB (Acetylene Black)	770	0.7
Vu (Vulcan XC 72)	230	1.0

MEAs made with Pt catalysts on each of these carbon supports, along with a broader set of carbon black supports with higher graphitization, were subjected to a support-targeting accelerated stability test intended to simulate unusual or unintentional operating conditions. The test consists of 5000 cycles between 1.0 V and 1.5 V to induce carbon oxidation, which may lead to electrode failure due to collapse of the electrode macropore structure. The results, reported in detail in the published supplemental information,[1] confirmed previous findings of higher corrosion resistance for more graphitized carbons.[42–46] The less graphitic carbons also tend to have higher surface areas, which accelerate carbon corrosion. Differences in the surface functionalization may also impact carbon corrosion or the anchoring of Pt particles on the support. Unfortunately, even the compact

carbons with the highest graphitization did not satisfy the DOE target of < 30 mV loss at 1.5 A/cm^2 after 5000 cycles.

The relatively low carbon surface area and small number of surface functional group of graphitized carbons make preparing a supported catalyst with good particle size distribution very difficult. Furthermore, recent engineering effort in fuel cell system control has substantially mitigated the exposure of the electrode to high potential, making the tolerance of the cathode support to carbon oxidation less important. Consequently, going forward in this study we will focus on the three types of carbons listed in Table 5.1 to investigate the effect of carbon morphology on catalyst stability.

Pt and Pt-Co nanoparticles were synthesized on each carbon support, at 20wt% for Pt catalysts and 30wt% for Pt-Co catalysts, using wet impregnation synthesis methods. Table 5.2 summarizes measurements of the size and some electrochemical properties of these catalysts. Mean particle diameters were measured by SAXS and STEM (detailed STEM results are discussed below). The SAXS and STEM measurements of the mean particle diameters are generally similar in magnitude, with discrepancies of less than 15% for each sample. The bulk SAXS measurements provide validation for the STEM measurement methods, which provide more detailed results that are discussed below. The Pt catalysts were selected to have a similar particle size to control for the impact of particle size effects in their performance and durability. All three have mean particle diameters in the 2-3 nm range, as indicated by both SAXS and STEM, providing ECSAs of around 85-100 m^2/g$_{Pt}$. The Pt-Co catalysts have larger particle sizes because of the higher temperatures required for their synthesis. Pt-Co/HSC and Pt-Co/AB have similar mean particle diameters in the 4-5 nm range and ECSAs around 65-75 m^2/g$_{Pt}$. Synthesis of a similar quality alloy on Vulcan carbon resulted in a larger 5-6 nm mean particle size and a somewhat lower ECSA of 50 m^2/g$_{Pt}$. The initial

134

Pt-Co composition, measured by ICP-AES, was $Pt_{0.77}Co_{0.23}$ for Pt-Co/HSC and $Pt_{0.70}Co_{0.30}$ for Pt-Co/Vu.

Table 5.2: Physical and electrochemical properties of Pt and Pt-Co catalysts at beginning of life.

Catalyst Type	Pt mean particle size (nm) by SAXS	Pt mean particle size (nm) by STEM	Pt ECSA (m^2/g_{Pt})	Pt accessibility under dry condition	ORR Mass Activity (A/mg_{Pt})
Pt/HSC (Ketjen, EC300J)	2.3	2.3	87	35%	0.50
Pt/AB (Acetylene Black)	2.6*		99	49%	0.30
Pt/Vu (Vulcan XC 72)	2.3	2.4	85	95%	0.18
Pt-Co/HSC (Ketjen, EC300J)	4.8	4.4	67	55%	0.60
Pt-Co/AB (Acetylene Black)	4.1		74	49%	0.53
Pt-Co/Vu (Vulcan XC 72)	5.9	5.2	50	97%	0.27

*Pt particle size by XRD

Porous carbon supports are distinct from solid supports because they have a significant fraction of the metal nanoparticles embedded in pores inside the carbon primary particles. The fraction of particles embedded in the carbon can be determined by electron tomography, although this is an arduous process and provides limited statistical sampling. Previous electron tomography experiments have shown that HSC typically supports a majority of Pt particles inside interior pores, while Vulcan supports almost all Pt particles on the carbon exterior.[34,47,48] A useful proxy to infer the fraction of particles on the carbon exterior is the utilization of Pt measured in a MEA with CO-stripping under dry conditions (10-20% RH)[34,49]. Measurements of the dry-cell utilization are reported in Table 5.2, with representative utilization curves presented in Figure 5.2. Both Pt/Vu and Pt-Co/Vu have very high dry-cell utilization (>95%), indicating that nearly all the metal particles are on the carbon exterior, as expected. Pt/HSC has a low dry-cell utilization of 35%, suggesting a majority of interior particles, while Pt-Co/HSC has a somewhat higher dry cell utilization of 55%, suggesting that around half of Pt-Co particles are on the carbon interior. Both

Pt/AB and Pt-Co/AB have intermediate dry cell utilizations around 49%, suggesting that about half of the metal particles are on the carbon exterior. The measurement of the dry cell utilization can be imprecise because the large-scale proton conductivity of the electrode may become disrupted before the carbon-interior pores are fully dried. This may cause the utilization to change rapidly in the 10-20% RH range. This was the case for the AB-supported catalysts, so their measurements should be considered very approximate. However, they showed significantly higher utilization under moderately dry conditions (20-40% RH) compared to the HSC-supported catalysts, suggesting that they support more particles on the carbon exterior.
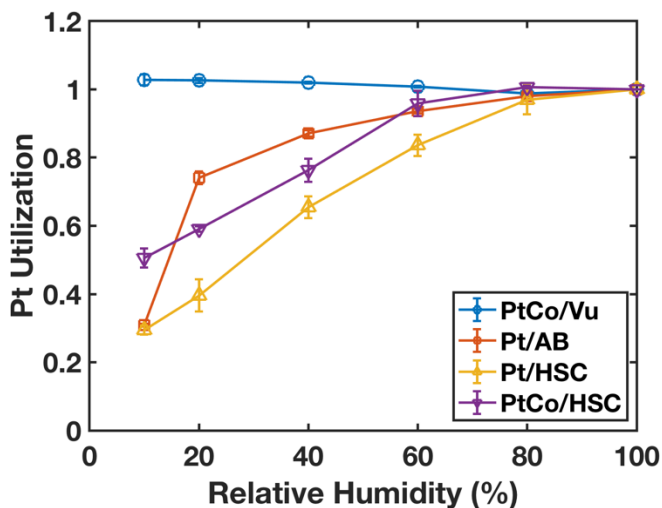
Figure 5.2: Pt utilization of different catalysts measured by CO stripping in MEAs at different relative humidity. The utilization is calculated as the ECSA measured by CO stripping normalized by the ECSA at 100% RH.

5.4.2 Electrochemical Performance and Durability

The differences in MEA performance and durability between Pt and Pt-Co catalysts on solid Vulcan supports and porous HSC supports are clearly evident in fuel-cell polarization curves, shown in Figure 5.1. In the beginning of life (BOL) MEAs, the higher mass activity of Pt-Co catalysts provides a 10-15 mV improvement relative to Pt catalysts at low current densities.

However, Pt-Co catalysts also suffer greater mass transport losses than Pt catalysts due to their lower ECSA, which approximately negates the benefit from mass activity at ~2 A/cm^2 current densities. The higher mass activity of HSC-supported catalysts provides ~30 mV better performance at low currents relative to Vulcan-supported catalysts. Vulcan can provide reduced mass transport losses (especially evident for Pt/V) due to the increased accessibility of particles on the carbon exterior. However, reduced mass transport losses only outweigh the activity gains provided by HSC at very high current densities around 2 A/cm^2 for Pt catalysts.

Figure 5.1 also shows performance losses after 10K and 30K cycles of a catalyst-targeted accelerated stress test. After 30K cycles, MEAs are also denoted "end of life" (EOL). All catalysts show a decrease in performance at low current densities due to decreasing mass activity, but at high currents the additional mass transport losses are especially severe. Both Vulcan-supported catalysts suffer much more dramatic losses than the corresponding HSC-supported catalysts.

Figure 5.3 shows a more detailed comparison of the electrochemical properties of the catalysts at beginning of life and after the catalyst AST. Figure 5.3(a,b) show the total ECSA of the cathode catalysts and the retained fraction of the BOL ECSA. As noted previously, all three Pt catalysts were selected to have similar ECSAs at BOL, and the Pt-Co alloy catalysts have somewhat lower ECSAs (especially Pt-Co/Vu) due to the higher temperatures required for alloy synthesis. The Pt-Co catalysts all retain a higher fraction of their initial ECSA after durability testing compared to the Pt catalysts, likely due to the stability provided by their larger particle sizes. It is notable that all the Pt-Co catalysts maintain total ECSAs equal to or higher than their Pt counterparts after either 10k or 30k cycles, so the higher ECSAs provided by Pt catalysts at BOL are not maintained throughout a practical fuel cell lifetime. For either Pt or Pt-Co catalysts, there is a general trend of higher ECSA retention for more porous supports. HSC-supported catalysts retain a significantly higher fraction of their ECSA than Vulcan-supported catalysts (37±2% for Pt/HSC vs. 24±2% for

Pt/Vu, 68±3% for Pt-Co/HSC vs. 57±2% for Pt-Co/Vu after 30K cycles). The intermediate AB

support behaves more similar to HSC for the Pt catalysts, and more similar to Vulcan for the Pt-Co

catalysts.
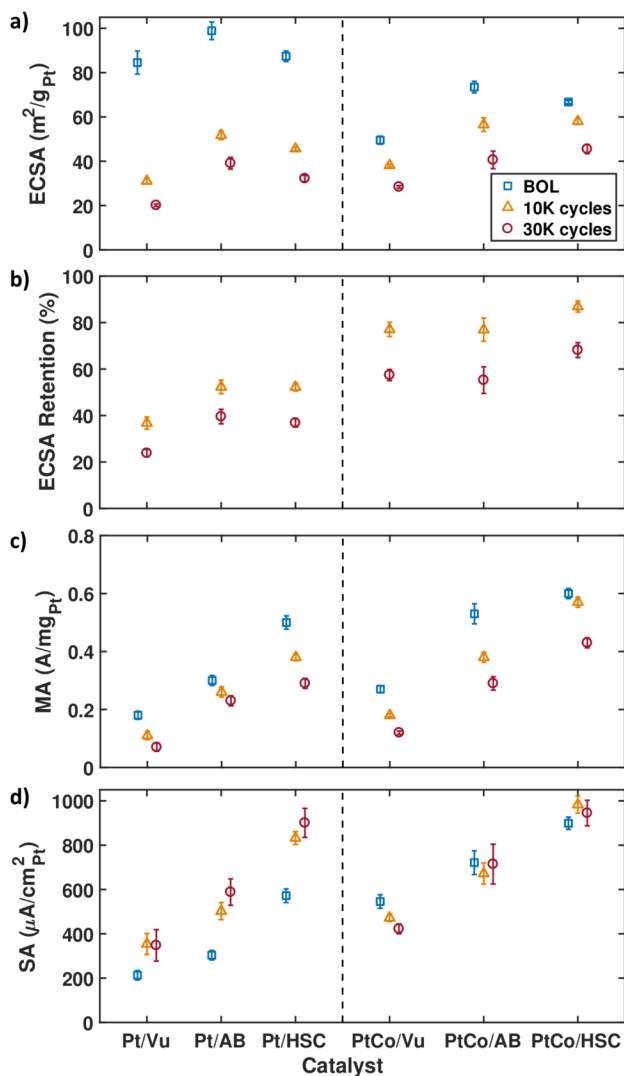
Figure 5.3: Comparison of electrochemical properties and durability in MEAs for Pt
(left) and Pt-Co (right) cathode catalysts with different carbon supports,
arranged with support porosity increasing from left to right. Values at
beginning of life (BOL), after 10k voltage cycles, and after 30k voltage
cycles (EOL) are shown with blue squares, orange triangles, and red circles,
respectively. (a) Electrochemical surface area measured with CO stripping,
normalized to initial Pt mass. (b) Fraction of initial ECSA retained after
voltage cycling tests, showing a trend of higher retention for more porous

138

carbon supports. (c) Mass activity (normalized to initial Pt mass) and (d) specific activity (normalized to measured ECSA) showing a trend of higher activity for more porous catalyst supports. Error bars represent one standard error of the mean.

Figure 5.3(c) shows the trends in catalyst mass activity and the activity durability. The Pt-Co catalysts all display higher mass activities than Pt catalysts on the same supports both at BOL and after durability testing. There is also a strong trend of higher mass activity with increasing support porosity, before and after cycling, despite generally similar ECSA and particle sizes. This is consistent with prior results, and reflects the detrimental effect of adsorbed ionomer, which can be limited on porous supports with Pt surfaces embedded in pores.[30–33] The specific activity of the catalysts, shown in Figure 5.3(d), reflects the same trends with support porosity and metal composition. The Pt catalysts all display a trend of increasing SA after durability testing, as previous researchers have observed[9], which is at least partly the result of increasing particle size.[10] This counteracts some of the loss in mass activity caused by the decrease in ECSA. The Pt-Co catalysts either maintain a stable SA after stability testing, in the cases of Pt-Co/HSC and Pt-Co/AB, or lose SA, in the case of Pt-Co/Vu. The Pt-Co catalysts experience a smaller increase in particle sizes relative to the Pt catalysts, as will be shown below, which would provide a smaller increase to their SA that is likely counteracted by the effect of Co losses. After the full 30k cycle durability test, the Pt and Pt-Co catalysts tend to converge to similar SA values on the same support, likely because of the more rapidly increasing particle size for Pt catalysts and Co loss from Pt-Co catalysts.

Because ECSA losses after durability testing are responsible for most of the mass activity degradation, as well as loss in high power performance, it is important to understand the mechanisms and develop strategies for mitigating ECSA loss. The following sections will focus on

139

understanding mechanisms through microscopic structural characterization and explaining the improved ECSA retention of the catalysts with more porous supports.

5.4.3 EDXS Quantification of Pt Mass in Pt Band

Accounting for the observed ECSA loss in terms of the catalyst and electrode microstructure requires quantification of both Pt mass losses and catalyst coarsening, as discussed in the introduction. The fraction of Pt mass lost by migrating into the membrane and redepositing in the Pt band after 30K cycles was measured using STEM EDXS mapping in cross-sectional MEA samples, as shown in Figure 5.4.
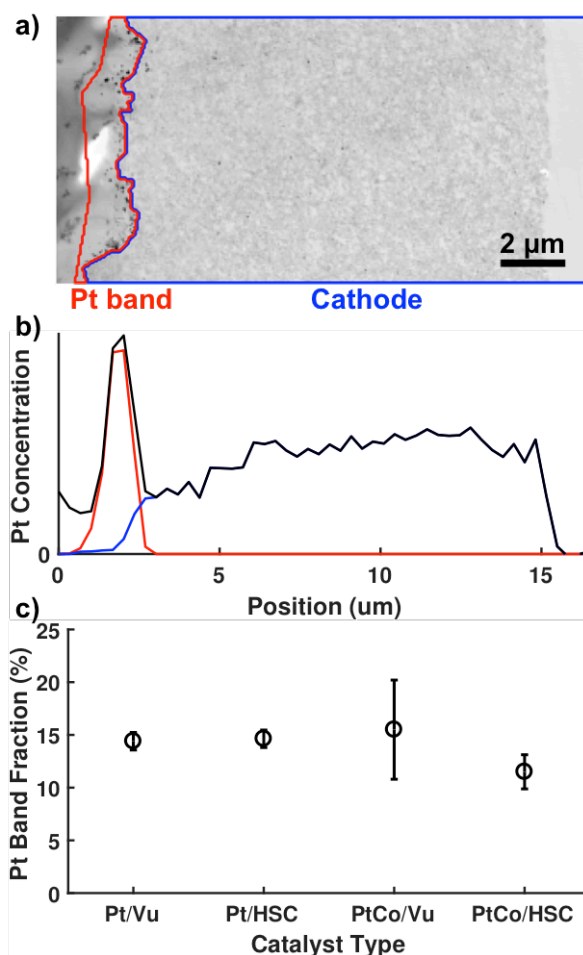
Figure 5.4: Quantification of Pt fraction in Pt band in end of life MEAs from STEM EDXS mapping. (a) Simultaneous bright field STEM image of cathode in EOL Pt/HSC sample, with masks selecting cathode and Pt band outlined in blue and red, respectively. (b) Profile of Pt concentration for the map in (a), with the black line showing all Pt signal, and the red and blue lines showing Pt signal from within the Pt band and cathode masks, respectively. (c) Comparison of average fraction of Pt found in the Pt band for different samples. Error bars represent one standard error of the mean.

Because the catalyst-targeted AST was conducted with hydrogen in the anode and nitrogen in the cathode, the Pt band forms in the membrane immediately beyond the cathode-membrane interface[16,18]. The cathode-membrane interface was observed to have micron-scale roughness, and so spectrum imaging with sufficient spatial resolution to identify the interface and separate Pt in

the membrane from Pt remaining in the cathode was necessary. Fortunately, the Pt particles that make up the Pt band are very large (tens of nanometers) and often cubic[13,50], and are thus easily distinguished from catalyst particles in the cathode based on their morphology.

To measure the relative amounts of Pt in the Pt band and remaining in the cathode, the Pt signal was integrated in each region of the EDXS maps, selected as shown in for a representative example in Figure 5.4(a). Figure 5.4(b) shows the vertically integrated profile of Pt in the map (black) along with the profile of Pt in the Pt band (red) and in the cathode (blue). A gradient in the Pt concentration is visible in the cathode region, with less Pt remaining in the cathode in regions closer to the membrane. This general pattern in Pt distribution has been reported in previous studies[8,13,14] and was observed in all EOL MEA samples analyzed. Such a distribution is expected due to diffusion of dissolved Pt in the electrode where the membrane acts as a "sink" where dissolved Pt becomes permanently deposited after chemical reduction by crossed-over hydrogen. For EOL Pt-Co samples, the cobalt distribution within the cathode follows the same profile as the Pt distribution, resulting in a Pt-Co composition that is roughly constant across the electrode (Figure 5.5).
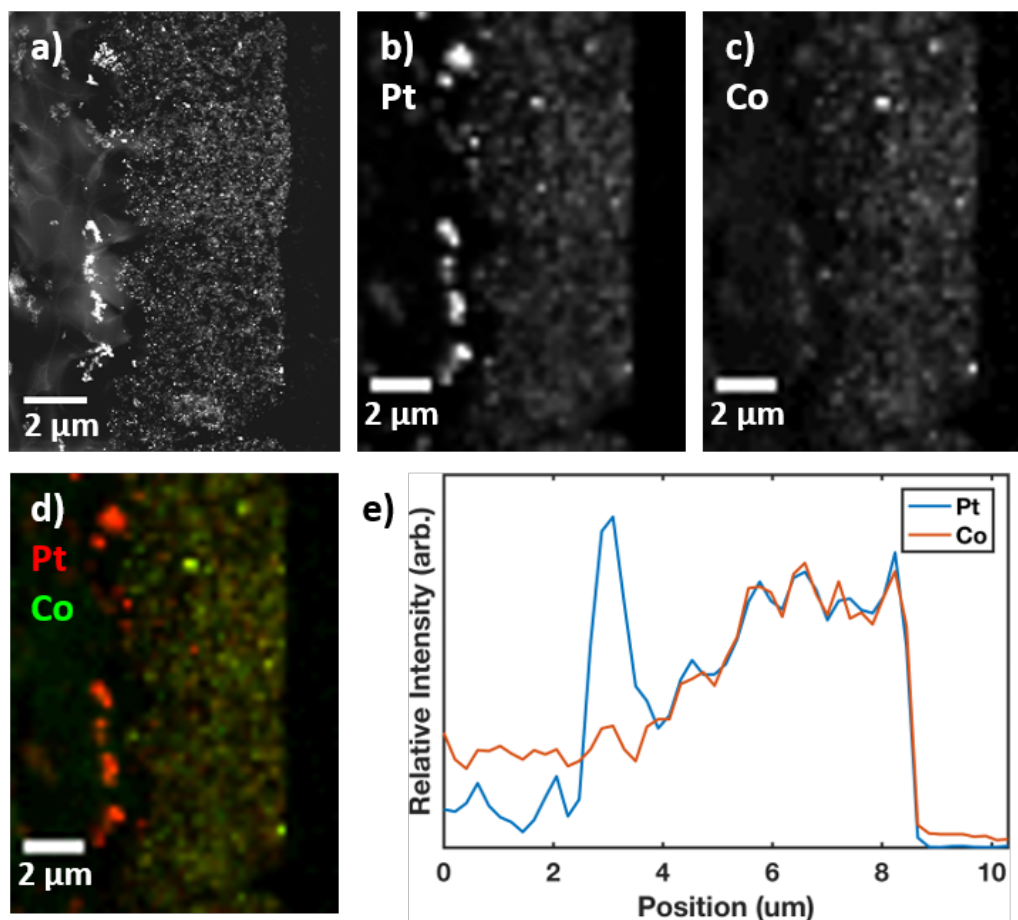
Figure 5.5: EDXS composition map of the cathode in EOL Pt-Co/Vu, oriented with the membrane to the left. (a) ADF STEM image of the region acquired before EDXS map acquisition. Composition maps for Pt (b) and Co (c) shown in greyscale and as a color composite (d) with Pt in red, and Co in green. (e) Composition profiles produced by summing the Pt and Co composition maps in the vertical direction.

To quantify the fraction of Pt in the Pt band, we integrate all of the Pt signal in the Pt band region and divide by the total Pt signal in both the cathode and the Pt band. A comparison of the fraction of Pt in the Pt band for different catalysts is shown in Figure 5.4(c). Very little variation in mass loss was observed between the samples, with all showing approximately 15% of Pt in the Pt band. Pt-Co/HSC may show slightly less Pt mass loss at ~12%, although this is a small difference

143

and not significant at the 2σ level. Separate measurements by electron probe micro-analysis and ICP support this finding with ~14% of Pt mass loss to the membrane regardless of catalyst and support types.

Considering that the catalysts in this study were selected to control for the known effects of particle size on the Pt dissolution rate, this finding suggests that the amount of Pt that migrates into the membrane is generally insensitive to the morphology of the carbon support. This may imply that the rate of Pt dissolution is very similar between the catalysts as well. Although it may be expected that the Pt-Co catalysts would experience less Pt dissolution due to their larger particle size, the presence of Co in the alloy may also facilitate the dissolution of Pt atoms. This finding suggests that other macroscopic factors such as electrode thickness, Pt^{2+} diffusion, and redeposition rates dominate.

5.4.4 Catalyst Particle Morphology and Particle Size Distribution

ADF STEM imaging of cathode catalyst particles in MEA cross-sections was performed to investigate the extent and mechanisms of catalyst coarsening. Figure 5.6 shows representative STEM images comparing the catalyst morphology for the different catalysts before and after voltage cycling, all with the same field of view.
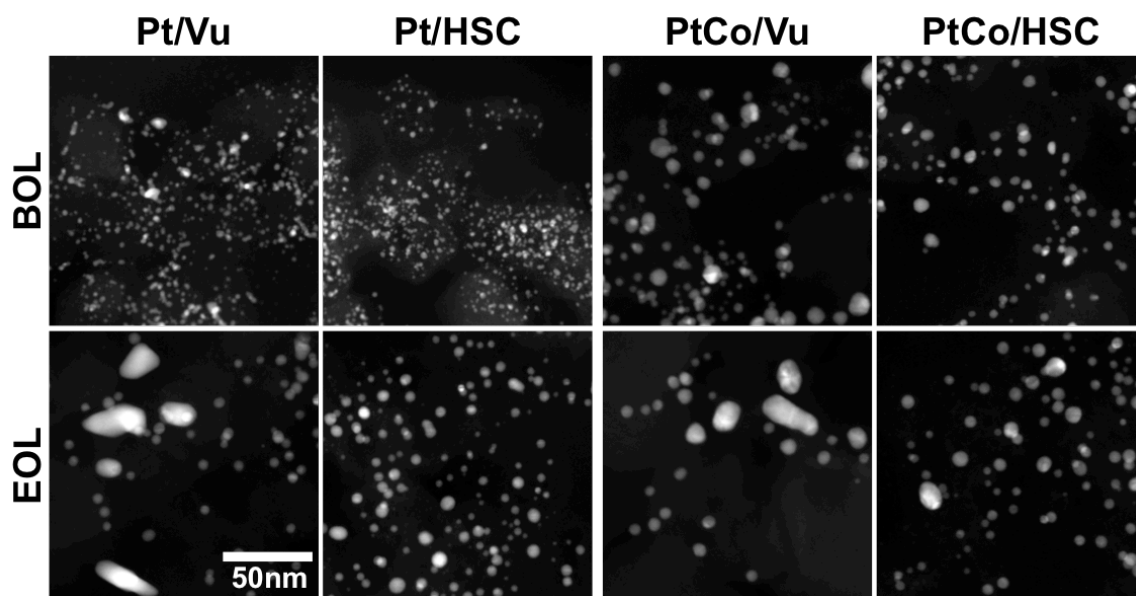
Figure 5.6: Representative STEM images taken in MEA cathodes at beginning of life (BOL, top) and end of life (EOL, bottom) with various catalysts (left to right: Pt/Vu, Pt/HSC, Pt-Co/Vu, Pt-Co/HSC), showing changes in particle sizes and morphology after electrochemical aging. All images are at the same scale.

At beginning of life, the Pt catalysts (Figure 5.6, left half) both generally show a small 2-3nm particle size and an overall good dispersion of particles on the carbon support, although Pt/Vu appears to have slightly more irregular particle shapes, while the particles in Pt/HSC are generally roughly spherical. After voltage cycling, both catalysts experience a clear growth in particle sizes, although the morphologies of the Pt particles become quite distinct. In Pt/Vu, some particles retain a relatively small size around 5 nm and a spherical morphology, but a minority of very large, irregular particles also forms. By contrast, in Pt/HSC essentially all particles retain a generally spherical morphology, good dispersion, and relatively small size around 5 nm.

A similar trend is evident for the Pt-Co catalysts (Figure 5.6, right half). Both Pt-Co/Vu and Pt-Co/HSC start with roughly spherical particles that are somewhat larger than those in their pure Pt counterparts, around 4-5 nm. Relative to their larger initial sizes, the coarsening of the Pt-Co

catalysts appears somewhat subtler. However, Pt-Co/Vu shows the same formation of large, irregular particles and growth of the smaller, spherical particles observed in Pt/Vu. Pt-Co/HSC shows a similar uniform growth of spherical particles to Pt/HSC.

The difference in morphology between the large, irregular particles observed on Vulcan-supported catalysts and the smaller, spherical particles observed on all catalysts at end of life suggests a different primary coarsening mechanism for the two populations. The irregular shapes of the larger particles intuitively suggest formation by coalescence, while the uniform growth of particles maintaining a spherical geometry suggests coarsening by Ostwald ripening. A difference in the prevalence of these mechanisms on the different carbon supports may be expected based on the difference in primary porosity between the carbons.
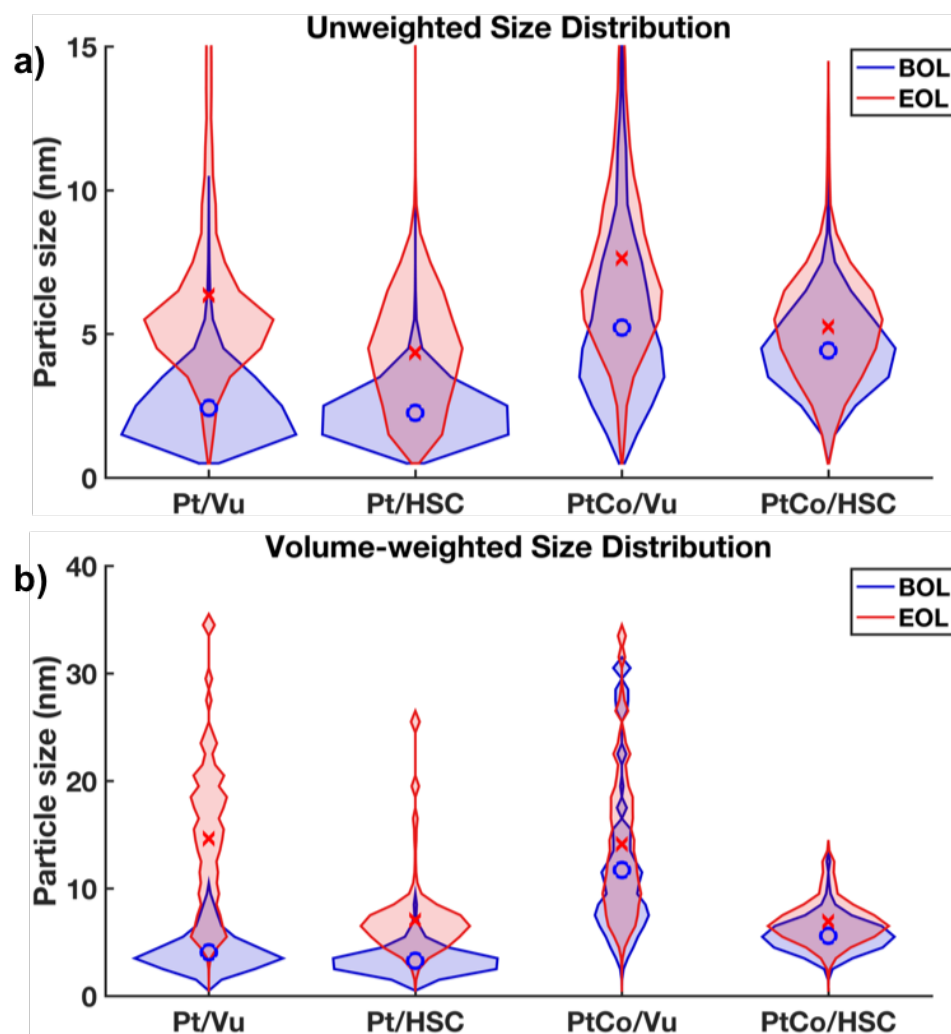
Figure 5.7: Violin plots of particle size distributions measured with STEM in MEA cathodes with different catalysts at beginning of life (blue) and end of life (red). The distributions in (a) are simple numerical histograms, while the distributions in (b) include a volume weighting factor to show the distribution of mass between particles of different sizes. Blue 'o' markers and red 'x' markers show the mean size for BOL and EOL distributions.

Further insight into the possible coarsening mechanisms and impacts for the catalyst performance can be gained by examining and comparing statistical size distributions for the different catalysts before and after cycling. Figure 5.7 shows violin plots of the particle size distributions for each sample measured using automated image analysis of STEM images including

thousands of nanoparticles per sample from a variety of electrode locations. (Tabulated values describing the size distributions are available in the published supplemental information.[1]) A local diameter approximation was used instead of the more common spherical approximation to allow irregular shaped particles to be included in the analysis. While some other studies have deliberately excluded irregular particles formed on the carbon support[13], this omission precludes study of the mechanisms forming these particles and their consequences.

Figure 5.7(a) shows conventional size distributions for each sample, which are equivalent to histograms showing the number of particles of a given size. The Pt/Vu and Pt/HSC catalysts both start with a relatively narrow size distribution, with most particles in the size range of 2-3 nm. After cycling, both distributions see an increase in the mean size and a broadening of the distribution, but the distribution shapes also change dramatically. The size distribution for Pt/Vu develops a long tail of large particles above 10 nm, while the distribution for Pt/HSC remains roughly symmetric, with almost no particles above 10 nm. Similar trends hold for the Pt-Co catalysts, although the Pt-Co/Vu distribution begins with a significant tail of larger particles. The distribution tail of larger particles in Pt-Co/Vu grows after electrochemical cycling. The Pt-Co/HSC distribution has a more uniform upward shift after cycling, remaining symmetric, as the Pt/HSC distribution does, although with a smaller overall shift relative to its larger starting size.

Granqvist and Buhrman noted that coalescence and Ostwald ripening are theoretically expected to produce different shapes in the particle size distribution.[24] Coalescence is expected to produce a lognormal-like size distribution with a heavy tail of larger particles. Ostwald ripening, by contrast, does not produce a tail of larger particles. Granqvist and Buhrman predicted that distributions formed by Ostwald ripening would have a heavy tail of smaller particles, although the relatively low stability of smaller Pt particles[21] under typical fuel cell conditions may remove this feature, which has not been observed for fuel cell catalysts, resulting in a roughly symmetric distribution.

148

Interpreting our observed size distributions with this framework suggests that the HSC-supported catalysts do not experience significant coalescence, but instead coarsen primarily by Ostwald ripening. The growth of heavy tails of large particles in the Vulcan-supported catalysts suggests that they do experience significant coarsening by coalescence. The shift in the distribution peaks to larger sizes and the loss of very small particles suggests that the Vulcan-supported catalysts coarsen by Ostwald ripening as well.

A plausible structural explanation of this outcome is that solid carbon supports like Vulcan permit the particles on their exterior surfaces to migrate and collide, while porous supports like HSC constrain the particles embedded in their interior pores, limiting their migration and coalescence. The pores in HSC have previously been shown to have a constrictive, bottleneck geometry.[34] Furthermore, the porous structure of HSC supports a better dispersion of particles both inside and outside the carbon support, resulting in larger interparticle distances compared to Vulcan.[28] This is expected to lower the probability that particle migration leads to particle collision and coalescence. Ostwald ripening, however, requires only the presence of dissolved Pt ions to be electrochemically redeposited. The consistency of the Pt band formation across catalysts shown in the previous section suggests that the different carbon supports result in similar rates of Pt dissolution, and likely similar degrees of Ostwald ripening. The greater interparticle spacing on HSC may also slow Ostwald ripening by lowering the rate of Pt redeposition on neighboring particles.

The heavy tail in the BOL Pt-Co/Vu size distribution is likely formed by particle coalescence at the higher temperatures required for alloy synthesis. It is intuitively reasonable to expect that the carbon morphology should impact thermal coalescence and electrochemical coalescence in a similar manner, with solid Vulcan permitting particle migration and coalescence and porous HSC constraining it. It is notable that the larger particles in Pt-Co/Vu at beginning of life do not have

irregular shapes like those formed during electrochemical cycling, possibly because the high temperature in synthesis provides a stronger driving force for particle reshaping.

It is notable also that there is significant convergence after cycling in the particle sizes between the Pt catalysts and the Pt-Co catalysts. The Pt catalysts start with much smaller typical particle sizes than the Pt-Co catalysts but end with only slightly smaller particle sizes. This is attributable in part to the much higher stability of particles around 5 nm relative to particles around 2 nm, which would result in much faster coarsening by Ostwald ripening for the smaller Pt particles.[21,27]

In addition to the conventional size distributions shown in Figure 5.7(a), it can be useful to examine volume-weighted size distributions, which show the distribution of Pt mass between particles of different sizes, shown in Figure 5.7(b). This clarifies the consequences of the formation of large particle tails in the distributions for Vulcan-supported size distributions. Although the larger particles that form on these catalysts are relatively few in number, the cubic scaling of volume with particle diameter means that these particles can account for a large fraction of the Pt mass in the catalyst. For instance, for EOL Pt/Vu and EOL Pt-Co/Vu, particles larger than 15 nm in diameter are so few in number that they are difficult to present in conventional number-weighted size distributions such as in Figure 5.7(a). However, these large particles account for roughly half of the Pt mass, as visible in the volume-weighted size distributions in Figure 5.7(b), and are therefore far from negligible.

5.4.5   Identifying Particle Coalescence with EELS Composition Mapping

Direct evidence of the coarsening mechanism for Pt-Co catalysts can be obtained by using composition mapping by electron energy loss spectroscopy to reveal the core-shell structure of particles formed after voltage cycling.[23] After dealloying or exposure to an acidic environment, Pt-

Co particles form a shell of Pt surrounding a Pt-Co core. Spongey or hollow structures may also form in large or Co-rich particles, especially if the particle diameter is around 10 nm or greater.[51] Such structures were observed only rarely for the catalysts in this study, possibly because of the relatively narrow BOS size distributions, and were not investigated in depth. Particle size growth by Ostwald ripening (or additional Co leaching) causes the thickness of the Pt shell to grow. Pt-Co particles that collide and coalesce retain their Pt-Co cores, separated by a Pt layer. Particles with multiple Pt-Co cores contained within the same Pt envelope can thus be identified as having undergone coalescence.[23]
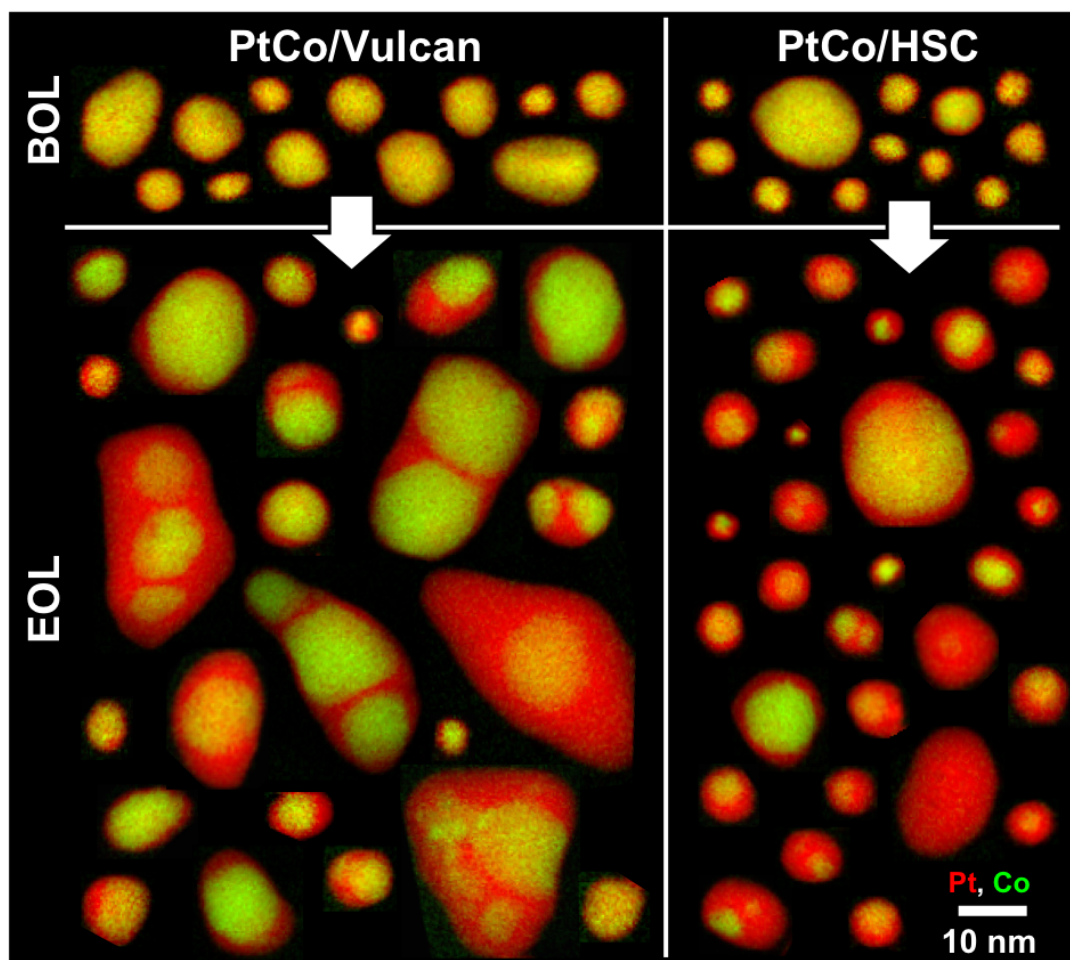
Figure 5.8: EELS composition maps of Pt-Co catalysts before (BOL, top) and after (EOL, bottom) 30K cycle catalyst stability test. The Pt $M_{4,5}$ signal is shown in red and the Co $L_{2,3}$ signal is shown in green, combining to yellow. In Pt-Co/Vu (left) multi-core, coalesced particles are common, especially forming the largest particles, while in Pt-Co/HSC multi-core particles are rare.

Figure 5.8 shows EELS composition mapping of Pt-Co/Vu and Pt-Co/HSC catalysts before and after voltage cycling. At beginning of life, both catalysts show very similar structure, with uniform, thin (~0.5 nm) Pt shells – formed during dealloying – surrounding generally uniform Pt-Co cores. After 30K voltage cycles, thicker Pt shells, due to either Ostwald ripening or Co leaching, have formed on particles in both catalysts, but distinct differences are apparent in their core shell

structure. In EOL Pt-Co/Vu many particles contain multiple Pt-Co cores, again indicating that coalescence is common on the Vulcan carbon support. The large, irregular particles in EOL Pt-Co/Vu are especially likely to contain multiple cores providing evidence that the large irregular particles described in previous sections are formed by particle coalescence. Among the particles mapped in EOL Pt-Co/Vu, ~35% of the particles larger than the median diameter of ~7 nm had more than one core, while none of the particles smaller than 7 nm did. Many of the larger particles in EOL Pt-Co/Vu that contain only one core are likely formed by thermal coalescence during the catalyst synthesis and make up the heavy tail of larger particles already present at BOL, as discussed in the previous section.

By contrast, multi-core particles are much less common in Pt-Co/HSC, indicating that coalescence is rare on the porous HSC support. Only two of the 30 EOL Pt-Co/HSC particles shown in Figure 5.8 have more than one core, and these particles are also not unusually large. With so few observed occurrences it is not possible to precisely quantify the frequency of coalescence, but it appears that coalescence is not a significant coarsening mechanism on the HSC support.

One relevant question is whether dissolution and redeposition occurs differently for Pt-Co particles within the carbon pores from the ones on the carbon exterior in Pt-Co/HSC. Without ionomer contacting particles on the carbon interior, factors impacting degradation such as proton activity and chemical/electrochemical potentials are not well understood. To investigate possible differences in the degradation of particles inside and outside the HSC carbon support, we performed an experiment combining 3D electron tomography and EELS mapping at the same location in an EOL Pt-Co/HSC sample (Figure 5.9). After tomography data acquisition, EELS maps were acquired for 37 Pt-Co particles, which were categorized as inside or outside the carbon support using the tomography reconstruction (Figure 5.9a,b). A representative subset of 21 of these EELS maps is shown in Figure 5.9a. A histogram of the shell thicknesses for the EOL Pt-Co/HSC

tomography sample is shown in Figure 5.9c. The BOL shell thickness is very uniform, and we will assume that any difference between BOL Pt-Co particles inside and outside the carbon is negligible. The shell thickness histograms are well-fit by lognormal distributions, which show a significant change in the shell thicknesses in BOL Pt-Co/HSC (from the EELS maps shown in Figure 5.8) to those in EOL Pt-Co/HSC.

The average shell thickness roughly doubles after electrochemical cycling, from about 0.5 nm to 1.0 nm. However, no significant difference was observed between the distributions of shell thicknesses for particles inside and outside the carbon support. This leads to the conclusion that both interior and exterior particles in Pt-Co/HSC experience electrochemical conditions leading to similar aging. Any differences in the degradation processes due to differences in the particles' environment, such as contact with the ionomer, lead to relatively small changes in the Pt-Co shell structure that were not significant enough to be observed in this study.
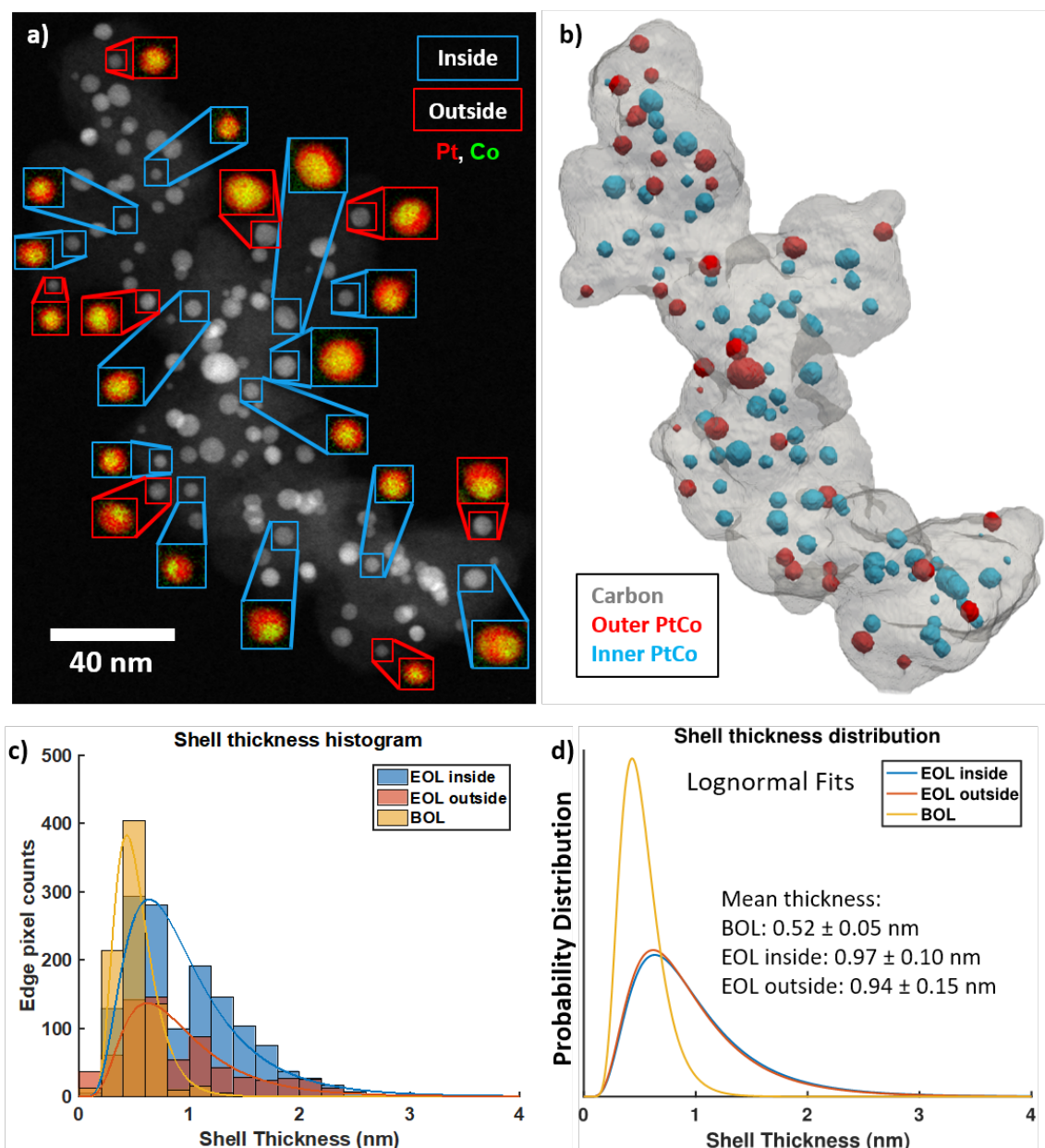
Figure 5.9: Combined EELS and electron tomography analysis of EOL Pt-Co/HSC catalyst. (a) ADF STEM image of catalyst aggregate chosen for analysis, with Pt-Co (red-green) EELS map overlays. Overlay line colors indicate particle positions relative to the carbon support, i.e. inside (blue) and outside (red) the carbon. (b) 3D surface rendering of electron tomography used for determining catalyst particle positions, showing carbon (grey), outer Pt-Co particles (red), and inner Pt-Co particles (blue). (c) Histogram of Pt shell thickness at Pt-Co particle edge pixels in EELS maps for inner and outer particles in EOL Pt-Co/HSC (blue, red respectively) and all

155

particles in BOL Pt-Co/HSC (yellow) with lognormal distribution fits. (d) Lognormal probability distributions of Pt shell thickness derived from fits.

The increased thickness of Pt shells observed for both Pt-Co catalysts implies some degree of Co loss. EDXS measurements made over the entire cathode (see the supplemental information for additional details) indicated that the relative Co content of the Pt-Co/HSC catalyst decreased by about 46%, while the relative Co content of the Pt-Co/Vu catalyst decreased by about 31%. The smaller Co loss for Pt-Co/Vu can be attributed to its larger average particle size, which results in more stable surfaces and a lower fraction of the volume near the particle surface where Co may dissolve more easily. It is notable that Pt-Co/HSC shows better specific activity retention than Pt-Co/V (Figure 5.3(d)) given its more severe cobalt loss. Earlier studies have shown that enhanced specific activity can be maintained if Pt shell thickness growth is very small.[11,52] The thicker Pt layers formed in Pt-Co/V at the concave junctions between coalesced particles, as reported by Xin, Mundy, et al.[23], may result in more severe loss of surface strain. The relationship between core-shell structure and surface strain is the subject of ongoing investigation.

5.4.6   Quantitative Account of ECSA Degradation

The quantitative STEM measurements of Pt mass loss to the Pt band and coarsening of the particle size distributions, presented in previous sections, may be considered together to attribute the observed ECSA loss between the different degradation mechanisms. Figure 5.10 shows the retained fraction of Pt mass in the electrode (blue triangles) and the retained specific surface area (SSA) of the catalyst in the electrode (green squares) measured with STEM techniques. Because the active catalyst surface area is the product of the SSA and the electrically connected Pt mass, the expected surface area retention after Pt mass loss and SSA loss is the product of the Pt mass retention and the catalyst SSA retention. The retained surface area calculated from STEM

measurements (red circles), is quantitatively consistent with the ECSA retention observed electrochemically (black circles). This implies that Pt migration to the membrane and catalyst coarsening together account for all of the ECSA loss within the margin of error, and other mechanisms, such as mass loss in the cathode by particle detachment or chemical redeposition, are negligible.
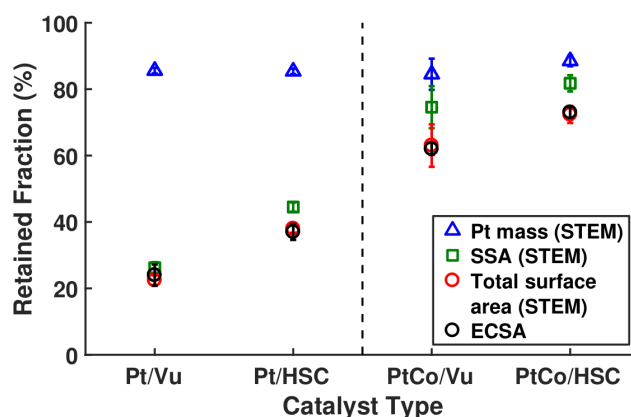
Figure 5.10: Comparison of observed ECSA retention (black circles) with quantitative STEM measurements of cathode Pt mass retention (blue triangles) and specific surface area retention (green squares) after 30k voltage cycles. The losses from Pt mass loss to the Pt band and SSA loss due to coarsening may be combined by taking the product of the mass retention and SSA retention, which is quantitatively consistent with the ECSA retention. Error bars represent one standard error of the mean.

The more severe coarsening and SSA loss of Vulcan-supported catalyst can be explained mechanistically by the results of the previous sections. Vulcan-supported catalysts suffer significant coarsening through both coalescence and Ostwald ripening mechanisms, while the porous morphology of HSC protects against coalescence, leaving only Ostwald ripening as a significant coarsening mechanism for HSC-supported catalysts. This results in a significantly improved ECSA retention for HSC-supported catalysts, leading to superior retention of mass activity and high power performance (Figure 5.1, Figure 5.3).

The porous morphology of HSC that protects against particle coalescence also appears to result in superior activity by limiting ionomer adsorption, suggesting that improving HSC supports to limit their deficiencies may be a promising direction for future research. Success has already been reported in designing more accessible HSC supports that reduce the transport resistance associated with transport inside support micropores.[6] Efforts directed toward developing more graphitic, carbon-corrosion-resistant supports with a similar porous morphology may also be valuable. Mitigation of coarsening due to Ostwald ripening will likely require different approaches. The similarity of Pt band formation across the catalysts studied here suggests that the rate of Pt dissolution, and likely also Ostwald ripening, is similar regardless of support morphology. Efforts to improve the chemical stability of alloy catalysts, such as chemical ordering[53], may prove effective at mitigating Ostwald ripening as well.

5.5   Conclusion

This investigation explored the role of the carbon support morphology in determining the degradation mechanisms occurring for Pt and Pt-Co fuel cell cathode catalysts. Electrochemical comparison of MEAs using a porous carbon support (HSC), a solid carbon support (Vulcan), and an intermediate carbon support (acetylene black) showed that the ECSA retention after a catalyst-targeting voltage cycling test tends to improve with increasing support porosity.

The mechanisms of ECSA loss underlying this trend were investigated using STEM, EDXS, and EELS measurements in post-mortem cross-section samples of the MEAs with HSC and Vulcan-supported Pt and Pt-Co catalysts. For all of these catalysts, EDXS quantification found similar Pt mass migrated from the electrode to the Pt band in the membrane: around 15%. The degree of catalyst coarsening, however, varied significantly between the different catalysts. Vulcan-supported catalysts showed more severe SSA loss through coarsening, especially through

the formation of large, irregularly shaped particles. Three lines of evidence indicate that these larger particles are formed primarily by coalescence: their irregular morphology, the lognormal-like size distributions, and the frequent presence of multiple Pt-Co cores in these particles. By contrast, the HSC-supported catalysts contained few large, irregular particles, maintained more symmetric size distributions, and rarely had multi-core Pt-Co particles. Catalysts on both types of carbon supports also showed growth in the size of smaller, more spherical particles. These smaller particles showed an increase in Pt shell thickness in EELS measurements of Pt-Co samples, indicating that they grew through Ostwald ripening. The electrochemically observed ECSA loss was quantitatively consistent with the loss that would be expected based on STEM measurements of Pt mass in the Pt band and catalyst coarsening, indicating that these are the only significant degradation mechanisms under these test conditions.

Together, these lines of evidence demonstrate that Ostwald ripening takes place as a significant coarsening mechanism for all catalysts, regardless of the support morphology, while particle coalescence only contributes significantly for catalysts with solid carbon supports. Porous carbon supports thus suppress coalescence, likely by restricting the migration of particles embedded in carbon pores and providing greater interparticle spacing. This is an encouraging result, as it demonstrates that design of the catalyst support morphology can provide an effective strategy for mitigating catalyst degradation through coalescence.

5.6   References

[1] E. Padgett, V. Yarlagadda, M.E. Holtz, M. Ko, B.D.A. Levin, R.S. Kukreja, J.M. Ziegelbauer, R.N. Andrews, J. Ilavsky, A. Kongkanand, and D.A. Muller, J. Electrochem. Soc. **166**, F198 (2019).
[2] H.A. Gasteiger, S.S. Kocha, B. Sompalli, and F.T. Wagner, Appl. Catal. B Environ. **56**, 9 (2005).

[3] A. Kongkanand and M.F. Mathias, J. Phys. Chem. Lett. **7**, 1127 (2016).

[4] G.S. Harzer, J.N. Schwämmlein, A.M. Damjanović, S. Ghosh, and H.A. Gasteiger, J. Electrochem. Soc. **165**, F3118 (2018).

[5] A.Z. Weber and A. Kusoglu, J. Mater. Chem. A **2**, 17207 (2014).

[6] V. Yarlagadda, M.K. Carpenter, T.E. Moylan, R.S. Kukreja, R. Koestner, W. Gu, L. Thompson, and A. Kongkanand, ACS Energy Lett. **3**, 618 (2018).

[7] R.K. Ahluwalia, X. Wang, J.-K. Peng, N.N. Kariuki, D.J. Myers, S. Rasouli, P.J. Ferreira, Z. Yang, A. Martinez-Bonastre, D. Fongalland, and J. Sharman, J. Electrochem. Soc. **165**, F3316 (2018).

[8] A. Kneer, J. Jankovic, D. Susac, A. Putz, N. Wagner, M. Sabharwal, and M. Secanell, J. Electrochem. Soc. **165**, F3241 (2018).

[9] F.T. Wagner, S.G. Yan, and P.T. Yu, in *Handb. Fuel Cells* (John Wiley & Sons, Ltd, Chichester, UK, 2010).

[10] M. Shao, A. Peles, and K. Shoemaker, Nano Lett. **11**, 3714 (2011).

[11] Q. Jia, J. Li, K. Caldwell, D.E. Ramaker, J.M. Ziegelbauer, R.S. Kukreja, A. Kongkanand, and S. Mukerjee, ACS Catal. **6**, 928 (2016).

[12] D.D. Papadias, R.K. Ahluwalia, N. Kariuki, D. Myers, K.L. More, D.A. Cullen, B.T. Sneed, K.C. Neyerlin, R. Mukundan, and R.L. Borup, J. Electrochem. Soc. **165**, F3166 (2018).

[13] P.J. Ferreira, G.J. la O', Y. Shao-Horn, D. Morgan, R. Makharia, S. Kocha, and H.A. Gasteiger, J. Electrochem. Soc. **152**, A2256 (2005).

[14] S. Chen, H.A. Gasteiger, K. Hayakawa, T. Tada, and Y. Shao-Horn, J. Electrochem. Soc. **157**, A82 (2010).

[15] A. Ohma, S. Yamamoto, and K. Shinohara, ECS Trans. **11**, 1181 (2007).

[16] J. Zhang, B.A. Litteer, W. Gu, H. Liu, and H.A. Gasteiger, J. Electrochem. Soc. **154**, B1006 (2007).

[17] P. Yu, M. Pemberton, and P. Plasse, J. Power Sources **144**, 11 (2005).

[18] W. Bi, G.E. Gray, and T.F. Fuller, Electrochem. Solid-State Lett. **10**, B101 (2007).

[19] Y. Shao-Horn, W.C. Sheng, S. Chen, P.J. Ferreira, E.F. Holby, and D. Morgan, Top. Catal. **46**, 285 (2007).

[20] K. More, R. Borup, and K. Reeves, ECS Trans. **3**, 717 (2006).

[21] E.F. Holby, W. Sheng, Y. Shao-Horn, and D. Morgan, Energy Environ. Sci. **2**, 865 (2009).

[22] C.E. Carlton, S. Chen, P.J. Ferreira, L.F. Allard, and Y. Shao-Horn, J. Phys. Chem. Lett. **3**, 161 (2012).

[23] H.L. Xin, J.A. Mundy, Z. Liu, R. Cabezas, R. Hovden, L.F. Kourkoutis, J. Zhang, N.P. Subramanian, R. Makharia, F.T. Wagner, and D. a Muller, Nano Lett. **12**, 490 (2012).

[24] C.G. Granqvist and R.A. Buhrman, J. Catal. **42**, 477 (1976).

[25] M.S. Wilson, F.H. Garzon, K.E. Sickafus, and S. Gottesfeld, J. Electrochem. Soc. **140**, 2872 (1993).

[26] C. Yu, E.F. Holby, R. Yang, M.F. Toney, D. Morgan, and P. Strasser, ChemCatChem **4**, 766 (2012).

[27] J.A. Gilbert, N.N. Kariuki, X. Wang, A.J. Kropf, K. Yu, D.J. Groom, P.J. Ferreira, D. Morgan, and D.J. Myers, Electrochim. Acta **173**, 223 (2015).

[28] B.T. Sneed, D.A. Cullen, K.S. Reeves, O.E. Dyck, D.A. Langlois, R. Mukundan, R.L. Borup, and K.L. More, ACS Appl. Mater. Interfaces **9**, 29839 (2017).

[29] X. Tuaev, S. Rudi, and P. Strasser, Catal. Sci. Technol. **6**, 8276 (2016).

[30] A. Kongkanand, V. Yarlagadda, T.R. Garrick, T.E. Moylan, and W. Gu, ECS Trans. **75**, 25 (2016).

[31] R. Subbaraman, D. Strmcnik, A.P. Paulikas, V.R. Stamenkovic, and N.M. Markovic,

ChemPhysChem **11**, 2825 (2010).

[32] S.S. Kocha, J.W. Zack, S.M. Alia, K.C. Neyerlin, and B.S. Pivovar, ECS Trans. **50**, 1475 (2013).

[33] K. Shinozaki, Y. Morimoto, B.S. Pivovar, and S.S. Kocha, J. Power Sources **325**, 745 (2016).

[34] E. Padgett, N. Andrejevic, Z. Liu, A. Kongkanand, W. Gu, K. Moriyama, Y. Jiang, S. Kumaraguru, T.E. Moylan, R. Kukreja, and D.A. Muller, J. Electrochem. Soc. **165**, F173 (2018).

[35] US Department of Energy Fuel Cell Technologies Office, *Multi-Year Research, Development, and Demonstration Plan: 3.4 Fuel Cells* (2017).

[36] T.R. Garrick, T.E. Moylan, M.K. Carpenter, and A. Kongkanand, J. Electrochem. Soc. **164**, F55 (2017).

[37] J. Ilavsky, P.R. Jemian, A.J. Allen, F. Zhang, L.E. Levine, and G.G. Long, J. Appl. Crystallogr. **42**, 469 (2009).

[38] J. Ilavsky, J. Appl. Crystallogr. **45**, 324 (2012).

[39] J. Ilavsky and P.R. Jemian, J. Appl. Crystallogr. **42**, 347 (2009).

[40] C.T. Rueden, J. Schindelin, M.C. Hiner, B.E. DeZonia, A.E. Walter, E.T. Arena, and K.W. Eliceiri, BMC Bioinformatics **18**, 529 (2017).

[41] T.F. Chan and L.A. Vese, IEEE Trans. Image Process. **10**, 266 (2001).

[42] N. Macauley, D.D. Papadias, J. Fairweather, D. Spernjak, D. Langlois, R. Ahluwalia, K.L. More, R. Mukundan, and R.L. Borup, J. Electrochem. Soc. **165**, F3148 (2018).

[43] L. Castanheira, W.O. Silva, F.H.B. Lima, A. Crisci, L. Dubau, and F. Maillard, ACS Catal. **5**, 2184 (2015).

[44] F. Forouzandeh, X. Li, D.W. Banham, F. Feng, S. Ye, and V. Birss, J. Electrochem. Soc. **162**, F1333 (2015).

[45] P.T. Yu, W. Gu, R. Makharia, F.T. Wagner, and H.A. Gasteiger, in *ECS Trans.* (ECS, 2006), pp. 797–809.

[46] F. Forouzandeh, X. Li, D.W. Banham, F. Feng, S. Ye, and V. Birss, J. Electrochem. Soc. **165**, F3230 (2018).

[47] T. Ito, U. Matsuwaki, Y. Otsuks, M. Hatta, K. Hayakawa, K. Maysutani, T. Tada, and H. Jinnai, Electrochemistry **79**, 374 (2011).

[48] T. Ito, U. Matsuwaki, Y. Otsuka, G. Katagiri, M. Kato, K. Matsubara, Y. Aoyama, and H. Jinnai, in *Handb. Fuel Cells* (John Wiley & Sons, Ltd, Chichester, UK, 2010).

[49] K. Shinozaki, H. Yamada, and Y. Morimoto, J. Electrochem. Soc. **158**, B467 (2011).

[50] P.J. Ferreira and Y. Shao-Horn, Electrochem. Solid-State Lett. **10**, B60 (2007).

[51] B.T. Sneed, D.A. Cullen, R. Mukundan, R.L. Borup, and K.L. More, J. Electrochem. Soc. **165**, F3078 (2018).

[52] K.M. Caldwell, D.E. Ramaker, Q. Jia, S. Mukerjee, J.M. Ziegelbauer, R.S. Kukreja, and A. Kongkanand, J. Phys. Chem. C **119**, 757 (2015).

[53] D. Wang, H.L. Xin, R. Hovden, H. Wang, Y. Yu, D. a. Muller, F.J. DiSalvo, and H.D. Abruña, Nat. Mater. **12**, 81 (2012).

6   CONCLUSION

6.1   Summary

Hydrogen fuel cells offer a promising opportunity for clean transportation, especially for heavy-duty and long-range vehicles. Continued research and development efforts are needed to reduce the cost of fuel cell systems and avoid cost constraints from scarce materials as production scales up to high volumes. Particular focus is needed to improve the performance and durability of platinum-based catalysts to make small amounts of platinum sufficient.

Platinum-alloy (such as Pt-Co) nanoparticles supported on carbon black remain the most promising catalyst demonstrated in fuel cell devices practical for transportation applications. These catalysts provide significantly enhanced oxygen reduction kinetics compared to pure Pt because compressive strain on particles' Pt shells alters their binding strength to reaction intermediates. However, these catalysts face challenges with maintaining high performance after experiencing degrading conditions in the fuel cell and with ensuring efficient transport of reactants to the active surfaces.

Understanding the mechanisms of degradation and reactant transport is essential to strategically improving these catalysts. (Scanning) transmission electron microscopy ((S)TEM) characterization that is statistically robust is a powerful tool to guide advancement of fuel cell catalysts by connecting their synthesis, structure, and performance.

Chapter 2 presented the development of a new approach to rapid strain mapping in complex samples such as catalyst nanoparticles using scanning nanobeam electron diffraction (NBED). By transforming NBED patterns into the exit wave power cepstrum (EWPC) space, crystal structure information can be separated from complicating factors such as specimen mistilt to provide precise, dose efficient strain measurements. This method was demonstrated to be effective for fuel cell catalyst nanoparticles by producing sub-nanometer resolution strain maps, even for particles tilted far from a major zone axis.

Chapter 3 used this newly-developed strain mapping technique in combination with an analytic continuum elastic model for core-shell nanoparticles to explore strain effects impacting oxygen reduction activity in real fuel cell catalysts. We showed that strain relaxation occurs because of both lattice dislocations and gradual relaxation across the shell caused by the core-shell geometry. In the case of dislocation-free, coherent strain, the strain at the particle surface is a simple function of the relative thickness of the particle shell and the lattice mismatch, allowing the ideal surface strain to be inferred from the average composition alone. A series of Pt-Co catalysts prepared with varying shell thicknesses showed that for relatively thin shells the catalyst activity follows an Arrhenius-law trend with the expected ideal coherent surface strain, while for thicker shells the activity fell below this expectation, likely as a result of dislocations.

Chapter 4 presented an investigation[1] of the connections between the morphology of different carbon support materials, the distribution of catalyst particles on the support, and the accessibility of the catalyst to reactants for high power fuel cell performance. We used electron tomography to produce 3D, nanometer-resolution images of different catalysts and employed automated segmentation procedures to allow robust statistical analysis of the catalyst structure. By comparison to electrochemical measurements of surface area and accessibility to gas and protons for solid (Vulcan) and porous (HSC) carbon supports, we determined different reactant transport

mechanisms for catalyst particles on the support surface and embedded within carbon pores. Particles on the carbon surface are accessible to protons conduction via the ionomer, as conventionally assumed, while particles embedded in the carbon are accessible to proton conduction through water condensed in the carbon pores at relatively high humidity. These results indicate that porous carbons prevent ionomer infiltration into their interior pores, leaving the surface of interior platinum particles free from ionomer adsorption and providing these catalysts with overall higher oxygen reduction activity.

Chapter 5 continued this study of the importance of the carbon support morphology with an investigation[2] of its impact on catalyst durability. This investigation compared the degradation of Pt and Pt-Co supported on solid Vulcan carbon and porous HSC carbon using electrochemical measurements and statistical analysis of STEM images and composition maps. STEM characterization showed that the porous HSC carbon support prevented active surface area loss through coalescence of nanoparticles and was able to quantitatively explain the improved durability observed electrochemically.

Together these investigations demonstrate the powerful role that STEM nanocharacterization can play as a rigorous, quantitative tool for investigating structure and mechanisms in complex electrochemical energy materials. They have further yielded practical results to advance the development of fuel cell catalysts by explaining the advantages of porous carbon supports in catalyst activity and durability.

6.2   Future Research Directions

The successful strain characterization for complex and non-ideal samples using scanning NBED presented here opens doors to investigate strain phenomena in a wide variety of materials,

including other chemically active materials such as battery electrodes and heterogeneous catalysts, microelectronic devices, and structural materials. Thorough characterization of strain in a variety of fuel cell catalyst systems has great potential to put the science of these catalysts on firm rational footing. Descriptions of the actual strain state driving trends in catalyst activity have been a missing link, leaving the field to rely often on speculation. Contrary to some first instincts, optimized catalysts typically do not have very interesting strain effects, showing only uniform strain in thin shells that are difficult to resolve and measure quantitatively with nanobeam diffraction. Degraded catalysts, however, can host a wide variety of more interesting phenomena worth further study. Fruitful investigations would include the strain profiles in non-spherical geometries, such as uneven shells or strongly faceted particles. Strain profiles should also be investigated in particles that are formed by coalescence and contain multiple cores and grain boundaries. In addition to strain characterization with NBED, these effects could be investigated theoretically using finite element modelling without significant difficulty. Some new development of analysis software will be necessary to handle all the complexities of catalyst nanoparticles, especially techniques to extract consistent Lagrange strain across nanoparticles containing multiple crystal grains.

4D STEM data in general contains a wealth of information beyond strain and crystallography that is well worth exploring. The ongoing revolution in computational techniques such as machine learning may be useful in this space. However, applications of new techniques should be considered with a skeptical eye as there is also great potential for distracting hype of apparently magical algorithms.

The significant improvements in oxygen reduction activity and durability for porous carbon supports investigated in Chapter 4 and Chapter 5 indicate that the development of new carbon supports may yield further advances for fuel cell catalysts. Some success has already been met on this front through the development of porous carbons with larger internal pores to improve oxygen

transport to embedded catalyst particles.[3] This development removes one of the major drawbacks of porous carbons – high oxygen transport resistance – and allows a reduction of over 40% in the Pt needed to achieve a given fuel cell power rating. Ongoing investigations of the structure of these accessible porous carbon supports suggest that these carbon supports are still far from optimized, with a pore structure that is constrictive and tortuous.

Many exciting catalyst materials with exceptional oxygen reduction activities in aqueous environments, such as octahedral Pt-Ni nanoparticles,[4,5] have so far shown disappointing stability in assembled fuel cell devices.[6] Shape-controlled catalysts are typically loaded onto carbon supports such as Vulcan after synthesis, and recent and ongoing research suggests that their stability suffers from poor adhesion to the carbon.[7] The development of carbon supports that are specifically optimized for shape-controlled nanoparticles is one promising avenue to make these catalysts viable for practical fuel cell applications. Strategies for this may include introducing chemical anchoring sites for the particles or altering the carbon morphology to maximize the carbon-Pt interface area, for example with strongly-faceted carbons. Loading shape-controlled catalysts onto the carbon support after synthesis prevents them from taking advantage of the stabilizing effect of internal carbon pores demonstrated in Chapter 5. However, it may be possible to synthesize a carbon support around previously synthesized particles to stabilize them, as some precursors can be carbonized at temperatures low enough to preserve nanoparticle faceting.[5,8,9]

Chapter 5 demonstrated that selecting the carbon support structure can be an effective strategy for suppressing one major degradation mechanism, coalescence, but not degradation mechanisms driven by platinum dissolution, namely Ostwald ripening and Pt-band formation. Efforts to further improve catalyst stability will need to focus on stabilizing the Pt to prevent dissolution. One strategy is to convert the typically chemically disordered alloy in Pt-M catalysts into a chemically ordered intermetallic structure. This approach has shown some promising results[10], but much

remains unknown about the mechanism of this improvement and the potential for further optimization. Another strategy is the addition of more strongly bonding secondary metals in place of or in addition to Co or Ni, such as Zn, Mn, or V, which could provide a more favorable alloy formation energy while still exerting compressive strain on the Pt surface.[11]

While alternatives to Pt-based catalysts are worth exploring, it is unlikely that alternative catalysts will be able to provide as favorable power density or efficiency for transportation applications. Furthermore, rapid reductions in the amount of platinum needed for automotive fuel cells are bringing us close to the level of precious metals (~5 g) currently used in catalytic converters for ICE vehicles.[6] Once fuel cells reach a comparable amount of Pt, its scarcity and cost will no longer be an obstacle to the deployment of fuel cell vehicles and the field will be able to declare victory in a sense. Further advances will still be important for improving fuel cell efficiency, but complete elimination of Pt is unnecessary.

6.3 References

[1] E. Padgett, N. Andrejevic, Z. Liu, A. Kongkanand, W. Gu, K. Moriyama, Y. Jiang, S. Kumaraguru, T.E. Moylan, R. Kukreja, and D.A. Muller, J. Electrochem. Soc. **165**, F173 (2018).

[2] E. Padgett, V. Yarlagadda, M.E. Holtz, M. Ko, B.D.A. Levin, R.S. Kukreja, J.M. Ziegelbauer, R.N. Andrews, J. Ilavsky, A. Kongkanand, and D.A. Muller, J. Electrochem. Soc. **166**, F198 (2019).

[3] V. Yarlagadda, M.K. Carpenter, T.E. Moylan, R.S. Kukreja, R. Koestner, W. Gu, L. Thompson, and A. Kongkanand, ACS Energy Lett. **3**, 618 (2018).

[4] C. Cui, L. Gan, H.-H. Li, S.-H. Yu, M. Heggen, and P. Strasser, Nano Lett. **12**, 5885 (2012).

[5] V. Beermann, M. Gocyla, S. Kühl, E. Padgett, H. Schmies, M. Goerlin, N. Erini, M. Shviro, M. Heggen, R.E. Dunin-Borkowski, D.A. Muller, and P. Strasser, J. Am. Chem. Soc. **139**, 16536 (2017).

[6] A. Kongkanand and M.F. Mathias, J. Phys. Chem. Lett. **7**, 1127 (2016).

[7] R. Rizo, R.M. Arán-Ais, E. Padgett, D.A. Muller, M.J. Lázaro, J. Solla-Gullón, J.M. Feliu, E. Pastor, and H.D. Abruña, J. Am. Chem. Soc. **140**, 3791 (2018).

[8] J. Lee, J. Kim, and T. Hyeon, Adv. Mater. **18**, 2073 (2006).

[9] M. Sevilla and A.B. Fuertes, Carbon N. Y. **47**, 2281 (2009).

[10] Y. Xiong, Y. Yang, H. Joress, E. Padgett, U. Gupta, V. Yarlagadda, D.N. Agyeman-Budu, X. Huang, T.E. Moylan, R. Zeng, A. Kongkanand, F.A. Escobedo, J.D. Brock, F.J. DiSalvo,

D.A. Muller, and H.D. Abruña, Proc. Natl. Acad. Sci. **116**, 1974 (2019).

[11] L. Ou and S. Chen, Sci. China Chem. **58**, 586 (2015).

A. DERIVATION OF THE STRAIN PROFILE IN A CORE-SHELL NANOPARTICLE FROM CONTINUUM ELASTIC THEORY

A.1 Background and Model Setup

Surface strain is known to be a key parameter determining the activity of Pt-M alloy fuel cell catalysts, as discussed in more detail in Chapter 3. A Pt shell forms upon exposure to acidic environments and experiences a compressive strain from the underlying alloy core. The shell structure and resulting strain may vary significantly based on the catalyst preparation and electrochemical aging, but modeling and characterization of the strain state in core-shell Pt-M particles reported in the literature has been limited. Here we describe a model of one important case – coherent strain in a uniform shell – using elastic continuum theory. Strain may also be relaxed through the introduction of dislocations, which we will investigate in the future.

Consider a core-shell particle with total radius R and core radius r_c. Our task is to determine the distribution of strain throughout the particle, and especially at the particle surface – where it may impact chemical bonding and catalytic activity – given R, r_c, the lattice mismatch between the core and shell, the elastic moduli of the material. We will assume isotropic materials properties.

A.2 Derivation of Strain Distribution

We will begin by following the analysis of a hollow spherical shell, subjected to internal and external pressures, described by Adel Saada in *Elasticity: Theory and Applications*.[1] We will present an abbreviated form of the mathematics, which Saada provides in more detail. This solution

can be applied to the core-shell problem simply by determining the effective pressure to ensure

contact between the core and the shell. This problem has been worked out in the literature[2-4] for

core-shell quantum dots, where the core-shell structure exerts a pressure on the core that alters its

band structure and the optical properties of the quantum dots. The treatment here takes a slightly

different focus, as our interest is in the impact of surface strain on the particle's catalytic activity

and microscopic profile of strain in the shell.

A.2.1 Calculation of the displacement field

Given its spherical geometry, the spherical shell problem is most easily approached in terms of

the Lamé's strain potential φ for the displacement field $\boldsymbol{u}$. The strain potential relates to the

displacement field by $\boldsymbol{u} = \frac{1}{2G}\nabla\phi$, where G is the shear modulus. With isotropic pressures, the

system exhibits complete spherical symmetry, so only the radial displacement in the shell $u(r)$

must be considered (all other displacements are zero). The solution to the Navier equations has the

form

$$\phi = \frac{C}{r} + Dr^2, \tag{A.1}$$

with constants C and D, so the displacement is

$$2Gu(r) = -\frac{C}{r^2} + 2Dr. \tag{A.2}$$

The constants C and D can be solved for by setting the inner stress at $r = r_c$ equal to the inner

pressure P_i and the outer stress at $r = R$ equal to the outer pressure P_o. The displacement can then

be determined as

$$u(r) = \frac{r(1+v)}{E}\left[P_i \frac{\left(\frac{1-2v}{1+v}\right) + \frac{1}{2}\left(\frac{R}{r}\right)^3}{\left(\frac{R}{r_c}\right)^3 - 1} + P_o \frac{\left(\frac{1-2v}{1+v}\right) + \frac{1}{2}\left(\frac{r_c}{r}\right)^3}{\left(\frac{r_c}{R}\right)^3 - 1}\right], \qquad (A.3)$$

where E is the Young's modulus and v is the Poisson ratio. For a core-shell particle, P_i is the contact pressure between the core and shell, while P_o is the ambient pressure. Because the contact pressure is expected to be vastly larger than atmospheric pressure, for the purposes of strain calculation we may approximate $P_o \approx 0$, and consider only the contact pressure $P = P_i$. This simplifies the displacement in the shell to

$$u_s(r) = \frac{r(1+v)}{E}\left[P \frac{\left(\frac{1-2v}{1+v}\right) + \frac{1}{2}\left(\frac{R}{r}\right)^3}{\left(\frac{R}{r_c}\right)^3 - 1}\right]. \qquad (A.4)$$

The definition of the pressure and displacement directions should be noted to ensure that the correct boundary condition is identified for core-shell contact. A positive pressure P inside the spherical shell induces a positive displacement on the shell. The direction of the forces experienced by the core and the shell are opposite, so the core experiences a negative displacement for the same positive pressure:

$$u_c(r) = -\frac{P}{3K}r, \qquad (A.5)$$

for bulk modulus K. Under this convention the pressure P is positive when the core is compressed while exerting a tensile stress on the shell. This will be the case for a positive lattice mismatch, defined as $\delta = (a_c - a_s)/a_s$ for relaxed lattice parameters a_c and a_s in the core and shell, respectively. Contact between the core and the shell enforces the boundary condition[4] on the core and shell displacements,

$$u_s(r_c) - u_c(r_c) = \delta r_c.$$
(A.6)

This condition allows us to solve for the contact pressure:

$$\delta r_c = \frac{r_c(1+v)}{E}\left[P\frac{\left(\frac{1-2v}{1+v}\right)+\frac{1}{2}\left(\frac{R}{r_c}\right)^3}{\left(\frac{R}{r_c}\right)^3-1}\right]+\frac{P}{3K}r_c$$

$$\frac{3K\delta}{P}=1+\frac{(1+v)}{(1-2v)}\left[\frac{\left(\frac{1-2v}{1+v}\right)+\frac{1}{2}\left(\frac{R}{r_c}\right)^3}{\left(\frac{R}{r_c}\right)^3-1}\right]=1+\left[\frac{\left(\frac{r_c}{R}\right)^3+\frac{1}{2}\left(\frac{1+v}{1-2v}\right)}{1-\left(\frac{r_c}{R}\right)^3}\right]=\left[\frac{\frac{3}{2}\left(\frac{1-v}{1-2v}\right)}{1-\left(\frac{r_c}{R}\right)^3}\right]$$

$$P=2K\delta\left(\frac{1-2v}{1-v}\right)\left(1-\left(\frac{r_c}{R}\right)^3\right)=\frac{2K(1-2v)}{1-v}\delta(1-\chi^3).$$
(A.7)

For convenience, we have defined core radius fraction $\chi = r_c/R$. Note that χ^3 is also the core volume as a fraction of the total particle volume, and $(1-\chi^3)$ is the shell volume as fraction of the total particle volume. The core pressure thus scales linearly with the lattice mismatch and with the shell volume fraction.

Substituting the pressure into the displacement relations yields

$$u_s(r)=\frac{2}{3}\frac{(1+v)}{(1-v)}\delta\chi^3 r\left[\left(\frac{1-2v}{1+v}\right)+\frac{1}{2}\left(\frac{R}{r}\right)^3\right],$$
(A.8)

$$u_c(r)=-\frac{2}{3}\frac{(1-2v)}{1-v}\delta(1-\chi^3)r.$$
(A.9)

This displacement profile is illustrated in Figure A.1 for a particle with core radius fraction χ=0.5 and lattice properties appropriate for a Pt_1Co_1 core and Pt shell.
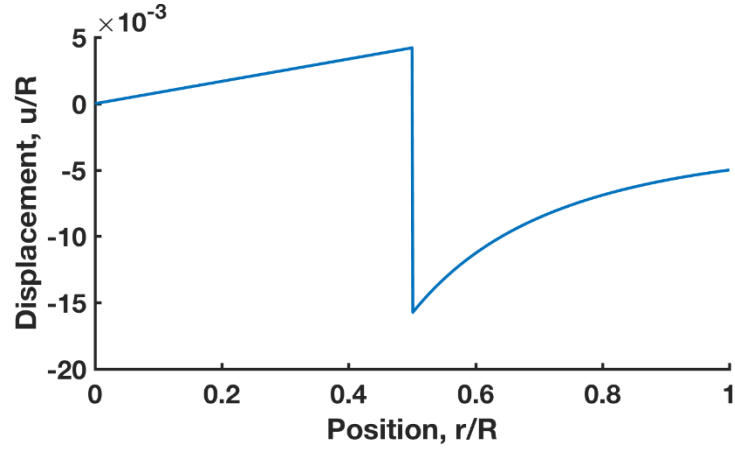
Figure A.1: Displacement from relaxed position for core shell particle with χ=0.5, ν=0.39 (appropriate for Pt), and a δ=-4% lattice mismatch (appropriate for a Pt1Co1 core and Pt shell). Note the linear displacement in the particle core from the expansive core pressure, the decaying compressive displacement in the shell, and the discontinuity at the interface.

A.2.2   Calculation of the strain fields

The radial and tangential strains $\varepsilon^{rr}, \varepsilon^{\theta\theta} = \varepsilon^{\varphi\varphi}$ may be calculated from the displacement by the relations

$$\varepsilon^{rr} = \frac{du_r}{dr}, \tag{A.10}$$

$$\varepsilon^{\theta\theta} = \varepsilon^{\varphi\varphi} = \frac{u_r}{r}. \tag{A.11}$$

Here the strain ε is the material strain, defined as $\varepsilon(r) = a(r)/a_0(r)$, with the lattice parameter $a(r)$ referenced to the local relaxed lattice parameter $a_0(r)$. An alternative convention is the Lagrange strain, defined as $\varepsilon_L(r) = a(r)/a(r_0)$, which is referenced to the strained lattice parameter at some reference point r_0. The Lagrange strain is experimentally straightforward to measure because it does not require prior knowledge of the local relaxed lattice.

In the particle core, there is a simple isotropic pressure-induced strain:

$$\varepsilon_c^{rr} = \varepsilon_c^{\theta\theta} = \varepsilon_c^{\varphi\varphi} = \frac{P}{3K} = -\frac{2(1-2\nu)}{3(1-\nu)}\delta(1-\chi^3). \tag{A.12}$$

In the particle shell, the strain varies spatially with radial position:

$$\begin{aligned}
\varepsilon_s^{rr} &= \left(\frac{(1+\nu)P}{E\left(\left(\frac{R}{r_c}\right)^3 - 1\right)}\right)\left[\left(\frac{1-2\nu}{1+\nu}\right) - \left(\frac{R}{r}\right)^3\right] \\
&= \left(\frac{2(1+\nu)}{3(1-\nu)}\right)\delta\chi^3\left[\left(\frac{1-2\nu}{1+\nu}\right) - \left(\frac{R}{r}\right)^3\right],
\end{aligned} \tag{A.13}$$

$$\begin{aligned}
\varepsilon_s^{\theta\theta} = \varepsilon_s^{\varphi\varphi} &= \left(\frac{(1+\nu)P}{E\left(\left(\frac{R}{r_c}\right)^3 - 1\right)}\right)\left[\left(\frac{1-2\nu}{1+\nu}\right) + \frac{1}{2}\left(\frac{R}{r}\right)^3\right] \\
&= \left(\frac{2(1+\nu)}{3(1-\nu)}\right)\delta\chi^3\left[\left(\frac{1-2\nu}{1+\nu}\right) + \frac{1}{2}\left(\frac{R}{r}\right)^3\right].
\end{aligned} \tag{A.14}$$

Strain profiles for particles with different core radius fractions are illustrated in Figure 3.1 and discussed in Chapter 3.

A.2.3 Strain at the particle surface

The most interesting quantity for catalytically active nanoparticles is the strain at the particle surface:

$$\varepsilon_s^{rr}(r=R) = \frac{-3\nu}{E}\left(\frac{\chi^3}{1-\chi^3}\right)P = \frac{-2\nu}{1-\nu}\delta\chi^3 \tag{A.15}$$

$$\varepsilon_s^{\theta\theta}(r=R) = \frac{3(1-\nu)}{2E}\left(\frac{\chi^3}{1-\chi^3}\right)P = \delta\chi^3. \tag{A.16}$$

The tangential strain $\varepsilon_s^{\theta\theta}$ is the product of the lattice mismatch and the core volume fraction, while the radial strain ε_s^{rr} also includes a Poisson-ratio correction. This simple result is intuitively appealing. For the ideal case of coherent strain and uniform shell thickness the tangential strain is the same as the lattice mismatch averaged over the particle volume and can be determined from the average composition alone.

A.2.4   Implications of the model for catalytic nanoparticles
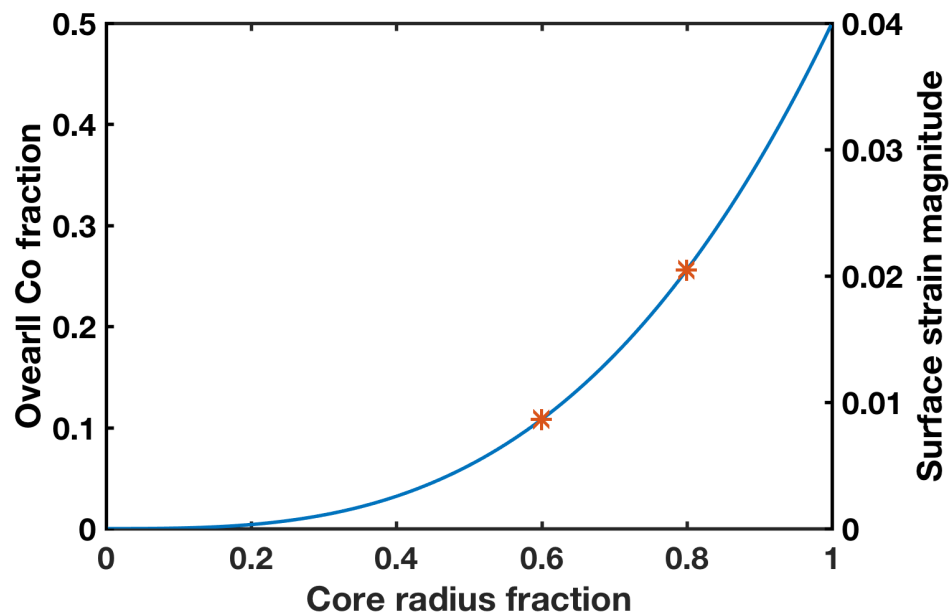
Figure A.2: Plot of relationship between core radius fraction χ, composition, and tangential surface strain magnitude. Stars mark points corresponding to 0.5 nm and 1 nm Pt shells on a 5 nm diameter particle with a Pt_1Co_1 core.

This model allows simple prediction of the change in strain state for Pt-Co catalysts after electrochemical aging or de-alloying treatments in the absence of particle coalescence or incoherent shell relaxation. For instance, 5 nm particles may have a 0.5 nm Pt shell ($\chi=0.8$) after an initial de-alloying, giving an average composition of about $Pt_{0.74}Co_{0.26}$ if they are prepared from a Pt_1Co_1 precursor. Even this thin shell in the initial state will result in a compressive surface strain of about

2%, only half that expected from the nominal lattice mismatch between the core Pt-Co and pure Pt. A cycling stability test or aggressive de-alloying may produce a thicker shell around 1 nm thick (χ=0.6) and reduce the overall composition to about $Pt_{0.89}Co_{0.11}$. This will reduce the surface strain by slightly more than half again, resulting in less than 1% compressive strain.

A.3   References

[1] A.S. Saada, *Elasticity: Theory and Applications*, 2nd ed. (J. Ross Publishing, Ft. Lauderdale, FL, 2009).
[2] X. Cai, H. Mirafzal, K. Nguyen, V. Leppert, and D.F. Kelley, J. Phys. Chem. C **116**, 8118 (2012).
[3] K. Gong and D.F. Kelley, J. Chem. Phys. **141**, 194704 (2014).
[4] J. Rockenberger, L. Troger, A.L. Rogach, M. Tischer, M. Grundmann, A. Eychmuller, and H. Weller, J. Chem. Phys. **108**, 7807 (1998).

B. USEFUL METHODS FOR HIGH RESOLUTION ELECTRON TOMOGRAPHY

B.1 Abstract

This appendix presents useful "tips and tricks" for producing high quality electron tomography reconstructions at ~1 nm resolution. The recommendations presented here are especially relevant to the challenging set of carbon-supported nanoparticle catalysts but may be of use for any electron tomography specimen.

B.2 Introduction

The conventional electron tomography experiment is conceptually simple: a series of images is acquired as the specimen is tilted about a single axis. However, many details must be considered during the experiment and postprocessing to produce high-resolution tomograms with sufficient quality. Beyond reducing resolution, imperfections in tomography data result in intensity artifacts that interfere with accurate data interpretation. In general, it is necessary to ensure that the data remains self-consistent and consistent with the assumed experimental geometry and projection imaging. The consequences of inconsistency are typically easiest to understand by consideration of the real-space reconstruction process, as inconsistency in the data will result in intensity back-projected to the wrong location. This leads to errant bright streaks or apparent voids in a variety of forms, depending on the source of the error.

Pt/C nanoparticle catalysts are demanding case for electron tomography. ~1 nm resolution is needed to reconstruct the Pt nanoparticles, and a relatively large field of view (>100 nm) is needed

to provide adequate sampling. When the carbon support is of interest as well it is critical to maintain good data quality. In annular dark field (ADF) scanning transmission electron microscopy (STEM) Pt yields much higher contrast than carbon (30X or more), such that even minor artifacts on Pt particles are severe in the intensity range of carbon and interfere with segmentation or qualitative interpretation.

The efforts to use STEM tomography to understand the consequences of carbon support morphology on the distribution of platinum particles led to several refinements to STEM tomography methods to ensure high quality, high resolution data, which are presented here. Basic methods for electron tomography have been covered in detail elsewhere[1], so here we will focus instead on "tips and tricks" to ensure good data quality. Automated tomography software is not necessarily configured to follow best practices that provide high-quality, self-consistent data. By being aware of likely pitfalls, the experimenter can avoid "mistakes" by the software that compromise data quality. When the software cannot be coaxed into good behavior, manual tomography allows the experimenter complete control to ensure the highest quality data.

B.3   Experimental Convenience

It is always best to attempt to collect images over the largest tilt range possible to minimize the missing wedge experimentally. Methods for full-rotation electron tomography of nanoparticle specimens are presented in Appendix C. Modern tomography holders and goniometers can provide ±80º of unobstructed tilt range, and so the specimen grid is commonly the limiting factor. A grid mesh of 200 or lower should typically allow ±70º tilt range or better. It is convenient to use a hexagonal mesh because this will provide a similar tilt range regardless of the grid orientation. For these reasons, I have typically used 100 mesh hexagonal grids with a thin carbon film for tomography experiments. These grids often allow nearly full use of the goniometer's tilt range.

179

Selection of the specimen location to be imaged in the tomography experiment is important and often time consuming. The location should be visible for the largest tilt range practical, without obstruction by other objects on the grid at any point in the range. Furthermore, the specimen location should be chosen so that it is not unnecessarily thick at any angle, as this will reduce the reconstruction quality. A useful strategy for identifying suitable locations is to trace out the edges of the local grid square or hexagon with the tracks in the "Search" tab in the user interface for FEI/Thermo Fischer microscopes. This allows the experimenter to constrain their search to areas near the center where the tilt range is maximized, saving time in verifying the tilt range for many candidate sites.

The Eucentric height setting should be carefully refined at the location of interest prior to the tomography experiment by minimizing the lateral motion of the specimen as the goniometer wobbles between -15º and +15º. This procedure brings the specimen to the same height as the tilt axis of the goniometer and is typically taught to all TEM operators. However, there is a second, little-known tilt axis alignment that can cause significant inconvenience during a tomography experiment. It is also possible for the tilt axis of the goniometer to be horizontally displaced from the optic axis of the microscope. When this occurs the height of the specimen will change each time the goniometer is tilted, requiring correction by the experimenter with the lenses or stage. This can add significantly to the time, dose, and patience required for the experiment.

While it is possible to correct such a displacement by shifting the beam, imaging with the beam far from the lens center may degrade the image quality. It is preferable to mechanically align the goniometer to bring the axis of rotation to the optic axis. This should be done by an instrument technician comfortable with adjusting the stage. The simplest way to identify the lateral displacement of the tilt axis is to track an image feature as the goniometer is tilted from 0º to a non-zero value. The axis offset can then be calculated by simple trigonometry.

Backlash of the goniometer (hysteresis when reversing the direction of tilt) can add significant imprecision to the tilt angle and should be avoided during the tomography experiment by tilting in a consistent direction. If the tilt direction needs to be reversed temporarily (e.g. to re-take a previous image) backlash can be corrected by over-tilting and then returning in the desired direction.

All experimental conditions that may introduce image distortions or intensity changes should be set prior to the experiment and left unaltered. This includes brightness and contrast, beam current, camera length, beam shift and diffraction shift.

B.4   Specimen Integrity

It is perhaps obvious that alteration of the specimen during the experiment should be avoided, however it is not always clear when this is occurring or what the source is. Beam damage and carbon contamination can both compromise the specimen integrity, which can lead to artifacts from self-inconsistent data (e.g. if beam damage causes the specimen to shrink or move) that can be even more problematic than producing a tomogram of a damaged or contaminated specimen. The best practice for recognizing if this occurs is to take "before" and "after" images at 0º. It is also useful to compare the mid-tilt-series image at 0º to the "before" image as often problems can be recognized at this stage and the experiment can be aborted to save time. Changes in the specimen are most easily recognized by comparing registered image pairs, which can be conveniently done during the experiment by using the StackReg plugin in ImageJ,[2,3] for example. If the experimenter quickly recognizes that their sample is being damaged or contaminated, they can adjust the experiment without wasting time reconstructing low quality data.

The experimenter must also consider the possibility of specimen degradation prior to the start of the experiment, which cannot easily be identified by before and after imaging. Potential causes

of this include possible etching of carbon or organic samples by plasma cleaning or incompatibility of the specimen with vacuum.[4]

Carbon catalyst supports can be especially challenging specimens for tomography because they can easily be compromised by carbon contamination but may also be etched by plasma cleaning. (This adds to the challenges of low scattering signal and propensity to damage.) For these or similar specimens, it can be useful to cool the specimen using a cryo-tomography holder to immobilize contaminants. At liquid nitrogen temperature, ice will accumulate on the specimen, but this can be avoided by holding the specimen temperature at -100ºC using a stable holder temperature controller. This procedure adds significant complexity to the tomography experiment, however, and adds many more opportunities for the experiment to fail.

More recently we have seen success for catalyst carbon supports by following a different procedure: low-voltage TEM. A lower voltage such as 80 kV can significantly reduce the damage rate, and TEM provides a more favorable relative contrast for carbon, making artifacts from Pt particles less severe. TEM can also effectively eliminate carbon contamination if a large specimen area outside of the field of view is illuminated. In this case the contaminants deposit far enough away from the site of interest that they are not disruptive. This is likely a more promising approach for Pt/C catalysts and typically produces higher quality data with less difficulty.

B.5   Image Distortions

Artifacts can be introduced by image distortions that vary over the tilt series, or in some cases ones that are static but violate the assumed geometry. Some level of imperfection is unavoidable, but it is important to consider and limit the scale of inconsistencies in the data. A useful rule is that variations limited to roughly the scale of a pixel are tolerable.

One important source of image distortions is the microscope optics. Changing the lens currents will cause the image to rotate and change magnification. Significantly varying the lens defocus will thus lead to self-inconsistency in the tilt series and should be avoided. I typically avoid allowing the defocus to become larger than ~1 µm, using the stage to adjust the height when necessary. Shifting the image can result in similar distortions and should be avoided. In STEM, the scan directions may not be precisely orthogonal, resulting in an image that is somewhat sheared. Because this is a static distortion it can be corrected by shearing the image in postprocessing. The impact of image shear on the tomogram is very similar to the impact of an incorrectly rotated tilt axis, and the two problems are not easily distinguished. To achieve the best quality STEM tomography reconstruction both image shear and rotation should be fine-tuned.

The other major source of distortion in images is sample drift. In TEM, a drifting sample will produce a blurred image that is otherwise undistorted. In STEM, as the sample drifts under the scanning beam it will stretch (for drift in the slow scan direction) and shear (for drift in the fast scan direction). These distortions create self-inconsistency in the tomography data leading to artifacts in the reconstruction. Drift-distortion of STEM images can be suppressed relatively easily by acquiring a stack of images with a short dwell time in place of a single image at each tilt. The images can later be registered by translational cross correlation and summed to produce a single, low-distortion, high signal to noise image at each tilt. The distortion will be reduced by a factor equal to the number of images in each stack, and in practice the fast-scan dwell time can be chosen such that the drift is on the order of a pixel per frame to make drift distortion negligible.

B.6   Postprocessing

In postprocessing it can be useful to apply an intensity and background correction to level any undesirable variations and make the tomogram intensity more interpretable. This is relatively

simple for an isolated object filling a minority of the pixels in the field of view. For STEM a suitable correction is to subtract the modal value (the background intensity) from each image and then divide by the mean intensity of the image. This provides equal intensity and weighting to every image in the tilt series, and for weighted back-projection reconstructions makes zero intensity interpretable as void. The same correction can be used for TEM following inversion of the image.

Precise alignment is most reliably achieved manually. Under some special circumstances automated procedures such as cross correlation and center of mass calculation can provide precise alignments, but they are typically unreliable and useful only as a first rough alignment step. Catalyst nanoparticles such as Pt make excellent fiducial markers for alignment, but if the specimen contains no similar intrinsic guiding features it is most convenient to add fiducial markers such as gold nanoparticles during sample preparation. When aligning to a fiducial point it is important to avoid progressive alignment drift, and so comparing to a fixed reference image is more reliable than aligning each image to the previous one. A precise fine-tuning of the tilt axis placement and STEM shear correction is best done by comparison of complete weighted-back-projection reconstructions with small perturbations to the alignment.

B.7   References

[1] P. Ercius, Three-Dimensional Electron Tomography of Integrated Circuit Devices, Cornell University, 2009.

[2] C.T. Rueden, J. Schindelin, M.C. Hiner, B.E. DeZonia, A.E. Walter, E.T. Arena, and K.W. Eliceiri, BMC Bioinformatics **18**, 529 (2017).

[3] P. Thevenaz, U.E. Ruttimann, and M. Unser, IEEE Trans. Image Process. **7**, 27 (1998).

[4] B.D.A. Levin, Transmission Electron Microscopy of Vacuum Sensitive, Radiation Sensitive, and Structurally Delicate Materials, Cornell University, 2017.

C. SAMPLE PREPARATION AND METHODS FOR FULL-RANGE TOMOGRAPHY OF NANOPARTICLES

C.1 Abstract

Electron tomography has become a valuable and widely used tool for studying the 3D nanostructure of materials and biological specimens. However, the incomplete tilt range provided by conventional sample holders limits the fidelity and quantitative interpretability of tomographic images by leaving a "missing wedge" of unknown information in Fourier space. Imaging over a complete range of angles eliminates missing wedge artifacts and dramatically improves tomogram quality. Full-range tomography is usually accomplished using needle-shaped samples milled from bulk material with focused ion beams, but versatile specimen preparation methods for nanoparticles and other fine powders are lacking. In this appendix, we present a new preparation technique in which powder specimens are supported on carbon nanofibers that extend beyond the end of a tungsten needle. Using this approach, we produced tomograms of platinum fuel cell catalysts and gold-decorated strontium titanate photocatalyst specimens. Without the missing wedge, these tomograms are free from elongation artifacts, supporting straightforward automatic segmentation and quantitative analysis of key materials properties such as void size and connectivity, and surface area and curvature. This approach may be generalized to other samples that can be dispersed in liquids, such as biological structures, creating new opportunities for high-quality electron tomography across disciplines.[i][1]

C.2   Introduction

Electron tomography is a widely-used tool in biological and physical science and engineering due to its ability to reveal the 3D structure of inhomogeneous specimens at nanometer length scales [2]. Tomography provides valuable information unavailable in conventional 2D imaging by resolving structures that are ambiguous in projection and allowing quantitative measurement of intrinsically 3D geometric properties such as surface area and volume. A 3D tomogram is produced by combining the information in a series of 2D projection images taken at different specimen tilts, where, conceptually, each image contributes information to fill a corresponding 2D plane in the 3D Fourier transform of the specimen. Ideally, the specimen would be imaged over a complete 180° rotation to provide knowledge of the specimen covering all of Fourier space. In practice, however, a complete rotation cannot be achieved with conventional specimen holders in a (scanning) transmission electron microscope ((S)TEM), as the sides of the holder or grid obscure the sample at high tilts (above about ±75° for commercial electron tomography holders currently available). The lack of images at high tilts leaves a "missing wedge" of unsampled information in Fourier space. The missing wedge degrades reconstruction quality by introducing blurring along the optic axis and shadow artifacts in the perpendicular direction in the reconstructed plane (e.g. Mastronarde, 1997; Midgley & Weyland, 2003). These artifacts reduce the 3D imaging resolution, introduce spurious intensity variations, and distort apparent shapes in the tomogram. In complex, real-world structures this makes qualitative interpretation challenging and compromises the accuracy of segmentation and quantitative analysis.

Multiple methods have been developed to mitigate or solve the missing wedge problem, from algorithms that reduce artifacts to milling needle-shaped samples for imaging over a complete angular range. Recently developed reconstruction algorithms, such as discrete tomography [5] and

compressive sensing tomography [6–8], have shown some ability to reduce artifacts caused by the missing wedge. These algorithms are based on assumed prior knowledge of the specimen, which provides a means to make an informed guess at the missing information. However, the assumptions embedded in each algorithm and its reconstruction parameters are not universally applicable and the reconstruction will thus depend on subjective choices made by the user. Furthermore, these advanced algorithms remain poorly understood in terms of possible artifacts and failure conditions [9]. Thus, these algorithms warrant caution and further study, and should not be considered a replacement for more complete experimental data.

Experimentally, partial reduction of the missing wedge has been demonstrated with specialized tilting schemes [10] including dual axis tomography [3,11], which reduces the missing wedge to a missing pyramid, and conical tomography [12], which reduces it to a missing cone. Unfortunately, these tilting schemes add to the complexity, duration, and radiation dose of tomography experiments and complicate the process of image alignment and reconstruction. Whenever possible, imaging the specimen over a full 180° rotation is preferable to these approaches as it eliminates the missing wedge without significantly increasing the complexity of the tomography experiment.

Full-range electron tomography has been accomplished using micropipette specimens [13], half-grid specimens [14–16] in custom-built holders or in commercial on-axis and micro-pillar tomography holders [17–21], available from vendors including Fischione, Hitachi, and Mel-Build. Glass or carbon micropipettes can be effective containers for biological specimens where a large field of view (microns or hundreds of nanometers) is desired [13,22]. Most full-range tomography experiments for materials have been accomplished by using a focused ion beam (FIB) to extract and mill the specimen into a needle geometry [23]. This is ideal for bulk or interface specimens where FIB lift-out and thinning is a routine approach to sample preparation. Unfortunately, these methods are poorly

suited to an important class of nanomaterials studied via electron tomography: fine powders, such as catalyst particles. Such materials are important for a wide variety of applications – including chemical processing and energy conversion and storage – and the details of their 3D nanostructure are often critical in determining materials properties. While micropipettes can be used to contain particulate specimens for electron tomography, their large size and thickness is incompatible with the high resolution often needed for nanomaterials. Fine powders could in principle be prepared by FIB milling if they can be embedded without changing their structure, although even then FIB preparation is slow, expensive, and risks damage to specimens and thus should be avoided if possible. Some full rotation tomography specimens have been prepared by collecting powders on a metal point or micro-pillar sharpened by FIB milling [15,24,25], however these specimens typically extend unobstructed only a short distance beyond the non-electron-transparent support, providing a very limited field of view for tomography. Good clearance from a metal point can be achieved in tomography of elongated materials such as carbon nanotubes [26]. The objective of this work is to apply the clearance provided by nanotubes and nanofibers to enable practical preparation of full-range tomography specimens for a variety of fine powder material samples.

Here we present a new sample preparation method for full-range tomography using carbon nanofibers (CNF) as a 1D sample support to provide an unobstructed view of the sample through a complete rotation, as illustrated in Figure C.. This approach is suitable for a variety of materials such as nanoparticles, nanostructured microparticles, and nanofibers. This simple, bench-top procedure requires no special equipment beyond a full rotation tomography holder and allows for high quality tomography reconstructions without the missing wedge. The method can be adapted to any type of on-axis or micro-pillar holder. We demonstrate this technique for two technologically relevant nanoparticle specimens: 1) a Pt/CNF fuel cell catalyst in which the CNF structure and

188

spatial relationship to Pt is of interest and 2) a gold-decorated strontium titanate ($SrTiO_3$ or STO) nanoparticle photocatalyst in which the carbon fiber is used as an ignorable specimen support.
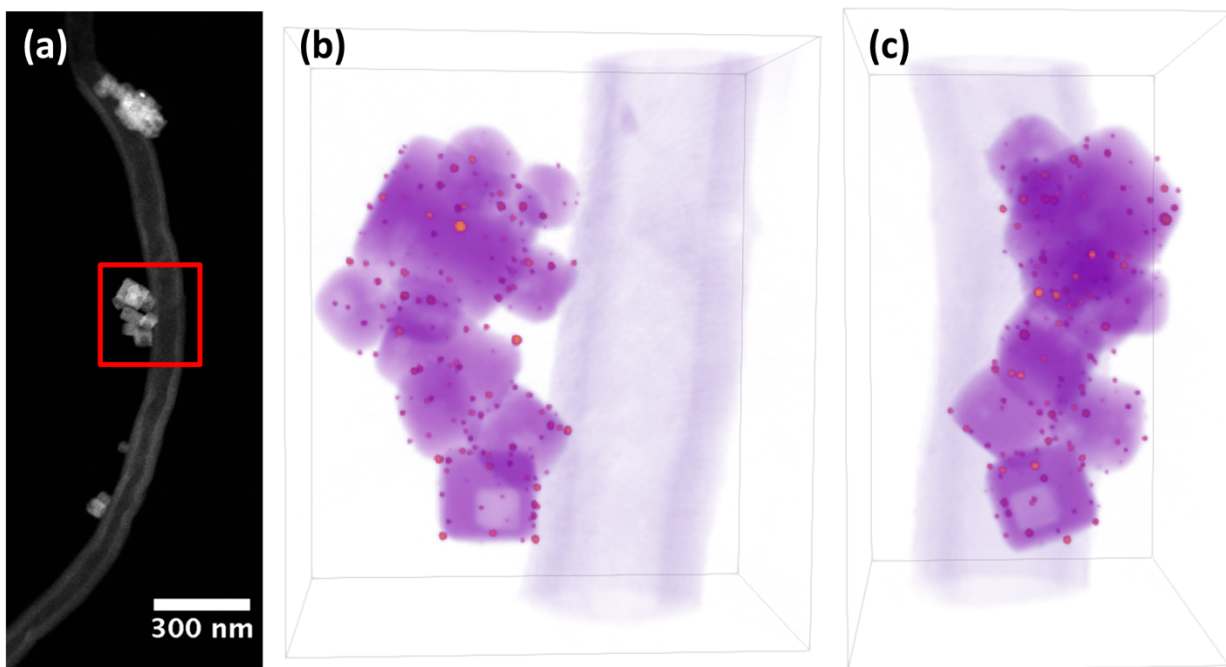

Figure C.1. (a) ADF STEM image of Au/STO particle supported on carbon nanofiber for full-range electron tomography. Red square indicates region selected for tomography reconstruction. (b,c) Volume rendering of Au/STO tomogram, where orange indicates Au particles, magenta indicates STO, and purple indicates the carbon fiber. Dimensions of rendered volume are 280 nm x 192 nm x 327 nm.

C.3 Materials and Experimental Methods

C.3.1 General Sample Preparation Approach

Samples for this investigation were supported on carbon nanofibers that adhere to the tip of a tungsten needle, which was loaded into an on-axis TEM holder (Figure C.2). Carbon nanofibers were collected on the needle by dipping the needle tip in a suspension of nanofibers in alcohol, which may also contain a small concentration of binder. Subsequently, particle samples may be

loaded onto the nanofibers by dipping the needle tip again in a suspension containing the sample. A brief, step-by-step summary of the procedure is provided in the appendix for practical reference.

In an ideal sample, a single nanofiber extends beyond the tip of the needle and other nanofibers that have been collected. It is convenient for the fiber to be oriented roughly parallel to the needle axis, although angles over 45 degrees can be acceptable. The general arrangement of nanofibers on the needle tip can be observed in a visible light microscope (VLM), most easily in dark field mode (Figure C.3b,e). A VLM is useful for preliminary screening and guidance during the sample preparation, as the needle can be re-dipped until a suitable quantity and arrangement of fibers is achieved. Each sample takes only a few minutes to prepare, so it is convenient to prepare 5-10 samples that appear acceptable in VLM screening before proceeding to screen samples in the (S)TEM, so that at least one sample that is suitable for tomography is produced.

In this investigation, we used Omniprobe Autoprobe-250 tungsten needles which we cleaned in batches by cathodic etching in argon plasma using a Bal-Tec SCD 050 sputter coater. We have observed that without cleaning, the needle tips may bend or curl upon contacting a liquid surface. Cleaning either with 25% oxygen 75% argon plasma or with cathodic etching in argon plasma was found to be effective. Nanoparticle and nanofiber suspensions were dispersed using a bath ultrasonicator and pipetted into a shallow ceramic multi-welled plate for the dipping procedure. Samples were screened using an Olympus BH-2 visible light microscope with an Infinity 2 camera at 500X magnification. Visible light images shown in Figure C.3b,e were given a simple extended-depth-of-field enhancement by summing three images at different specimen heights.

C.3.2 Preparation of a Simple Nanofiber Sample: Pt/CNF

Our first example of this preparation is a commercial fuel cell catalyst consisting of platinum nanoparticles chemically synthesized on carbon nanofibers, Pt/CNF. 3D tomographic images of this material are useful for measuring properties such as the distribution of Pt nanoparticle sizes, shapes, and locations on the carbon. The platinum nanoparticles are supported on the carbon fibers in the as-synthesized material, rather than being loaded on during sample preparation. This simplifies the sample preparation procedure. The Pt/CNF powder was dispersed in methanol at a concentration of approximately 0.5mg/mL and collected onto the needle tip in a single dipping step. No binding agent was added, as the sample interaction with the tungsten needle was sufficiently strong for fibers to adhere and remain on the needle. Tomography data for the Pt/CNF sample is available in a separate open data publication [27].

C.3.3 Generalized Preparation of a Particle Sample: Au/STO

This preparation procedure can be extended to many types of nanoparticles and nanostructures by collecting the sample on carbon nanofibers which are adhered to the needle tip. To demonstrate the more general procedure, we prepared a nanostructured water-splitting photocatalyst consisting of gold nanoparticles chemically deposited on cubic strontium titanate (STO) particles, referred to here as Au/STO. 3D tomographic images of this material are useful for measuring properties such as the faceting and pore structure of the STO and the sizes and spatial distribution of the Au particles. In this case carbon nanofibers purchased from US Research Nanomaterials (Research Grade Large Inner Diameter Thin Multi-Wall Carbon Nanotubes, id: US4440) were used as a specimen support. These fibers have a nominal outer diameter of 30-60nm and inner diameter of 20-50nm. Several other types of carbon nanotubes and nanofibers were investigated, but did not meet all the criteria needed for this application, including sufficiently small size for acceptable

suspension, tubes/fibers which are straight enough to encourage fibers to extend well beyond the needle tip, and thin enough fibers or tube walls to maintain a low background signal during tomography data acquisition.

The interaction between the carbon fibers and tungsten needle was found to be relatively weak, causing the fibers to commonly fall from the needle tip within minutes of preparation. This problem was corrected by suspending the nanofibers at 0.5mg/mL in a solution containing a small concentration of Nafion polymer, made by diluting Nafion 1100EW to 0.02wt% Nafion in ethanol. This bound the fibers to the needle for the remaining preparation steps and tomography experiment, with no contamination observed during tomography. In our experience, with the added Nafion binder, the fibers remain on the needle for at least several weeks after successful sample preparation. In some cases, solvated binder alone may be insufficient to adhere fibers to the tungsten needle. In these cases, priming the needle surface by dipping in M-Bond and then in a dry carbon nanofiber powder before curing can promote adhesion. Needle tips were then dipped in a nanoparticle suspension at 0.5mg/mL concentration for 5-10 seconds to collect nanoparticles on the fibers.

C.3.4 STEM Imaging and Tomography

For STEM experiments, samples were loaded in a Fischione Instruments 2050 on-axis tomography holder with a custom-designed collet (made by Fischione) for compatibility with 0.508mm diameter Omniprobe Tungsten Probe Tips. Samples were cleaned with 5% oxygen, 95% argon plasma for 45 seconds in a Fischione Model 1020 plasma cleaner with a shielded specimen holder port. STEM imaging and tomography was performed in an FEI Tecnai F20 with a Schottky field emission gun and a 200 kV accelerating voltage. A convergence angle of ~6.9 mrad was used to provide sub-nanometer resolution over a large depth of field. Image signal was collected on an

annular dark field (ADF) detector with a camera length of 300mm for the Pt/CNF sample, and 200mm for the Au/STO sample.

To reduce distortions in STEM images introduced by sample drift and scan noise, at each tilt in the tomography experiments we acquired a series of fast-scan images with 1-2 second per frame and 16 seconds total acquisition. After data acquisition each image series was aligned by cross-correlation and summed to produce a high signal-to-noise ratio image at each tilt, averaging out scan noise and limiting distortions to around 1-2 pixels. Images were taken with 1024x1024 pixels per frame and a 0.36nm pixel size.

Because our stage goniometer is unable to tilt through a complete 180° range, the full-range tilt series must be acquired in two parts, with an internal rotation by the tomography holder in between. We acquired each full-range tomography tilt series by recording a half-series tilting with the microscope goniometer from approximately -45° to +45° in 1° or 2° steps, then incrementing the sample tilt by approximately 90° using the holder's internal manual rotation, and then recording a second half-series. The holder's manual rotation was found to be imprecise, so additional images were recorded at each end of each half series, to ensure full coverage of the angular range. For Pt/CNF, images were recorded at 1° intervals from -46° to +47° at the first holder position, and -47° to +48° at the second. For Au/STO, images were recorded at 2° intervals from -54° to +54° at the first holder position and -54° to +54° at the second.

Images in each tilt series were aligned to a common coordinate system then shifted and rotated to center the axis of rotation. For Au/STO, the image alignment was done manually using a gold nanoparticle in the sample as a fiducial marker. For Pt/CNF, the images were aligned along the tilt axis using cross-correlation of the 1D image signal projected onto the tilt axis, then aligned perpendicular to the tilt axis using the image center of mass. A shear operation was then applied to

correct a ~1% non-orthogonality in the image scan directions. Shear and rotation operations used linear interpolation. The shear correction magnitude and the precise angular offset between the half series in each data set were determined by minimizing visually apparent artifacts in the reconstruction. Prior to tomography reconstruction, images were binned by two, resulting in a 0.71 nm pixel size. Tomograms were reconstructed using the weighted back-projection (WBP) algorithm, implemented using the *iradon* function in MATLAB. 3D visualizations were rendered using the open source tomography platform *tomviz*. Surface curvature calculations were done in MATLAB using the Patch Curvature and Smooth Triangulated Mesh packages [28,29] by Dirk-Jan Kroon.
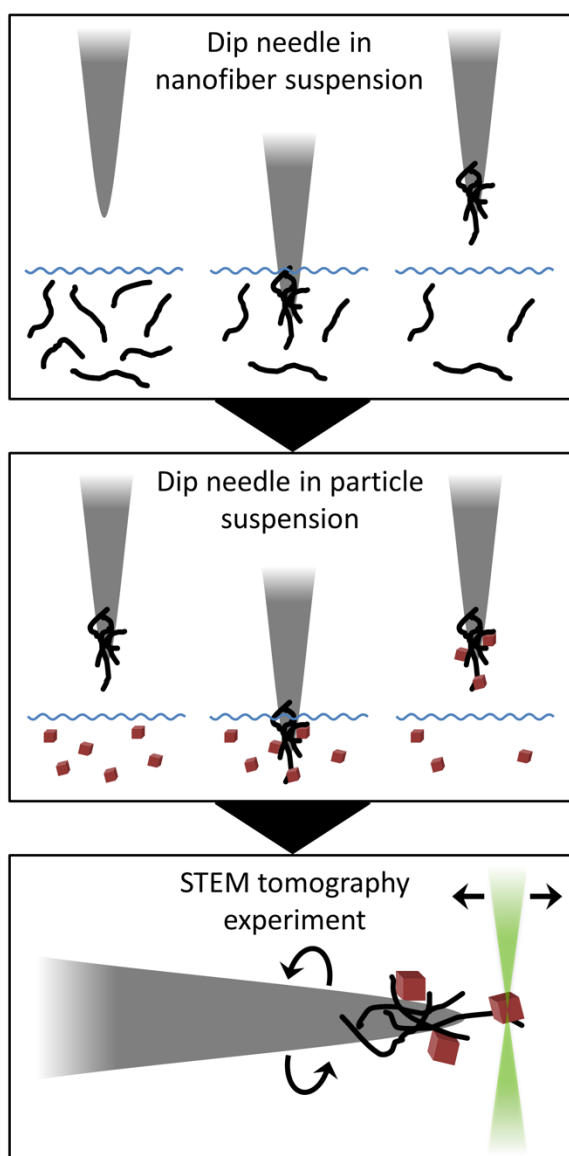
Figure C.2. Schematic cartoon of sample preparation method. First, a tungsten needle is dipped in a suspension of nanofibers in order to collect fibers on the needle tip. To prepare a general nanoparticle sample, the needle is then dipped in a nanoparticle suspension to collect particles on the nanofiber support. Sample is loaded into an on-axis tomography holder for the tomography experiment in the scanning transmission electron microscope (STEM).
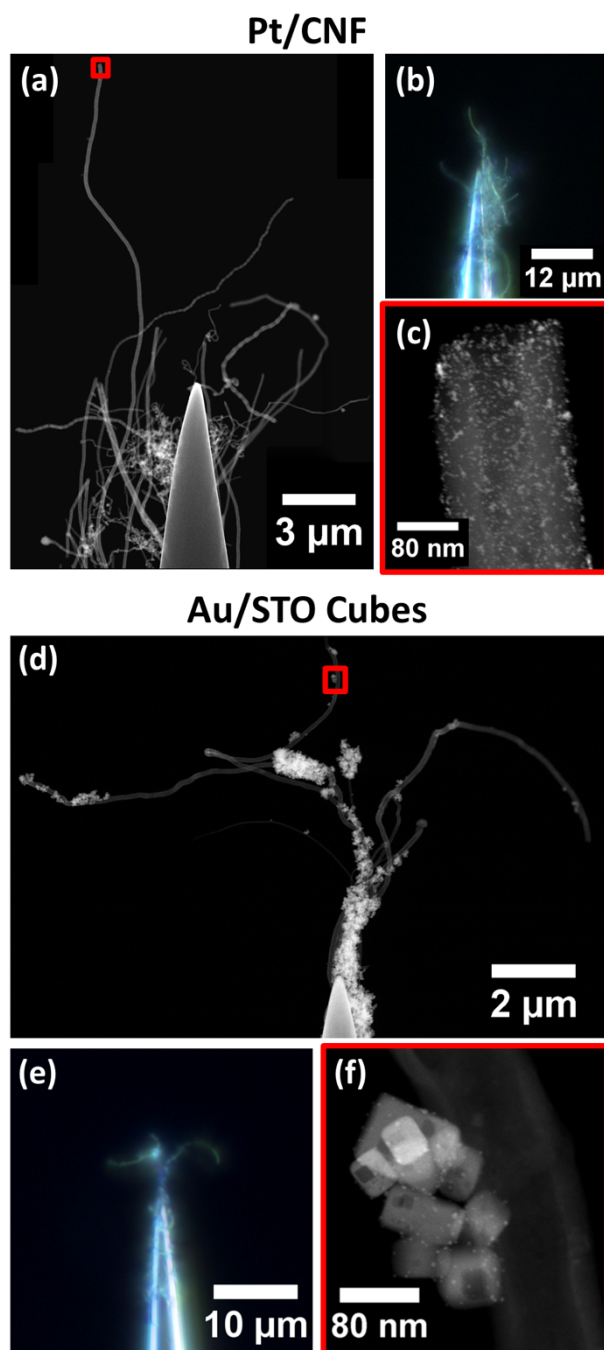
Pt/CNF

Au/STO Cubes

Figure C.3. Images of Pt/CNF (a-c) and Au/STO (d-f) specimens as prepared by needle-dip method. Large-scale sample structure is shown in STEM stitched composite images (a,d) and in dark field visible light microscope images with extended depth of field (b,e). Areas selected for tomography are shown in STEM images (c,f) from regions highlighted in red boxes in (a,d). Composites made with Fiji Pairwise Stitching Plugin [30].

C.4   Results and Discussion

The composite STEM images in Figure C.3 show large areas of each sample that are suitable for tomography. The outermost extent of unobstructed fiber contains several microns of material in the Pt/CNF sample, and multiple complete specimen agglomerates in the Au/STO sample. This provides the opportunity to choose the region of interest for tomography or include a larger area to improve statistical sampling in quantitative studies.

Tomograms for Pt/CNF and Au/STO are presented in Figure C.4 and Figure C.5, respectively, with 3D volume renderings shown alongside tomogram cross-sections from across the volume to demonstrate the consistent, high quality of the reconstruction. In each tomogram, the small metal nanoparticles are well-resolved and round in appearance, showing no elongation due to the missing wedge or artifacts caused by motion of the nanoparticles. This suggests that the carbon nanofiber supports are mechanically stable and robust to beam-induced damage. Occasionally fibers in the samples have insufficient mechanical connection to the tungsten needle and exhibit high frequency vibration during imaging. However, this problem is easily recognized during sample screening in the (S)TEM, as the vibrations prevent formation of an acceptable image. Some mild streak artifacts are visible around the metal nanoparticles, likely due to diffraction or channeling contrast from high-density metals, although these do not interfere with either qualitative interpretation or quantitative analysis of the tomograms.
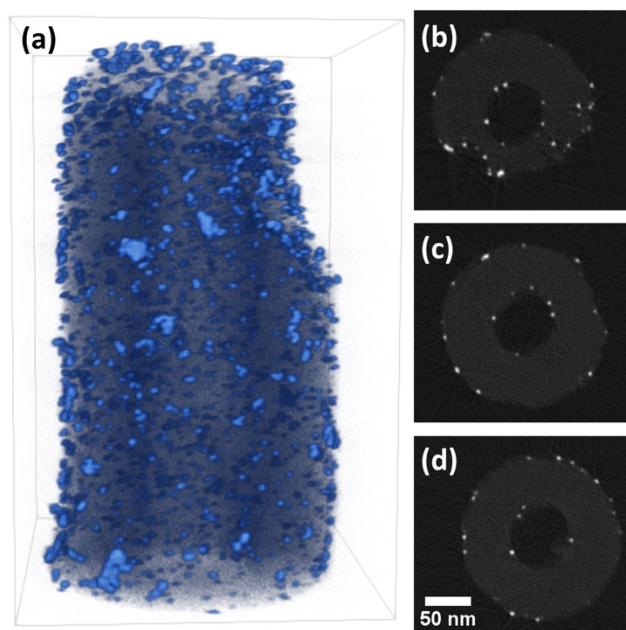
Figure C.4. Visualization of Pt/CNF reconstruction. (a) 3D volume rendering with light blue indicating high intensity (platinum) and dark blue-black indicating low intensity (carbon). (b-d) 2D slices through reconstruction that are perpendicular to specimen tilt axis selected from the top, middle, and bottom of the reconstruction. Slices are shown with 0.85 gamma correction and full intensity range. Dimensions of rendered volume are 251 nm x 216 nm x 337 nm.
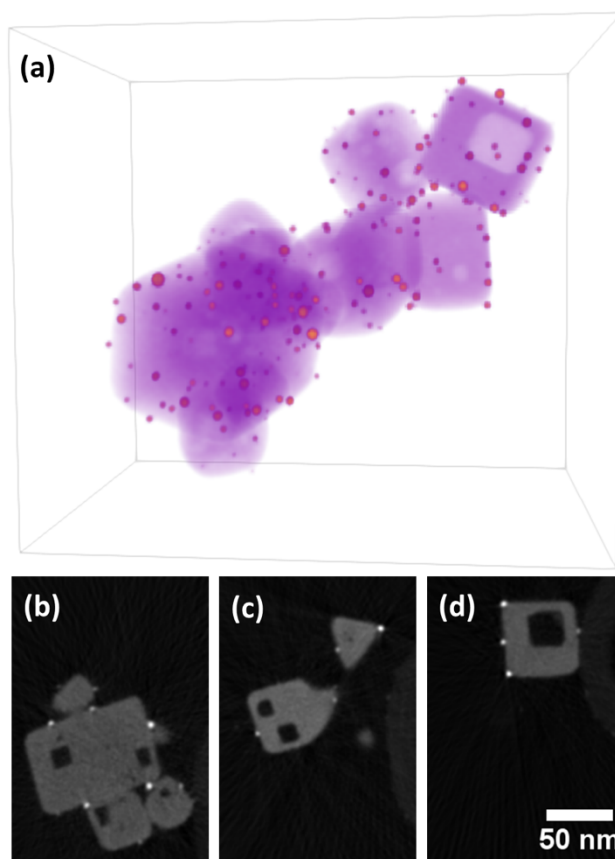
Figure C.5. Visualization of Au/STO reconstruction. (a) 3D volume rendering with orange indicating high intensity (gold nanoparticles) and purple indicating low intensity (STO). (b-d) 2D slices through reconstruction that are perpendicular to specimen tilt axis selected from the left, middle, and right of the reconstruction. Noise was reduced using a 1.25px radius Gaussian blur. Dimensions of rendered volume are 158 nm x 203 nm x 215 nm.

Figure C.5 shows no evidence of problems caused by the presence of the Nafion binder in the Au/STO sample. Nafion was observed in the sample primarily at points of contact between carbon nanofiber supports, but not coating the sample particles or wide areas of the nanofibers. Thus, despite the sensitivity of Nafion to the electron beam, no instability of the nanofiber support structure occurred during the tomography experiment. Furthermore, no accumulation of carbon contamination was observed, indicating that the Nafion was not mobile.

Eliminating the missing wedge significantly improves quantitative analysis of electron tomograms, as discussed in previous works (including Biermans et al., 2010; Kawase et al., 2007). Here we will focus on the segmentation of materials in a tomogram, as this is an essential prerequisite for quantitative analysis. When possible, it is preferable to segment tomograms automatically rather than manually, as this removes a large amount of subjective judgment and improves the efficiency of analysis to provide better throughput and statistical sampling. The simplest automatic segmentation approach is to separate materials based on intensity thresholds, chosen either manually or with an algorithm such as Otsu's method. This is particularly well suited to ADF STEM tomography, which provides atomic-number sensitivity. Accurate threshold segmentation requires that the histogram have distinct, well-separated peaks for each material of interest, and overlaps between the peaks will result in categorization errors for some voxels.
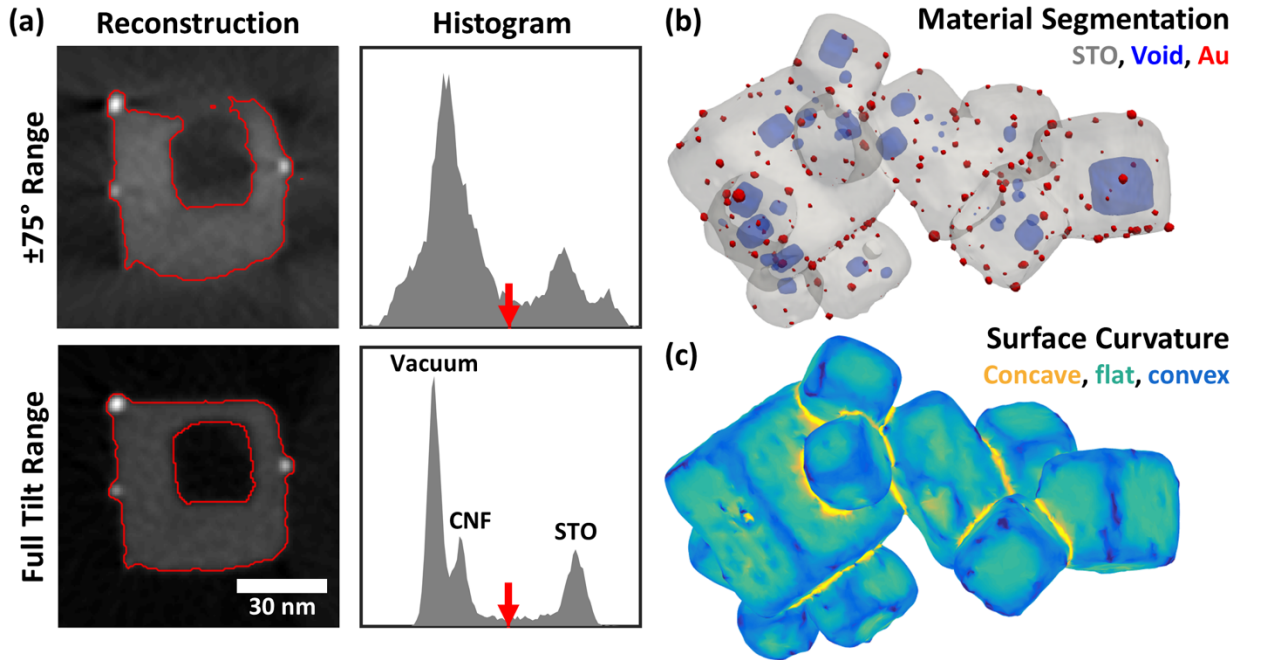

Figure C.6. (a) Comparison of Au/STO tomogram cross-sections and intensity histograms for ±75° tilt range and full tilt range. Red lines show the result of automatic threshold segmentation to separate the Au/STO sample from the background void and carbon fiber support. The threshold, chosen using

200

Otsu's method, is indicated with the red arrow in each intensity histogram. Histograms cover the same intensity range for each tomogram. (b) 3D surface rendering of full-range tomogram segmented by threshold and morphological filtering, showing Au particles, STO, and internal voids. (c) 3D rendering of STO surface in full-range tomogram with color indicating local mean curvature, separating curved convex (blue) and concave (yellow) regions from flat facets (green).

We illustrate the impact of the missing wedge on segmentation for the Au/STO tomogram in Figure C.6. For this tomogram, we seek to identify three distinct materials: Au, STO, and background (including both void and carbon fiber support). We proceed by first separating all specimen material (Au and STO) from the background, and then distinguishing between Au and STO. Before segmentation, a 1.5 pixel Gaussian blur is applied to reduce the impact of Poisson noise. This noise reduction narrows the three peaks in the histogram.

Missing wedge artifacts introduce spurious intensity variations that impair the accuracy of threshold segmentation, as illustrated in Figure C.6a. In the Au/STO tomogram reconstructed with a ±75° tilt range (considered a good range for conventional electron tomography,) the background and STO peaks are broad and overlapping, precluding accurate segmentation. The consequence is a mischaracterization of the specimen structure: edges are distorted so that flat faces appear curved and the STO wall separating the interior void is not resolved. These effects are especially severe for edges oriented in the direction of the missing wedge because essential information in that direction is missing in Fourier space. Furthermore, shadow artifacts that appear adjacent to highly scattering objects, such as the Au particles, could be mistaken as voids. For the full-range tomogram, peaks for each material are relatively sharp and the STO peak is well separated from the background so segmentation will be accurate and robust to the choice of threshold. Peaks for the vacuum and weakly scattering carbon are also resolved. The resulting segmentation accurately captures the structure of the Au/STO particle, including the surface geometry and void connectivity.

Although the Au particles occupy too few voxels to appear as a distinct peak in the histogram, they have much higher intensity than the STO and are easily selected by a threshold. However, because STO falls at an intermediate intensity, "bubbles" of blurred intensity around the bright Au particles will be selected by the STO thresholds and must be removed. One approach to correct this is the application of morphological filters to the binarized volumes. Using a 3.5nm diameter spherical structure element, we applied a morphological close operation on the combined Au+STO component, followed by a morphological open on the STO component. This removes the "bubble" artifact around the Au particles, as well as some noise in binarized volumes. A 3D rendering of the resulting segmentation, shown in Figure C.6b, demonstrates clean separation of the materials and accurate representation of the specimen morphology and void structure across the tomogram.

The undistorted results of segmentation for full-range tomography enable accurate quantification of a wide variety of structural properties relevant to powder samples. For instance, surface geometry plays a central role in the performance of catalytic nanomaterials, as different facets and step edges provide different catalytic activity. Electron tomography has been used for quantitative analysis of surface geometry in heterogeneous catalysts and other nanomaterials [31,32]. While missing wedge artifacts in conventional electron tomography introduce significant distortions in the apparent surface geometry, full-range tomography allows the surface of a powder specimen to be more accurately identified and analyzed. To illustrate, we calculated the mean curvature of the STO surface in the Au/STO tomogram (Figure C.6c). An isosurface mesh was extracted from the segmented STO component, and then down-sampled and smoothed to remove artifacts due to the discrete voxels of the segmented volume. For each vertex, the local curvature was calculated using a least-squares fit to the neighboring vertices, up to third-nearest neighbors [28]. Figure C.6c shows a rendering of the isosurface mesh where the color of each triangular face is determined by the average of the mean curvature values at its three vertices. This allows flat facets,

convex edges, and concave surfaces at cube junctions to be easily recognized and quantified, providing a route to connect the surface geometry to the chemical properties of the specimen.

C.5 Conclusions

Full-range electron tomography provides superior 3D reconstructions for quantitative analysis when compared to conventional electron tomography, which suffers distortions introduced by the missing wedge. Sample preparation methods that have been previously demonstrated for full-range tomography are poorly suited to nanostructured powder specimens, which are commonly studied with electron tomography. In this work, we present a new sample preparation technique for full-range tomography, where particles are collected on carbon nanofibers, which act as weakly scattering supports that extend well beyond the end of a tungsten needle. The demonstrated procedure is simple and produces samples compatible with commercial on-axis tomography holders using inexpensive consumables and equipment commonly available in sample preparation labs. This approach allows the creation of high-quality tomograms, as we have demonstrated for Pt/CNF fuel cell catalyst and Au/STO photocatalyst specimens using the simple, well-understood weighted back-projection algorithm. Full-range tomography enables accurate automatic segmentation and quantitative analysis. The sample preparation approach presented in this work could enable full-range electron tomography across a variety of samples that can be dispersed in liquid to provide accurate, quantitative analysis of their 3D nanostructure.

C.6 Specimen Preparation Procedure Summary

1) Clean needles with oxygen or argon plasma.

2) Mix fibers in ethanol and Nafion binder (as needed) and ultrasonicate until well dispersed. Suggested concentration: 0.5 mg fibers per 1 mL ethanol, 0.02 wt% Nafion solution.

3) Pipette ~1mL of fiber suspension into a shallow container, such as a ceramic multi-welled plate.

4) Dip needle tip in fiber suspension for a few seconds. Check for fiber collection and arrangement in visible light microscope, and repeat dipping until acceptable fiber arrangement is collected. If fibers do not adhere well to needle, needle surface may be primed by dipping in M-Bond and then in a dry carbon nanofiber powder before curing.

5) Repeat step (4) for several needles.

6) If the fibers collected are the sample of interest, skip to checking samples in TEM. If a sample will be loaded onto the fibers, proceed with step (7).

7) Mix sample in ethanol and ultrasonicate until well dispersed. Suggested concentration: 0.5 mg sample per 1 mL ethanol.

8) Pipette ~1mL of sample suspension into shallow container.

9) Dip needle tip in sample suspension for a few seconds. Check in visible light microscope – sample collected may or may not be visible, and fibers may rearrange each time they are dipped. Re-dip at your discretion. Repeat for each needle with collected fibers.

10) Check samples in (S)TEM until a suitable sample is found.

C.7 Acknowledgements

C.8 References

[1] E. Padgett, R. Hovden, J.C. DaSilva, B.D.A. Levin, J.L. Grazul, T. Hanrath, and D.A. Muller, Microsc. Microanal. **23**, 1150 (2017).

[2] M. Weyland and P. Midgley, in *Transm. Electron Microsc.*, edited by C.B. Carter and D.B. Williams (Springer International Publishing, Cham, Switzerland, 2016).

[3] D.N. Mastronarde, J. Struct. Biol. **120**, 343 (1997).

[4] P.A. Midgley and M. Weyland, Ultramicroscopy **96**, 413 (2003).

[5] K.J. Batenburg, S. Bals, J. Sijbers, C. Kübel, P.A. Midgley, J.C. Hernandez, U. Kaiser, E.R. Encina, E.A. Coronado, and G. Van Tendeloo, Ultramicroscopy **109**, 730 (2009).

[6] B. Goris, W. Van den Broek, K.J. Batenburg, H. Heidari Mezerji, and S. Bals, Ultramicroscopy **113**, 120 (2012).

[7] R. Leary, Z. Saghi, P. a Midgley, and D.J. Holland, Ultramicroscopy **131**, 70 (2013).

[8] Z. Saghi, D.J. Holland, R. Leary, A. Falqui, G. Bertoni, A.J. Sederman, L.F. Gladden, and P.A. Midgley, Nano Lett. **11**, (2011).

[9] Y. Jiang, R. Hovden, D.A. Muller, and V. Elser, Microsc. Microanal. **20**, 796 (2014).

[10] T. Dahmen, P. Trampert, N. de Jonge, and P. Slusallek, MRS Bull. **41**, 537 (2016).

[11] I. Arslan, J.R. Tong, and P.A. Midgley, Ultramicroscopy **106**, 994 (2006).

[12] S. Lanzavecchia, F. Cantele, P.L. Bellon, L. Zampighi, M. Kreman, E. Wright, and G.A. Zampighi, J. Struct. Biol. **149**, 87 (2005).

[13] D.P. Barnard, J.N. Turner, J. Frank, and B.F. McEwen, J. Microsc. **167**, 39 (1992).

[14] N. Kawase, M. Kato, H. Nishioka, and H. Jinnai, Ultramicroscopy **107**, 8 (2007).

[15] T. Ito, U. Matsuwaki, Y. Otsuka, G. Katagiri, M. Kato, K. Matsubara, Y. Aoyama, and H. Jinnai, in *Handb. Fuel Cells* (John Wiley & Sons, Ltd, Chichester, UK, 2010).

[16] T. Ito, U. Matsuwaki, Y. Otsuks, M. Hatta, K. Hayakawa, K. Maysutani, T. Tada, and H. Jinnai, Electrochemistry **79**, 374 (2011).

[17] E. Biermans, L. Molina, K.J. Batenburg, S. Bals, and G. Van Tendeloo, Nano Lett. **10**, 5014 (2010).

[18] X. Ke, S. Bals, D. Cott, T. Hantschel, H. Bender, and G. Van Tendeloo, Microsc. Microanal. **16**, 210 (2010).

[19] Z. Saghi, G. Divitini, B. Winter, R. Leary, E. Spiecker, C. Ducati, and P.A. Midgley, Ultramicroscopy **160**, 230 (2016).

[20] X. Wang, F.A. Shah, A. Palmquist, and K. Grandfield, ACS Biomater. Sci. Eng. **3**, 49 (2017).

[21] M. Andrzejczuk, A. Roguska, M. Pisarek, M. Hołdyński, M. Lewandowska, and K.J. Kurzydłowski, Micron **95**, 35 (2017).

[22] C.M. Palmer and J. Löwe, Ultramicroscopy **137**, 20 (2014).

[23] J. Hernández-Saz, M. Herrera, and S.I. Molina, *FIB Nanostructures* (Springer International Publishing, Cham, 2013).

[24] H. Jinnai, R.J. Spontak, and T. Nishi, Macromolecules **43**, 1675 (2010).

[25] K.F. Jarausch and D.N. Leonard, Imaging Microsc. **9**, 24 (2007).

[26] T. Kizuka, T. Sumi, S. Bansho, and T. Saito, Jpn. J. Appl. Phys. **40**, L56 (2001).

[27] B.D.A. Levin, E. Padgett, C.-C. Chen, M.C. Scott, R. Xu, W. Theis, Y. Jiang, Y. Yang, C. Ophus, H. Zhang, D.-H. Ha, D. Wang, Y. Yu, H.D. Abruña, R.D. Robinson, P. Ercius, L.F. Kourkoutis, J. Miao, D.A. Muller, and R. Hovden, Sci. Data **3**, 160041 (2016).

[28] D.-J. Kroon, MATLAB Cent. File Exch. (2014).

[29] D.-J. Kroon, MATLAB Cent. File Exch. (2010).

[30] S. Preibisch, S. Saalfeld, and P. Tomancak, Bioinformatics **25**, 1463 (2009).

[31] H. Jinnai, Y. Nishikawa, R.J. Spontak, S.D. Smith, D. a Agard, and T. Hashimoto, Phys. Rev. Lett. **84**, 518 (2000).

[32] E.P.W. Ward, T.J. V Yates, J.-J. Fernández, D.E.W. Vaughan, and P.A. Midgley, J. Phys. Chem. C **111**, 11501 (2007).